UNIVERSITY OF TASMANIA

AMC
AUSTRALIAN MARITIME COLLEGE

Numerical Modelling of Hydrofoil Fluid-Structure Interaction

Suzanne Ruth Hutchison

Submitted in fulfilment of the requirements for the degree of

Doctor of Philosophy

Academic Supervisors:

Assoc. Prof. Paul Brandner
Prof. Gregory Walker
Dr. Jonathan Binns
Dr. Alan Henderson

March, 2012

Declaration of originality and authority of access

This thesis contains no material which has been accepted for a degree or diploma by the University or any other institution, except by way of background information and duly acknowledged in the thesis, and to the best of my knowledge and belief no material previously published or written by another person except where due acknowledgement is made in the text of the thesis, nor does the thesis contain any material that infringes copyright.

This thesis may be made available for loan and limited copying in accordance with the *Copyright* Act 1968.

.....

Suzanne R. Hutchison (March 26, 2012)

Acknowledgements

Foremost I would like to express my gratitude and thanks to my supervisors, Assoc. Prof. Paul Brandner, Prof. Gregory Walker, Dr. Jonathan Binns and Dr. Alan Henderson for their ongoing support, guidance and encouragement. Additional thanks to Brendon Anderson for support and encouragement.

I would also like to thank the Australian Maritime College (AMC) and Defence Science and Technology Organisation (DSTO) for the opportunity to undertake this research. The financial support for this study was provided through an Australian Postgraduate Award, DSTO and the cavitation research laboratory at the AMC.

To my fellow office buddies throughout my time of study Hugh, Ronie, Bryce and Polly, thanks for putting up with me good and bad. I would like to express my gratitude to my fellow-PhD students for the entertaining lunch time discussions and encouragement, it is greatly appreciated. A special thanks to Lou Mason for continually asking questions and forcing me to talk about my topic. I would also like to thank all the AMC and DSTO staff for creating a friendly environment in which to undertake my studies.

Lastly I would like to with all my heart thank my family. Thank you to my parents for always encouraging me to pursue anything that I set my mind to. To my brothers and their wives, in-laws and sister in-law thank you for understanding and being supportive. To my extended family and friends thanks for always being interested in what I'm undertaking.

I wish to thank my husband Chris, for marrying me and then a month later letting me start a PhD. Thank you for listening, encouraging, proof reading, being supportive and just generally being you.

Abstract

Marine propellers operate in unsteady non-uniform wake regions generated by the hull and control surfaces subjecting the propeller to unsteady loading. Hydroelastic tailoring of propeller blades is a method to reduce unsteady loading as a propeller blade passes through a wake deficit. This project seeks to gain greater insight into the effect of hydroelastic tailoring on a propeller by simplifying the problem into a single hydrofoil with a sinusoidal pitch oscillation. In this study, a hydrofoil with a NACA 0009 section and a trapezoidal planform area was used to investigate bending hydroelastic effects numerically using fluid-structure interaction modelling. The complexity of the numerical model was varied in a systematic manner, starting with a two-dimensional foil through to a three-dimensional two-way coupled fluid-structure interaction simulation. The commercial package ANSYS was used with CFX for computational fluid dynamics and ANSYS mechanical for the structural simulation.

In this study ANSYS was demonstrated to be a suitable tool to simulate fluid-structure interaction in the case of an oscillating hydrofoil in pure pitch. The computational fluid dynamics results were validated in two-dimensions using NACA 0012 and 0015 sections for both static and dynamic cases using published experimental results. In three-dimensions, stainless steel and aluminium, were investigated in addition to the rigid (uncoupled) case. This study varies independent parameters including Reynolds number, reduced frequency, amplitude of pitch oscillation and the mean incidence controlling the hydrofoil response.

Comparison of static one-way and two-way coupled results shows that there are small but apparent differences between predicted bending deformations. However, bending deformations were shown to virtually have no effect on forces and moments, at least up to moderate incidences. Rigid three-dimensional lift and moment predictions show similar behaviour to both the two-dimensional unsteady viscous predictions and classical linear inviscid theory for cases of zero mean incidence. In particular, lift and moment vary linearly with amplitude of oscillation for all reduced frequencies. The lift and moment amplitude minima occur at reduced frequencies of about 0.6 and 0.7 respectively for both two and three-dimensional predictions; However, in the three-dimensional case the amplitudes, relative to the lift and moment at static incidence are reduced. For a four degrees mean incidence, the amplitudes of the lift and moment minima are significantly reduced for two and three-dimensional predictions compared with the zero degree mean incidence case. Above a reduced frequency of one, for four degrees mean incidence, the rigid three-dimensional lift and moment amplitude predictions no longer vary linearly with incidence amplitude. The dynamic coupled analysis typically showed bending deformations to be similar to those for static predictions at a zero mean incidence but to be reduced for a four degrees mean incidence at maximum incidence. Lift and moment for the dynamic coupled cases are only slightly influenced for reduced frequencies less than one depending on material properties and Reynolds number. For a reduced frequency greater than one the lift and moment show a slight increase and vary non-linearly with the incidence amplitude.

Contents

List of Figures

List of Tables

Nomenclature

A	Amplitude
A_{excit}	Excitation amplitude
Ay	Tip motion amplitude
AR	Aspect ratio
A_{ref}	Reference Area
a_s	Speed of sound
b	Span
$C(k)$	Theodorsen's coefficient
C_D	Drag coefficient
C_{D0}	Drag coefficient corresponding to the equivalent static drag at maximum dynamic α.
C_L	Lift coefficient
C_{L0}	Lift coefficient corresponding to the equivalent static lift at maximum dynamic α
C_M	Moment coefficient
C_{M0}	Moment coefficient corresponding to the equivalent static moment at maximum dynamic α
C_p	Pressure coefficient
$C_{\delta L}$	Displacement due to bending coefficient
C_τ	Wall shear coefficient
Cn	Courant number
c	Chord
(c)	Damping matrix
$\bar{c}$	Mean chord
D	Drag
D_o	Diameter
E	Young's modulus
F(t)	Load vector with respect to time
f	Frequency
f_n	Natural frequency
G	Shear modulus
I	Second Moment of Area
J	Advance coefficient
J_I	Polar moment of inertia
K	Spring constant

(K)	Stiffness matrix
k	Reduced frequency
L	Lift
M	Moment
M	Mass matrix
m	Mass
m_a	Added mass
N	Frequency of rotation of a propeller
n	Harmonic order number
P	Propeller pitch
p	Pressure
Re	Reynolds number
Re_c	Reynolds number using a reference chord of unit length(i.e. $c = 1$)
r	Radius
S	Span
St	Strouhal number
$S(k)$	Sears' coefficient
t	Time
T	Period
t	Model thickness
U	Velocity
$\overline{U}$	Total mean axial velocity
u	Nodal displacement vector
$\dot{u}$	Nodal velocity vector
$\ddot{u}$	Nodal acceleration vector
W_g	Up wash velocity normal to the chord
Greek letters	
α	Incidence angle
$\bar{\alpha}$	Mean dynamic incidence angle
α_{ss}	Static stall incidence angle
α_{max}	Maximum unsteady incidence angle
α_{min}	Minimum unsteady incidence angle
β	Fluid pitch angle
β_i	Induced pitch angle
β_P	Fluid pitch angle
Γ_{disp}	Mesh stiffness
γ_b	Loading on the foil surface under harmonic forcing
γ_w	Vortex sheet strength in the wake
Δ	Change in variable from mean
δ_m	Mesh displacement relative to previous model
δ	Deflection
ζ	Damping factor
θ	Twist in degrees
λ	Wave length of spatially non-uniform flow
λ_p	Wave length of propeller rotation

λ_g	Wave length of the gust
μ	Viscosity
ν	Kinematic viscosity, μ/ρ
ρ	Density
τ	Wall shear
Φ_D	Drag phase lag with respect to the α
Φ_L	Lift phase lag with respect to the α
Φ_M	Moment phase lag with respect to the α
ω	Circular frequency
ω_p	Propeller circular frequency
Subscript	
Al	Aluminium
m	Material
rms	Root Mean Square
SS	Stainless Steel
w	Water
∞	Free stream variable

Abbreviations

2D	2-Dimensional
3D	3-Dimensional
BEM	Boundary Element Model
CFD	Computational Fluid Dynamics
CRL	Cavitation Research Laboratory
DARPA	Defence Advanced Research Project Agency
FEA	Finite Element Analyses
FSI	Fluid-Structure Interaction
LDV	Laser Doppler Velocimetry
NAB	Nickel-Aluminium-Bronze alloy
RANSE	Reynolds Average Navier Stokes Equation
SST	Shear Stress Transport
VLM	Vortex Lattice Model

Chapter 1

Introduction

Although there has been extensive investigation of Fluid Structure Interaction (FSI) and/or aeroelastic effects in aeronautical applications, such as; gas turbine blades, helicopter rotors, wind turbine blades and aeroplane wings; limited investigation of these effects have been conducted for low aspect ratio hydrofoils and marine propellers. Helicopter rotor blades, wind turbine blades and aeroplane wings are usually investigated using two dimensional (2D) fluid dynamics analysis. Marine propellers are, in relation to the above, low in aspect ratio and inherently three dimensional (3D). Additionally, marine propellers operate in unsteady non-uniform wake regions generated by the hull and control surfaces subjecting the propeller to unsteady loading.

Propellers have traditionally been made from a nickel-aluminium-bronze (NAB) alloys, which have excellent corrosive resistance and a high yield strength but are expensive to machine, prone to fatigue-induced cracking and have relatively poor acoustic damping [2]. Possible alternatives to NAB cited by Mouritz et al. [80] are stainless steel, titanium alloy, sonaston and composites. In recent times there has been growing interest into the use of hydroelastic tailoring of propeller blades to reduce the acoustic signature, dampen vibrations, delay cavitation and broaden the efficiency peak. Hydroelastic tailoring makes use of material properties to alter the amplitude of deflection. This varies the geometry and the flow physics to favourably alter the resulting response of the structure and delay onset of cavitation.

This chapter introduces the concept of hydroelasticity, previous and related work to propeller hydroelasticity, motivation and the link from a propeller to an oscillation hydrofoil and methodology undertaken in this thesis.

1.1 Hydroelasticity

Hydroelasticity is akin to aeroelasticity in which significant mutual interaction occurs between inertia (dynamics), elastic (solid mechanics) and fluid dynamics [25]. Hydroelastic phenomena can be visualised using items in our everyday environment,

such as; a tree that responds to the wind and bends, seaweed or kelp flutters in the tide reacting to the turbulent flow; a flag flapping or a leaf deforming in the wind. Examples of hydroelastic phenomena in sailing is the effect of a composite mast bending depending on whether the yacht is sailing upwind or downwind [6, 79]; and a sail adapting shape depending on the separated regions and the fluid flowing around it [102]. Figure 1.1 shows a schematic of a union plot with each circle representing a field of study relating to hydroelasticity. Where the circles overlap a combined area is produced symbolising a situation were each field of study has an influence on each other. These areas overlap producing the following areas of study (figure from [49] adapted to hydrodynamics):

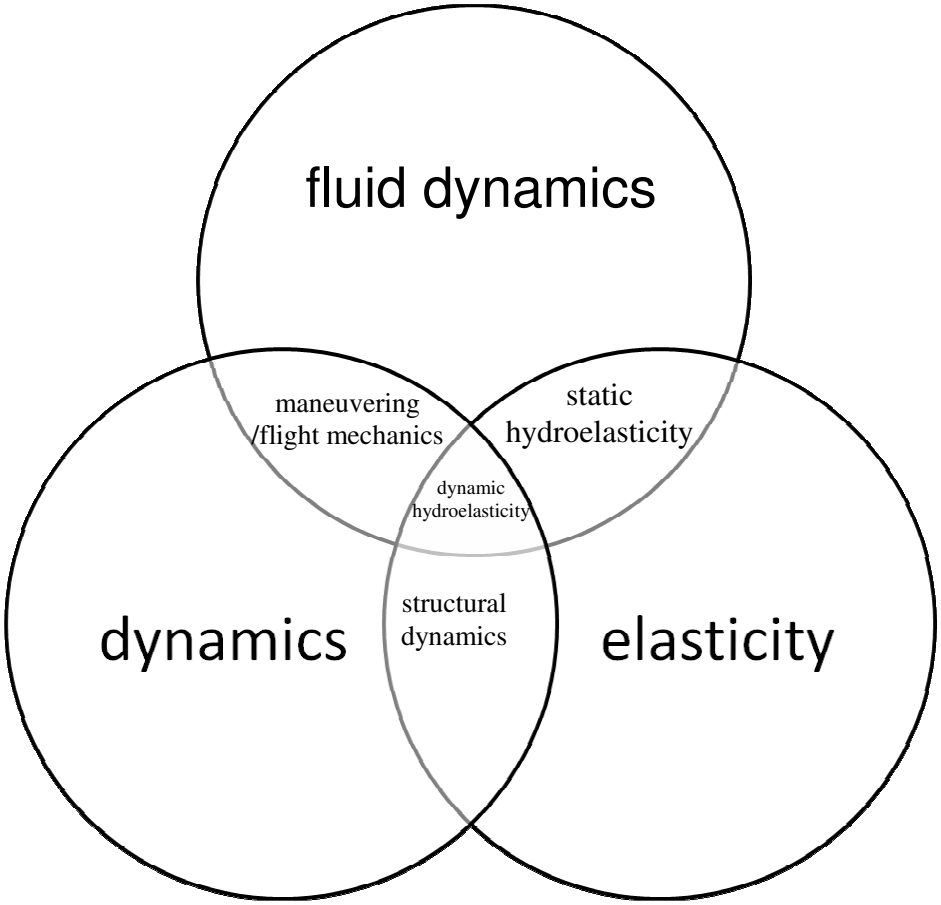

Figure 1.1: Schematic of the field of hydroelasticity [49]

1. Between elasticity and dynamics (structural dynamics);
2. Between fluid dynamics and dynamics (maneuvering or flight mechanics);
3. Between fluid dynamics and elasticity (static hydroelasticity),
   Where inertial forces have little effect; and,

4. Among all three (dynamic hydroelasticity),
   Where the inertial forces become important, and phenomena such as flutter, galloping or vortex induced vibration occur.

Any of areas in points 1, 3 or 4 can fall under the hydroelastic banner but due to historical reasons only points three and four tend to be considered hydroelastic [11]. It can be difficult to distinguish between static and dynamic hydroelasticity as the change can be dictated by the point at which the inertial interaction is significant or there is a natural mode of vibration in the static problem that may cause an instability forcing the system dynamic.

A common term used when discussing hydroelasticity is FSI: a descriptive term that explains the physics during a hydroelastic reaction, as shown in Figure 1.2. This figure shows the positive feedback of the system. In a static FSI case, fluid flow and the structure are coupled through the force exerted on the structure by the fluid, resulting in the fluid force causing the structure to deform. As the structure deforms, its orientation to the flow changes, and the fluid force may change. The orientation and velocity of the structure relative to the fluid flow determines the fluid force. As the fluid exerts a force on the structure, the structure exerts a reaction force on the fluid [11].

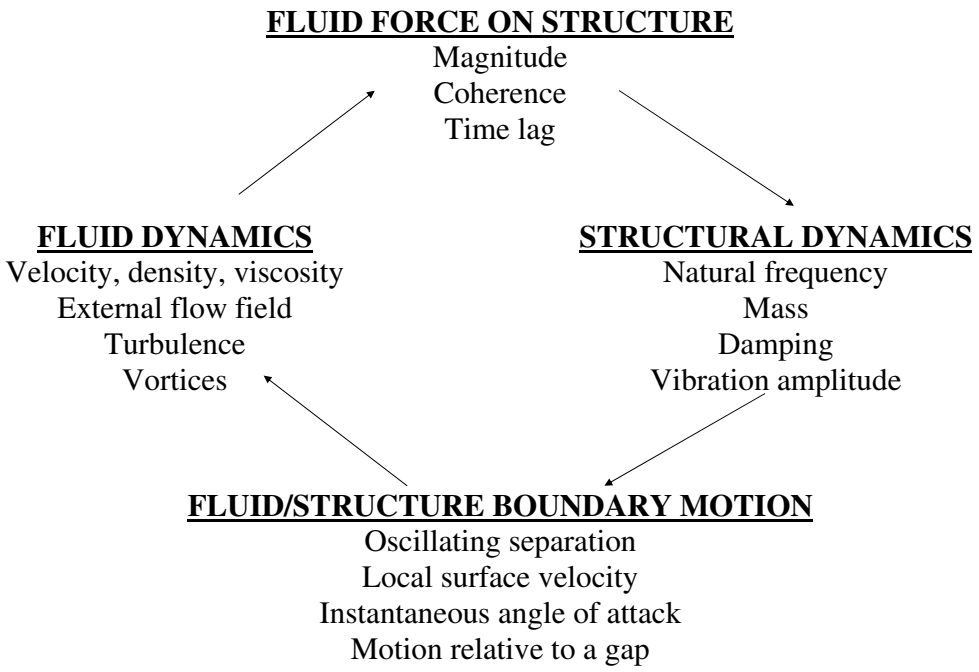

Figure 1.2: Feedback loop between the fluid and structure [11]

1.2 Marine Propellers

Mouritz et al. [80], reviewed recent composite applications in naval ships and submarines. Composites for marine propellers have the advantage that fibres can be aligned with the major hydrodynamic loadings and centripetal forces, to minimise strain. Improved vibration damping properties and fatigue performance can also be achieved. Composites have the potential to reduce the magnitude of resonant vibrations in the engine and propeller shaft by about 25%, resulting in less hull vibration and noise [80]. Other possible benefits include lower electrical/magnetic signatures, lower noise signatures, reduced corrosion and increased cavitation inception speeds by using flexible blades [80].

Milcachy et al. [78] proposed a method for the design of flexible composite shape-adaptive propellers. They used a steady flow analysis with a linear propeller's variation in efficiency with respect to advance ratio. Applying an iterative optimisation they found an optimum loaded shape, then derived the unloaded shape and resulting composite lay-up for a hydrofoil and a propeller. They also proposed a 'closed form' expression for the efficiency gain. They did not include any dynamic or vibration considerations, but focused on the structural aspect with little information about the nature of the hydrodynamic loading.

1.2.1 Experimental Modelling

Searle et al. [85] tested and completed sea trials with four composite propellers and a NAB propeller all with the same geometry for benchmarking. These tests were preliminary but demonstrated that composite propellers could be as efficient as the NAB propeller. Secondly, the tests showed that it is possible to tailor the elasticity of the material to change the shape of the propellers efficiency envelope.

Gowing et al. [40] conducted experiments on a self twisting hydrofoil. The foil was constructed using laminated construction techniques to produce an orthotropic composite material that twists as the load is applied. They thought that this concept could be utilised on a propeller blade so that the blade would twist in response to loads. The twisting results in the tip deflecting and reducing the loading and strength of the tip vortex and the likelihood of cavitation. This demonstrated hydroelastic tailoring of the foil can be utilised to delay cavitation, with the lift and drag characteristics remaining unchanged.

As part of a three year Office of Naval Research (ONR) sponsored project, an experimental investigation of flexible composite propellers was conducted by Chen et al. [24]. They published the design, fabrication and testing of pitch-adapting composite propellers. They investigated the potential performance improvements through pitch adaptation with composite propellers through delayed cavitation and vibration performance, reduced weight and manufacturing cost. Lifting-surface theory, panel methods and finite element analysis (FEA) were used throughout the design phase to optimise the shape whilst coupling hydrodynamic loading with

structural deformation. The loaded body was calculated in FEA to obtain the deformed shape. This deformed shape was then used to recalculate fluid forces.

Three propellers were selected out of the final four designs; one rigid (P5474) and two pitch adaptive. The rigid propeller was not truly rigid and did exhibit some change in rake. Of the two flexible propellers, P5475 had a larger pitch change than P5487. The experimental results showed the efficiency improvement was up to 5% for the flexible propeller when compared with the rigid. To provide some context, Breslin and Andersen [17] provides some information about unconventional propellers that details power reduction in percentages for ducted propellers of 5-20%. Although perhaps a situation closer to hydroelastic reponse is an optimization problem with an improvement in efficiency of approx 4% [56] or a 6% improvement due to addition of antifouling paint[57].

The flexible propeller's performance improvements were more significant in wake inflow than in open water. This was due to each blade having the ability to automatically adjust its pitch distribution to better align to the local variation in the wake as it rotated [106]. In the paper's review discusion, Mr Eckhard Praefke noted, as shown in figure 1.3, that the deflection of the two flexible propellers (P5475 and P5487) were almost directly in line but the rigid propeller (P5474) showed the opposite behaviour. He suggested that perhaps the behaviour might be the result of the effect of added mass on the dynamic blade deflections.

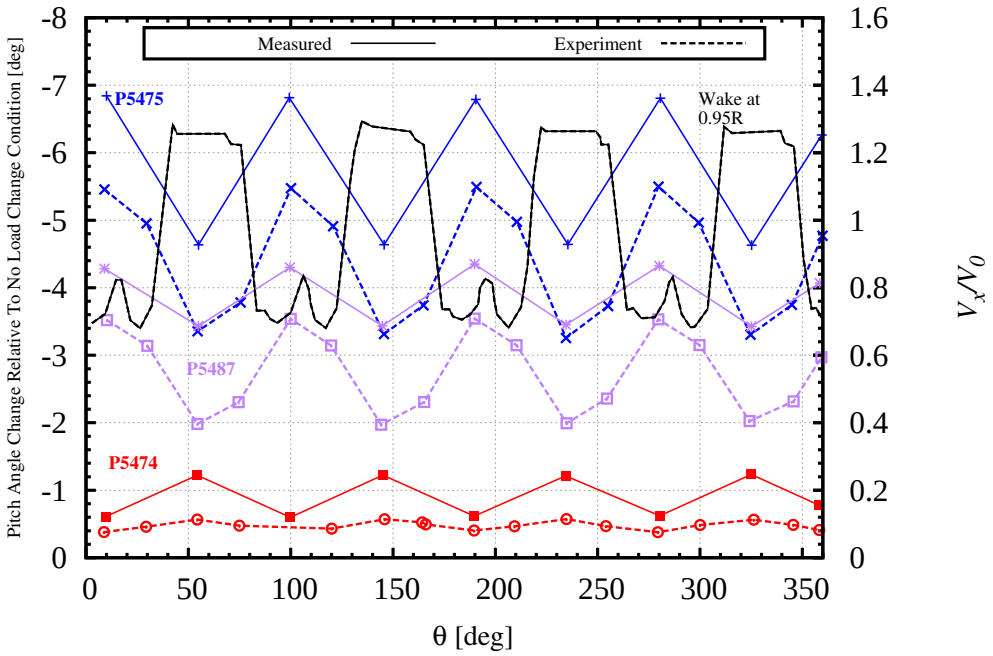

Figure 1.3: Measured and predicted pitch change of P5474, P5475 and P5487 in a four cycle wake [24] showing the phase of three propeller's with varying flexibility

1.2.2 Numerical Modelling

Two of the most common terms when referring to the type of FSI are one-way and two-way analyses. These terms reflect how the loads and deflections are transferred. A one-way analysis solves the fluids and then uses the resultant loads to calculate the structural deflection. A two-way model will iterate between the fluid and structural models to obtain a converged solution.

Uncoupled Models

Classical hydrodynamic models of propeller action normally fall into four categories: momentum or blade element models, lifting line models, lifting surface models and boundary element models (BEMs) [20]. Momentum models proposed by Rankine in 1865 are based on the axial motion of the water as the propeller is idealised as a disk. This theory was based on three assumptions: the propeller consisted of an infinite number of blades and hence did not account for blade shape; the propeller operated in an ideal fluid; and, the propeller can generate thrust without causing rotation in the slip stream [20]. This model was later modified which allowed the propeller to impart swirl. This theory is known as the Rankine-Froude momentum theory. In 1878 Froude developed blade element theory. Momentum or blade element models are based on dividing the blade into a large number of spanwise strips. Each strip can be regarded as a foil section subjected to a resultant incident velocity [20]. This velocity consists of an axial velocity combined with a rotational velocity, which varies linearly along the blade. Froude theory forms the basis of modern blade element methods [20].

The lifting line model is a mathematical model of propeller action; it assumes the aerofoil blade sections are replaced by a single line vortex whose strength varies from section to section. Lifting line models are ideal for aeroplane propellers due to their high aspect ratio but not for marine propellers with a low aspect ratio [20]. The vortex-lattice model (VLM) are a subsection of lifting surface models. The VLM is based on the concept of straight line segments of vortices joined together to make vortex panels that cover the propeller blade [20]. The VLM places vortex and source lattices on the mean camber surface of the blade and therefore does not capture the effect of blade thickness [64]. The VLM was first applied to an unsteady propeller by Kerwin and Lee [62].

BEMs or panel methods are based on dividing the propeller surface into elements and applying the appropriate sources/sinks (no circulation), and dipoles (allows circulation). One well known BEM code for predicting propeller flow is PROPCAV (PROPeller CAVitation) [63]. The BEM code has been developed to model a 3D cavitating unsteady flow model of a propeller by Young and Kinnas [109] and has been further expanded to include supercavitating propellers [108, 110–112] and surface piercing propellers [104, 107, 108, 112, 113]. Both the lifting surface and BEM methods accounted for viscous drag by standard drag coefficients and have been extended to couple with structural codes.

Coupled Models

Traditionally fluid forces and structural responses were calculated uncoupled. Fluid forces were calculated assuming an infinitely rigid blade with no geometric variation and then used to calculate the structural deflections. The first published attempt to estimate the strength of propeller blades was made by Taylor [92]. To apply the beam stress formula to a propeller he assumed the blade was a cylindrical section. The deflections were based on a simple cantilever beam loaded linearly over the length [84]. The simple cantilever beam approach worked well for conventional blade geometry without skew and with relatively high aspect planforms [4]. In all of these models, the fluid loads acting on the blade surface were obtained by employing either the quasi-steady method, lifting line method, or lifting surface method.

In 1962 Breslin [18] wrote a review and extension of theory for near-field propeller-induced vibratory effects. In 1980 Brooks [19] developed a theory for a flexible propeller operating in a spatially non-uniform inflow and conducted a series of experimental studies. The theoretical model is based only on the first mode of vibration. This study concluded that propellers in non-uniform flow fields can develop widely differing unsteady response where the excitation is near the blade's fundamental natural frequency. The hydrodynamic induced damping is a key contributor to blade behaviour. The damping is determined primarily by blade geometry and the fundamental mode shape. In some cases, the unsteady loading near resonance may reduce the unsteady forces over a large frequency range. This occurs typically for propellers with large hydrodynamic damping and for loading frequencies above the propeller's natural frequency [19].

Two-Way FSI

Atkinson and Glover [4] in 1988 made the first step in creating a practical design tool to account for two-way coupled FSI. They used an unsteady lifting surface analysis developed by Szantyr [91] coupled with a finite element model using thick shell elements to analyse the performance of a propeller. This procedure was applied to both a highly skewed and a low aspect propeller blade. The hydroelastic effects of the highly skewed propeller showed that it can generate high stress regions and significantly affect the propeller performance. The low aspect propeller behaved differently such that in both cavitating and non-cavitating cases the blade exhibited high local deflections around the outer edge and near the blade tip. In the cavitating analyses the hydroelasticity greatly affected the size and shape of the produced cavity.

Lin and Lin [69] developed a non-linear coupling procedure with a non-cavitating steady lifting surface method. The calculation included thrust, torque and efficiency coefficients, and deflections. The coupling procedure used displacements as unknowns for the structural calculations and vortex strength in the fluid. They

concluded that reducing blade thickness increased deflection, thrust and torque but did not alter efficiency. This work considered the effect of geometric non-linearity.

Young developed a fully coupled 3D BEM combined with a 3D FEM to determine the hydroelastic response of surface piercing [104, 109, 110], supercavitating [111] and cavitating [109] propellers. Young used the BEM code PROPCAV coupled with the 3D transient FEM code DYNAFLOW, as well as ABAQUS in later work with composite propellers [105, 116]. Young [104] details two hydroelastic coupling methods, a BEM to a FEM and BEM to a single degree of freedom (SDOF) model. Details of the BEM and FEM coupling can be found in [105, 110, 111]. The hydroelastic coupling method assumed small blade deformations, allowing linear decomposition of the perturbation velocity potential. Applying Bernoullis equation, the total pressure was expressed in terms of the rigid and elastic blade components, with the change in load stiffness and damping matrices due to the contribution of centrifugal and Coriolis' forces given in Young [105]. Added mass and hydrodynamic damping matrices were computed using the BEM and are superimposed via user-defined hydroelastic elements in ABAQUS [105, 116, 117]. Coupling of the hydrodynamics with a structural analysis model to include the effect of blade vibration is described in [113].

Young et al. [117] used the BEM/FEM model to predict steady and unsteady performance of flexible composite propellers operating in a spatially-varying wake. They compared the results of rigid and flexible blades traversing a wake deficit. The rigid composite propeller as described in [117], undergoes predominantly bending with minimal twisting [114]. Whereas the flexible propeller undergoes coupled bending and twisting deformations. To validate their predictions Young [106, 116] and Young et al. [117] compared their results with experimental data for two composite propellers from tests conducted by the Naval Surface Warfare Center, Carderock division (NSWCC) as described in the previous section. These tests were conducted in open water [105, 106, 117] and behind a four cycle wake screen [106, 117]. The measurements included thrust, torque, blade deflection, cavitation inception, and dynamic strains. From these studies, Young [105] concluded that flexible composite propellers can achieve higher propeller operating efficiency than their metallic counterparts by allowing the blade to de-pitch near the tip to reduce the load. This work makes an argument for the need for hydroelastic prediction in the case of more extreme geometries (highly skewed), where high stress concentrations, severe blade distortions and/or resonant blade vibrations may occur [115]. Young concluded that pure bending without twisting has negligible influence on the propeller performance [114]. The flexible propeller showed an improved efficiency either side of the design advance coefficient (J) value [114].

Liu and Young [70] used a BEM/FEM coupled solver, developed by Young to study the deformation coupling effects on hydroelastic behaviour of composite marine propellers. A sample design was used to investigate the influence of material properties and fibre orientations on the twisting deformation. A correlation was identified between the twisting deformation, pitch alteration, and propeller efficiency. Young et al. [118] investigated the effects of the anisotropic behaviour of

composite marine propellers in both open water and an unsteady wake. Preliminary analyses indicated that self-twisting composite propellers may be more susceptible to hydroelastic instability failures during 'Crash-back'. To investigate this operating condition advanced FSI analysis is necessary. 'Crash-back' is an emergency operating condition of a submarine when the submarine reverses its power while travelling forward [87].

1.3 Motivation

This project seeks to gain greater insight into the effect of hydroelastic tailoring on a submarine propeller by simplifying the problem into a single hydrofoil with a sinusoidal pitch oscillation. This approach enabled the investigation of the effect of bending deformation in isolation using a simple hydrofoil analogy to a propeller operating in a non-uniform flow. This enables investigation into hydroelastic trends across a broad range of oscillation frequencies and changes in amplitude without experimental limitations.

Recent increases in computer power coupled with advances in numerical methods, enables coupled two-way analyses of FSI in a reasonable time frame for simple geometries and reasonable grid sizes. This is not to say that numerical simulations can completely replace experiments, since experiments are essential to validate computational simulation.

The major motivation of this thesis is to use RANSE methods in FSI prediction and to investigate the effect of bending deformation in isolation using a simple hydrofoil analogy to a propeller operating in a non-uniform flow.

1.4 Problem Development

The propeller operates in the aft body of a submarine. A 'typical' submarine consists of four control surfaces on the aft body and a fairwater in the mid section as shown in Figure 1.4. The shape of the after body and control surface preceding the propeller causes deficits in the wake. As the propeller blade rotates through these deficits the local blade section incidence and velocity magnitude vary. The blade response will vary depending on the dynamic, elastic and hydrodynamic properties of the propeller and coupling effects of different motions, added mass and damping.

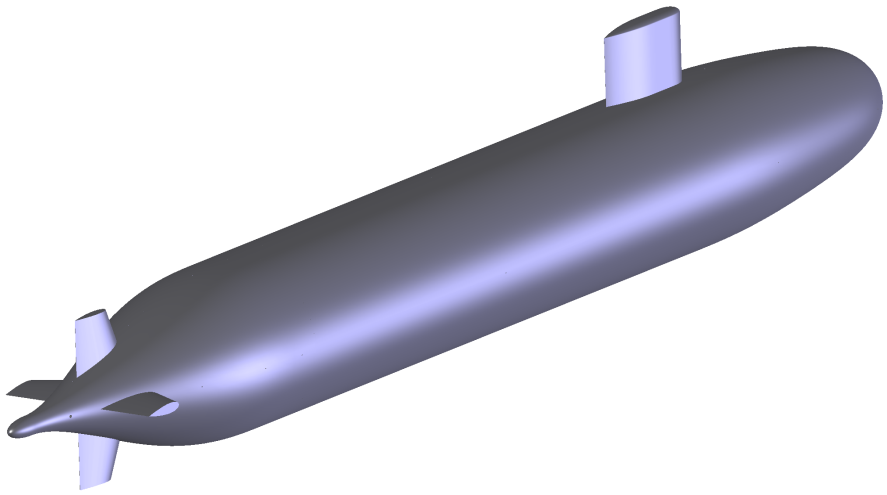

Figure 1.4: DARPA SUBOFF submarine geometry

To compare a hydrofoil with a propeller; the 'gust response' of a propeller blade passing through a wake deficit is compared with a 2D foil (flat plate) unsteady sinusoidal 'gust response', see Figure 1.5.

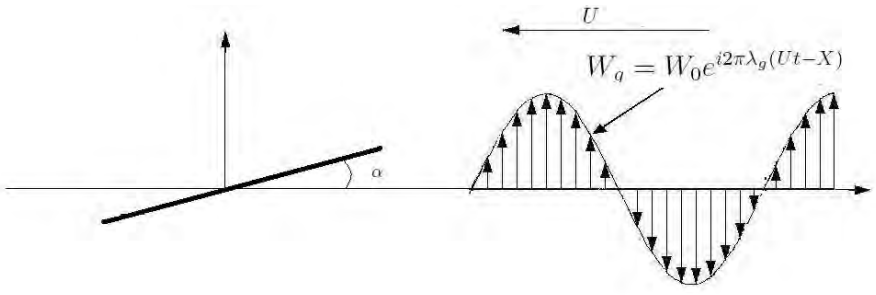

Figure 1.5: Foil (flat plate) in a travelling gust

Blade sections are first set at an angle to the plane of rotation according to the local pitch, see Figures 1.6 and 1.7 for propeller notation and angle definitions.

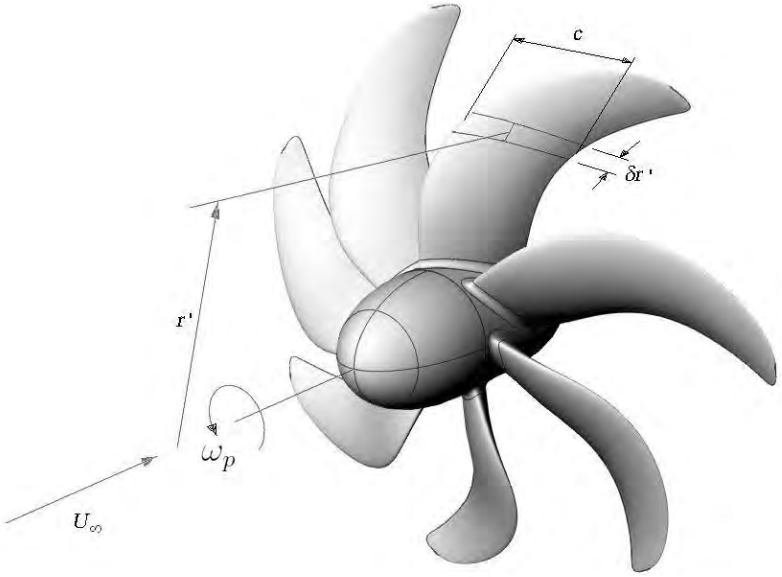

Figure 1.6: Propeller notation diagram [14]

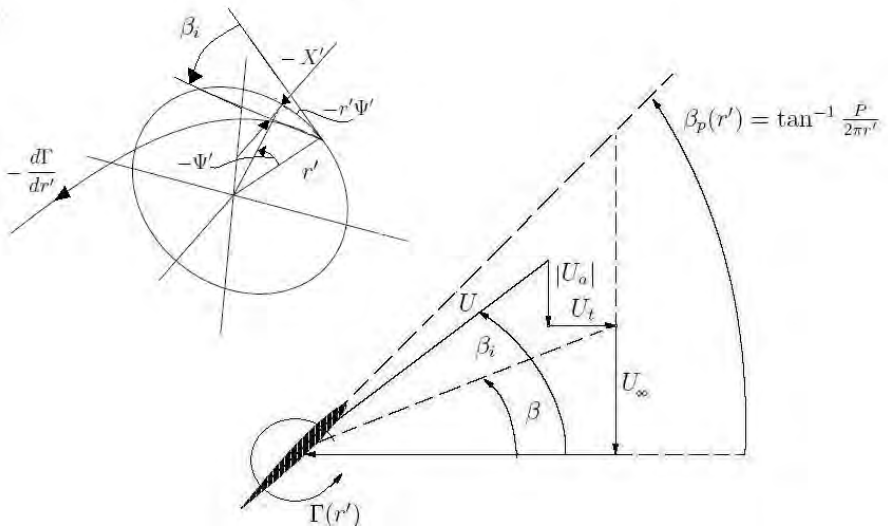

Figure 1.7: Helical vortex element and inflow velocities [17]

$$\beta_p(r) = \arctan\frac{P(r)}{2\pi r} = \arctan\frac{P(r)}{D_o\pi} = helixangle \tag{1.1}$$

$$\alpha = \beta_p - \beta_i = \beta_p(r) - \arctan\frac{U_\infty(1+a)}{r\omega_p(1-ar)} \tag{1.2}$$

The terms aU_∞ and $a'r\omega_p$ are the induced velocities. From Breslin and Andersen [17], when the propeller is lightly loaded the free or trailing vortices can be considered to be convected by the undisturbed flow relative to the blades and consequently induced pitch angle (β_i) can be replaced by the fluid pitch angle:

$$\beta_a(r) = \arctan\frac{U_a(r)}{r\omega_p} \tag{1.3}$$

which removes the induced velocities and implicitness in equation 1.2. Therefore the lightly loaded (linear) propeller is analogous to a wing where trajectories of the trailing vortices are assumed to be independent of the wing loading. The advance coefficient (J) is:

$$J = \frac{U_\infty}{ND_o} = \frac{2\pi U_\infty}{\omega_p D_o} \tag{1.4}$$

From Breslin and Andersen [17] we can consider each blade individually as it rotates through a spatially distributed wake in terms of harmonics. With the wake harmonic order of numbers (n), the wavelength at any radius is:

$$\lambda_p = \frac{2\pi r}{n} \tag{1.5}$$

and the frequency of rotation (N) of the propeller is:

$$N = \frac{\omega_p}{2\pi} = \frac{U}{\lambda_p} = \frac{f}{n} \tag{1.6}$$

or:

$$\omega_i = n\omega_p \tag{1.7}$$

$$= n(2\pi N) \tag{1.8}$$

Then, using general expressions for a travelling gust and knowing the wavelength from equation 1.5 the velocity variation of the first harmonic in time becomes:

$$U_a = U_\infty + \frac{\Delta U}{2}\left(cos\left(n\omega_p t\right)\right) \tag{1.9}$$

Substitution of equation 1.9 into equation 1.3 gives:

$$\beta_a(r) = \arctan\left(\frac{U_\infty + \frac{\Delta U}{2}\left(cos\left(n\omega_p t\right)\right)}{r\omega_p}\right) \tag{1.10}$$

Substitution of equation 1.4 into equation 1.10 gives:

$$\beta_a(r) = \arctan\left(\left(\frac{J}{\pi}\right)\left(1 - \left(\frac{\Delta U}{2U_\infty}\right)\left(cos\left(n\omega_p t\right)\right)\right)\right) \tag{1.11}$$

$$\alpha = \arctan\frac{P(r)}{D_o\pi} - \arctan\left(\left(\frac{J}{\pi}\right)\left(1 - \left(\frac{\Delta U}{2U_\infty}\right)\left(cos\left(n\omega_p t\right)\right)\right)\right) \tag{1.12}$$

Then assuming a P(r)/D_o of 1 and a J of 1 gives:

$$\alpha = \arctan\frac{1}{\pi} - \arctan\left(\left(\frac{1}{\pi}\right)\left(1 - \left(\frac{\Delta U}{2U_\infty}\right)\left(cos\left(n\omega_p t\right)\right)\right)\right) \tag{1.13}$$

Because we wish to find the maximum variation in α we need the difference between the maximum and minimum from equation 1.13 which gives:

$$\Delta\alpha = \arctan\left(\left(\frac{1}{\pi}\right)\left(1 - \left(\frac{\Delta U}{2U_\infty}\right)\right)\right) - \arctan\left(\left(\frac{1}{\pi}\right)\left(1 + \left(\frac{\Delta U}{2U_\infty}\right)\right)\right) \tag{1.14}$$

To obtain the equivalent propeller reduced frequency we substitute 1.8 and 1.6 into the standard reduced frequency equation from Sears theory [13], [17], [68]:

$$k = \frac{\omega c}{2U} = \frac{nc}{2r} \tag{1.15}$$

Equation 1.15 shows that the reduced frequency of a propeller can be adjusted by the chord length (c) to radius ratio (r) and is dependent on the harmonic number (n).

When the harmonic numbers and mean axial velocities are combined with the derivation, an idealised comparison of a propeller to a single hydrofoil can be made. For this comparison the harmonic with the largest amplitude and resulting change in axial amplitude is needed. The flow in the aft region consists of the boundary layer of the hull and the wake from the control surfaces and fairwater. Results from experiments investigating the flow around the axi-symmetric body of the DARPA (Defence Advanced Research Project Agency) SUBOFF model with various appendages shows the largest harmonic amplitude is generated by the four control surfaces [42, 52]. Large amplitudes are present at harmonic numbers (n) of 4, 8 and 12 and an approximate change in axial velocity ($\frac{\Delta U}{U_{ref}}$) ≈ 0.23 respectively is shown in Figures 1.8 and 1.9. These correspond to a reduced frequency ($nc/2r$) of 0.8, 1.6 and 2.4 assuming a $c/r \approx 0.4$ and a change in amplitude of oscillation ($\Delta\alpha$) $\approx 1.9°$.

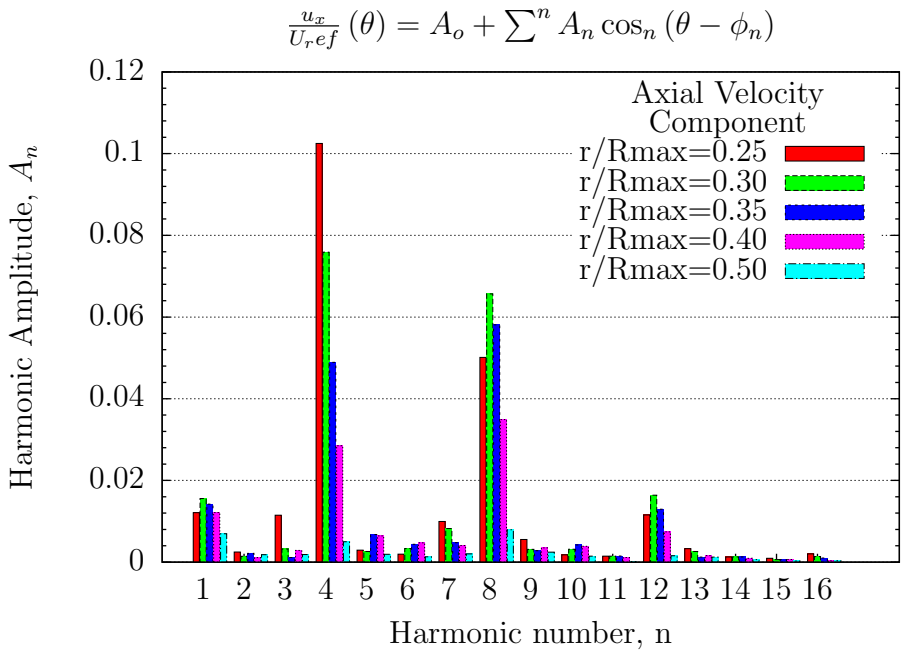

Figure 1.8: Experimental wake harmonics of DARPA SUBOFF submarine with large amplitudes at harmonic numbers of 4, 8, and 12 [52] at $x/Length = 98.7\%$ (approx. position of propeller) aft of nose

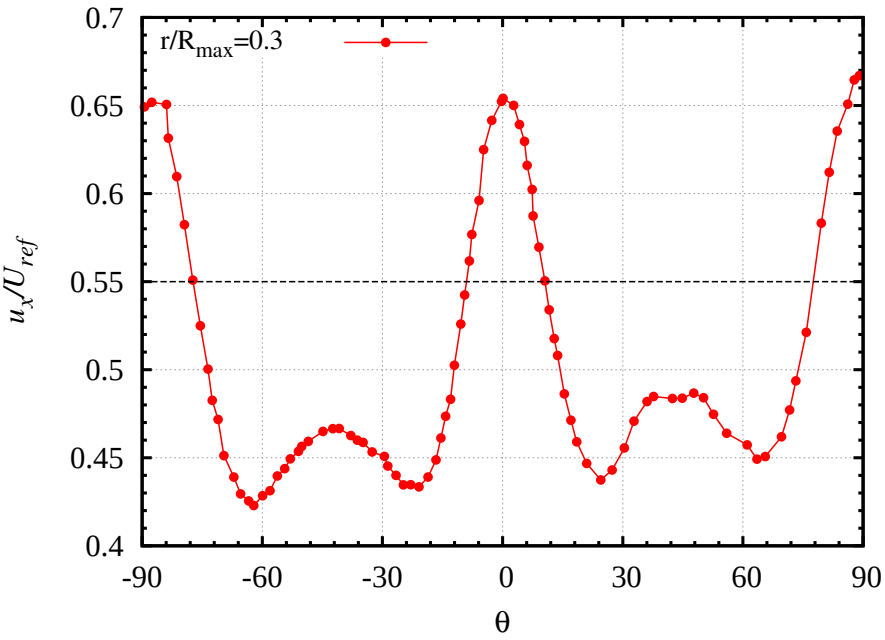

Figure 1.9: DARPA SUBOFF submarine wake velocity at $x/Length = 98.7\%$ (approx. position of propeller) aft of nose [52]

1.5 Methodology

This thesis numerically models a flexible 3D hydrofoil with a sinusoidal incidence variation by systematically increasing the model complexity. To be able to accurately predict and model FSI with a stable numerical solution, a solid understanding of the rigid body dynamics was required. This was undertaken by the investigation of the rigid body dynamics behaviour both statically and dynamically. To validate the RANSE codes ability to predict unsteady behaviour in comparison to classical theories, and other numerical methods such as the panel codes. This methodology allowed for the numerical model's sophistication to be built-up in a systematic manner starting with a two-dimensional hydrofoil. The steps followed were:

1. 2D rigid body fluid dynamics,
   (a) Steady state/stationary
   (b) Unsteady/dynamically oscillating
2. 3D rigid body fluid dynamics,
   (a) Steady state/stationary
   (b) Unsteady/dynamically oscillating
3. 3D steady two-way coupled FSI, and:
4. 3D unsteady two-way coupled FSI.

The first step using a 2D model enabled validation with experiments and comparison to analytical theories such as; Theodorsen and Sears, panel code and evaluation of the available RANSE models. This is detailed in Chapter 2. Chapter 3 uses the 2D mesh extended in the spanwise direction to create the 3D model. This 3D model is compared to the 2D results and then two-way coupled and calculated statically (Chapter 4) and dynamically (Chapter 5).

1.5.1 Geometry selection

A NACA 4 digit section was selected as the base section for the hydrofoil. The 4 digit NACA section was first published in 1933 for the purpose of practical design and construction of airplane wings [50]. The section was chosen because; the section has good stall characteristics, the centre of pressure movement is small across a large range of Reynolds number, the boundary layer transitions to turbulent flow near the leading edge is stable and transitions in the same location regardless of operating conditions. This minimizes the effect of transition on the modelling. A trapezoidal planform of 120 mm root chord length, 60 mm tip chord length and 300 mm span was chosen giving an aspect ratio of 2 as defined in equation 1.16. This planform

or aspect ratio was chosen as being representative of a typical submarine propeller blade.

$$AR = \frac{b^2}{A_{ref}} = \frac{b}{\bar{c}} \tag{1.16}$$

A constant thickness of 9% (NACA 0009) was chosen for the hydrofoil to provide sufficient flexibility to allow an FSI response. The structural properties of the hydrofoil are described later. For details of the section shape coordinates see Abbott and von Doenhoff [1].

The fluid domain geometry for the numerical model was based on the water tunnel test section of the AMC cavitation research laboratory (CRL). The test section is not representative of the freestream and some blockage will occur [5]. Modelling the CRL test section will allow for comparisons when the experimental tests are conducted in further work and account for some of the blockage effects. The CRL water tunnel test section is 2.60 m long and has an inlet cross section of 0.60 m wide x 0.60 m deep and an outlet 0.60 m wide x 0.62 m deep with the sloping face on the opposite side to were the model is mounted [15].

The inlet was simplified for ease of a structured grid as shown in Figure 1.10. The domain was assumed to be a constant cross section throughout, to simplify the model. The inlet was located 2.5 c upstream (at upper left of Figure 1.10) from the leading edge, the outlet was located 11.5 c (at bottom right of Figure 1.10). The walls of the tunnel were modelled to match the blockage of the tunnel section and interaction of the foil with the tunnel boundary layer. The shortening of the inlet length will not allow the boundary layers to be developed to the same thickness as in the tunnel test section but there the interaction is modeled.

1.5.2 Fluid Dynamics

The dimensionless parameters of interest in the fluid model include Reynolds number (Re), co-efficient of pressure (C_p), wall shear co-efficient (C_τ), lift co-efficient (C_L), drag co-efficient (C_D) and moment co-efficient (C_M): Reynolds number is defined in the following equation:

$$Re = \frac{\rho U_\infty c}{\mu} \tag{1.17}$$

The static 2D results are compared with experimental results for C_p:

$$C_p = \frac{p - p_\infty}{\frac{1}{2}\rho {U_\infty}^2} \tag{1.18}$$

The wall shear (C_τ) (equation 1.19) is compared between Panel code (XFOIL) and RANSE (ANSYS) numerical models:

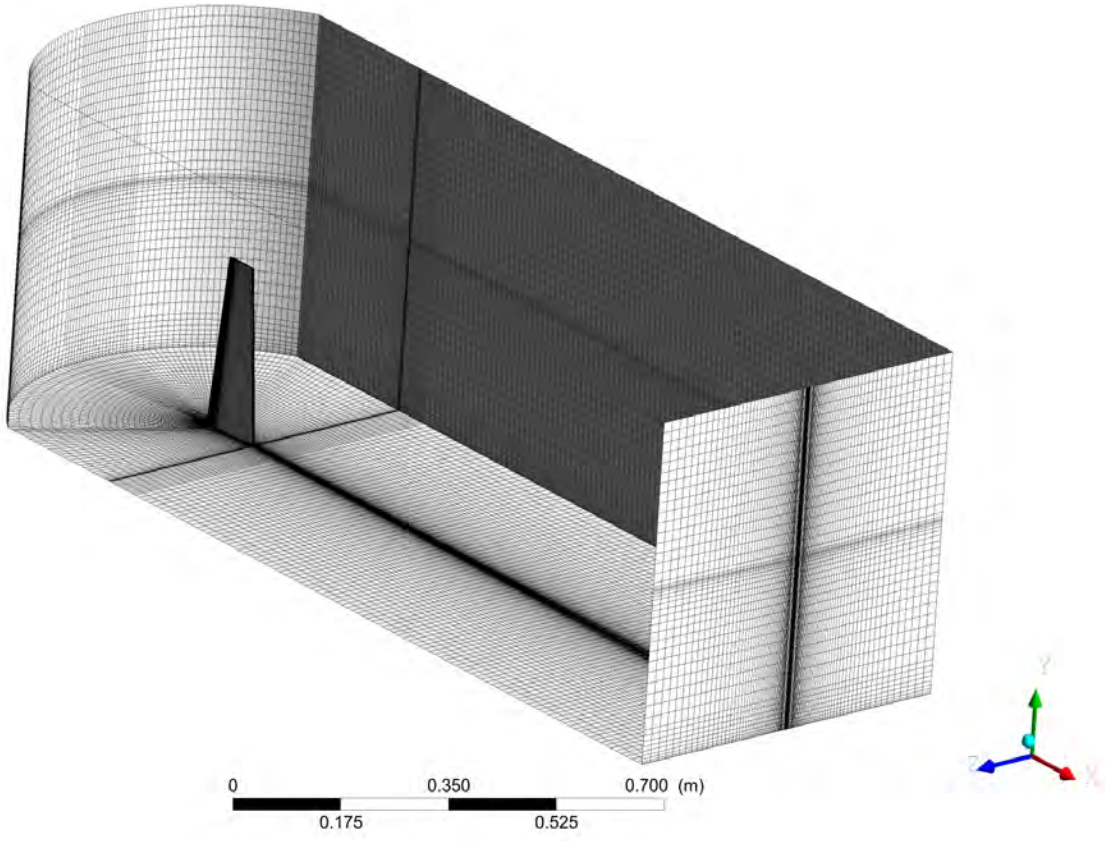

Figure 1.10: Computational domain

$$C_\tau = \frac{\tau}{\frac{1}{2}\rho {U_\infty}^2 A_{ref}} \tag{1.19}$$

The force coefficients C_L, C_D and C_M in equations 1.20, 1.21 and 1.22 respectively are compared at all stages of analysis. These coefficients are also used for grid convergence studies.

$$C_L = \frac{L}{\frac{1}{2}\rho {U_\infty}^2 A_{ref}} \tag{1.20}$$

$$C_D = \frac{D}{\frac{1}{2}\rho {U_\infty}^2 A_{ref}} \tag{1.21}$$

$$C_M = \frac{M}{\frac{1}{2}\rho {U_\infty}^2 A_{ref} c} \tag{1.22}$$

1.5.3 Structural Parameters

The dimensionless parameter investigated on the structure at the tip of the hydrofoil is:

$$C_{\delta L} = \frac{\delta EI}{LS^3} \tag{1.23}$$

This parameter is a combination of non-dimensional deflection (δ/L) and the stiffness parameter for a cantilever beam ($k_{stiff} = EI/L$) [95]. This parameter and the hydrofoils twist (θ) is used to compare the deflections in the coupled analyses at the tip of the hydrofoil.

1.5.4 Dynamics

The non-dimensional parameters of interest in the dynamic analyses are the frequency ratio, reduced frequency and reduced natural frequency as described in equations 1.24, 1.25 and 1.26. The origins of the reduced frequency will be expanded on in Chapter 2

$$\text{frequency ratio} = \frac{f}{f_n} \tag{1.24}$$

$$k = \frac{1}{\text{reduced velocity}} = \frac{\omega c}{2U_\infty} \tag{1.25}$$

$$k_n = \frac{\omega_n c}{2U_\infty} \tag{1.26}$$

1.5.5 Material Selection

Additional non-dimensional parameters of interest for material selection were the density ratio equation 1.27, the frequency ratio and reduced natural frequency equations 1.25 and 1.26.

$$\text{density ratio} = \frac{\rho_m}{\rho_w} \tag{1.27}$$

By expanding equation 1.24 using $f_n = (1/2\pi)\sqrt{(k_{stiff}/m)}$ [97] and ($k_{stiff} = EI/L$) [95] we find that:

$$\frac{f}{fn} \propto \frac{E}{\rho_m} \tag{1.28}$$

Based on previously described parametric dependencies an isotropic homogeneous material was selected. An isotropic homogeneous material was chosen for simplicity and serves the purpose of minimizing variables when modelling the FSI. Aluminium, stainless steel and brass were selected to investigate their specific non-dimensional parameters in this modelling case. Table 1.1 compares the structural properties of the three materials investigated.

Table 1.1: Structural parameters

	Stainless Steel	**Aluminium**	**Brass**	**Units**
Density	7.75	2.77	8.50	T/m^2
E	193	71	36	GPa
$f_n(1st)$ in air	106	108	-	Hz
$f_n(1st)$ in water	66	46	36	Hz
ρ_m/ρ_w	7.76	2.77	8.52	
E/ρ_m	24.87	25.61	4.22	1 x 10^6

Stainless steel and aluminium have been selected as their first mode of vibration in air is less than 2% difference (Table 1.1). These two materials have different mass ratios but identical reduced natural frequencies (first mode of vibration) in air and similar reduced natural frequencies (first mode of vibration) in water. Brass was not investigated in this thesis as it has a difference density ratio. The natural frequencies in air were calculated using ANSYS CFX and then a flat plate approximation was used to calculate the change in frequency due to imersion in water from Blevins [12]. The modal calulation is desribed in chapter 5.

1.5.6 Test Matrix selection

The velocity range was determined by the CRL water tunnel limits of 2-12 m/s giving the two Reynolds numbers of 3.36×10^5 to 1.12×10^6 (based on the root chord corresponding to a freestream velocity of 2.5 and $8.3m/s$). The reduced natural frequency (k_n) was calculated using the natural frequencies from Table 1.1. The corresponding reduced natural frequencies in air and water at standard temperature and pressure conditions is shown in Table 1.2.

Table 1.2: Structural natural frequency range

	Stainless Steel	**Aluminium**
k_n in air@2.5m/s	16	16
k_n in air@8.3m/s	5	5
k_n in water@2.5m/s	10	7
k_n in water@8.3m/s	3	2

Static incidence angles (α) of 0, 2, 4, 6, 8, and 10° were modelled. The static incidence angles were run with a dynamically deformed mesh, which enabled a check of the mesh behaviour at large angles of incidence. Ranges of reduced frequency, $0 - 3.1$; incidence amplitude of $1, 2, 3$ and 5°; and, mean dynamic incidence of 0 and 4° were selected for the dynamic numerical models. These values are based

on the problem development in section 1.4 which used a propeller having an estimated reduced frequency of $(nc/2r)$ of 0.8, 1.6 and 2.4 and a change in incidence amplitude of approximately 1.9°. The mean incidence of 0° was selected to enable comparison with previous analytical theory and the 4° mean incidence case. The mean incidence of 4° was selected as propeller blades typically operate at a fluid pitch of approximately 4°. Based on these numbers a test matrix was selected for the rigid body dynamic case and is shown in Table 1.3. The rigid 2D and 3D matrices were larger than the coupled case due to the smaller run time. This enabled an extensive investigation of the trends of C_L, C_D and C_M and the respective phase angle to the pitch oscillation to determine the coupled test matrix. The coupled dynamic run matrix is shown in Table 1.4.

Table 1.3: NACA 0009 oscillating about 1/2c run matrix RANSE rigid body dynamic

k	$\bar{\alpha}$	$\Delta\alpha$
0.031	0,4°	1,2,3,5°
0.094	0°	3°
0.157	0°	3°
0.188	0°	3°
0.251	0°	3°
0.314	0,4°	1,2,3,5°
0.534	0°	3°
0.785	0,4°	1,2,3,5°
1.571	0,4°	1,2,3,5°
3.142	0,4°	1,2,3,5°

Table 1.4: NACA 0009 oscillating about 1/2c test matrix RANSE dynamic hydroelastic

k	$\bar{\alpha}$	$\Delta\alpha$
0.031	0,4°	3°
0.314	0,4°	3°
0.785	0,4°	3°
1.571	0,4°	3°
3.142	0,4°	3°

Chapter 2

Numerical Validation

To be able to accurately predict and model FSI with a stable numerical solution a solid understanding of the rigid body dynamics was required. A review of current methods both analytical and numerical for prediction of a hydrofoil undergoing a sinusoidal pitch variation in two and three-dimensions is described in this chapter. This review provides a basis for selection of the CFD model used in later chapters and validation of the computation grid and moving mesh method in 2D. Both steady state and a rigid 2D oscillating foil in pure pitch is detailed in this study.

Steady state studies were conducted by dynamically deforming the mesh to the required incidence angle, then using the deformed mesh to compute the RANSE solution. Grid independence and temporal convergence were undertaken for a NACA 0009 section with geometrically similar meshes used for experimental validation. Validation was conducted for steady state using experimental results from Gregory and O'Reilly [41] with a NACA 0012 section. Dynamic validation was conducted with results from Piziali [83] using a NACA 0015 section. The validation studies were conducted with $k-\epsilon$, $k-\omega$ and Shear Stress Transport (SST) turbulence models to assess each model's effectiveness. The use of different foil sections for the convergence and validation studies was necessary to provide direct comparison with available experimental data. Preliminary work for this chapter was published by the author of this thesis in Hutchison et al. [53].

Additional computational comparisons were undertaken between panel codes and RANSE simulations to expand on the static and dynamic properties of the models and to investigate their limitations. Unsteady dynamic results for RANSE simulations for a reduced frequency range of 0.031-3.142 with an oscillation incidence up to and including 5° with no cavitation were evaluated for comparison with results from other chapters.

2.1 Previous and Related Work

In 1922 studies began into the field of unsteady flow about airfoils. In 2005, Cebeci et al. [23] wrote in regard to Prandtl.

> ...in 1922 he proposed the problem of incompressible flow past an oscillating airfoil neglecting the influence of viscosity and thus to take the Laplace equation as a governing equation. He pointed out that, according to Kelvins theorem, every change in C_L must be accompanied by the detachment of a vortex from the airfoils trailing edge.

In 1924, Birnbaum showed that the reduced frequency parameter has a special significance in the study of an oscillating airfoil [23]. The reduced frequency parameter is a measure of the wave length of the shed vortical wake from the oscillating foil to the semi-chord.

The characteristics of unsteady flow about a foil are significantly different from those for a steady flow. For unsteady flow the stagnation point will vary with time and flow reversal will begin to develop in the velocity profiles. Unsteady flow about a foil can have flow reversal without stall and the point of zero wall shear does not necessarily coincide with stall [23]. The stall characteristics of an unsteady foil can exceed those of the static case and are significantly affected by frequency and amplitude of oscillation. An unsteady foil is generally referred to as pre-stall, light stall or dynamic stall. The pre-stall condition is when the foil is oscillated in the range prior to static stall, light stall is normally defined as oscillating the foil around the static stall incidence and dynamic stall or post stall is oscillating the foil to an amplitude higher than static stall. This thesis only concentrates on the pre-stall range with a maximum incidence analysed in the dynamic case of 9°, see Section 1.5 for complete test matrix selection details.

Since 1924, work in this area has been progressed in various experimental, analytical and numerical studies. An overview of the previous and related work for 2D oscillating hydrofoils is given in the following sections.

2.1.1 Experimental

NASA in the late 1970s and early 1980s conducted a number of experiments into dynamic stall and unsteady loading of airfoils [21, 22, 48, 71–73, 76]. These studies obtained C_L, C_D and C_M measurements by integrating surface pressures. They also investigated boundary layer transition, separation and reattachment characteristics, as well as flow reversal and chordwise unsteady pressures. McCroskey et al. [73] found that in general, unsteady motion is more important than airfoil shape when determining dynamic stall characteristics.

In 1982, McCroskey and Pucci [76] conducted ten specific experiments on the foil sections; NACA 0012, Vertol VR-7 and NLR-7301 undergoing pitch oscillations

to evaluate unsteady viscous theories and computation methods. McCroskey and Pucci [76] and McCroskey [75] identified four distinct regimes of viscous-inviscid interactions corresponding to varying degrees of unsteady flow separation. These were; no stall, weak interactions; stall onset, mild interactions; light stall, strong interactions, and; deep dynamic stall, viscous dominated. If a foil oscillates with a maximum incidence which is below the static stall incidence, the boundary layer on both upper and lower surfaces will remain fully attached, except for a small separation bubble near the upper surface on the leading edge for maximum incidence less than 5°, which produces transition from laminar to turbulent flow. Jumper et al. [60] conducted experimental studies for an airfoil undergoing constant pitching about the mid chord with an analytical prediction for C_L. This paper showed reproducibility of the results for pre-stall, dynamic stall and post-stall conditions.

Koochesfahani [65] demonstrated experimentally that thrust production for a foil due to pitching motion occurs only above certain reduced frequencies. He also found that the structure of the wake can be substantially modified by amplitude of oscillation, frequency and shape of the wave form. In 1993, Piziali [83] conducted a comprehensive set of experiments investigating the pressure distributions on a foil undergoing pitching motions for 2D and 3D airfoils for the development of computational and empirical methods. In 1994, Hart [43] investigated experimentally unsteady flow induced by periodic change of incidence. These experiments provided details of the change in boundary layer profile on the suction and pressure sides and phase lag for 2D and 3D hydrofoils for varying reduced frequency.

Tsang et al. [98] used a direct force measurement technique employing piezoelectric load cells to investigate a 2D NACA 0012 section airfoil undergoing dynamic stall. Experiments were carried out at a Reynolds number of 7.7×10^4 and reduced frequencies of 0.005, 0.01, 0.02, and 0.04. They investigated the effect of reduced frequency, mean dynamic incidence and amplitude of oscillation concluding that, this range of reduced frequency in the pre-stall condition, has little effect on C_{Lmax}. By using an FFT they suggested non-linear interaction between the pitching airfoil and the fluid force by the presence of higher harmonics in addition to the primary oscillation frequency.

Berton et al. [7–9] applied embedded Laser Doppler Velocimetry (LDV) to measure velocity in the boundary layer of rotary wings and for oscillating or rotating models. Models included a flat plate, airfoil and half wing in 2D and 3D configurations. They carried out flow visualization on a NACA 0012 section airfoil at a Reynolds number of 1×10^4 and 2×10^5 oscillating in pitch through stall conditions, using smoke illuminated by a light sheet to take pictures of the wake sheet. These studies focused on large incidence pitch variations and the characteristics of the laminar separation bubble. They showed the different flow features during upstroke and downstroke as reattachment, large separation bubble and high vortical flow.

Lee and Gerontakos [67] tested a NACA 0012 section foil at a Reynolds number of 1.35×10^5 oscillating sinusoidally at reduced frequency of 0.025, 0.05, 0.5 and 0.1 to investigate the behaviour of the unsteady boundary layer. Closely spaced arrays of hotfilm sensors were used to investigate pre-stall, stall and post-stall conditions.

To supplement the hot-film data, surface pressure distributions, hot-wire wake measurements and smoke-flow visualisations were obtained. Lee and Gerontakos found only small values of reduced frequency were required to delay the onset of the various boundary-layer events, and produce significant variations in magnitude of C_L, C_D and C_M peak values.

2.1.2 Analytical Solutions

Analytically determining airloads on an oscillating airfoil was first attempted by Glauert [39] in 1929 and later solved by Theodorsen [94]. The theory developed by Theodorsen [93], Von Karman and Sears [100], and Wagner [101] is some of the most referenced literature used to explain unsteady loading for unsteady flow about thin-airfoils. These analytical solutions were for both frequency and time domains. They all give exact closed-form solutions for the pressure distributions and hence the forces and moments for an airfoil either pitching or heaving for 2D incompressible flow [68]. Theodorsen's and Sears' problem is compared in this chapter, as comparisons in this thesis are made in the frequency domain. Comparisons with Theodorsen's prediction is made with the CFD solution in Chapter 3.

The approach of Theodorsen [94] gives a solution to the unsteady airloads on a 2D harmonically oscillated airfoil in inviscid, incompressible flow subjected to a small disturbance, shown in Figure 2.1(a). The airfoil is represented by the thick black line of length c, the shed wake vorticity indicated by γ_w and the bound vorticity on the foil is indicated by γ_b. Both the airfoil and the shed wake are represented by a vortex sheet. The shed wake extends as a planar surface from the trailing edge downstream to infinity. This assumption of a planar wake is justified if the incidence angle disturbances remain small [68]. Theodorsen's theory assumes any possibility of lag in the adjustment of flow is applied at the trailing edge [10]. Bisplinghoff et al. [10] gives a detailed explanation of the mathematics behind Theodorsen's approach. Theodorsen's theory introduces amplitude reduction and phase lag effects on the circulatory part of the C_L response.

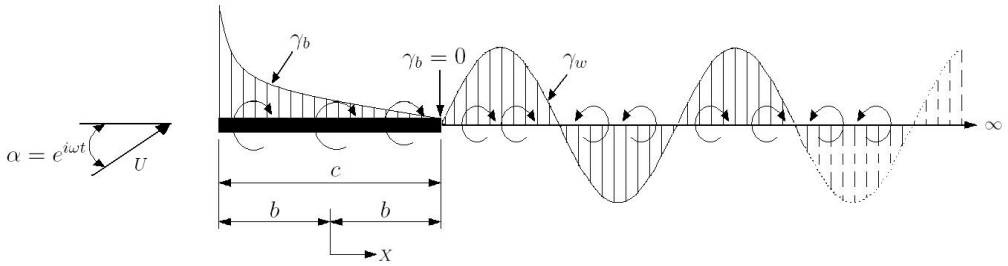

(a) Theodorsen

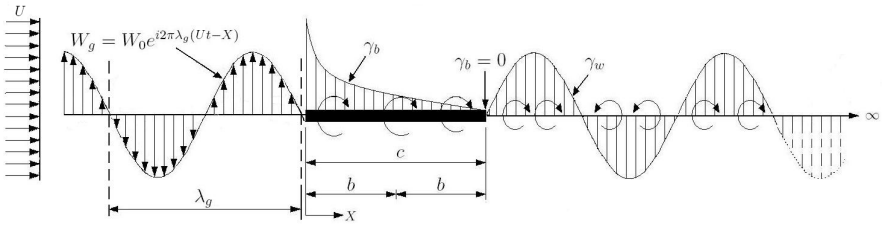

(b) Sears

Figure 2.1: Model of a thin airfoil encountering a sinusoidal vertical gust [68]. Comparison of Theodorsen and Sears problem derivations.

Von Karman and Sears [100], analysed this problem as a thin airfoil moving through a sinusoidal vertical gust field W_g. The gust is considered as an up wash velocity that is uniformly convected by the freestream, as shown in Figure 2.1(b). The assumptions are that the flow can be considered 2D and the airfoil thickness and the amplitude of oscillation are small compared with the chord [86]. In Von Karman and Sears [100], the mid chord was the reference point for the original work. The Sears function can be adapted for a leading edge reference point as this is equivalent to a frequency dependent phase shift. The lift and moment in Von Karman and Sears [100] are both expressed in components: Quasi-steady, apparent mass and wake effect. Both Theodorsen and Von Karman and Sears used Bessel functions to solve for the coefficients.

The significance of the apparent mass contribution to both total C_L and phase angle for pure pitch oscillation about the mid chord is shown in Figure 2.2 (C_L is normalised by $2\pi\bar{\alpha}$ where, $\alpha = \bar{\alpha} sin\omega t$ considering a pure harmonic variation in α, that is $\alpha = \bar{\alpha} e^{i\omega t}$). The phase of the force lags the oscillation amplitude which means the lift build-up occurs more slowly than the rate of oscillation indicated by the reduced frequency (Figure 2.2(b)).

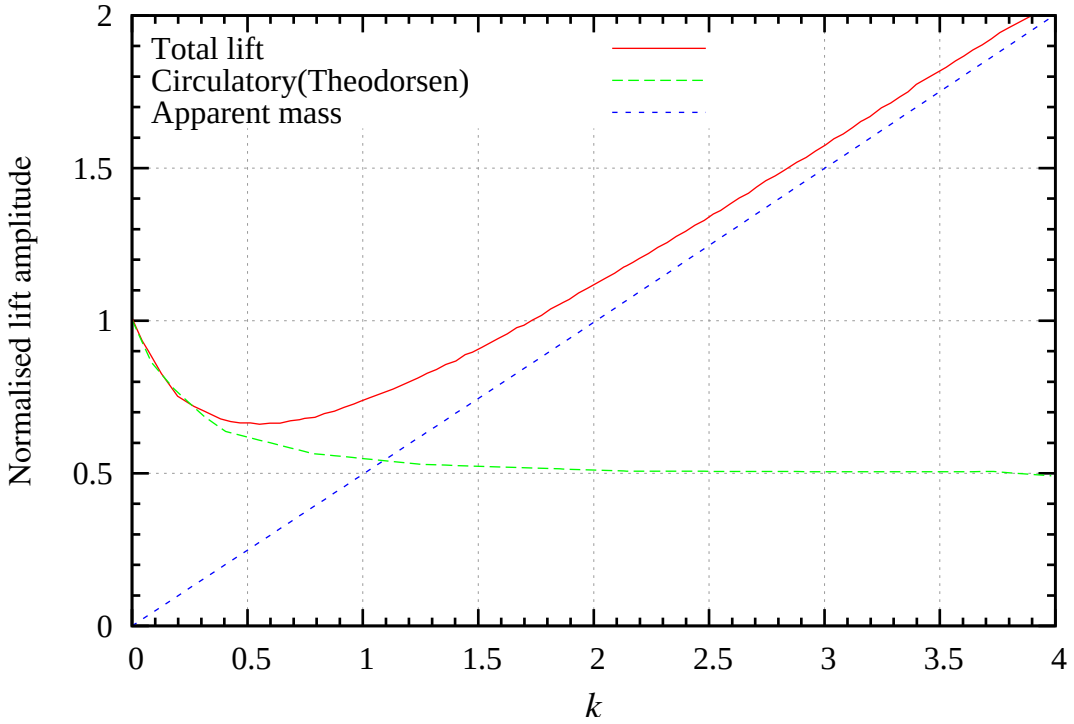

(a) Lift amplitude

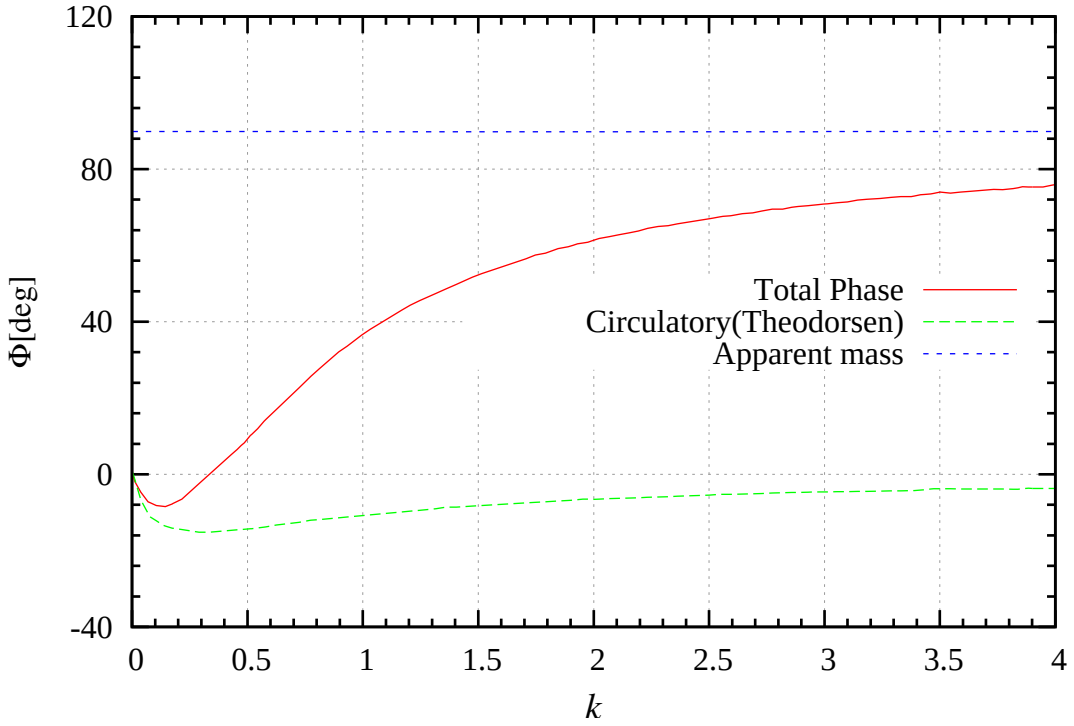

(b) Lift phase

Figure 2.2: Circulatory and apparent mass contributions to unsteady lift response for a pure sinusoidal incidence oscillation [68] with small incidence angle

A comparison of the coefficients obtained from Theodorsen and Sears theories is shown in Figure 2.3. The amplitude is shown in Figure 2.3(a) and the phase in Figure 2.3(b). In these figures $|C(k)|$ and $|S(k)|$ are Theodorsens and Sears function and $|S'(k)|$ is Sears function computed relative to the leading edge. These figures show while the difference is small for reduced frequency less than 0.2 as reduced frequency increases the error becomes increasingly large [61]. The unsteadiness of the airfoil traversing a gust becomes significant above 0.1 or higher.

Kerwin [61] noted that the unsteadiness of the airfoil traversing a gust becomes significant when the reduced frequency is above 0.1 or higher. Ericsson and Reding [35] showed the Karman-Sears wake lag can be approximated by the constant lag effect only as long as reduced frequency is low, approximately less than 0.16 (k=$\frac{\omega c}{U_\infty}$). At higher frequencies, a constant phase lag is the best approximation.

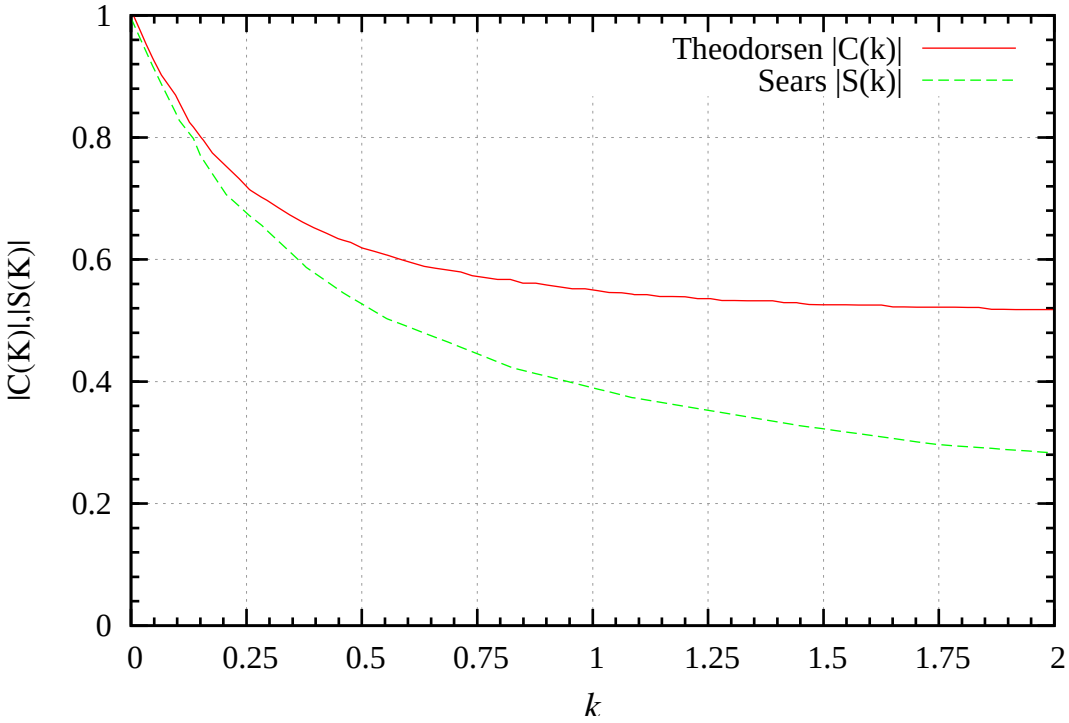

(a) Lift amplitude

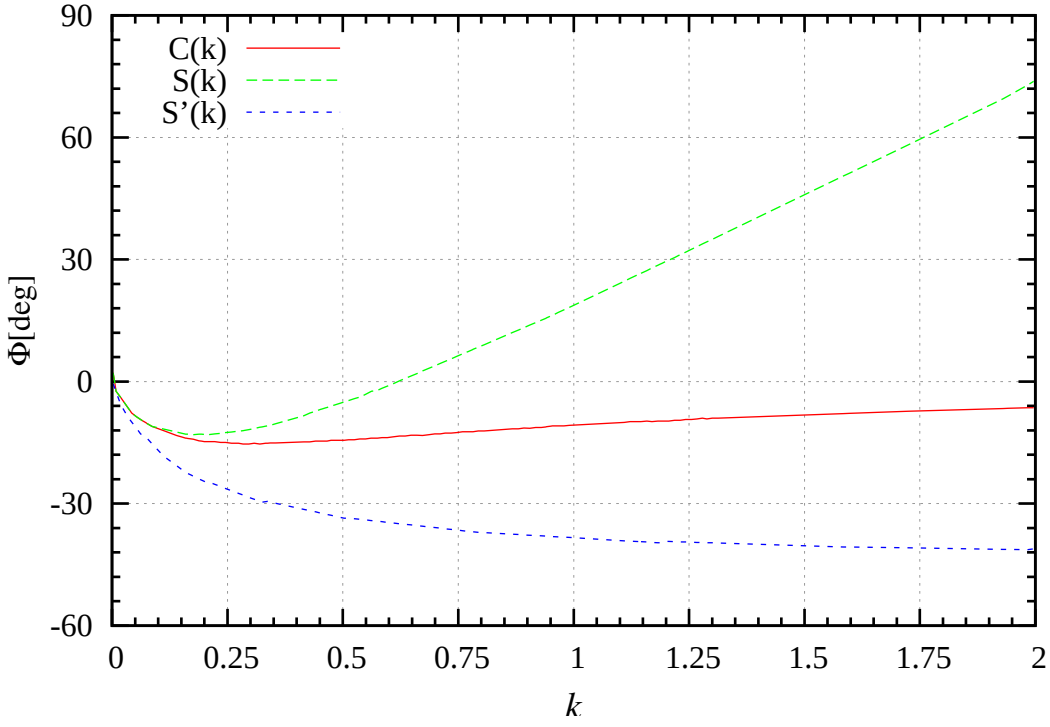

(b) Lift phase angle

Figure 2.3: Comparison of Theodorsen and Sears functions in terms of lift amplitude and phase angle as a function of reduced frequency [68] with small incidence angle

2.1.3 Numerical Solutions

McCroskey [74] conducted some of the earliest numerical investigations. He developed simple formulae to describe the detailed inviscid, incompressible flow field of unsteady flow about an airfoil with thickness and camber. Ekaterinaris [33] and Ekaterinaris and Menter [34] conducted detailed numerical analyses to investigate the use of $k - \epsilon$ and SST models to predict dynamic stall. They observed that, in general, none of the turbulence models could predict the hysteresis effect during the downstroke. It has been shown that upwind-biased schemes, even though more computationally intensive, provide an improved solution of unsteady flows because they have no dependence on the specified numerical dissipation parameters and they appear to have less grid sensitivity compared with central difference schemes [33]. More recently a series of numerical simulations of dynamic stall for 3D foils using various planform shapes was completed providing detailed information on the interaction of dynamic stall and the tip vortex [88–90]. Spentoz et al. [88–90] studies obtained C_L, C_D and C_M measurements by integrating surface pressures. They also investigated boundary layer transition, separation and reattachment characteristics, as well as flow reversal and chordwise unsteady pressures and compared results with experimental results. Spentzos et al. [89] highlighted that high reynolds number experiments are rare and that there was a need for further investigations. Spentzos et al. [90] conducted further comparison with experiments and identified that there was strong similarities in the flow topology of wing with different planforms.

2.2 Methodology

2.2.1 RANSE Set-up

The unsteady flow field was solved with the commercial package ANSYS CFX version 12.1 with a 2D, one layer deep, structured mesh consisting of hexahedral elements. The inlet had specified velocity components and a turbulence intensity of 0.5%. This turbulence intensity value is the approximate value of the AMC Tom Fink Cavitation Tunnel [16]. The geometry is based on the AMC Tom Fink Cavitation Tunnel details are contained in Section 1.5.1. The domain outlet had constant pressure with zero turbulence gradient. A symmetry boundary condition was applied in the spanwise direction on either side of the one layer deep mesh. The foil was moved dynamically with a specified displacement. The high resolution advection scheme was used for the validation data; it was later changed to a specific blend factor of one to make it second-order accurate [36] for the remaining dynamic analyses. A transient scheme of second order backward Euler convergence was used with a maximum of 10 internal calculating loops with a maximum residual target of $1\text{x}10^{-4}$.

2.2.2 Mesh Development

The structured grid for the present study was constructed using a C-topology with an H-topology at the trailing edge as shown in Figure 2.4. The inlet velocity boundary was located 2.5 c upstream from the leading edge, the outlet pressure opening was located 11.5 c downstream from the trailing edge and the first cell height was 0.02% c, corresponding to an average y^+ of 1.

2.2.3 Grid Independence and Temporal Convergence

Steady state convergence was conducted by dynamically deforming the mesh to the required incidence. This procedure was conducted for incidence angles (α) of 2, 5 and 10° until a grid independent solution was reached. Grid independence and temporal convergence studies were conducted on the NACA 0009 section and a similar mesh was then used to model the NACA 0012 and NACA 0015 sections. A displacement diffusion mesh deformation model was used to generate the mesh for steady flow computations at 0, 2, 5 and 10° incidences and Re values of $3\text{x}10^5$ and $10\text{x}10^5$. It was found that a grid with 27284 elements had an average error of 0.2% using the Richardson extrapolation technique, which is less than the typical requirement of 1%.

A plot of the convergence in C_L is shown in Figure 2.5. The resulting mesh was then used to assess time step convergence with a reduced frequency of 0.25 and Re of $3\text{x}10^5$. Temporal convergence was used to determine the number of time steps per period required using three criteria; average Courant number for one cycle, force on

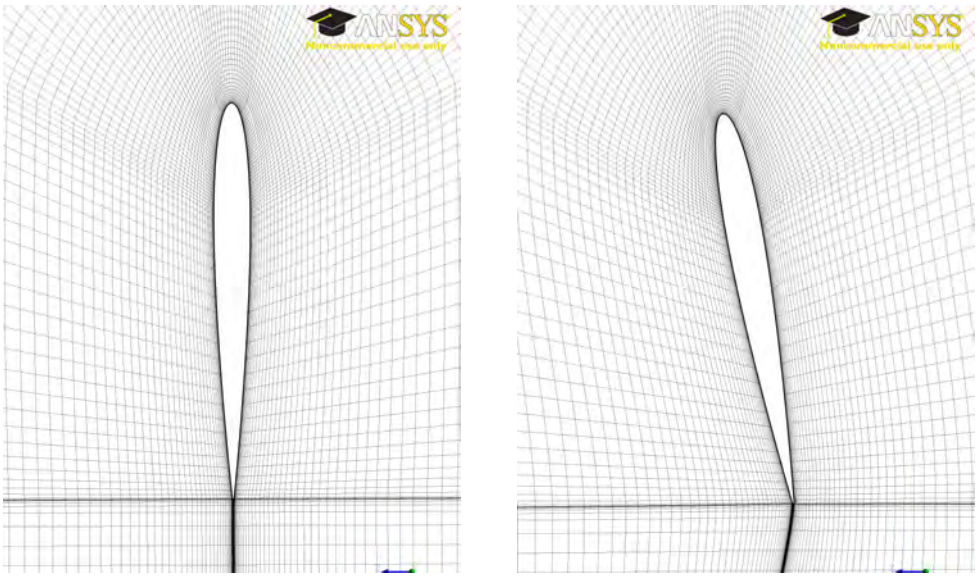

(a) Undeformed α=0° (b) Deformed α=10°

Figure 2.4: C-grid topology for NACA 0009 section

the foil and velocity at a point 1/2 chord behind the foil. The temporal convergence plots for force and velocity at a point in the wake is shown in Figure 2.6. A total of 100 time steps per period was selected, this had an average $C_n < 1$ for the duration of one cycle. The simulated time covered 5 complete cycles, the first cycle contains transients from the steady start up solution after which the second and the third cycle are identical.

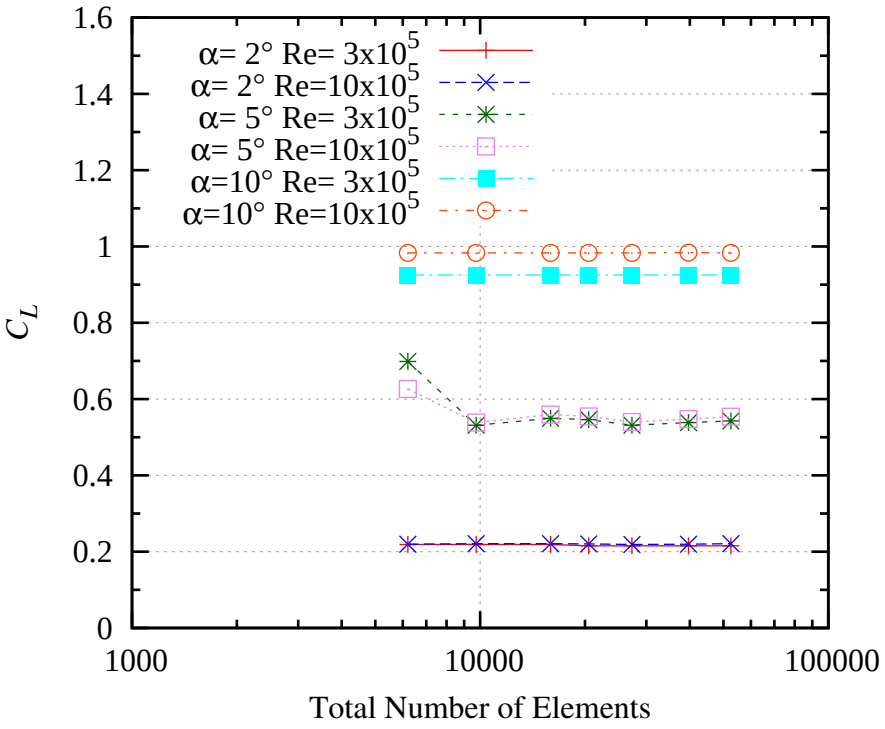

Figure 2.5: C_L static convergence

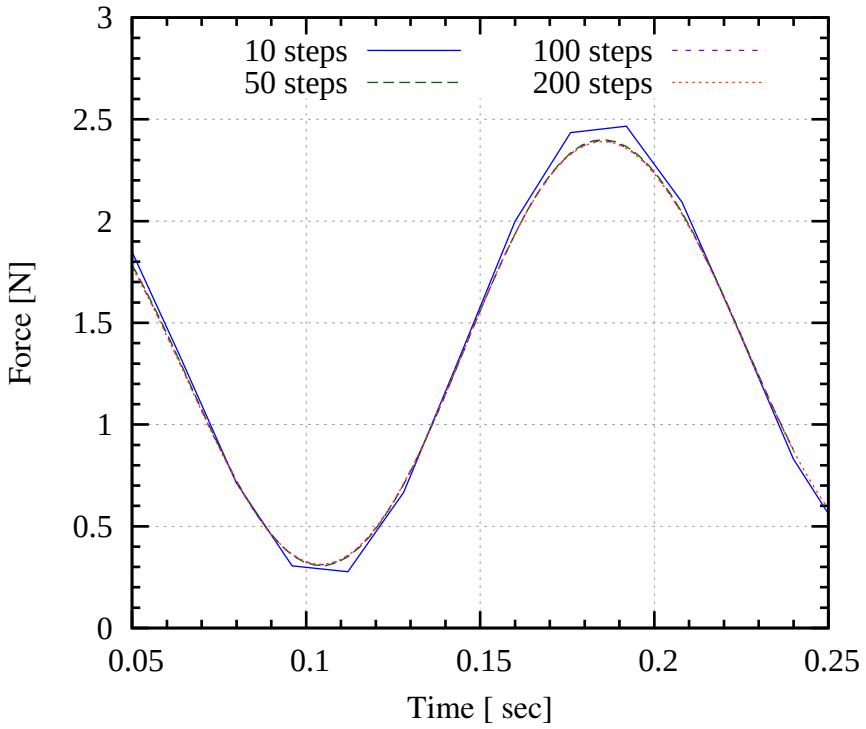

(a) Force on the foil

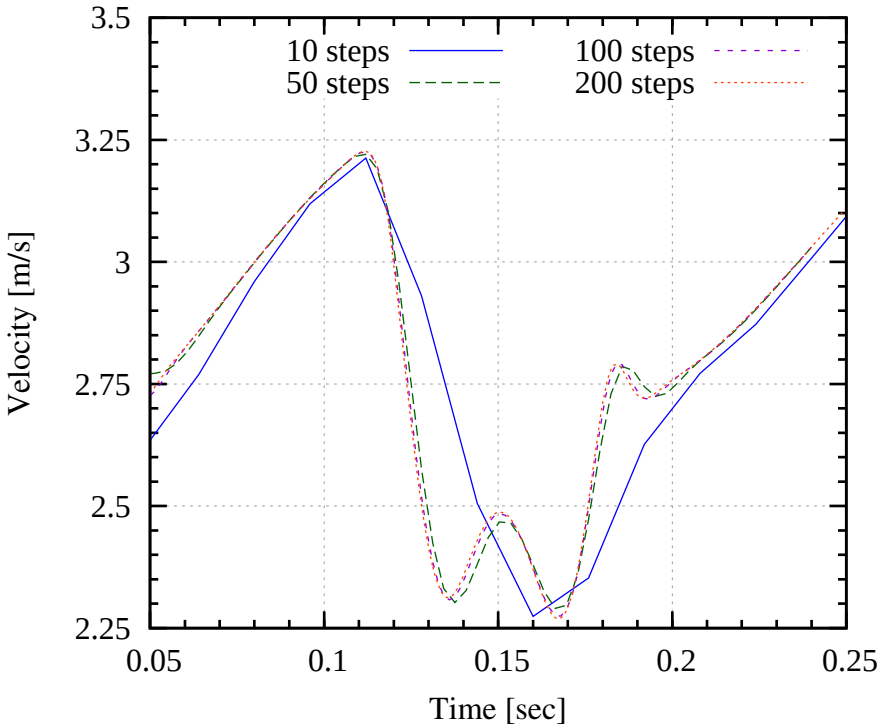

(b) Point in wake

Figure 2.6: Plot of temporal convergence

2.2.4 Mesh Deformation

The mesh deformation model utilised in ANSYS CFX version 12.1 is a displacement diffusion mesh deformation model [37]. This enables motion on a specified boundary which in this case is the foil surface. Equation 2.1 is used to determine the diffusion of the motion to the remaining nodes in the domain. The mesh stiffness was chosen by iterating between the 2D and 3D solutions in combination with the convergence study to allow for a 10° pitch and tip deflection in the same direction as the pitch without a fold in the mesh. The steady state convergence was conducted with the deformed mesh resulting from the deformation at 0, 2, 5 and 10° incidences. The 2D and 3D steady state convergence is conducted in section 2.2.3 and 3.1.2 respectively.

$$\nabla \cdot (\Gamma_{disp} \nabla \delta_m) = 0 \tag{2.1}$$

where:

δ_m = displacement relative to the previous model

Γ_{disp}= mesh stiffness, in this case equation 2.2

$$\Gamma_{disp} = \frac{1[m^5 s^{-1}]}{\text{Volume of Finite Volumes}} \tag{2.2}$$

2.3 Static Computation

2.3.1 Validation

Steady state experimental validation was conducted with data from Gregory and O'Reilly [41] using a pressure coefficient Equation 1.18 on a smooth NACA 0012 section at a Re_c of 2.88x10^6 for incidence angle of 0, 2, 4, 6, 8, and 10°. Results from these experiments were compared with XFOIL and the $k-\epsilon$, $k-\omega$, and SST turbulence models is shown in Figure 2.7. Re_c uses a reference chord of unit length (i.e. $c = 1$). Good agreement is shown across all of the incidence angles for the $k-\epsilon$, and SST models. At an incidence angle of 10° the $k-\omega$ model showed decreased pressure at the trailing edge and a leading edge fluctuation on the suction side that was not characteristic of the experimental results, the $k-\omega$ was not used in any further comparisons. Although the residuals had converged, the convergence had an oscillation which suggested that the foil had stalled. The $k-\epsilon$, SST and XFOIL predictions compared well with experiment, therefore these were investigated further. Close to stall the $k-\epsilon$ predicted the trailing edge pressure closest to experiment.

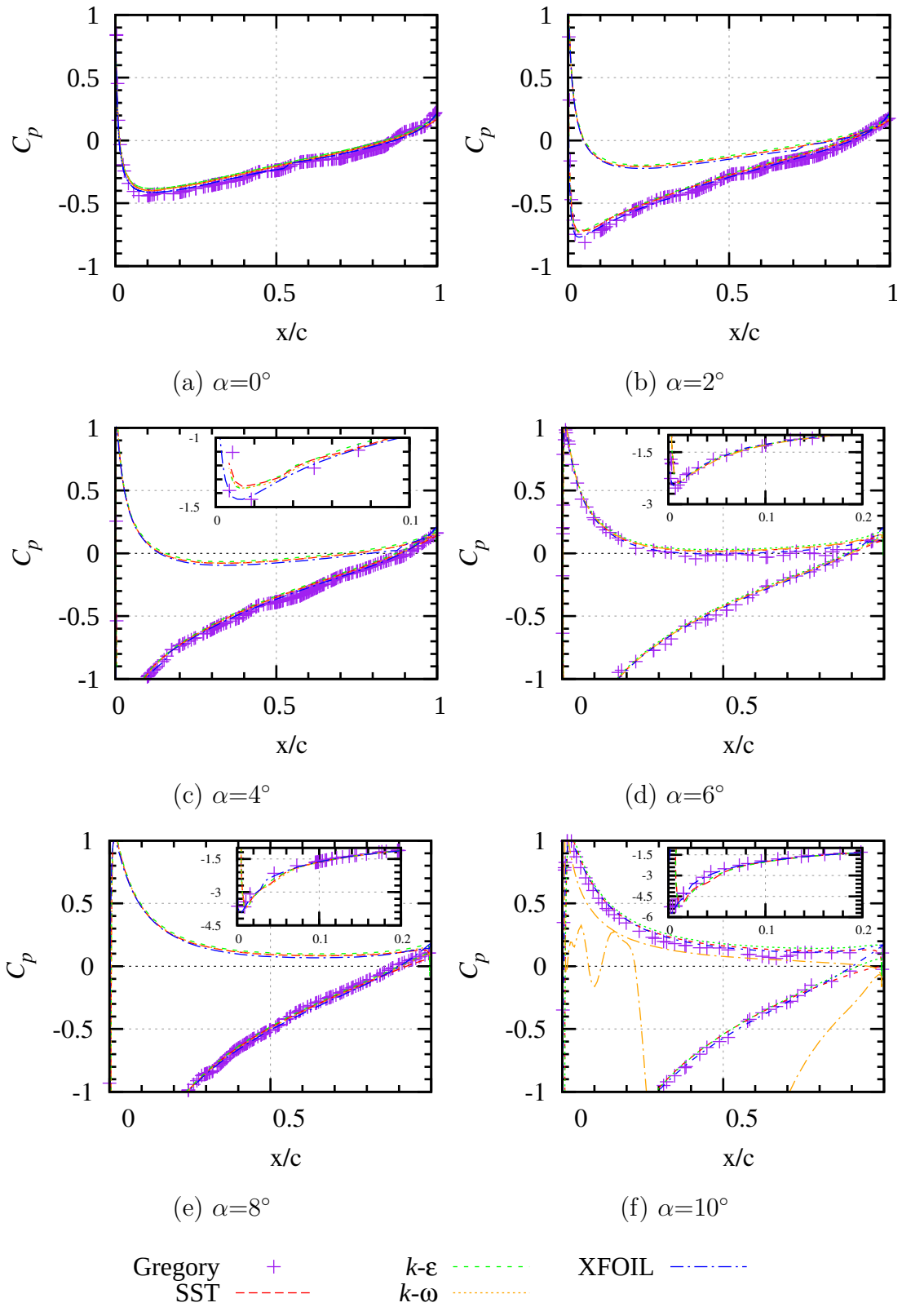

Figure 2.7: Comparison of computed and experimental chordwise (x/c) pressure coefficients (C_p) for a NACA 0012 section.

2.3.2 Results and Discussion

Once convergence and validation were established the computed wall shear coefficient and force coefficients from RANSE simulations for steady flow were compared with XFOIL [26] predictions. The XFOIL background amplification factor was set at 4.28 to match the RANSE model turbulence intensity of 0.5%. The values of C_L and C_D for a NACA 0009 section using XFOIL and $k-\epsilon$ and SST turbulence models were predicted for incidence angles 2, 5 and 10° as shown in Figure 2.8. The $k-\epsilon$, and SST models compared well in C_L with XFOIL results and data from Abbott and von Doenhoff [1] with a slight variation at α=10°. C_D predicted by $k-\epsilon$, and SST models were higher than the XFOIL calculation. The difference in C_D can be seen in the difference in predicted wall shear coefficient on the pressure side of the foil (Figure 2.9).

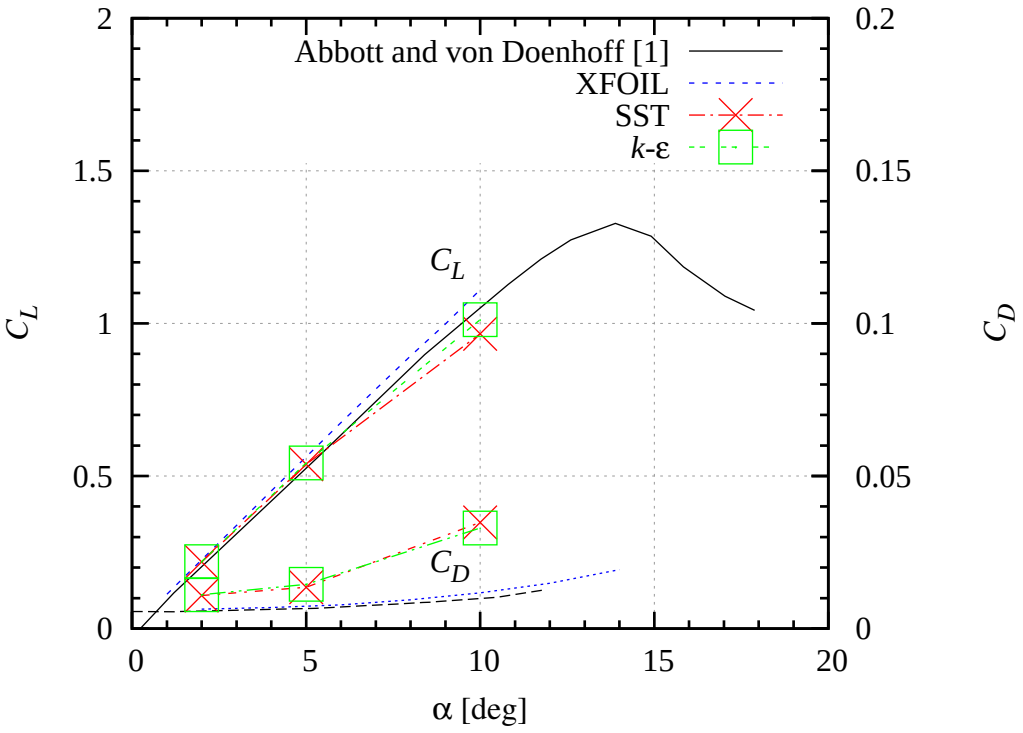

Figure 2.8: Comparison of data from Abbott and von Doenhoff [1] and computed XFOIL and RANSE results for C_L and C_D at varying incidence angles (α) for NACA 0009 section

The comparison for incidence angles 2, 5 and 10° computed using XFOIL and RANSE results for C_L and C_D for a NACA 0009 section is shown in Figure 2.9. The positive chordwise values represent the pressure side of the foil and the negative values the suction side. The suction side for incidence angle of 2 and 5° shows a greater extent of reduced wall shear for XFOIL than the $k-\epsilon$ and SST models. The magnitude of wall shear at incidence angle of 2 and 5° are higher for the $k-\epsilon$ and SST models than XFOIL. The $k-\epsilon$ model has the greatest difference on the pressure side, but on the suction side the $k-\epsilon$ and SST are more similar

in magnitude. At an incidence angle of 10° the suction side wall shear has a large difference in magnitude between XFOIL and RANSE equation turbulence models. Both of the RANSE models assume a turbulent boundary layer, although the SST model is recommended for high accuracy in the boundary layer simulations. The SST model is designed to give better accuracy in flows with adverse pressure gradients [37] and includes transport effects in the formulation of the eddy viscosity. This may explain the observed difference between the $k - \epsilon$ and SST models with wall shear predictions. Both the $k - \epsilon$ and SST models are further investigated for static and dynamic force calculation in the next sections.

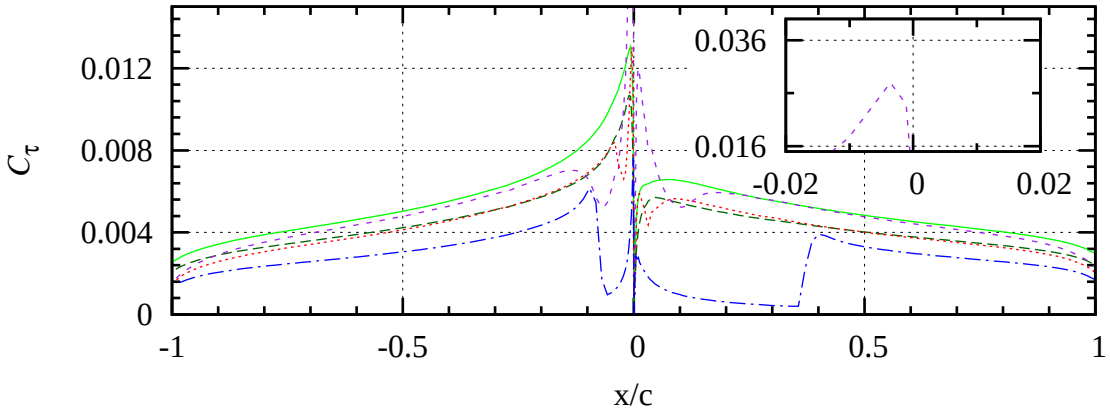

(a) α=2°

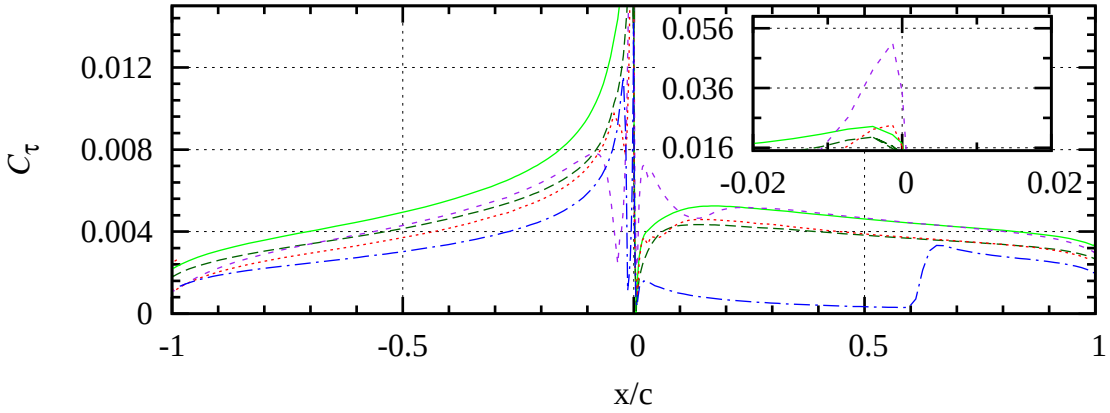

(b) α=5°

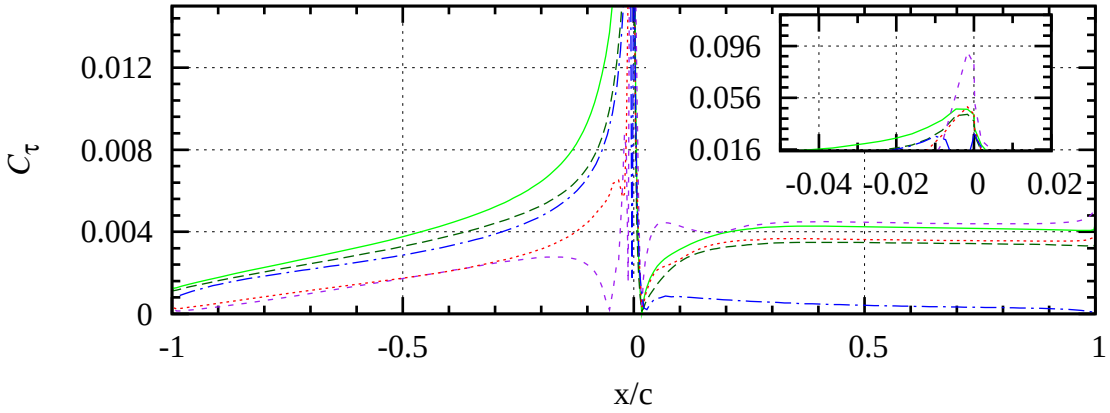

(c) α=10°

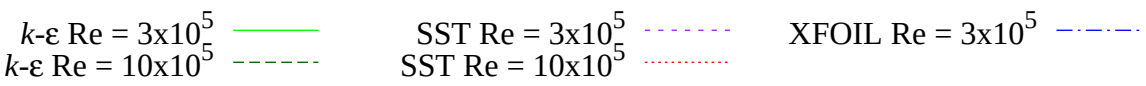

Figure 2.9: Comparison of computed chordwise (x/c) wall shear coefficients (C_τ) for a NACA 0009 section

2.4 Dynamic Computation

2.4.1 Validation

Dynamic validation was conducted using experimental results contained in Piziali [83]. These experiments were conducted at a Reynolds number of 1.98×10^6 and a pitch centre at 1/4 c for a NACA 0015 section. Details of the test matrix for this validation study is contained in Table 2.1.

Table 2.1: NACA 0015 section 1/4c dynamic validation with Piziali [83]

k	$\bar{\alpha}$	$\Delta\alpha$
0.038	4°	2,4°
0.093	4°	2,4°
0.131	4°	2,4°
0.188	4°	2,4°

Piziali [83] conducted a detailed series of oscillating wing aerodynamic tests with fast response pressure transducers. The C_L, C_D and C_M were calculated from the pressure, normal to the chord, neglecting skin friction. The moment was calculated by integrating these pressures over the chord neglecting any moment due to the thickness of the foil.

Results from the $k-\epsilon$, and SST models were compared with the experimental results from Piziali [83]. The results compared well for reduced frequency values of 0.131 and 0.188 for both turbulence models. However, for the lower reduced frequency values of 0.038 and 0.093, when using the $k-\epsilon$ model, for an incidence amplitude of 2 and 4° and a mean incidence of 4°, as shown in Figure 2.10, although convergence was reached there was a large mean offset of C_D from the experimental data. The results compared well for all cases using the SST model. The SST model uses the $k-\omega$ model near solid walls and the $k-\epsilon$ model near the boundary layer edges and in free shear layers [23]. Therefore it could be assumed that both the $k-\epsilon$ and SST models would yield similar results but the SST model modifies the eddy viscosity by forcing the turbulent shear stress to be bounded for a constant time inside the boundary layer [23]. This may explain the offset of C_D at a reduced frequency of 0.038 and 0.093. From this comparison it was decided that the SST was to be used for the remainder of the numerical modelling. A full set of SST results is presented in Appendix A, Figures A.1- A.3.

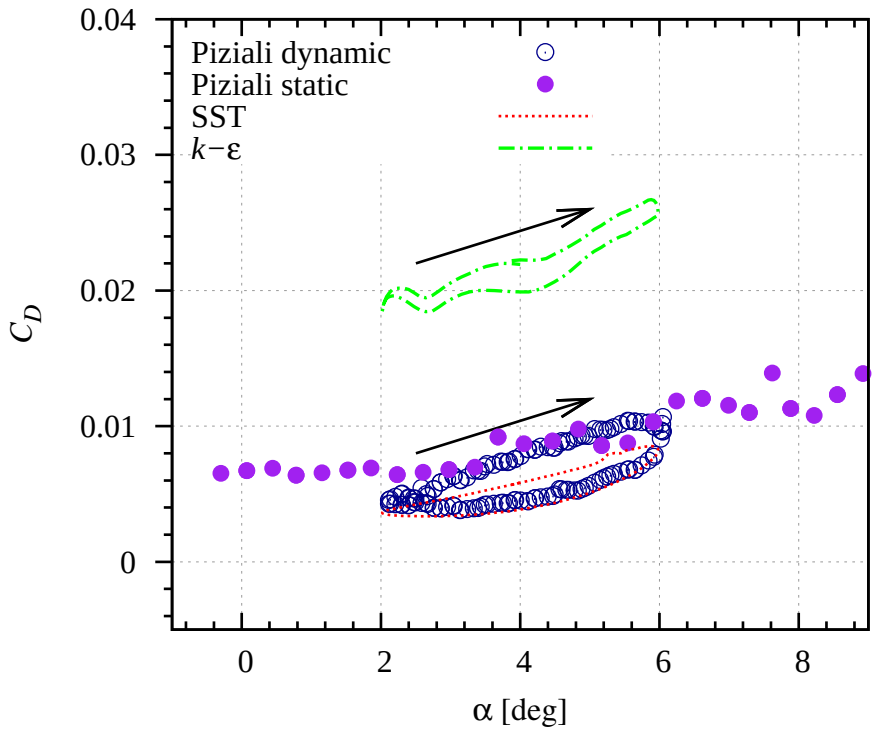

Figure 2.10: Comparison of computed and experimental C_D hysteresis loop with a reduced frequency of 0.131, mean incidence of 4° and incidence amplitude of 2° for a NACA 0015 section

As an example of the results contained in Appendix A the following describes one of the data sets. C_L, C_D, and C_M for a reduced frequency of 0.188, incidence amplitude of 2° and mean incidence of 4° are presented in Figures 2.11, 2.12 and 2.13 respectively. The arrows in the graphs indicate the direction of the hysteresis in time and show the upstroke i.e. for Figure 2.11 the hysteresis loop is in the clockwise direction. A slight over estimate of C_L and underestimate for C_D was apparent in the upstroke, but the downstroke compared well for both C_L and C_D. For C_M the results compared well on the upstroke but with the reversal of direction the change in the C_M slope is not as large as in the experimental data (Figure 2.13). This resulted in a lower moment on the downstroke. The variation in the downstroke can be attributed to the RANSE models assuming a fully turbulent boundary layer with no transition. If transition was modelled it would be expected that there would be a variation in the predicted pressure peak on the suction side of the airfoil at the leading edge resulting in a closer approximation [33]. This may cause a small under prediction of the twist in the full coupled dynamic models in Chapter 5.

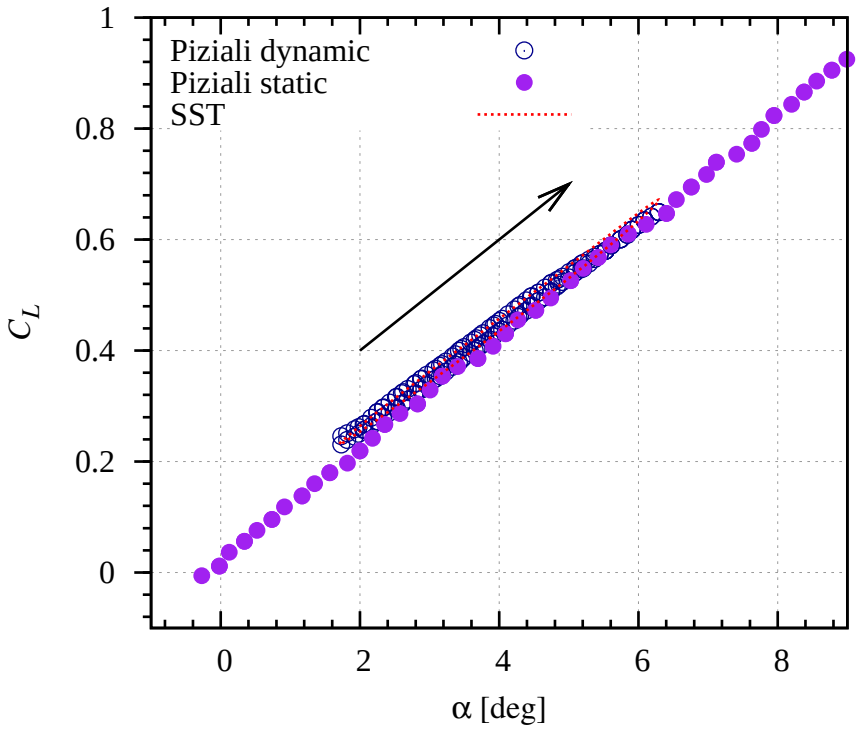

Figure 2.11: Comparison of computed and experimental C_L with a reduced frequency of 0.188, mean incidence of 4° and incidence amplitude of 2° for a NACA 0015 section

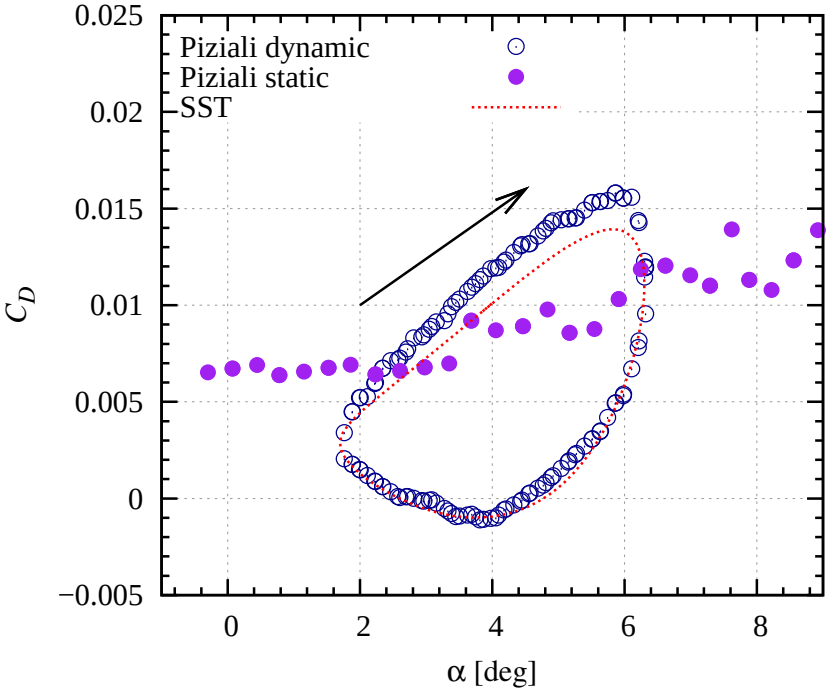

Figure 2.12: Comparison of computed and experimental C_D with a reduced frequency (k) of 0.188, mean incidence of 4° and a incidence amplitude of 2° for a NACA 0015 section

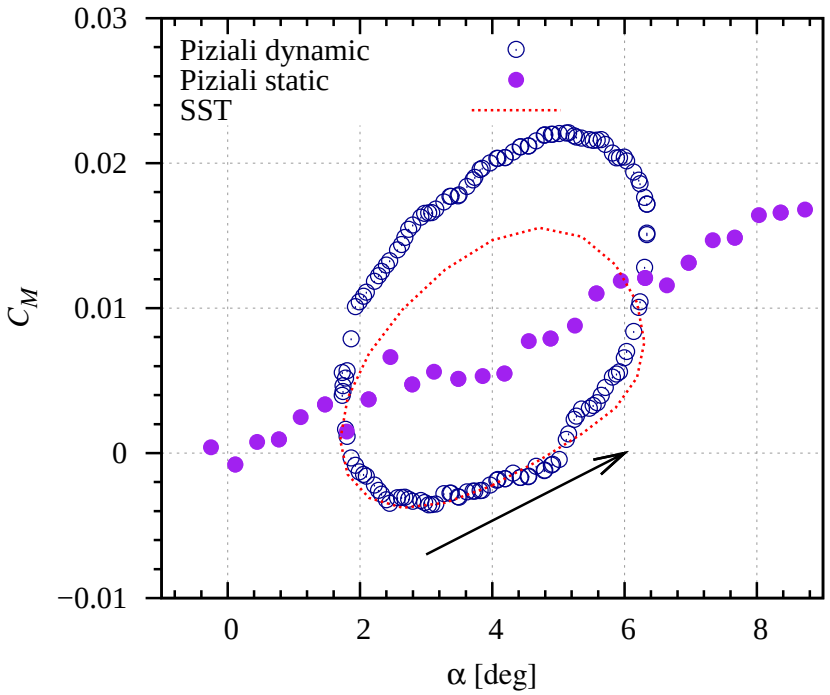

Figure 2.13: Comparison of computed and experimental C_M with a reduced frequency (k) of 0.188, mean incidence ($\bar{\alpha}$) of 4° and a incidence amplitude of 2° for a NACA 0015 section

2.4.2 Panel code and RANSE comparison

Following the dynamic validation of the RANSE model contained in the previous section, oscillating hydrofoil studies of a NACA 0009 section were conducted to compare solutions from the dynamic panel code which is a modified Hess and Smith method contained in Cebeci et al. [23] and SST models. The unsteady method can be used with an unsteady interactive boundary layer method. More details of the code are contained in Cebeci et al. [23]. Details of the test matrix is contained in Table 2.2. Comparisons could only be made for reduced frequency values up to 0.185 beyond which the panel code did not converge.

Table 2.2: NACA 0009 section 1/2c test matrix for panel code comparison

k	$\bar{\alpha}$	$\Delta\alpha$
0.031	0,4°	3°
0.314	0,4°	3°
0.785	0,4°	3°

The SST and unsteady panel code results for C_L and C_M at mean incidence of 4° is shown in Figure 2.14. From these figures it can be concluded that the unsteady panel method predicts low reduced frequency values well where no hysteresis is evident; but over predicts the hysteresis for both C_M and C_L at reduced frequency values of 0.314 or higher.

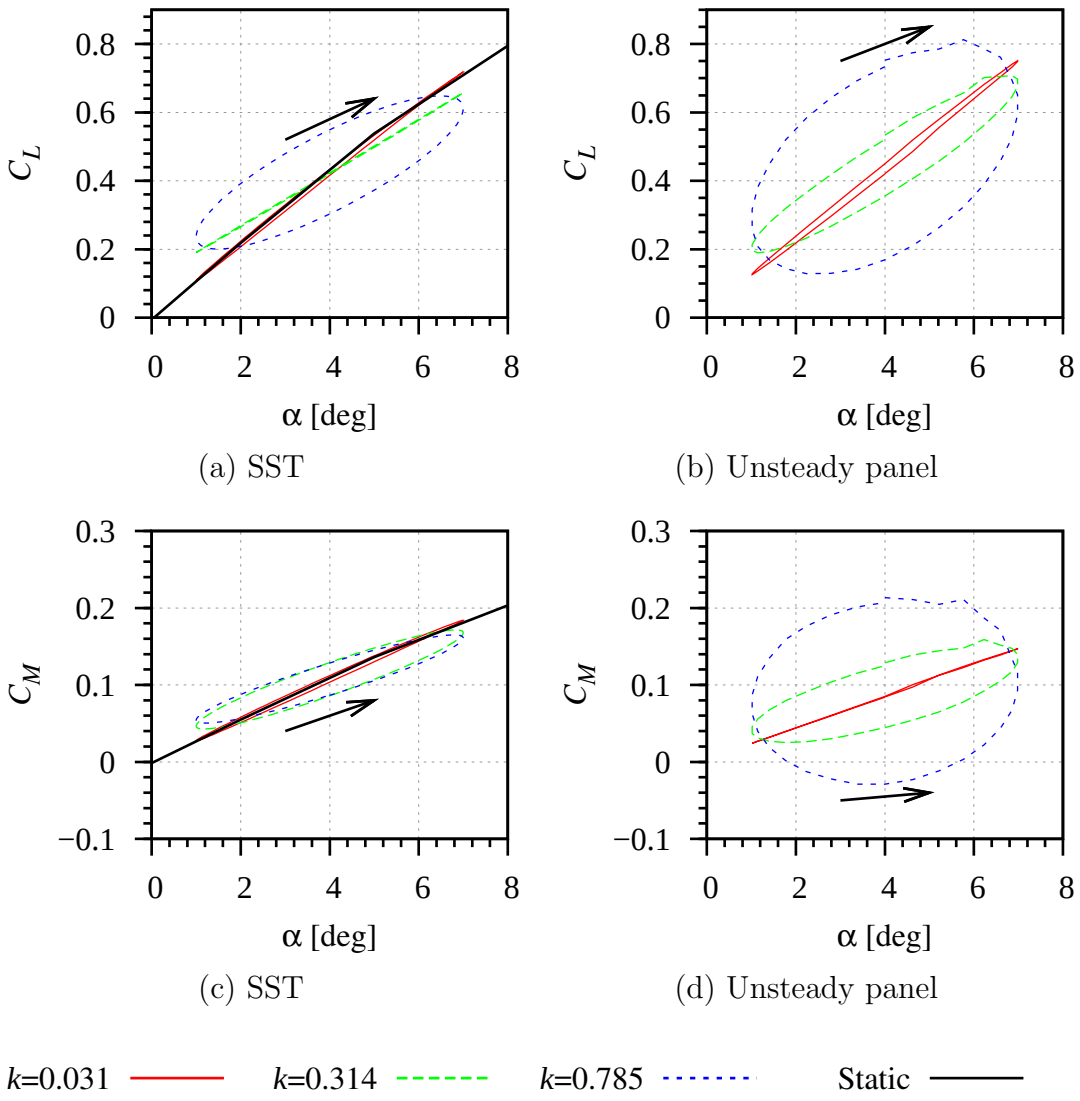

(a) SST (b) Unsteady panel

(c) SST (d) Unsteady panel

Figure 2.14: Comparison of computed SST and unsteady panel code dynamic C_L and C_M for a mean incidence of 4°

2.5 Chapter Summary

This chapter has reviewed previous numerical methods and conducted validation with published experimental results. A RANSE method for simulation of an hydrofoil oscillation in pure pitch was selected from validation results. The SST turbulence model provided the best comparisons with co-efficient of pressure experimental data from Gregory and O'Reilly [41] and dynamic validation by comparing the force coefficients with experimental data from Piziali [83]. After conducting validation of the RANSE code a comparison with an unsteady panel code from Cebeci et al. [23] was conducted. The unsteady panel method compared well to the SST model at low reduced frequency values where no hysteresis is evident but over predicts the hysteresis for both C_M and C_L at reduced frequency values of 0.314 or higher.

This chapter demonstrates that RANSE solutions provide a more accurate simulation for an unsteady hydrofoil oscillating in pure pitch. It is therefore concluded that for reduced frequencies in the range from 0.013-3.142 the SST model gives the more reliable solution.

Chapter 3

Rigid Body Fluid Dynamics

The investigation of a 3D NACA 0009 hydrofoil with trapezoidal planform at steady incidence angle and unsteady oscillation in pure pitch is described in this chapter. It uses the previously developed 2D grid as a basis for the 3D fluid dynamic grid and compares the static and dynamic characteristics of rigid 2D and 3D foils. The effect of 3D fluid flow is investigated by comparing results to 2D as well as comparisons with Theodorsen's 2D analytical theory, which was explored in chapter 2. This chapter presents static results and indicative dynamic hysteresis plots for C_L, C_D and C_M at 0 and 4° mean incidence, and maximum C_L, C_D, C_M and phase angle of the force and moment for the unsteady pitch oscillation.

3.1 Methodology

From Chapter 2, the SST model was shown to give the most accurate results in the dynamic case. The current chapter investigates initially steady state and then dynamic behaviour of a hydrofoil sinusoidally oscillating in pure pitch. Steady state incidence angles analysed were 1, 3, 4, 5 and 10°. Details of the test matrix for the dynamic case at a mean incidence of 0 and 4° for variation in incidence amplitude and reduced frequency are shown in Table 3.1. The pitch centre of the hydrofoil oscillation is located at 1/2 c. All cases were run for Reynolds numbers of 3.36×10^5 and 1.12×10^6. Results for RANSE simulations were summarized using their maximum C_L, C_D and C_M and phase angle to the incidence oscillation with respect to reduced frequency. The phase angle was determined through a least squares fit of a sine function of the order of peaks over one cycle. For example, C_D has a double peak for a mean incidence of 0° therefore the least squares fit was conducted for the second harmonic, this is discussed in section 3.2.2. These runs were completed over 1.5 cycles with results converging after half a cycle: it was noted from the 2D analyses that once the run was converged the hysteresis plot started and finished at the same point over a cycle.

Table 3.1: NACA 0009 1/2c run matrix RANSE

k	$\bar{\alpha}$	$\Delta\alpha$
0.031	0,4°	0,1,2,3,5°
0.094	0°	3°
0.157	0°	3°
0.188	0°	3°
0.251	0°	3°
0.314	0,4°	0,1,2,3,5°
0.534	0°	3°
0.785	0,4°	0,1,2,3,5°
1.571	0,4°	0,1,2,3,5°
3.142	0,4°	0,1,2,3,5°

3.1.1 Mesh Development

The basis for the 3D grid was the previously validated 2D grid which was extrapolated to the 3D geometry, as shown in Figures 3.1 and 3.2. The structured grid was constructed using a C-topology with an H-topology at the trailing edge and a Y-grid extrapolated from the tip of the foil as shown in Figure 3.2(b). The 3D foil as described in Section 1.5.1 is a trapezoidal planform of 120 mm root chord length, 60 mm tip chord length and 300 mm span. The inlet velocity boundary was located 2.5 × the root chord upstream from the leading edge. The outlet pressure opening was located 11.5 × the root chord downstream from the trailing edge. The domain was 0.6 m wide × 0.6 m deep.

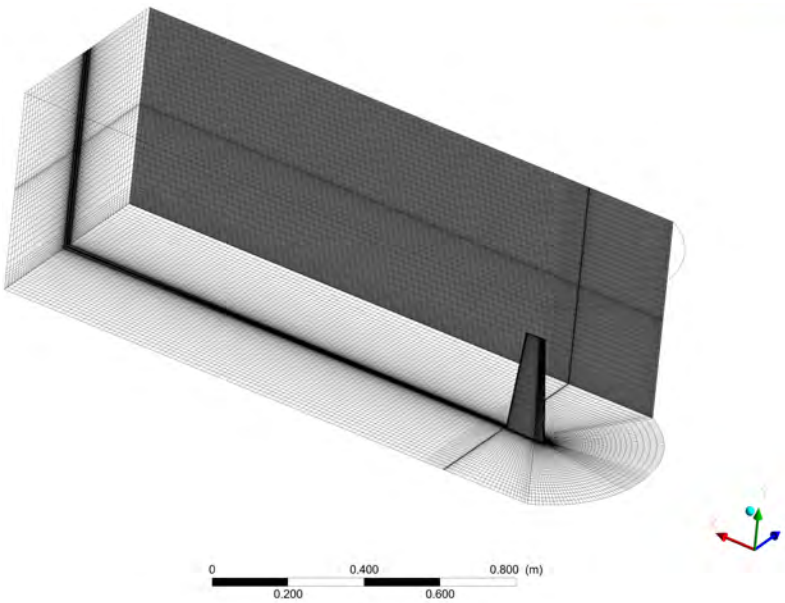

Figure 3.1: Detail of entire computational domain mesh.

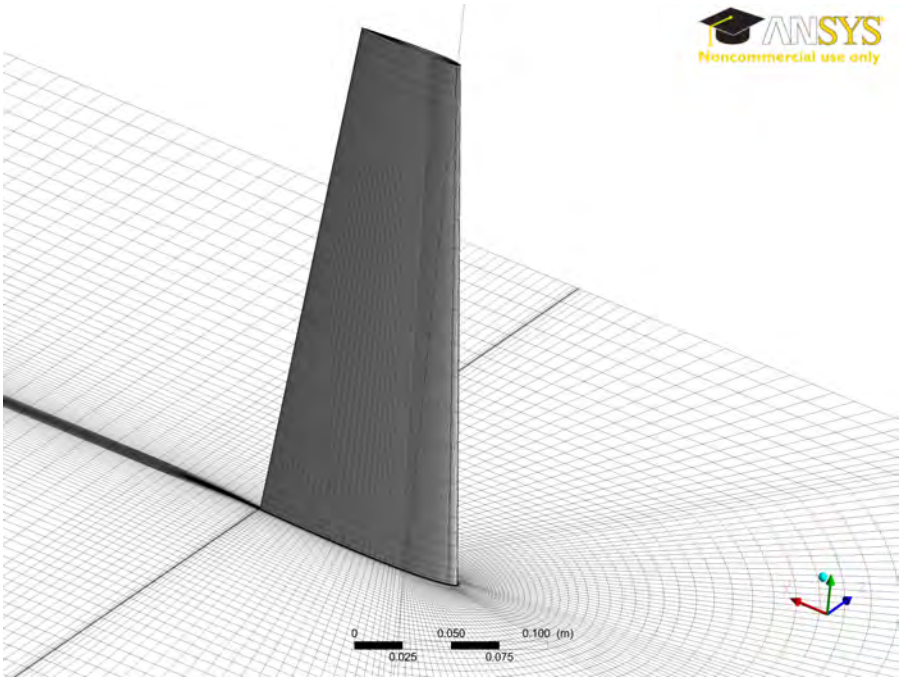

(a) Foil

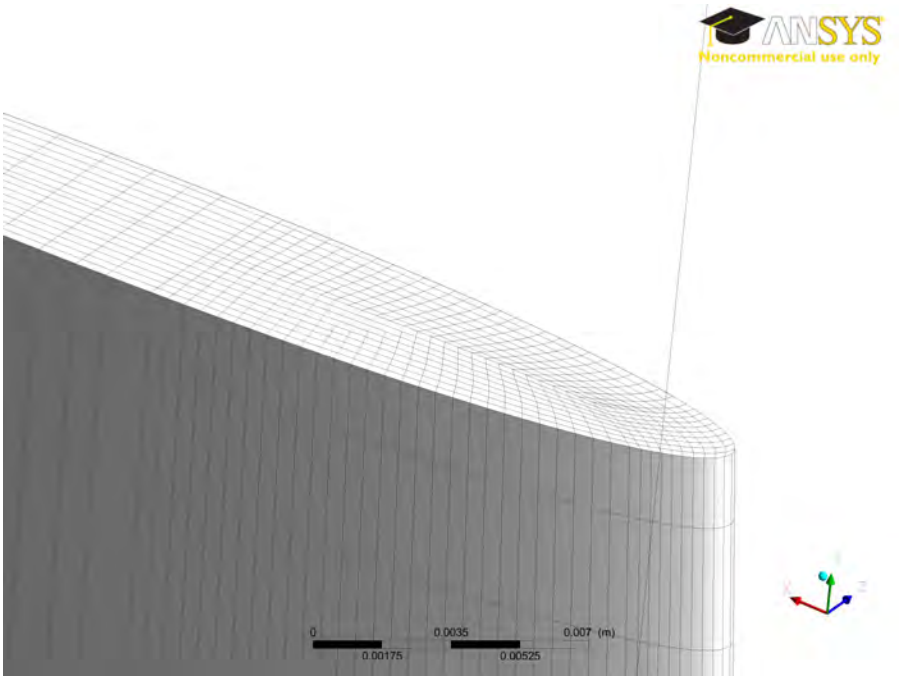

(b) Tip

Figure 3.2: CFD 3D mesh of the hydrofoil.

3.1.2 Grid Independence and Temporal Convergence

Steady state convergence was conducted by dynamically deforming the mesh to the required incidence angle (this method is detailed in Chapter 2). This procedure was conducted for incidence angles of 2, 5 and 10° until a grid independent solution was reached. A plot of the C_D convergence for the 3D CFD mesh with increasing number of elements is shown in Figure 3.3. This mesh was also checked to ensure that there was no cell inversion at an incidence angle of 10° when the tip is deflected. A grid with 1 303 723 elements, corresponding to 30 elements along the span was selected.

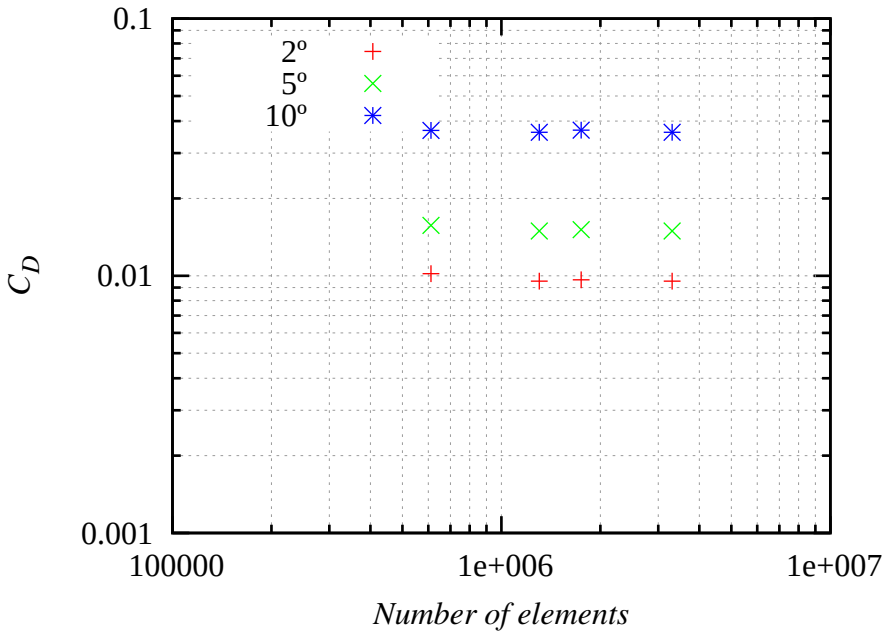

Figure 3.3: CFD 3D convergence C_D.

The temporal convergence plots for force and velocity at a point in the wake are shown in Figure 3.4(a) and 3.4(b) respectively, at a reduced frequency of 3.142 and Re of 3x10^5. A total of 100 time steps per period was selected. The simulated time covered 3 complete cycles, the first cycle contains transients from the steady start up solution after which the second and the third cycle are identical. The resulting forces in 3D on the hydrofoil through three pure sinusoidal pitch oscillations is shown in Figure 3.5. The points plotted in red represent each time step in Figure 3.5(a). This figure illustrates that the 3D run is similar to the 2D and also converges within half a cycle. The convergence is also indicated by the hysteresis cycle forming a closed loop.

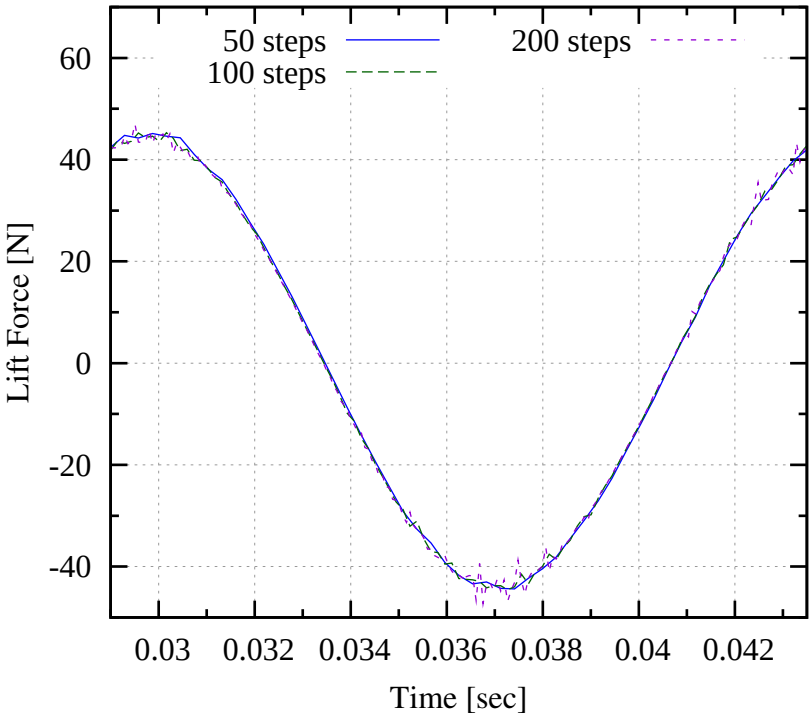

(a) Lift Force on the foil

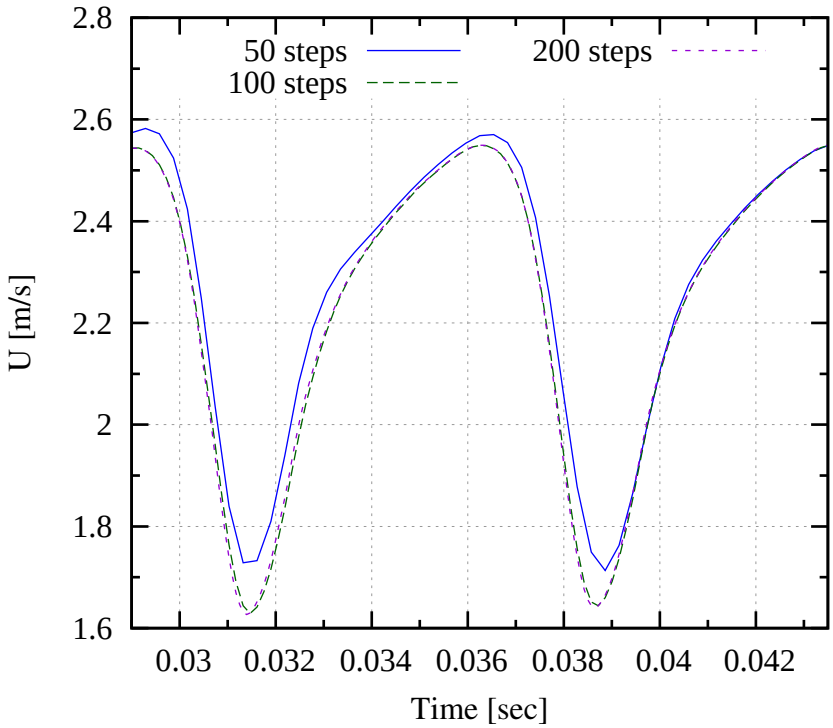

(b) Velocity at a point located at the mid span, 1.5 chord lengths behind the foil

Figure 3.4: Plot of temporal convergence

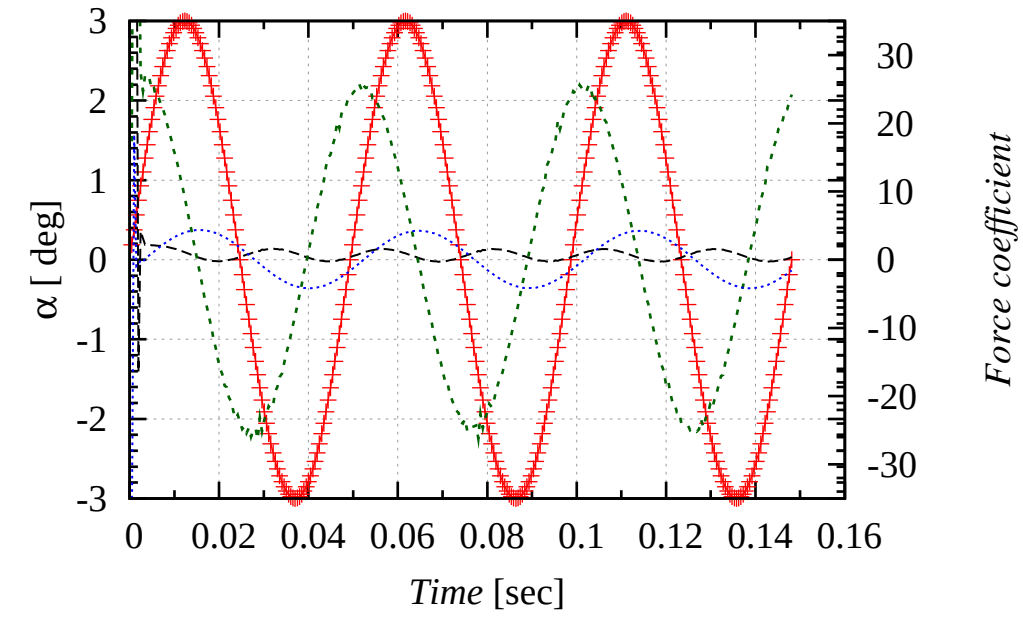

(a) Time

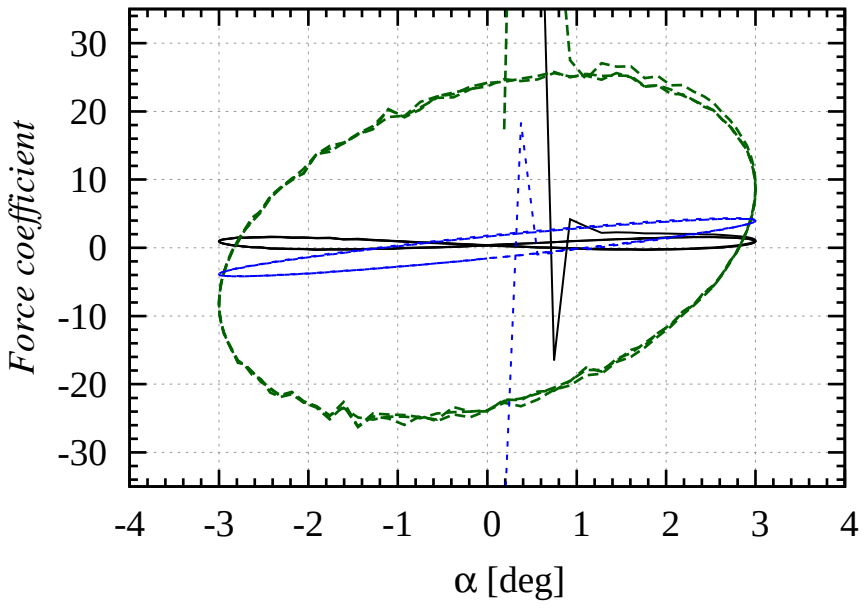

(b) Hysteresis

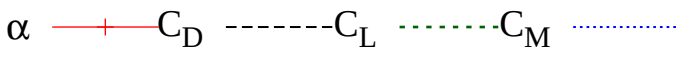

Figure 3.5: Forces on the hydrofoil through 3 pure sinusoidal pitch oscillations.

3.2 Results and Discussion

This section is divided into steady state, and unsteady fluid dynamics sections. The steady state results compare the values of C_L, C_D and C_M for the 2D and 3D models. The 2D results were shown to be Reynolds number independent in Hutchison et al. [53], as such only one Reynolds number is presented for comparision to 3D. The unsteady fluid dynamics section is divided in three sections presenting qualitative results, hysteresis loops and the summary results for the maximum values and their corresponding phase angles (Φ) between C_L, C_D and C_M and the dynamic incidence over a cycle.

3.2.1 Steady State

2D and 3D comparisons of static C_L and C_D is shown in Figure 3.6. The slope of the 2D and 3D C_L curves are 0.11 and 0.06 respectively and have no dependence on Reynolds number (Figure 3.6). The slope of the 2D curve of 0.11 is the same as predicted by theory of finite span in White [103], but the 3D curve is 5% less. This has been attributed to the trapezoidal planform as the theory is based on a rectangular planform. The 3D C_D curve shows a Reynolds number dependence and a small increase in magnitude from the 2D curve. The 3D C_D curve with the lower Reynolds number has the greatest increase from the 2D curve of approximately 0.01 at an incidence angle of 10°. The 2D and 3D comparisons of static C_M curves is shown in Figure 3.7. The slope of the 2D and 3D C_M being 0.025 and 0.012 respectively.

3.2.2 Unsteady Fluid Dynamics Forces and Moments

This section presents hysteresis plots for the C_L, C_D and C_M at 0 and 4° mean incidence. A summary of the maximum amplitude of C_L, C_D and C_M over a cycle is also presented. The reference chord for the 3D co-efficient calculations was the root chord of 120 mm.

This section begins with a descriptive set of figures to illustrate some of the complexities in the fluid around the foil and within the wake. The pressure on the wall intersecting the foil at 0 and 4° mean incidence, at a Reynolds number of 1.12×10^6, incidence amplitude of 3° and reduced frequency of 0.785 at varying dynamic incidence angles is shown in Figures 3.8 and 3.9. The upstroke is the top two sets of figures and the downstroke is the bottom two figures. The pressure over a cycle is symmetric at 0° mean incidence(Figures 3.8). The high pressure region at the tip of the NACA section will move around the leading edge throughout an oscillation. At 4° mean incidence the pressure distribution over a cycle is not symmetric between the downstroke and the upstroke; rather the region of minimum pressure increases and decreases on the suction side with the largest suction region at the mean incidence on the upstroke (Figures 3.9).

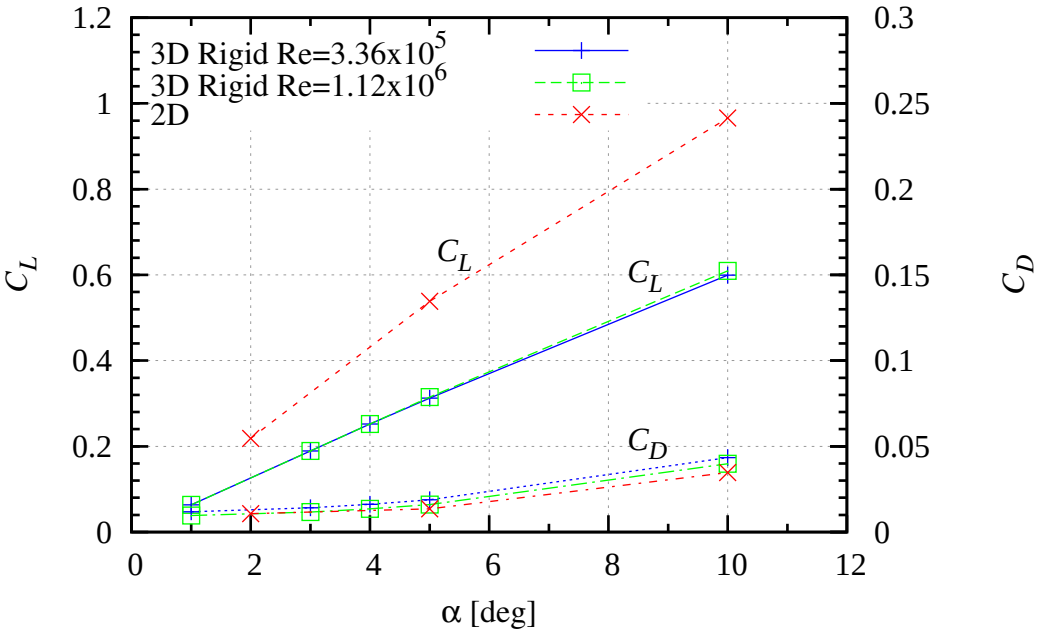

Figure 3.6: Static 2D and 3D comparison of C_L and C_D at varying incidence angles (α).

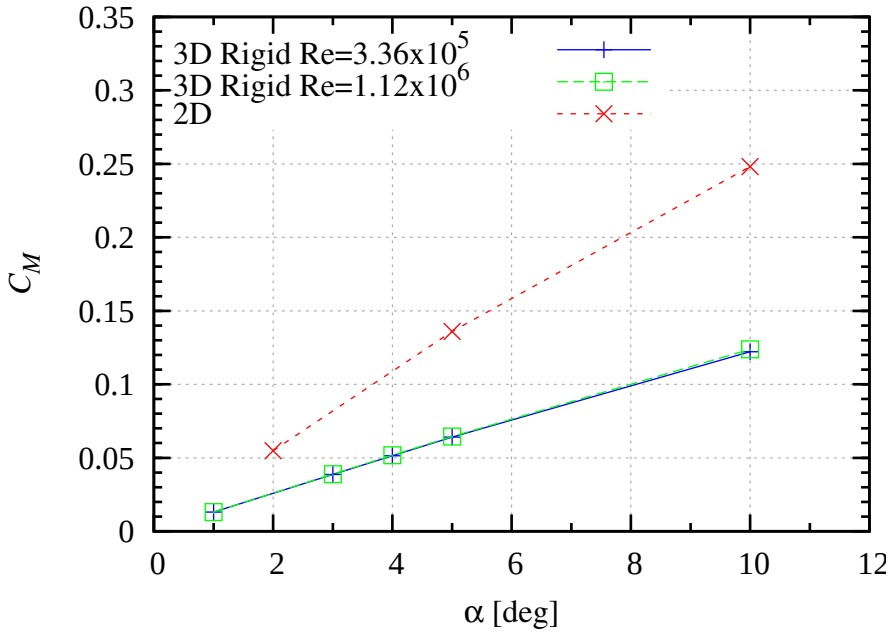

Figure 3.7: Static 2D and 3D comparison of C_M at varying incidence angles (α).

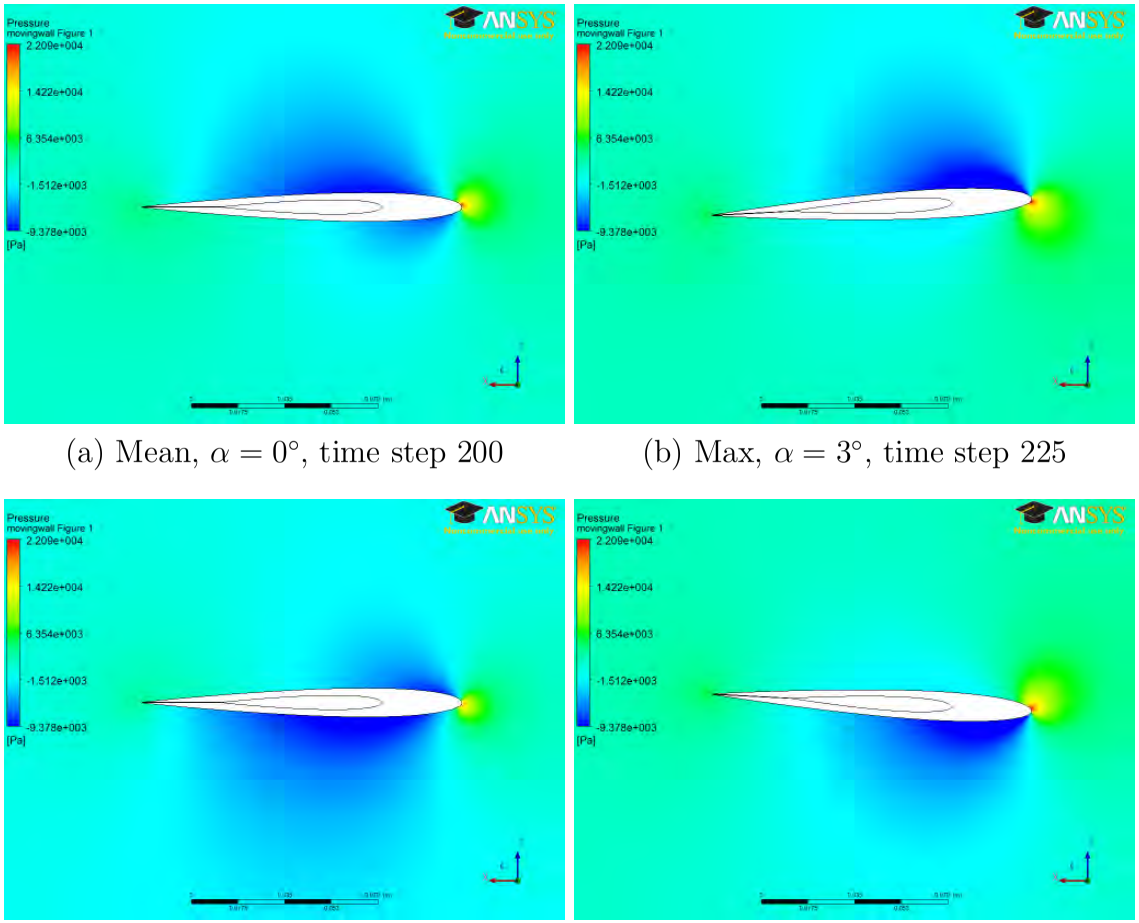

(a) Mean, $\alpha = 0°$, time step 200

(b) Max, $\alpha = 3°$, time step 225

(c) Mean, $\alpha = 0°$, time step 250

(d) Min, $\alpha = -3°$, time step 275

Figure 3.8: Pressure on the wall intersecting the foil for mean incidence of 0°, Reynolds number of 1.12×10^6, incidence amplitude of 3° and reduced frequency of 0.785 at varying incidence angles (α), showing the symmetric pressure distribution over a cycle.

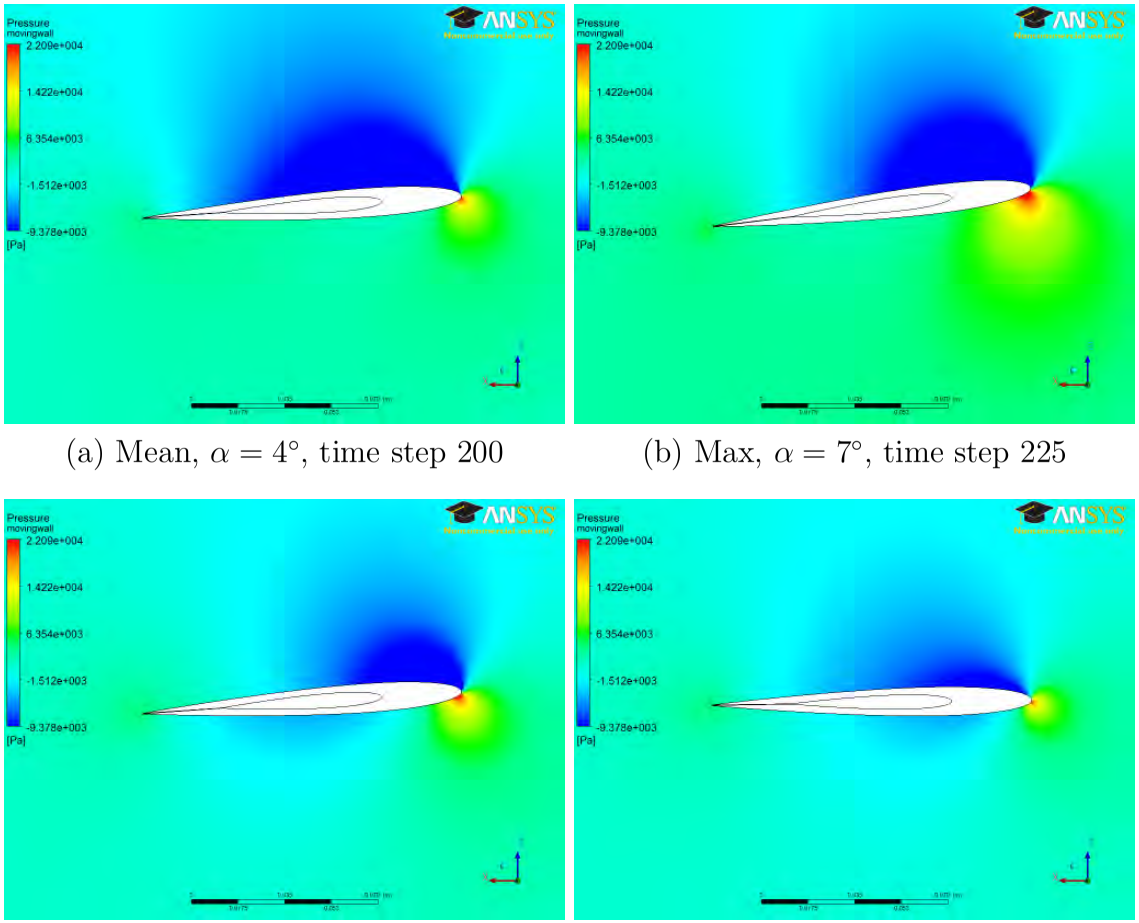

(a) Mean, $\alpha = 4°$, time step 200

(b) Max, $\alpha = 7°$, time step 225

(c) Mean, $\alpha = 4°$, time step 250

(d) Min, $\alpha = 1°$, time step 275

Figure 3.9: Pressure on the wall intersecting the foil for mean incidence of 4°, Reynolds number of 1.12×10^6, incidence amplitude of 3° and reduced frequency of 0.785 at varying incidence angles (α), showing the asymmetric pressure distribution over a cycle.

To look at the vorticity in the wake and around the foil the Q-criterion was used from -100 to 100 $[s^{-2}]$. The Q-criterion is the second invariant of the velocity gradient tensor [38] i.e. a measure of vorticity in the wake. The hydrofoil in Figures 3.10 and 3.14 is at the mean incidence, at a Reynolds number of 1.12×10^6 and a reduced frequency of 0.785. The spanwise effect at a Q-criterion at -100 $[s^{-2}]$ is shown in Figure 3.10. This shows that the flow is 2D for most of the foil's span with a vortex at the tip and the root of the foil. The nature of the wake was looked at further at the tip and mid span of the foil. The effect of mean incidence change in the wake for an incidence amplitude of 3° at the mid span and tip of the foil respectively, is shown in Figures 3.11 and 3.12. The effect of change of incidence amplitude from 1 to 5° at the mid span of the foil at a mean incidence of 4° is shown in Figure 3.13. The wake travelling downstream at the tip and mid span for a 0° mean incidence is compared in Figure 3.14.

At the tip of the foil there is a pronounced difference in the behaviour of the tip vortex at 0 and 4° mean incidence, although at the tip the pressures about the foil are symmetric for both 0 and 4° mean incidences. The spacing and magnitude of the vorticity travelling downstream varies between the 0 and 4° mean incidences (Figure 3.12). When the foil oscillates at 0° mean incidence the positive Q-criterion wavelength corresponds to the twice the oscillation frequency. In contrast, at the tip at 4° mean incidence, the wave length between a positive region is equal to the oscillation frequency. The size of these regions has increased to approximately twice the size of the region in the 0° mean incidence case. This is due to the two regions effectively merging into one when the foil is oscillated at 4° mean. The tip vorticity in the 4° mean incidence case is biased to one side of the foil and gets shed downstream once an oscillation cycle is complete. A possible implication of this is that the 0 and 4° mean incidence may have a different signature in the wake. This difference is not visible in the integral properties.

The spacing and magnitude of the vorticity travelling downstream at the foil's mid span is approximately equal for both 0 and 4° mean incidences (Figure 3.11). As the incidence amplitude is increased from 1 to 5° the spacing between the vorticity in the wake remains the same, although the width of the wake is increased in the z direction (Figures 3.13). In summary, the magnitude of wake vorticity increases with increased incidence amplitude but the frequency at which the vorticity travels downstream remains equal at the mid span.

The pressure at the mid span and root of the foil are not symmetric at a point in time, but are symmetric at 0° mean incidence throughout a cycle. At 4° mean incidence, the Q value around the foil is more asymmetric (Figure 3.11(b)), although at 0° mean incidence does have a small asymmetry (Figure 3.11(a)). As the incidence amplitude is increased from 1 to 5° the vorticity around the foil also increases when the incidence amplitude increases (Figures 3.13). Around the tip of the foil the invariant Q value around the foil is also symmetric in both cases. The differences between 0 and 4° mean incidences is discussed further in the summary of forces and moments in Section 3.2.2.

The wake travelling downstream at the tip and mid span at a 0° mean incidence

is compared in Figure 3.14. This figure shows that the positive regions travelling downstream from the foil are approximately half a cycle apart, i.e. 90° out of phase.

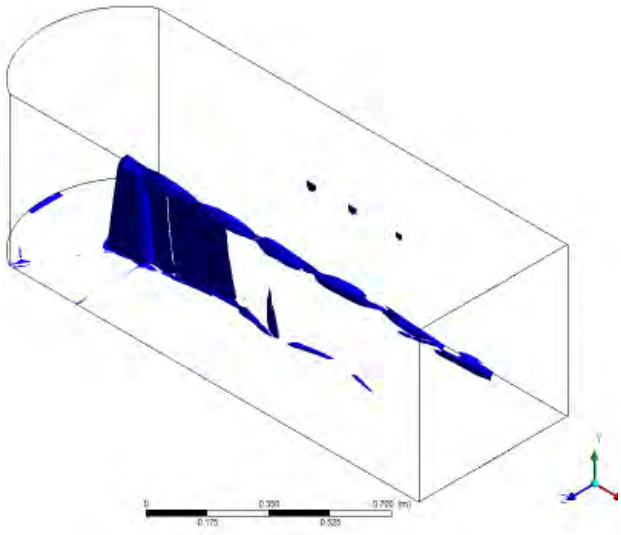

(a) $\bar{\alpha} = 0°$

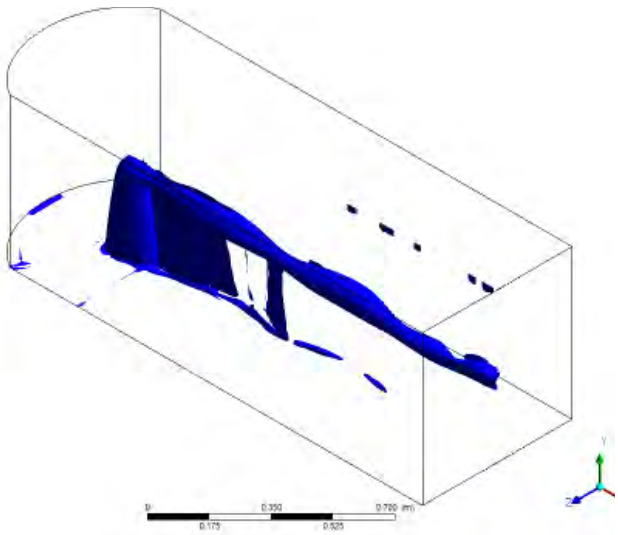

(b) $\bar{\alpha} = 4°$

Figure 3.10: Isosurface of -100 Invariant Q value for Reynolds number of 1.12×10^6, incidence amplitude of 3° and reduced frequency of 0.785 at a dynamic incidence equal to the mean incidence angle ($\alpha = \bar{\alpha}$).

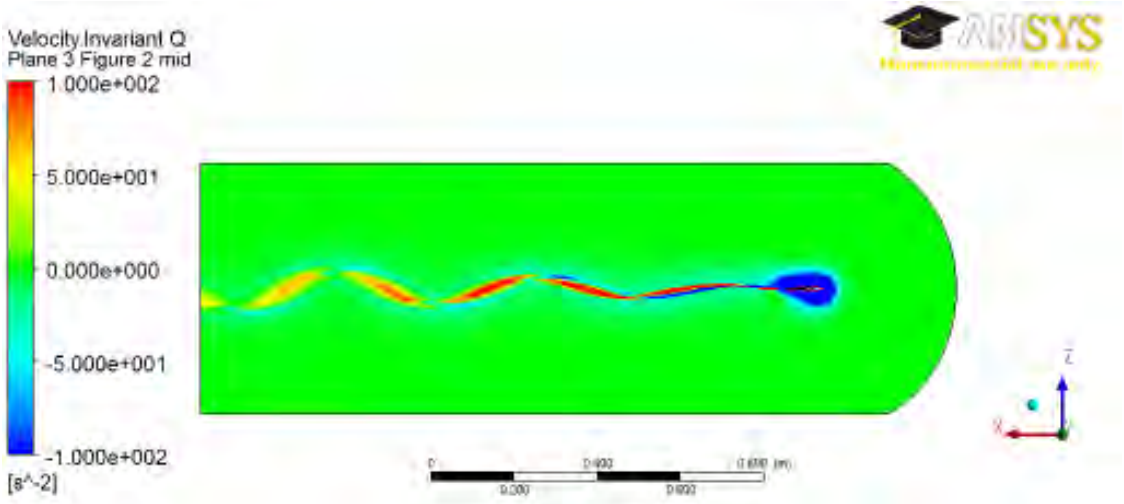

(a) $\bar{\alpha} = 0°$

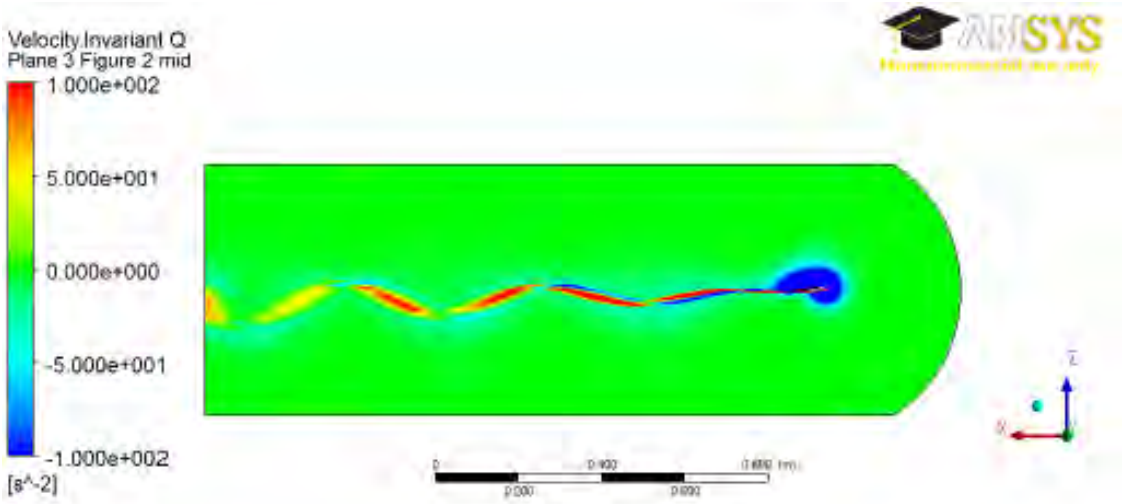

(b) $\bar{\alpha} = 4°$

Figure 3.11: Invariant Q value at the foil mid span for Reynolds number of 1.12×10^6, incidence amplitude of 3° and reduced frequency of 0.785 at a dynamic incidence equal to the mean incidence angle ($\alpha = \bar{\alpha}$). This figure shows the effect of changing the mean incidence on the mid span.

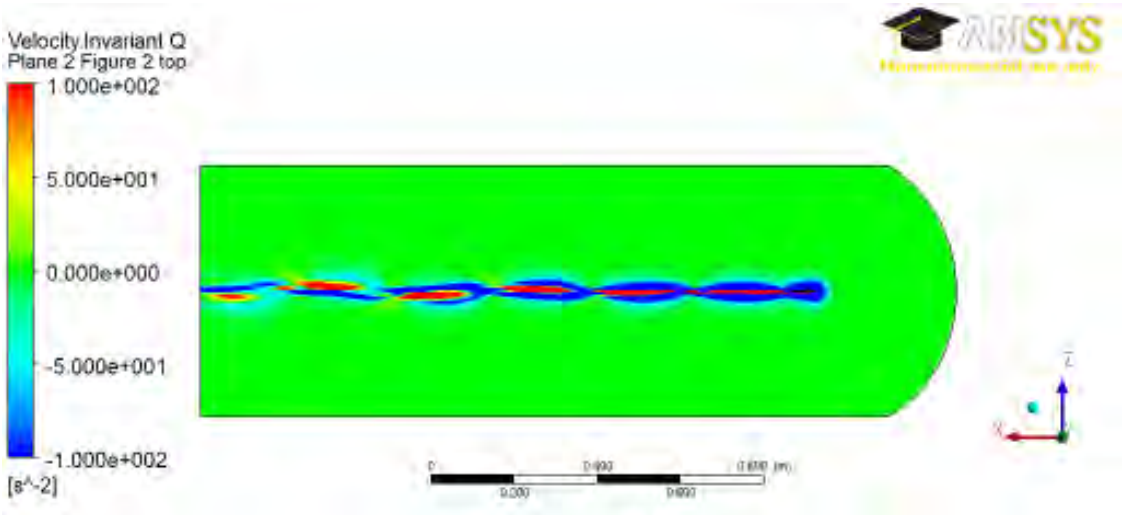

(a) $\bar{\alpha} = 0°$

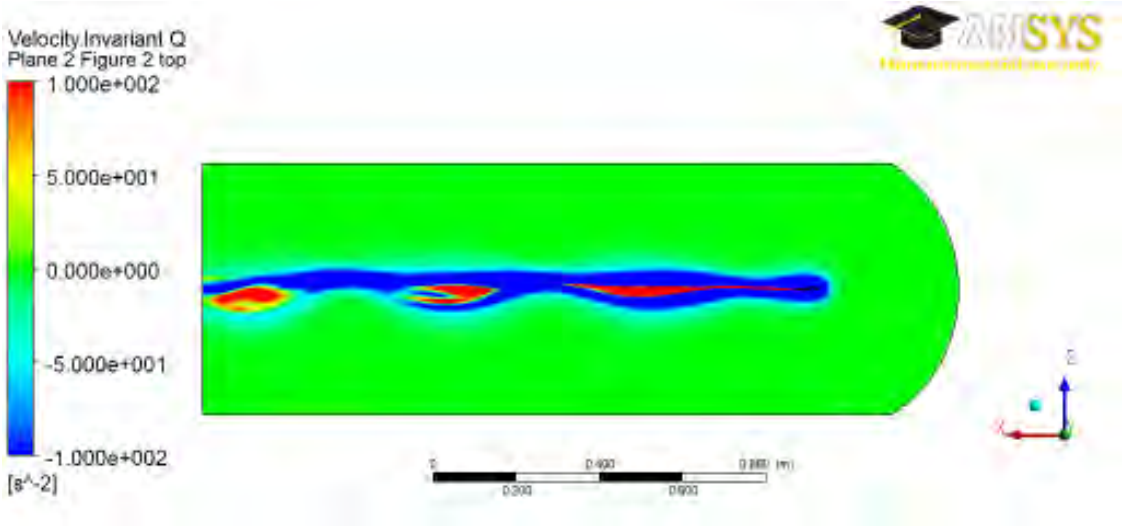

(b) $\bar{\alpha} = 4°$

Figure 3.12: Invariant Q value at the tip of the foil for Reynolds number of 1.12×10^6, incidence amplitude of 3° and reduced frequency of 0.785 at a dynamic incidence equal to the mean incidence angle ($\alpha = \bar{\alpha}$). This figure shows the effect of changing the mean incidence on the tip.

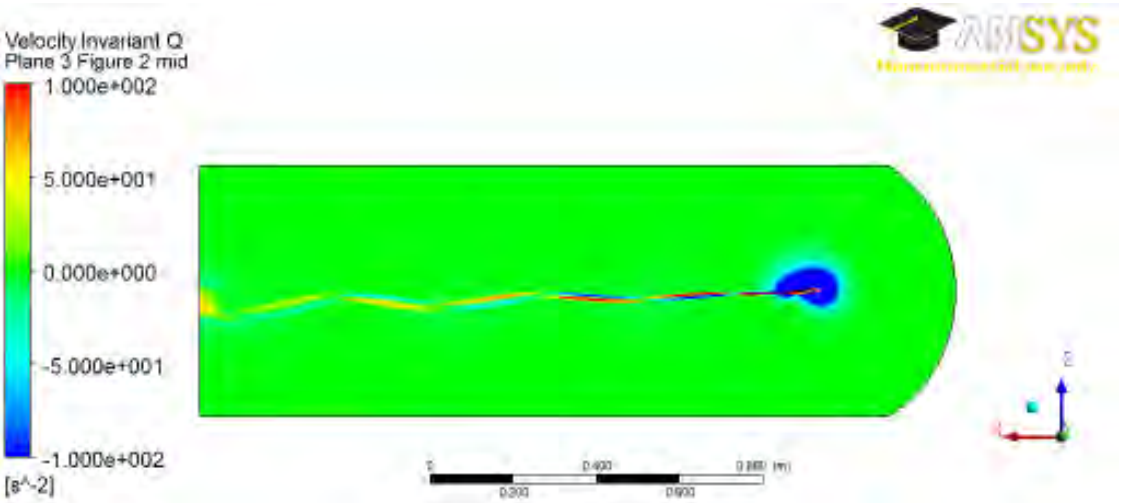

(a) $\Delta\alpha$ =1°

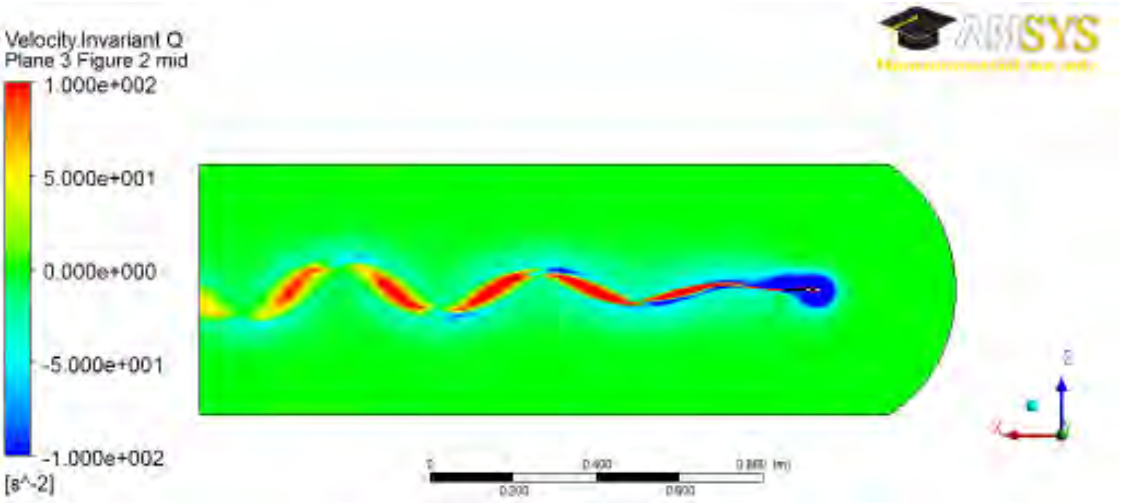

(b) $\Delta\alpha$ =5°

Figure 3.13: Invariant Q value at the foil mid span for mean incidence of 4°, Reynolds number of 1.12×10^6 and reduced frequency of 0.785 at a dynamic incidence equal to the mean incidence angle ($\alpha = \bar{\alpha}$). This figure shows the effect of incidence amplitude.

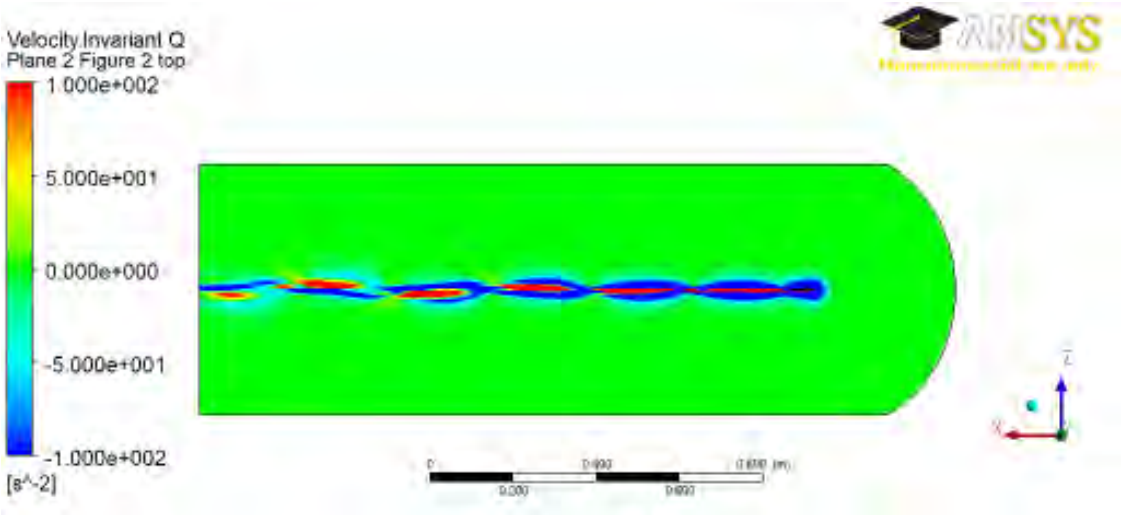

(a) Tip of the foil

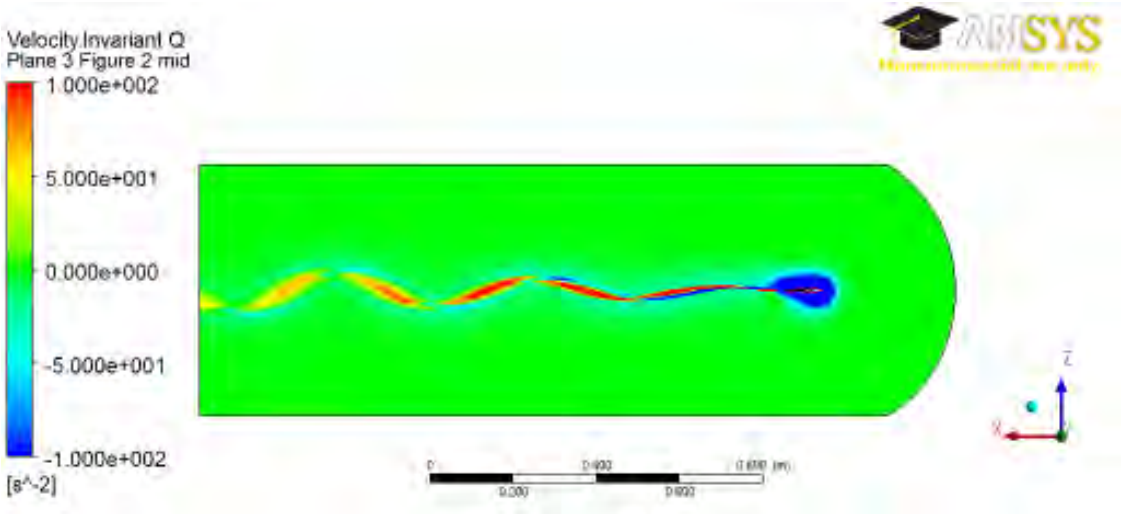

(b) Mid span of the foil

Figure 3.14: Invariant Q value at the tip and mid span for 0° mean incidence at a Reynolds number of 1.12×10^6, incidence amplitude of 3° and reduced frequency of 0.785 at a dynamic incidence equal to the mean incidence angle ($\alpha = \bar{\alpha}$).

Hysteresis

Hysteresis plots for the cases shown in Table 3.2 is shown in Figures 3.15- 3.18. This is a 'T' of the larger test matrix in Table 3.1. These figures present the 2D results on the left and 3D on the right for C_L, C_D and C_M respectively. In the first two sets of six, Figures 3.15 and 3.16, the reduced frequency is varied for 0 and 4° mean incidence values with a constant change of dynamic incidence of 3°. For the second two sets of six, Figures 3.17 and 3.18, the incidence amplitude is varied for 0 and 4° mean incidence values with a constant reduced frequency of 0.785. The trend of the maximum C_L, C_D and C_M is discussed in more detail in the next section. Note the arrow indicates increasing incidence in all cases.

Table 3.2: Hysteresis figures

Figure	$\bar{\alpha}$	k	$\Delta\alpha$
Figure 3.15	0°	0.031,0.314,0.785,1.571,3.142	3°
Figure 3.16	4°	0.031,0.314,0.785,1.571,3.142	3°
Figure 3.17	0°	0.785	0,1,2,3,5°
Figure 3.18	4°	0.785	0,1,2,3,5°

The dynamic C_L and C_M vary about the static C_L and C_M curves (Figures 3.15 to 3.18). The change in lift is associated with the circulation growth on the hydrofoil, the circulation will increase, decrease and change direction throughout a cycle as it oscillates as shown in Figures 3.8 and 3.9. C_L and C_D hysteresis loops are in the clockwise direction, whilst C_M hysteresis loops are anticlockwise. The C_M loop is opposing the change of incidence which is considered to be a stable condition. If the loop was in the opposite direction, it shows a reinforcing of the change in incidence, which is indicative of flutter. Flutter is not investigated in this thesis and was not present in any of the results.

A double peak for C_D is present at a 0° mean incidence but not at a mean incidence of 4°. The C_D hysteresis curves follow the same mean shape as the static C_D curve but the mean magnitude changes with reduced frequency and change of dynamic incidence. The 4° mean incidence does not pass through where the C_D is minimised except at an incidence amplitude of 5°. This indicates lift and drag are odd and even functions respectively of the dynamic incidence. There is less variation between the maxima and minima of the forces for the 3D than the 2D cases. The peak of the cycle occurs at approximately the same point in time for both 3D and 2D. These differences in the dynamic case are not proportional to the steady state 2D to 3D relationship. This difference can be explained in terms of the spanwise circulation/lift reducing to zero at the tip and the pressure equalising over the tip in the 3D case. The 3D spanwise C_P variation is further discussed and compared in Figure 3.19.

The C_L hysteresis loop variation with increasing reduced frequency is shown in Figures 3.15(a), 3.15(b), 3.16(a) and 3.16(b). At the lowest reduced frequency of

0.031 the dynamic C_L loop remains on the static C_L curve throughout the cycle. At a reduced frequency of 0.314 the peak reduces and the lift loop changes slope. From Theodorsen's theory presented in Chapter 2 a reduced frequency of 0.314 occurs just prior to the minima of the maximum lift and at the point at which the lift phase angle changes from a lag to a lead. The C_L loops hysteresis increases at reduced frequencies of 0.785, 1.571 and 3.142. These three reduced frequencies intersect at the same point at the maximum incidence angle.

The C_D loop variation with reduced frequency about a mean incidence of 0° is shown in Figures 3.15(c) and 3.15(d). The 2D loop has hysteresis evident at the lowest reduced frequency. In the 3D case hysteresis is not present until a reduced frequency of 0.314. At a reduced frequency of 0.031 the C_D loop is offset from the static curve in both 2D and 3D. In 2D the C_D mean reduces with reduced frequency and begins to produce thrust for part of the cycle at a reduced frequency of 3.142 (Figure 3.15(c)). It is typical for a foil undergoing a pitch oscillation to produce thrust only above a certain reduced frequency and incidence amplitude [65]. In 3D, the mean C_D reduces less than the 2D cases for a given reduced frequency (Figure 3.15(d)). Although at a reduced frequency of 3.142 the foil does produce thrust for part of the cycle, it is proportionally less than the time of producing thrust in the 2D case.

The C_L, C_D and C_M hysteresis variation of reduced frequency at 4° mean incidence is shown in Figures 3.16(c) and 3.16(d). The C_D loops in 2D and 3D both vary about the static curve with no shift in the mean, although there is increase hysteresis as the reduced frequency increases. Above a reduced frequency of 0.785 and 1.571, thrust is produced for part of the cycle in 2D and 3D respectively. Reduced frequencies 0.314, 0.785, 1.571 and 3.142 all intersect at the point of maximum incidence angle for both 0 and 4° mean incidences. At 0 and 4° mean incidences the C_D loops change direction between the upstroke and downstroke over an increased incidence angle change with the increase in reduced frequency. That is, the phase angle of the maxima and minima both increase with reduced frequency.

The variation in C_M hysteresis loop with increasing reduced frequency is shown in Figures 3.15(e), 3.15(f), 3.16(e) and 3.16(f). Similarly to C_L, at the lowest reduced frequency of 0.031, the C_M loop remains on the static C_M curve. Reduced frequencies 0.314 and 0.785 show the maxima and minima reducing in magnitude. At reduced frequencies of 1.571 and 3.142 the C_M maxima and minima begin to increase in magnitude. At the maximum incidence the C_M loops remaining less than the corresponding static curve values except for at a reduced frequency of 3.142. The moment curves unlike C_L and C_D curves intersect at incidences below the maxima and minima.

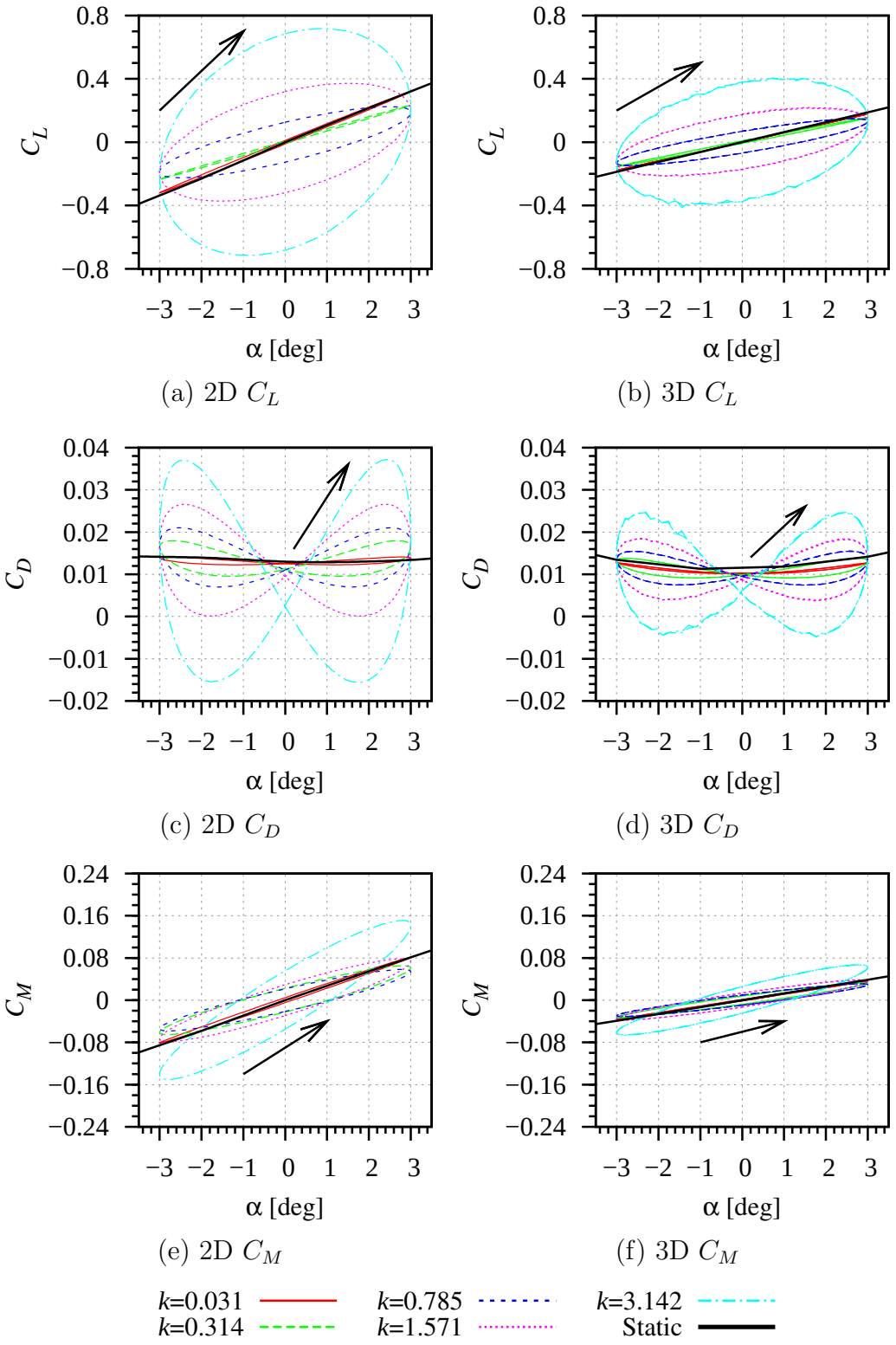

(a) 2D C_L (b) 3D C_L

(c) 2D C_D (d) 3D C_D

(e) 2D C_M (f) 3D C_M

Figure 3.15: Hysteresis 2D and 3D comparison for C_L, C_D and C_M variation over a cycle for mean incidence of 0° and incidence amplitude of 3° and varying reduced frequency (k).

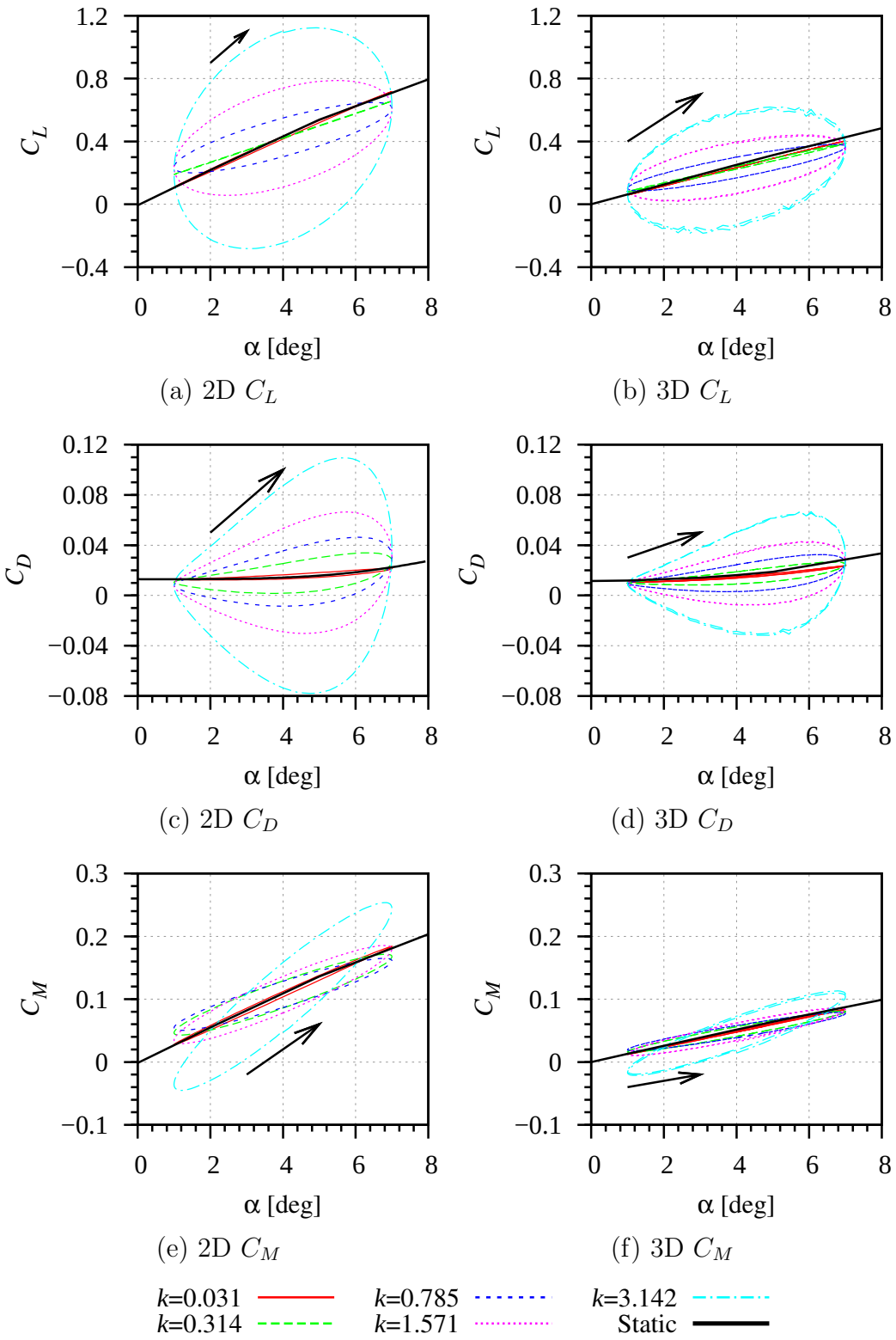

Figure 3.16: Hysteresis 2D and 3D comparison for C_L, C_D and (C_M) variation over a cycle for mean incidence of 4° and incidence amplitude of 3° and varying reduced frequency (k).

The variation in C_L loops for a change in incidence amplitude with a 0° mean incidence is shown in Figures 3.17(a) and 3.17(b). The C_L loops increase linearly with increasing incidence amplitude for both 2D and 3D. The variation in C_L loops for a change in incidence amplitude at 4° mean incidence is shown in Figure 3.18(a) and 3.18(b). The 2D case for the 4° mean show a similar trend to the 0° mean incidence. The 3D case shows the maxima and minima increase in magnitude as the incidence amplitude increase but is offset from the static results. This static offset appears to be different for each of the incidence amplitude. This trend is continued through the C_M loops as shown in Figures 3.17(e), 3.17(f), 3.18(e) and 3.18(f) and C_D loops at 4° mean incidence as shown in Figures 3.18(a) and 3.18(b). Figures 3.17(c) and 3.17(d) show the C_D loops at 0° mean incidence. These loops show the variation with increasing amplitude at a reduced frequency of 0.785.

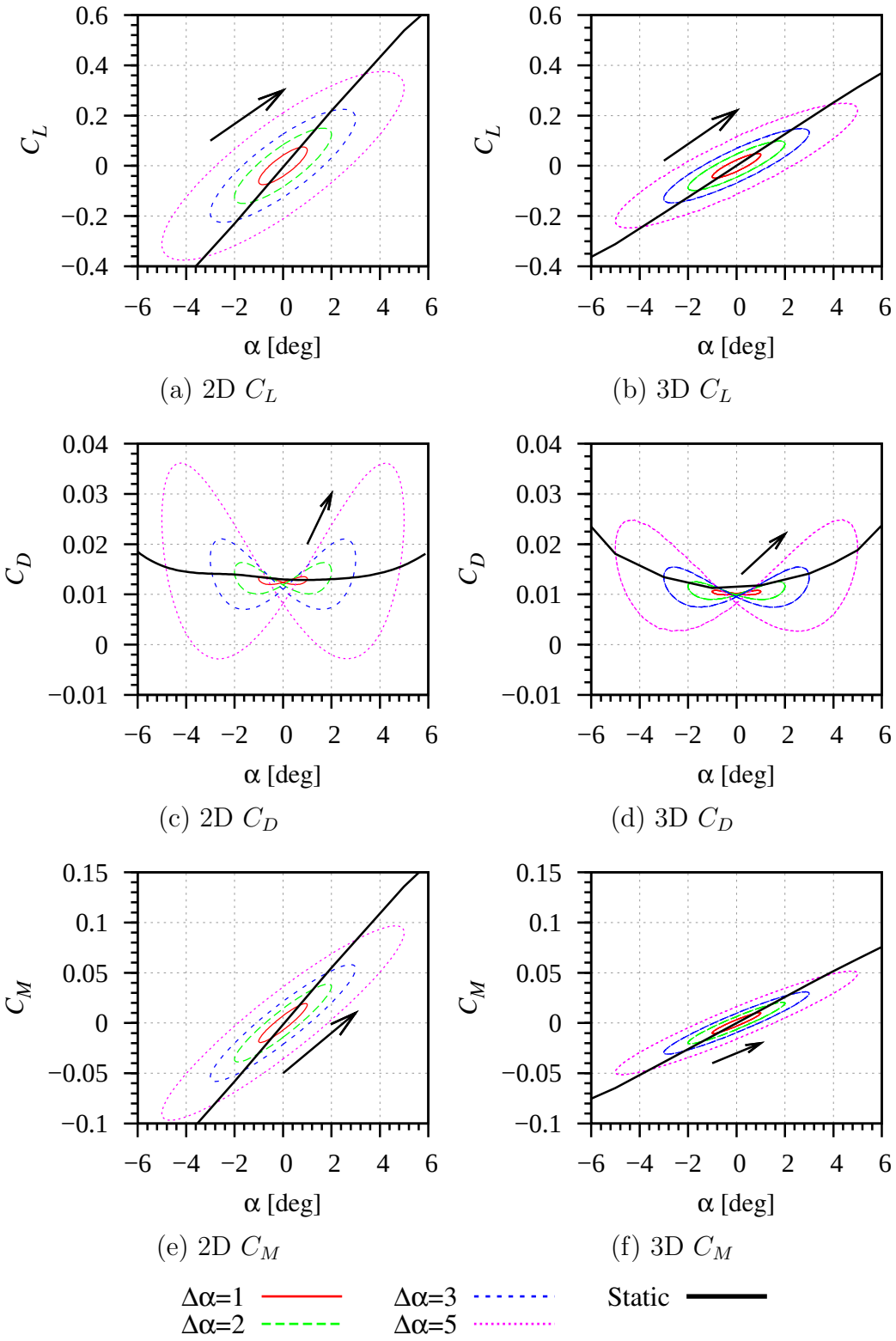

(a) 2D C_L (b) 3D C_L

(c) 2D C_D (d) 3D C_D

(e) 2D C_M (f) 3D C_M

Figure 3.17: 2D and 3D comparison of the hysteresis loop for C_L, C_D and C_M over a cycle for mean incidence of 0° and reduced frequency of 0.785 and varying incidence amplitude ($\Delta\alpha$).

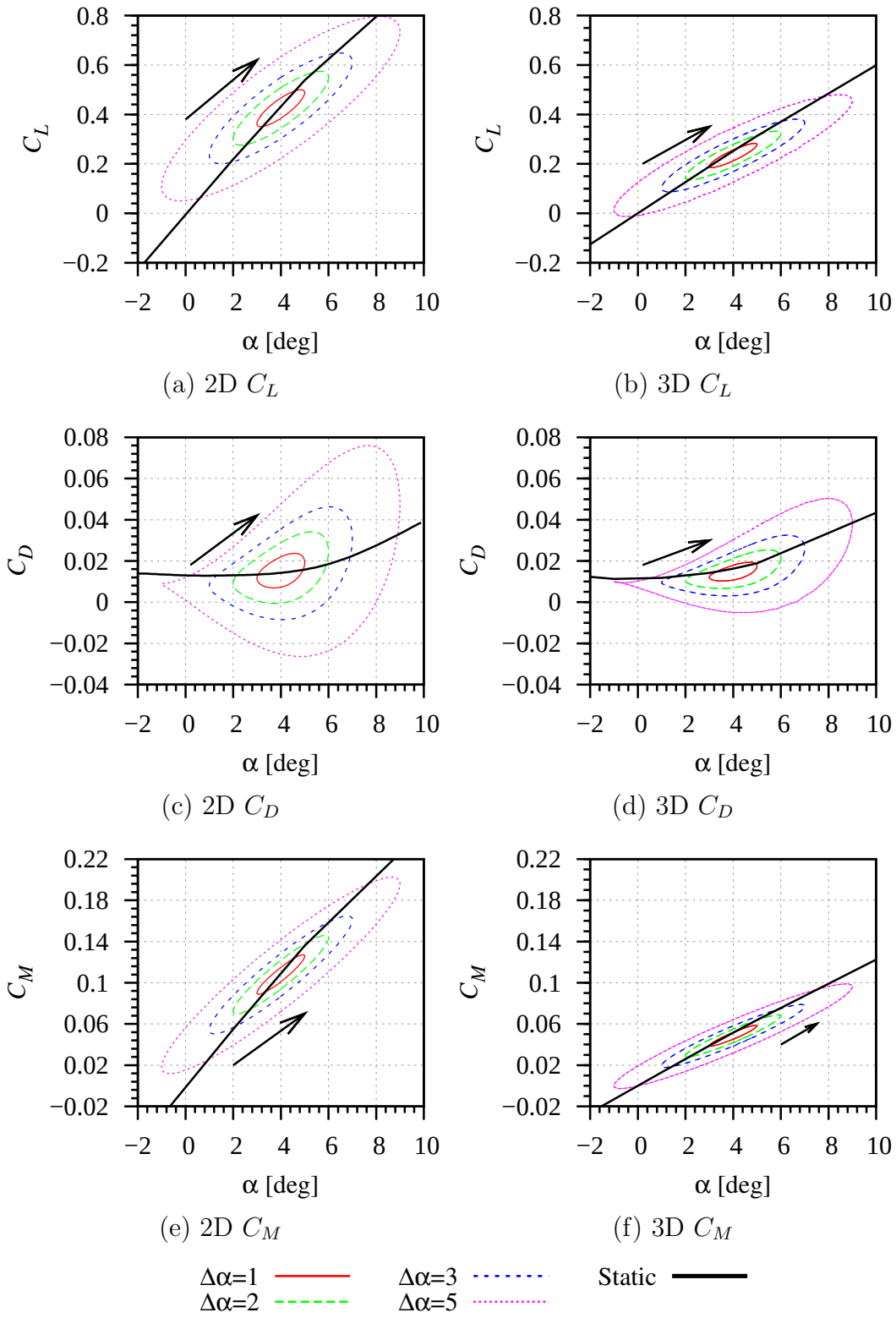

(a) 2D C_L (b) 3D C_L

(c) 2D C_D (d) 3D C_D

(e) 2D C_M (f) 3D C_M

Figure 3.18: Hysteresis 2D and 3D comparison for C_L, C_D and C_M variation over a cycle for mean incidence of 4° and reduced frequency of 0.785 and varying incidence amplitude ($\Delta\alpha$)

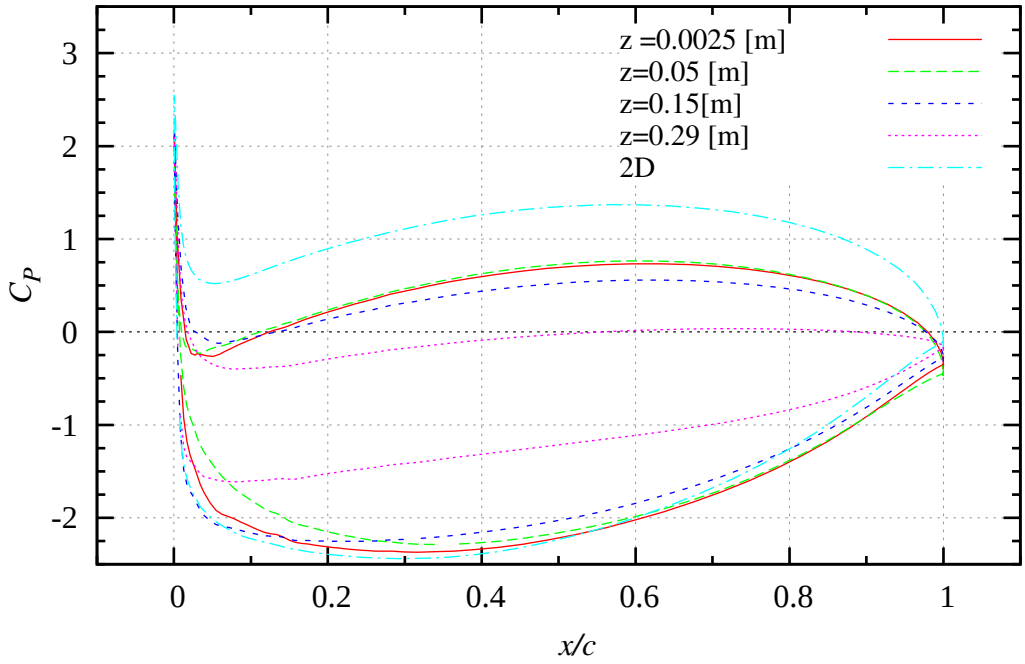

Figure 3.19: 2D and 3D comparison of computed C_p at a reduced frequency (k) of 3.142 at a incidence amplitude ($\Delta\alpha$) of 3° for a mean incidence ($\bar{\alpha}$) of 0 and Reynolds number (Re) of 3.36×10^5 at the mean incidence during the dynamic cycle.

The 2D and 3D comparison of computed C_p is shown in Figure 3.19. It can be seen from this figure that the C_p is less at all 3D spanwise locations than the 2D case. This plot illustrates C_p reducing closer to the tip. This difference can be explained in terms of the spanwise circulation/lift reducing to zero at the tip and the pressure equalising over the tip in the 3D case.

Summary plots

The maximum C_L, C_D and C_M throughout one cycle and the associated phase angle is shown in Figures 3.20 to 3.31. These plots are shown with a spline fit a complete set of figures with splines and points is contained in Appendix B. The force results are normalised on the static force at the maximum incidence. Each set of results relating to C_L, C_D and C_M and associated phase angle has one figure presenting the 3D comparison of computed maximum force at varying reduced frequency and for a 0 and 4° mean incidences and an incidence amplitude of 1, 2, 3, and 5° at a Reynolds number of 3.36×10^5. This is followed by a comparison of 2D to 3D and 3D Reynolds number of 3.36×10^5 to 1.12×10^6 for 0 and 4° mean incidence and a change of incidence amplitude of 3°. From Hutchison et al. [53] it was found that there is no dependence on Reynolds number for the 2D unsteady results. Figures 3.21 and 3.23 have an additional comparison with 2D analytical predictions from Theodorsen's theory from [68].

A minima in C_L/C_{L0} for 0° mean incidence occurs at a reduced frequency of approximately 0.6 (Figure 3.20). For 4° mean incidence there is minimal variation before a reduced frequency of 0.785 with an almost constant relationship between C_L/C_{L0} and reduced frequency. At a reduced frequency greater than 1.1, the results are dependent on incidence amplitude. The lift amplitude increases with increasing incidence but is always lower than the value obtained at a 0° incidence. A reduced frequency of one is the point at which a particle in the freestream will travel a distance equal to the root chord length over one cycle. Therefore, at frequencies higher than one, a particle does not travel a full chord length over a cycle and will influence the next cycle by affecting the trailing edge streamlines. This, combined with the asymmetry of the pressure around a foil at 4° mean incidence (Figures 3.8 and 3.9), is attributed to be the cause of the difference between 0 and 4° mean incidences at a reduced frequency greater than one.

Theodorsen's prediction, are compared to the RANSE 2D and 3D results in Figure 3.21. The 2D magnitude and position of the minima matches the prediction from Theodorsen's analytical prediction. The slope of Theodorsen's analytical predictions slope is approximately the same as the 2D and 3D 0° mean incidence but the RANSE solution predicts a greater rate of change in C_L/C_{L0} at the minima. The minima for 0° mean incidence is less for the 3D case compared to the 2D case, but they occur at the same reduced frequency value. The slope of the results for the increase in C_L/C_{L0} after the minima is steeper for the 2D case than the 3D case for both 0 and 4° mean incidences. There is no variation in Reynolds number for 3D results.

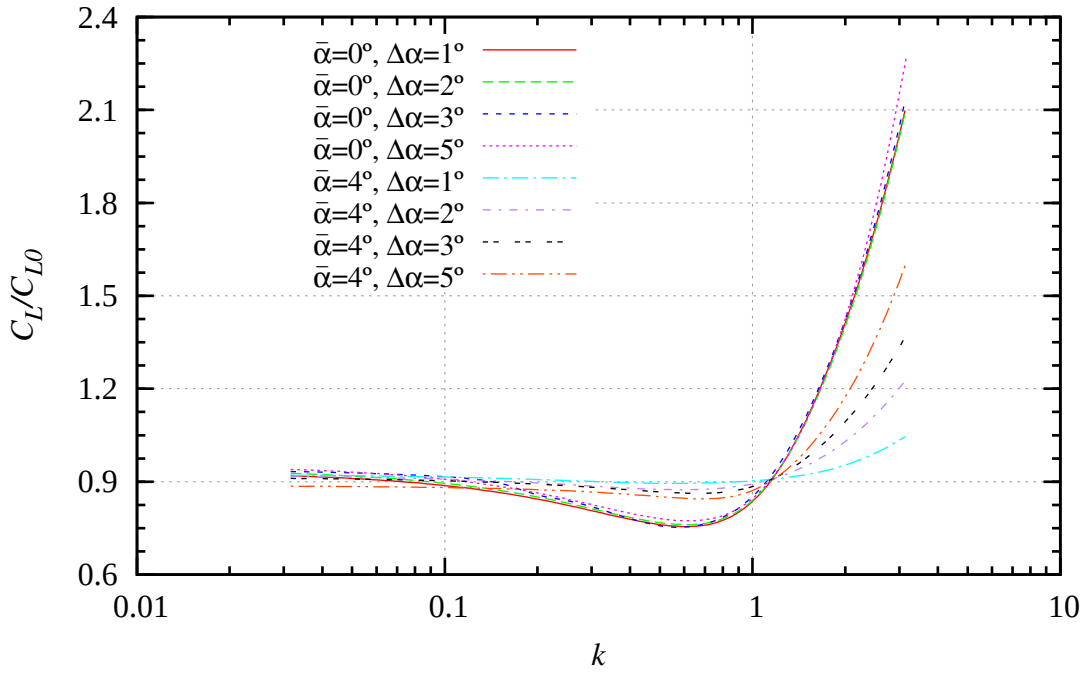

Figure 3.20: 3D comparison of computed normalised maximum C_L for varying reduced frequency (k) at a Reynolds number of 3.36×10^5 for a mean incidence ($\bar{\alpha}$) of 0 and 4° at incidence amplitudes ($\Delta\alpha$) of 1, 2, 3, and 5°.

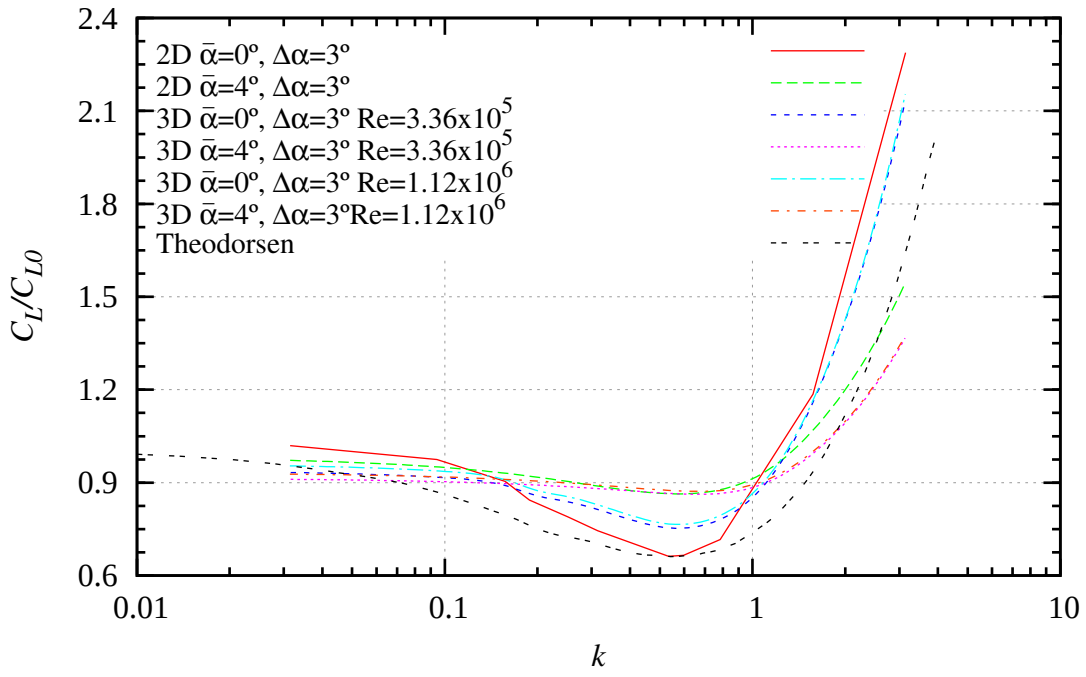

Figure 3.21: 2D and 3D comparison of computed normalised maximum C_L at varying reduced frequency (k) at a incidence amplitude ($\Delta\alpha$) of 3° for a mean incidence ($\bar{\alpha}$) of 0 and 4° and Reynolds number (Re) of 3.36×10^5 and 1.12×10^6.

The lift phase angle from the dynamic incidence is shown in Figure 3.22 and 3.23. Until reduced frequencies greater than 0.2 there is no phase angle between the maximum lift and maximum incidence (Figure 3.22). The lift phase angle matches for both 0 and 4° mean incidence at a reduced frequency less than one. The lift phase angle diverges and has a small dependence on change of incidence amplitude similar to C_L/C_{L0} at a reduced frequency greater than one. As the incidence amplitude increases to 5° at a 4° mean incidence the phase angle approaches the 0° mean incidence data. This is interesting as it suggests that the closer the oscillation goes to oscillating through 0° incidence it approaches the phase angle of 0° incidence. The lift phase angle for 0° mean incidence does not vary with change of incidence amplitude.

Theodorsen' analytical prediction shows a steady decrease in lift phase angle to the minima at a reduced frequency of 0.15, in comparison the RANSE lift phase angle prediction decreases from a reduced frequency of approximately 0.03 (Figure 3.23). The lift phase angle in 2D has a greater slope than the 3D after the minima at reduced frequency of approximately 0.15. The mean incidence angle only effects 3D lift phase angle results.

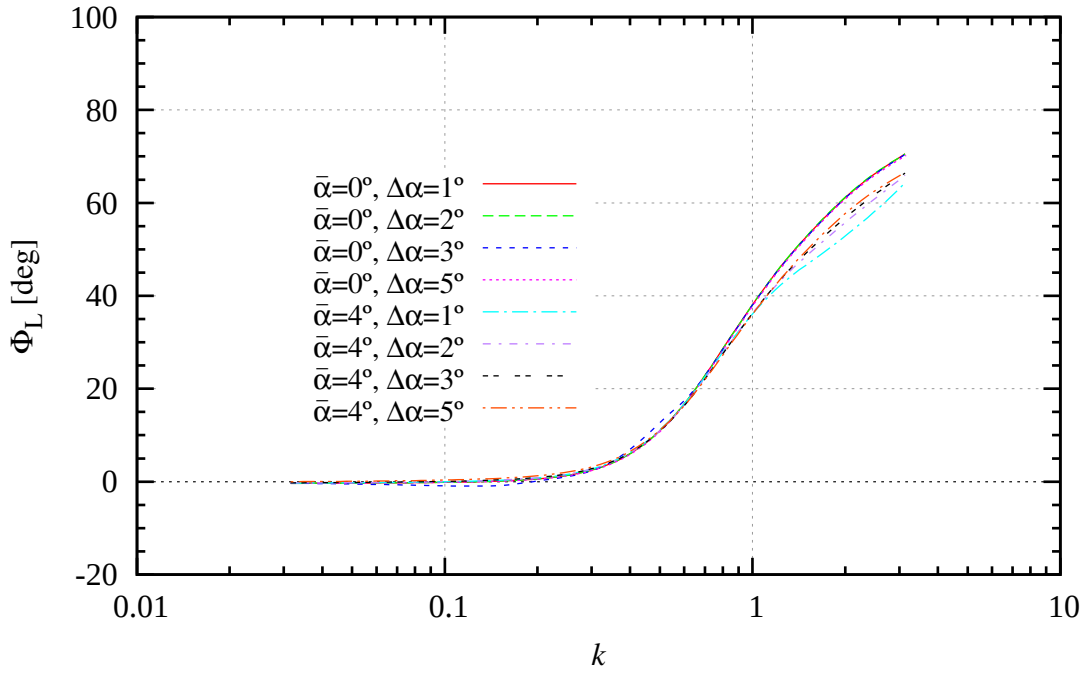

Figure 3.22: 3D comparison of computed lift phase angle (Φ_L) for varying reduced frequency (k) at a Reynolds number of 3.36×10^5 for a mean incidence ($\bar{\alpha}$) of 0 and 4° at incidence amplitudes ($\Delta\alpha$) of 1, 2, 3, and 5°.

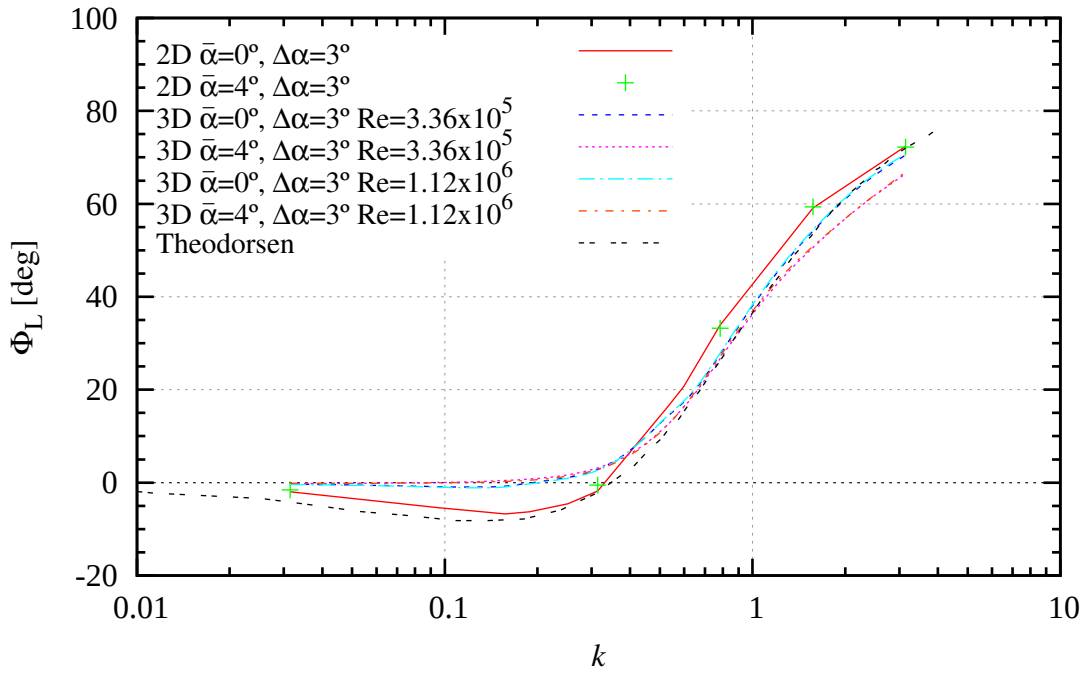

Figure 3.23: 2D and 3D comparison of computed maximum lift phase angle (Φ_L) at varying reduced frequency (k) at a incidence amplitude ($\Delta\alpha$) of 3° for a mean incidence ($\bar{\alpha}$) of 0 and 4° and Reynolds number (Re) of 3.36×10^5 and 1.12×10^6.

C_D/C_{D0} has a dependence on mean incidence and change of incidence amplitude as shown in Figure 3.24. The dependence is greater with the increase in mean incidence and incidence amplitude; this is also shown in the hysteresis plots in the previous section. Comparison of 2D and at both Reynolds numbers for 3D shows a dependence on Reynolds number C_D/C_{D0} (Figure 3.25). This is similar to the trend expected in a steady state case for C_D. A 4° mean incidence has a higher value of C_D/C_{D0} for a given reduced frequency. In 2D, a greater C_D/C_{D0} variation with reduced frequency than the 3D case is shown but it shows the same mean incidence trend.

The relationship of drag phase angle variation with respect to reduced frequency for 4° mean incidence is approximately linear with the log of reduced frequency and has no dependence on change of incidence amplitude (Figure 3.26). There is a small dependence on Reynolds number at 4° mean incidence (Figure 3.27). From 2D to 3D the magnitude of drag phase angle is reduced, whilst they are both constant with log of the reduced frequency.

The relationship of drag phase angle variation with respect to reduced frequency for 0° mean incidence is dependant on the change of incidence amplitude. A large minima occurs for an incidence amplitude of 1° at a reduced frequency of approximately 0.8 (Figure 3.26). This minima becomes less pronounced as the incidence amplitude increases. The 2D minima is more pronounced at 0° mean incidence (Figure 3.27). The minima in the data at a 0° mean incidence is explained by Figure 3.15 from the previous section. At a small reduced frequency the C_D changes from the maxima to minima rapidly over a change in incidence amplitude of less than 1°. This change occurs between the upstroke and downstroke over a 0.08° change in C_D amplitude. This suggests that a small increase or decrease in the rate of change of C_D can have a large effect on the drag phase angle. This is more exaggerated in the 2D case and hence has an effect for larger incidence amplitude.

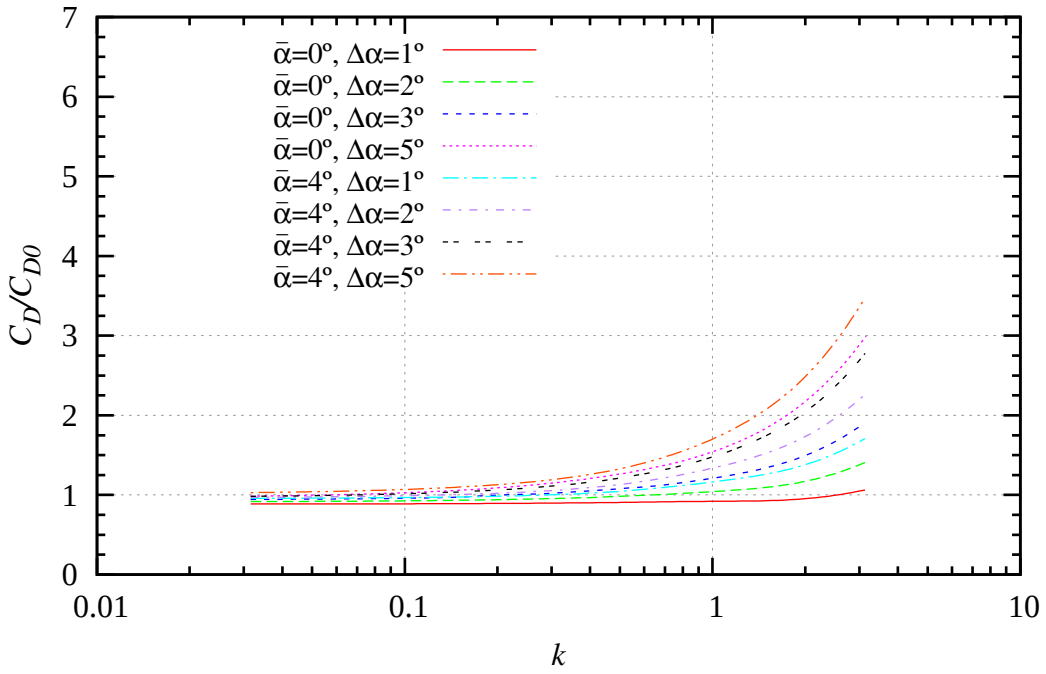

Figure 3.24: 3D comparison of computed normalised maximum C_D for varying reduced frequency (k) at a Reynolds number of 3.36×10^5 for a mean incidence ($\bar{\alpha}$) of 0 and 4° at incidence amplitudes ($\Delta\alpha$) of 1, 2, 3, and 5°.

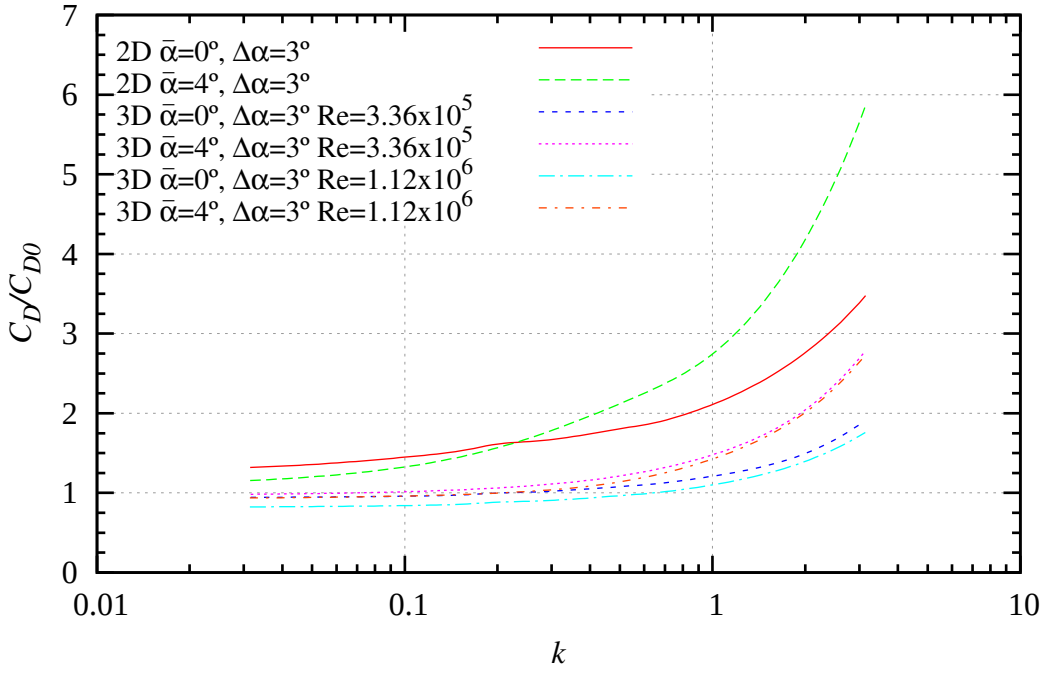

Figure 3.25: 2D and 3D comparison of computed normalised maximum C_D at varying reduced frequency (k) at a incidence amplitude ($\Delta\alpha$) of 3° for a mean incidence ($\bar{\alpha}$) of 0 and 4° and Reynolds number (Re) of 3.36×10^5 and 1.12×10^6

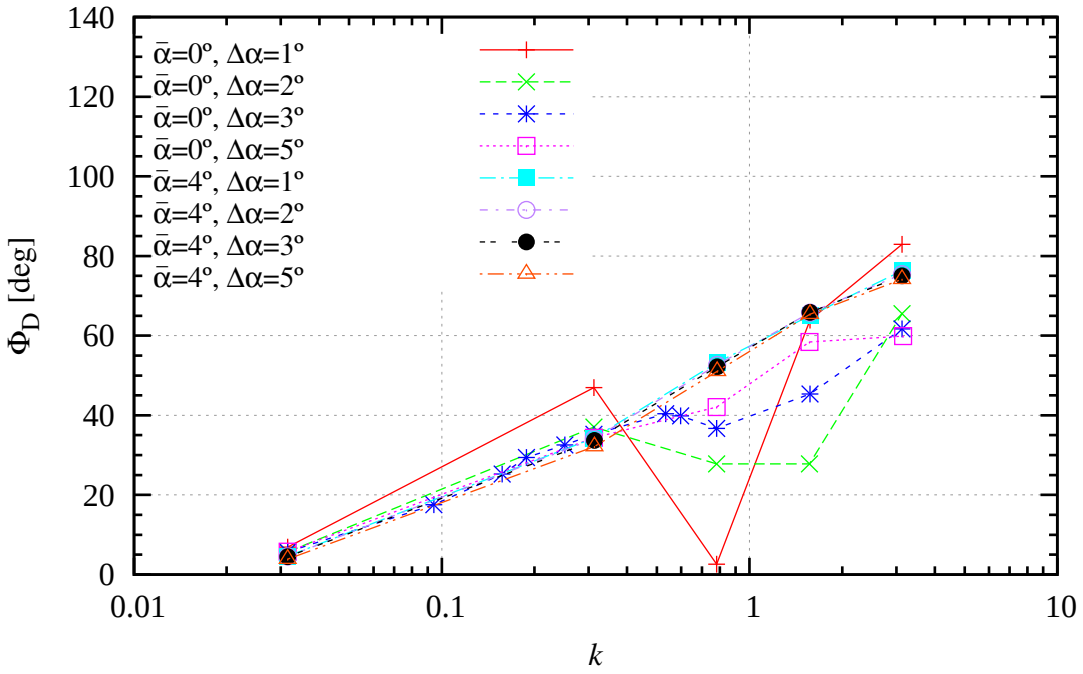

Figure 3.26: 3D comparison of computed drag phase angle (Φ_D)for varying reduced frequency (k) at a Reynolds number of 3.36×10^5 for a mean incidence ($\bar{\alpha}$) of 0 and 4° at incidence amplitudes ($\Delta\alpha$) of 1, 2, 3, and 5°.

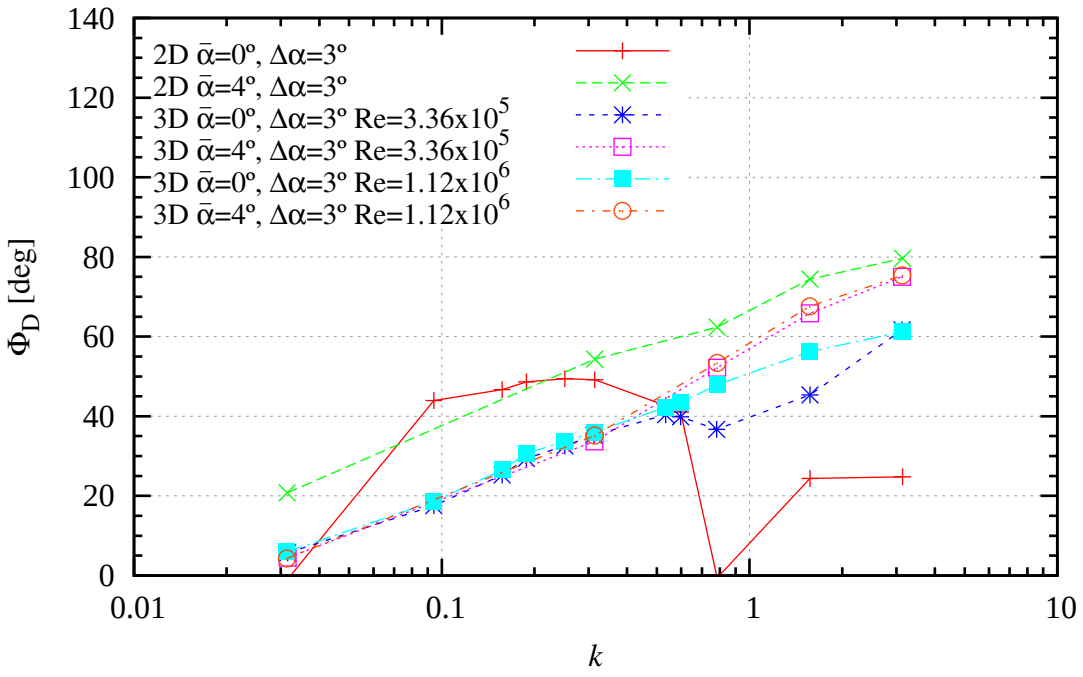

Figure 3.27: 2D and 3D comparison of computed maximum drag phase angle (Φ_D) at varying reduced frequency (k) at a incidence amplitude ($\Delta\alpha$) of 3° for a mean incidence ($\bar{\alpha}$) of 0 and 4° and Reynolds number (Re) of 3.36×10^5 and 1.12×10^6.

The maximum C_M variation with reduced frequency is shown in Figure 3.28. C_M/C_{M0} varies similarly to C_L/C_{L0}, but the minima is at a greater reduced frequency. A minima in C_M/C_{M0} for 0° mean incidence at a reduced frequency of approximately 0.7. At 4° mean incidence There is minimal variation in magnitude until a reduced frequency of 1.1. There is a small increase in the magnitude of C_M/C_{M0} as the incidence amplitude increases with reduced frequency. Figure 3.29 compares 2D and 3D for both Reynolds numbers. The 2D slope of the results for the increase in C_M/C_{M0} after the minima is steeper for the 2D case than the 3D case for both 0 and 4° mean incidences (Figure 3.28). This figure shows no dependence on Reynolds number. The minima at 0° mean incidence is less for the 3D case compared to the 2D case, but they occur at the same reduced frequency value, this trend is also similar to C_L/C_{L0}.

At a reduced frequency less than 0.3, the moment phase angle is similar for both 0 and 4° mean incidences; except at an incidence amplitude of 3° and a 0° mean incidence (Figure 3.30). The moment phase angle has a small dependence on incidence amplitude at a reduced frequency greater than 0.3 and for 4° mean incidence. The moment phase angle is not dependant on Reynolds number (Figure 3.31). The 2D result has a greater negative slope than the 3D cases and a similar minima to C_M/C_{M0}.

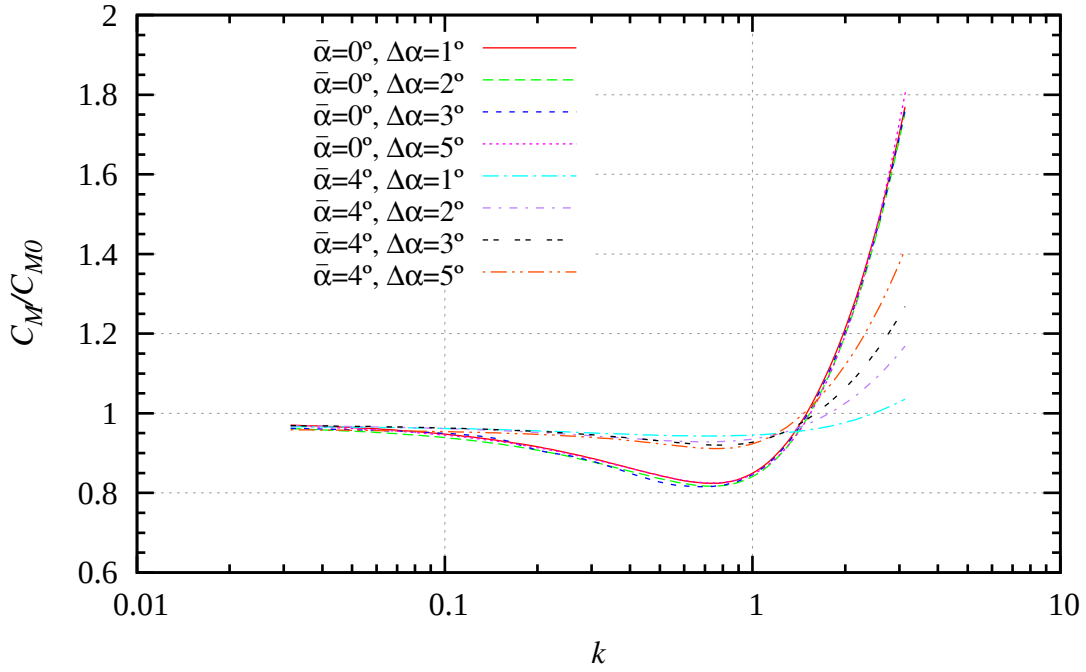

Figure 3.28: 3D comparison of computed normalised maximum C_M for varying reduced frequency (k) at a Reynolds number of 3.36×10^5 for a mean incidence ($\bar{\alpha}$) of 0 and 4° at incidence amplitudes ($\Delta\alpha$) of 1, 2, 3, and 5°.

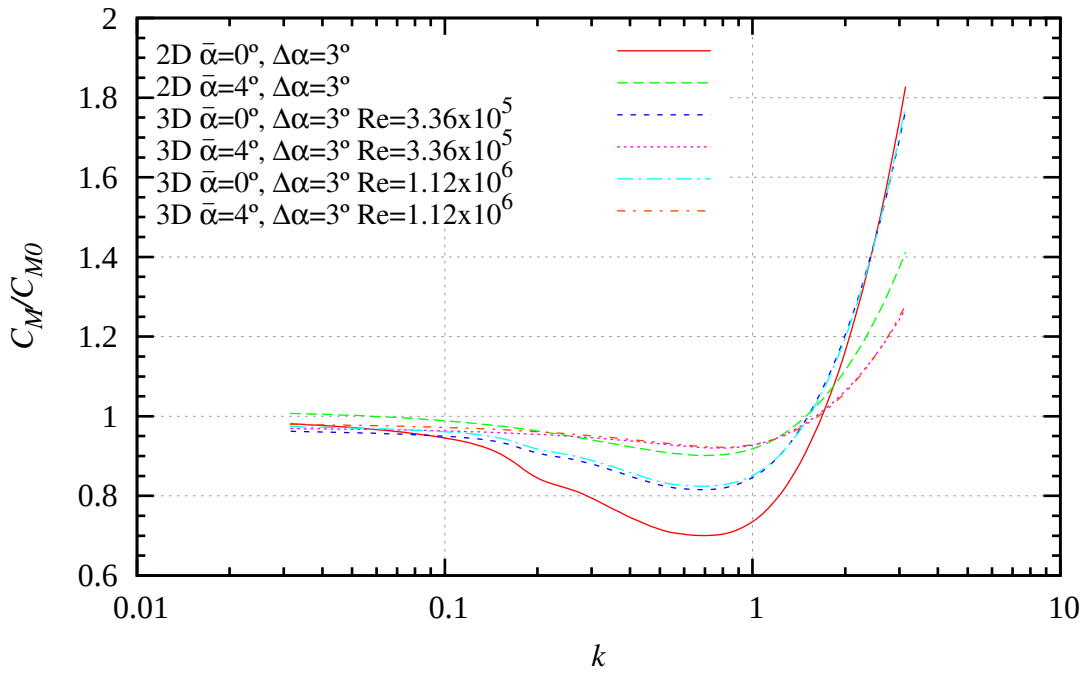

Figure 3.29: 2D and 3D comparison of computed normalised maximum C_M at varying reduced frequency (k) at a incidence amplitude ($\Delta\alpha$) of 3° for a mean incidence ($\bar{\alpha}$) of 0 and 4° and Reynolds number (Re of 3.36×10^5 and 1.12×10^6

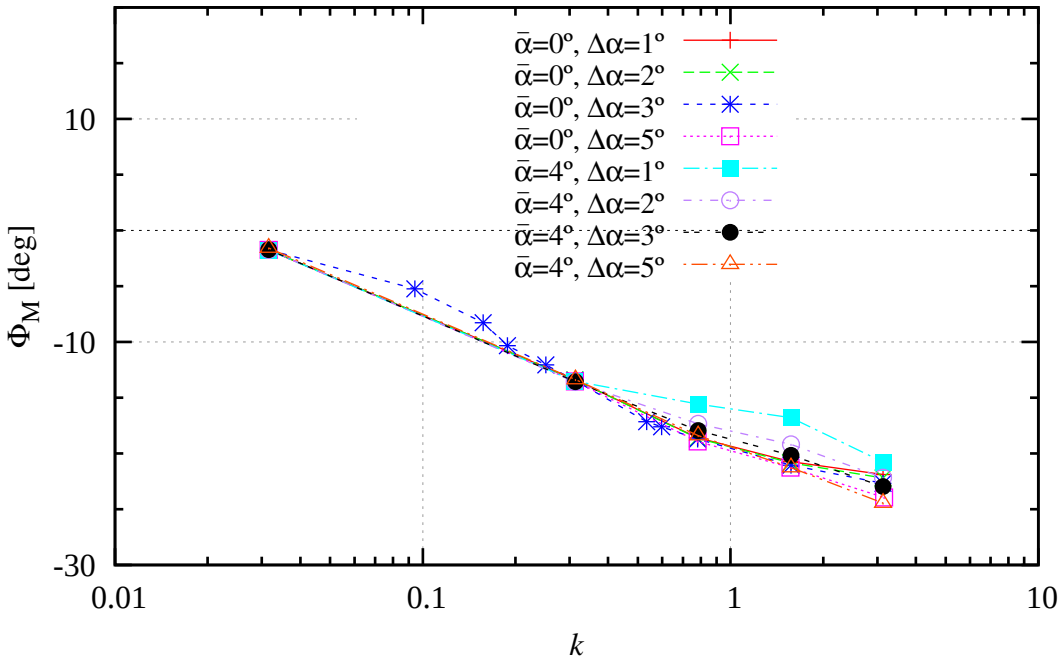

Figure 3.30: 3D comparison of computed moment phase angle (Φ_M) for varying reduced frequency (k) at a Reynolds number of 3.36×10^5 for a mean incidence ($\bar{\alpha}$) of 0 and 4° at incidence amplitudes ($\Delta\alpha$) of 1, 2, 3, and 5°.

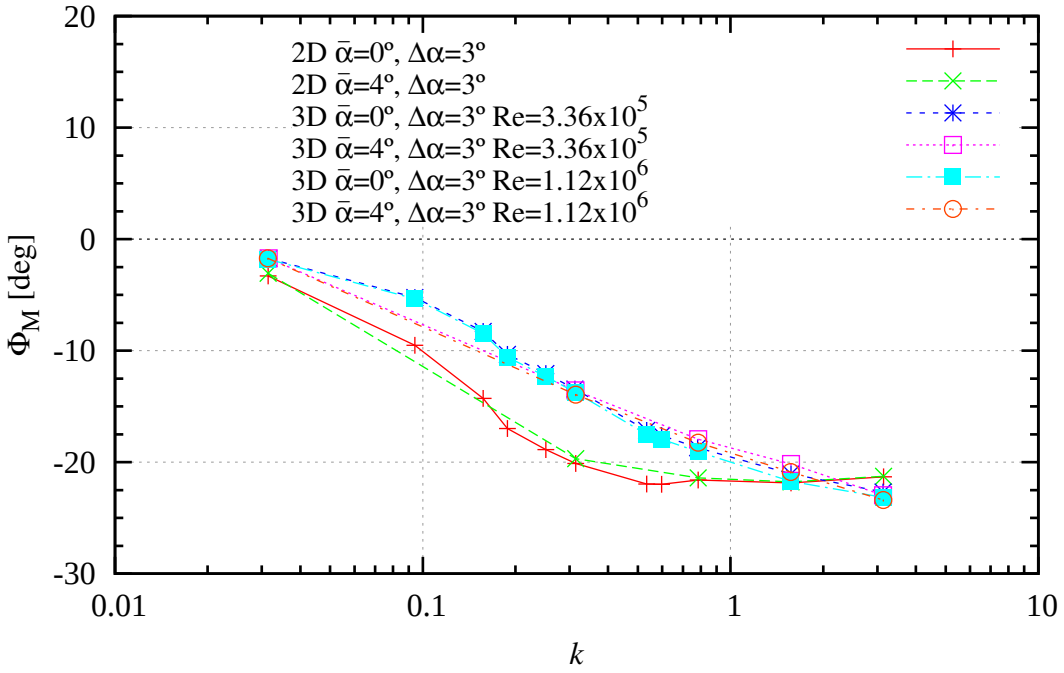

Figure 3.31: 2D and 3D comparison of computed maximum moment phase angle (Φ_M) at varying reduced frequency (k) at a incidence amplitude ($\Delta\alpha$) of 3° for a mean incidence ($\bar{\alpha}$) of 0 and 4° and Reynolds number (Re) of 3.36×10^5 and 1.12×10^6.

3.3 Chapter Summary

This chapter investigated the behaviour of 2D and 3D rigid body hydrofoils both in steady state and undergoing a pure pitch oscillation at 0 and 4° mean incidences with a change in incidence angle and reduced frequency. The main point from this chapter is that a 3D simulation is required as 2D over predicts unsteady forces/effects, and the mean incidence angle has an effect on the forces and moment with varying reduced frequency.

The slope of the 2D and 3D C_L curves are 0.11 and 0.06 respectively. The slope of the 2D is as expected from White [103], but the 3D is 5% greater than expected from finite span theory. This has been attributed to the trapezoidal planform as the theory is based on a rectangular planform. C_D increases in magnitude with decreasing Reynolds number, having the greatest increase of approximately 0.01 at an incidence angle of 10°. The slope of the 2D and 3D C_M are 0.025 and 0.012 respectively.

The spacing and magnitude of the vorticity travelling downstream at the foil mid span is approximately equal for both 0 and 4° mean incidences. As the incidence amplitude is increased from 1 to 5° the spacing between the vorticity in the wake remains the same, although the width of the wake is increased in the z direction. At the tip of the foil there is a pronounced difference in the behaviour of the tip vortex at 0 and 4° mean incidence, although at the tip the pressures about the foil are symmetric for both 0 and 4° mean incidences. The spacing and magnitude of the vorticity travelling downstream varies between the 0 and 4° mean incidences. When the foil oscillates at 0° mean incidence the positive Q-criterion wavelength corresponds to twice the oscillation frequency. In contrast, at the tip at 4° mean incidence, the wave length between a positive region is equal to the oscillation frequency.

The lift hysteresis varies about the static lift curve with increasing hysteresis as reduced frequency increases. The hysteresis is less in the 3D case compared to the 2D. This was attributed to the fact that 3D flow has the ability to equalise over the tip. The drag has a double harmonic at a mean incidence of 0° due to the static drag being a mirror about the incidence angle of 0° This means lift and drag are odd and even functions respectively of the dynamic incidence. The moment varies in a similar shape to the lift hysteresis loops but it does not vary around the static moment, suggesting that moment is dominated by the dynamics of lift and circulation. There is less variation between the maxima and minima of the forces in the 3D than in the 2D cases. From these analyses and comparisons we can conclude a simplified 2D analyses of a 3D object will over predict unsteady effects.

Rigid 3D lift and moment predictions show similar behaviour to both the present 2D unsteady viscous predictions and classical linearised inviscid theory for cases of 0° mean incidence. In particular, lift and moment normalised on to the static incidence value at maximum dynamic incidence and are linear with incidence amplitude for

all reduced frequencies for 0° mean incidence results. The amplitudes of the lift and moment minima occur at reduced frequencies of about 0.6 and 0.7 respectively for both 2D and 3D predictions. However, in the 3D case the amplitudes, relative to the lift and moment at static incidence, are reduced. At a mean incidence of 4°, the amplitudes of the lift and moment minima are significantly reduced for 2D and 3D predictions compared with the 0° mean incidence. Above a reduced frequency of one, for 4° mean incidence, the rigid 3D lift and moment amplitude predictions no longer vary linearly with incidence amplitude. The lift amplitude increases with increasing incidence but are always lower than the 0° incidence.

Reduced frequencies of 0.8, 1.6 and 2.4 were identified in chapter 1.4 as being representative of those experienced by a propeller operating in an unsteady flow field caused by wakes from the control surfaces and fairwater of a submarine. The approximate incidence amplitude is 2° with a 4° mean incidence. From this chapter we can conclude that a 2D analyses will predict a larger change in force from the maxima to minima. A 4° mean offset may reduce the effect of unsteady loading at a reduced frequency less than one but increase when the reduced frequency is greater than one, although the amplitudes for 4° mean incidence are less than those for 0° mean incidence. The effect of unsteadiness on lift and moment magnitude may not be pronounced in modes with an approximate reduced frequency less than 0.1 but drag and phase angle of all responses may be affected.

The implication of these conclusions on propeller design is that varying the mean incidence amplitude may have the largest effect on the forces and moments at a reduced frequency lower than one. In the case of a submarine as shown in Chapter 1, the first harmonic has a corresponding reduced frequency of 0.8 and an approximate mean incidence of 4°. Therefore, by reducing the mean incidence amplitude it maybe possible to reduce the maximum C_L. For other wake signatures it could be possible to adjust the response to achieve a lower maximum C_L by using equation 1.15 in combination with adjusting the mean incidence amplitude.

Chapter 4

Static Hydroelasticity

The investigation of the two-way FSI of a 3D NACA 0009 hydrofoil with trapezoidal planform at steady angles of incidence is described in this chapter. A structural model is developed for coupling with the 3D CFD model which was developed in Chapters 2 and 3. Fluid forces and structural deflections of a two-way coupled numerical simulation in ANSYS are presented. Comparisons are made with the rigid 3D (uncoupled) CFD static results. This chapter begins with a section on previous work relating to hydroelastic foils. Although, some of the related work is relevant to the next chapter, for consistency all the related hydroelastic work is discussed here.

4.1 Previous and Related Work

Hydroelastic foils have been extensively investigated at low Reynolds number for micro air vehicles [3], flapping wing propulsors [51, 58, 96, 99] and as a means to extract power [59, 119]. Many studies have investigated a heave/plunge motion as a way to generate thrust, however a foil oscillating in pure pitch requires a minimum reduced frequency to generate thrust [23] and as such have not been as extensively investigated.

Munch et al. [77] used an experiment of a NACA 0009 oscillating hydrofoil to validate a 2D model using a SST turbulence model. These tests were conducted at freestream velocities of 0.05, 5, 10 and 15 m/s. The model had a chord of 100 mm and span of 150 mm. The results compared well with experiment for an amplitude of oscillation of 2° and frequency of between 1-1500 Hz. Munch et al. [81, 82] later investigated FSI with a specific focus on hydraulic machines so as to identify the flow action in the case of vibrating blades.

Heathcote et al. [45, 46, 47] conducted experiments, including PIV measurements, with three foils with a NACA 0012 section with an aspect ratio of six and a rectangular planform. The foils tested had varying stiffness in the spanwise direction and were rigid in the chordwise direction. The experiments were conducted with

a zero freestream velocity [44, 46] and a Reynolds number ranging from 1×10^4 to 3×10^4. From these tests it was concluded that an intermediate flexibility was beneficial with an observed thrust benefit; however if the wing was too flexible, the tip and root began to move out of phase reducing the thrust benefit[47].

Some of the work closest to this thesis was conducted in the area of hydroelasticity by Ducoin et al. [30] who investigated the structural behaviour of a deformable NACA 66 hydrofoil in a forced ramped pitching motion for both cavitating and noncavitating flows. They conducted both experimental and numerical analyses with four pitching velocities investigated with a triangular pitching motion at reduced frequencies of 8, 10, 11, and 12. The incidence was varied from 0 to 15° for a zero flow case and Reynolds number of 0.75×10^6. Two foils were tested; a rigid [28] and a deformable [30] foil made from plastic. The rigid case used pressure transducers to record the pressures, and the flexible case, used a video camera to record the deflections [30]. After comparing results they concluded that in the noncavitating case, the hydrofoil displacements are affected by pressure fluctuation caused by laminar to turbulent transition for small pitch velocities. This was suppressed at high velocities [28, 30]. In the cavitating analysis the structural displacement was thought to affect the cavitation behaviour.

Ducoin et al. [27, 32] conducted both a numerical and experimental investigation into the effect of flexibility on a stationary foil in uniform flow. They compared coupled and uncoupled simulations to assess the effect of FSI with ANSYS CFD and Complete Structural Design. Uncoupled simulations were computed after the CFD simulations were solved with the foil assumed rigid and then the resulting forces were used to compute the structural deflections. Results from experimental visualisation of the foil displacement compared well to the coupled numerical simulations. The maximum vertical displacement in the coupled simulation was 10.7% higher in the coupled case while the change in lift was 10.6% higher. The change in lift was correlated to the change in pressure distribution at the foil tip due to the deflection. This corresponded to a large variation in the minimum pressure at the leading edge of the tip suction side. Ducoin et al. [31] used a RANSE $k - \omega$ SST model coupled with a transition model. They found that the structural response is strongly linked to hydrodynamic phenomena such as boundary layer transition and leading edge vortex shedding. An investigation of the effect of pitch velocity revealed that the increased speed influenced the boundary layer transition and hydrofoil loading which resulted in a higher incidence angle before stall [29, 31]. Hysteresis was evident after stall on the downstroke. Fluctuating displacements have been observed when leading edge vortex shedding occurs during stall, for both numerical and experimental approaches.

This thesis differs from Ducoin's work as the aim of this thesis is to investigate a hydrofoil oscillating in a pure sinusoidal pitch motion (not triangular) while not exceeding the static stall incidence.

4.2 Methodology

In two-way coupled analyses the CFD and structural solvers pass results between each other until convergence is reached. This process requires the CFD to converge on an initial solution and passes the forces to the structural ANSYS package; the structural package using these forces calculates the resulting hydrofoil deflection; the deflection is then passed to the connecting surface or FSI boundary and the CFD interface and surrounding mesh will deform to reflect the solution and solve again. This process continues until convergence is reached for the CFD, the structural solver and the interface.

This analyses used a steady state ANSYS and CFX numerical model. This means that there is no elapsed time although CFX still uses a pseudo-timestep[37]. The pseudo time is not shared with the mechanical solver. In a static structural (steady state) analysis, inertia and damping effects due to time variation are ignored. The static analyses are modelled non-linearly to allow for large deformations [55]. The element type used in the structural analyses was SOLID186. This is a high order 3-D solid element that exhibits quadratic displacement behaviour and supports large deflection [54]. The load for the coupling process used an under-relaxation factor of 0.75. The base of the foil is cylindrical to be used in the dynamic analyses is shown in Figure 4.1. In this analyses the hydrofoil is rigidly fixed around the cylinder labelled 'A'. This figure shows the fluid solid interface labelled 'B'.

Figure 4.1: Structural numerical model

A diagram of the structural foil (shown in yellow) within the CFD domain is shown in Figure 4.2.

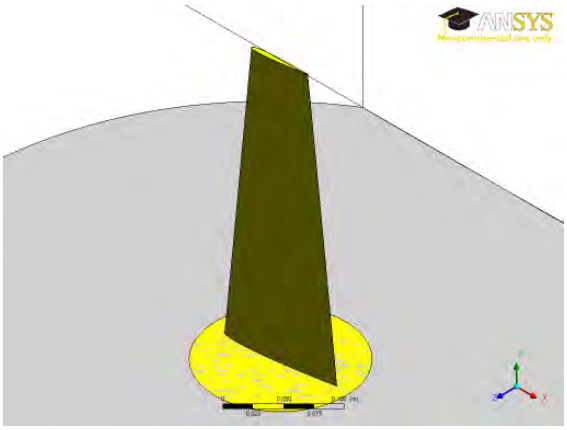

Figure 4.2: Structural numerical model constraints

A static two-way analysis was conducted at incidence angles of 1, 3, 4, 5 and 10° for both aluminium and stainless steel at a Reynolds numbers of 3.36×10^5 and 1.12×10^6. Results were compared for C_L, C_D, C_M and maximum tip deflection and twist.

4.2.1 Grid Independence and Temporal Convergence

The CFD model grid independence and temporal convergence was detailed in Chapter 3. The structural grid was checked for independence using the results from the converged CFD model at 10° and completing a one-way coupling using various meshes until the tip deflection converged. Results are shown in Table 4.1. Mesh B was selected and is shown in Figure 4.3.

Table 4.1: Structural grid convergence details of mesh constraints

Mesh	Maximum size of mesh on the foil[mm]	Number of cells around the NACA section	Maximum deflection δ_{max}
A	16	70	10.868
B	6	50	11.024
C	6	70	11.261
D	4	35	9.561
E	4	70	11.261
F	2	70	11.347

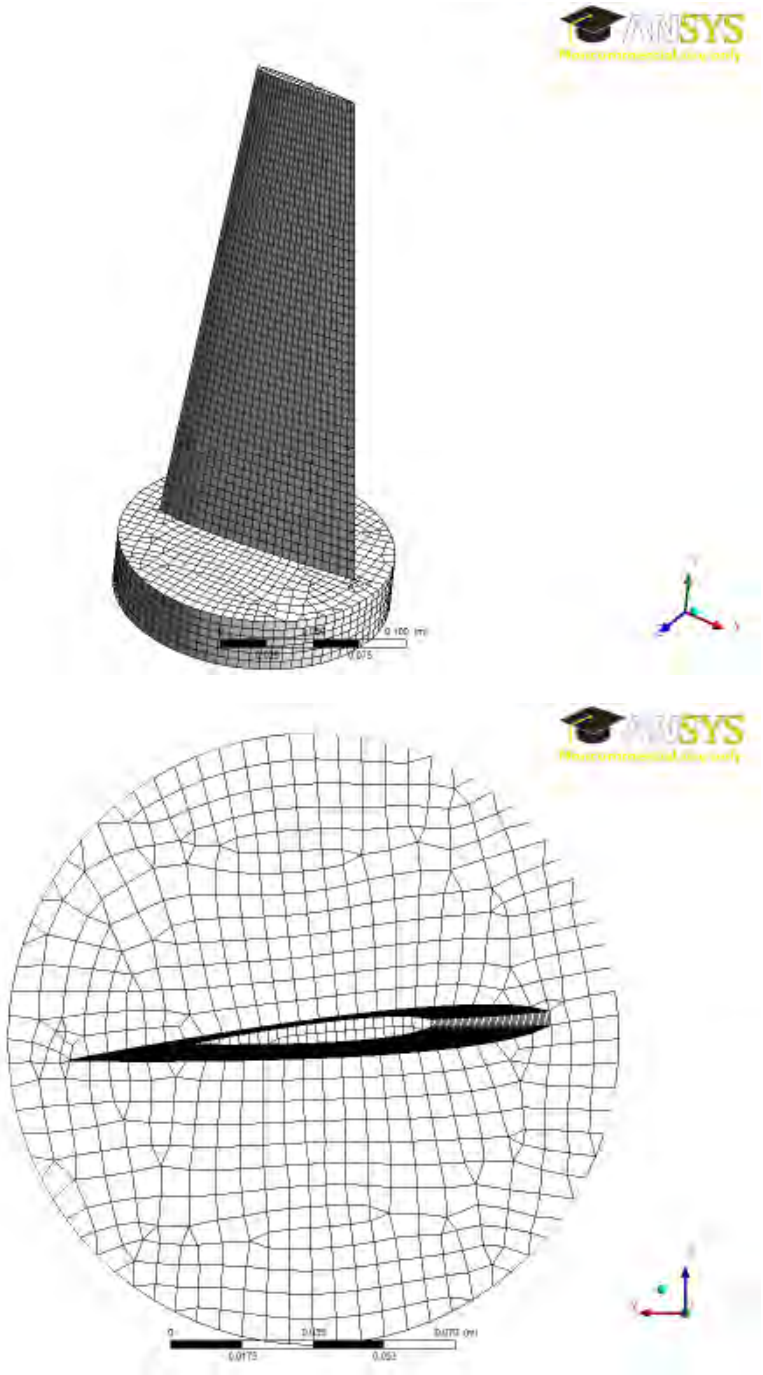

Figure 4.3: Structural numerical model within fluid domain

4.2.2 Coupling

At the beginning of the coupled analysis, an investigation into the coupling procedure and the effect of unmapped nodes was conducted. An unmapped node has all of neighbouring integration point faces completely non-matching with any integration points from the other side [66]. A data transfer type used was conservative interpolation mapping. This means, ANSYS structural transferred the load from an unmapped node to a mapped node. It was difficult to achieve zero unmapped nodes at the leading edge of the foil between the structure and CFD mesh due to the curvature. To investigate the effect of this, a sensitivity analyses was conducted for two variations in percentage unmapped nodes at the maximum incidence angle of 10° for a two-way coupled analyses. This resulted in a mesh which had 4.5% unmapped nodes on the CFD side and 3.6% on the structural side.

4.3 Results and Discussion

The investigation of a coupled (two-way FSI) static hydrofoil is divided into two parts. This section begins with qualitative results of pressure contours over the foil and at the root for rigid and coupled aluminium and stainless steel. This is then followed by results for C_L, C_D, C_M, deflection and twist at incidence angle of 1, 3, 4, 5 and 10° for Reynolds number of 3.36×10^5 and 1.12×10^6. Note, the planform area is considered the same as the undeformed mesh although it is recognised that the projected area will vary with deflection.

The variation in pressure on the rigid, aluminium and stainless steel foils, on the pressure side and suction side, for incidence angle of 5° is shown in Figure 4.4 and 4.5. All pressure distributions are very similar in magnitude and position, despite material and associated deflection changes. The variation of rigid, stainless steel and aluminium pressures on the wall at the root of the foil at incidence angle of 10° is shown in Figure 4.6. The outline of the deflected foil shape is shown in black. Again all pressure distributions are very similar in magnitude and position, despite material and associated deflection changes.

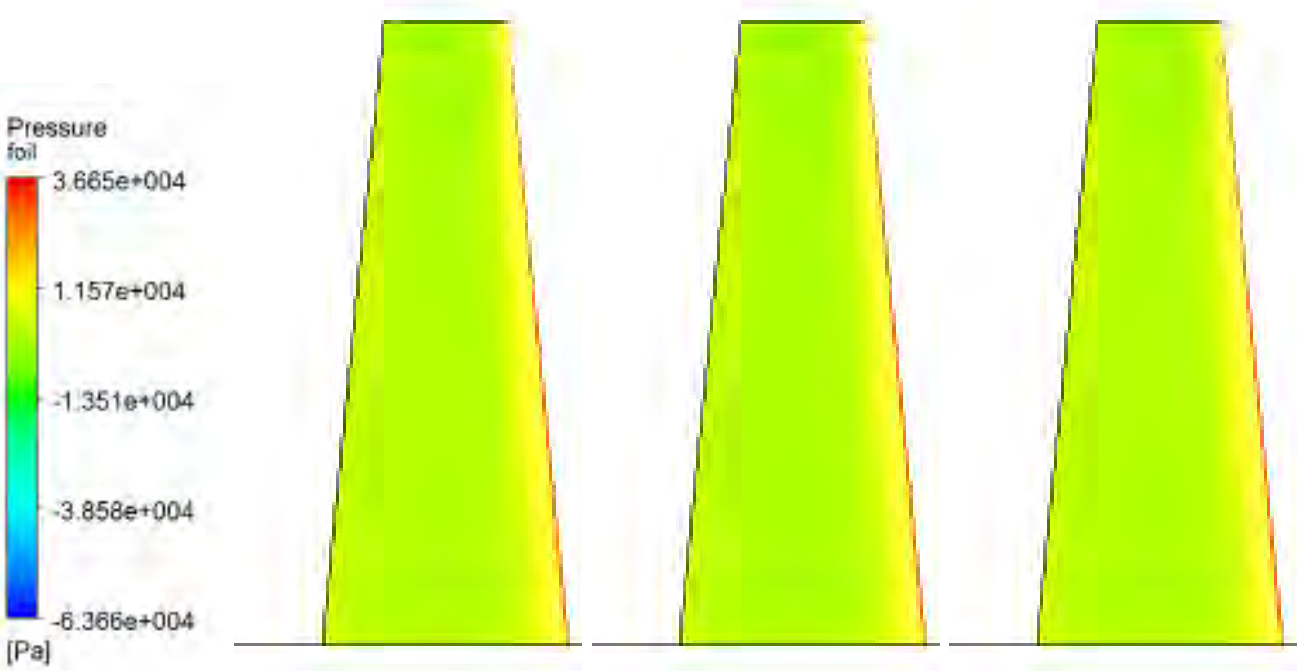

(b) Rigid (c) SS (d) Al

Figure 4.4: Comparisons of foil surface pressure distributions on the pressure side for rigid, stainless steel and Aluminium foil cases for incidence angle of 5° and Reynolds number of 1.12×10^6. These results show that the differences in geometry result in essentially no differences in pressure distribution.

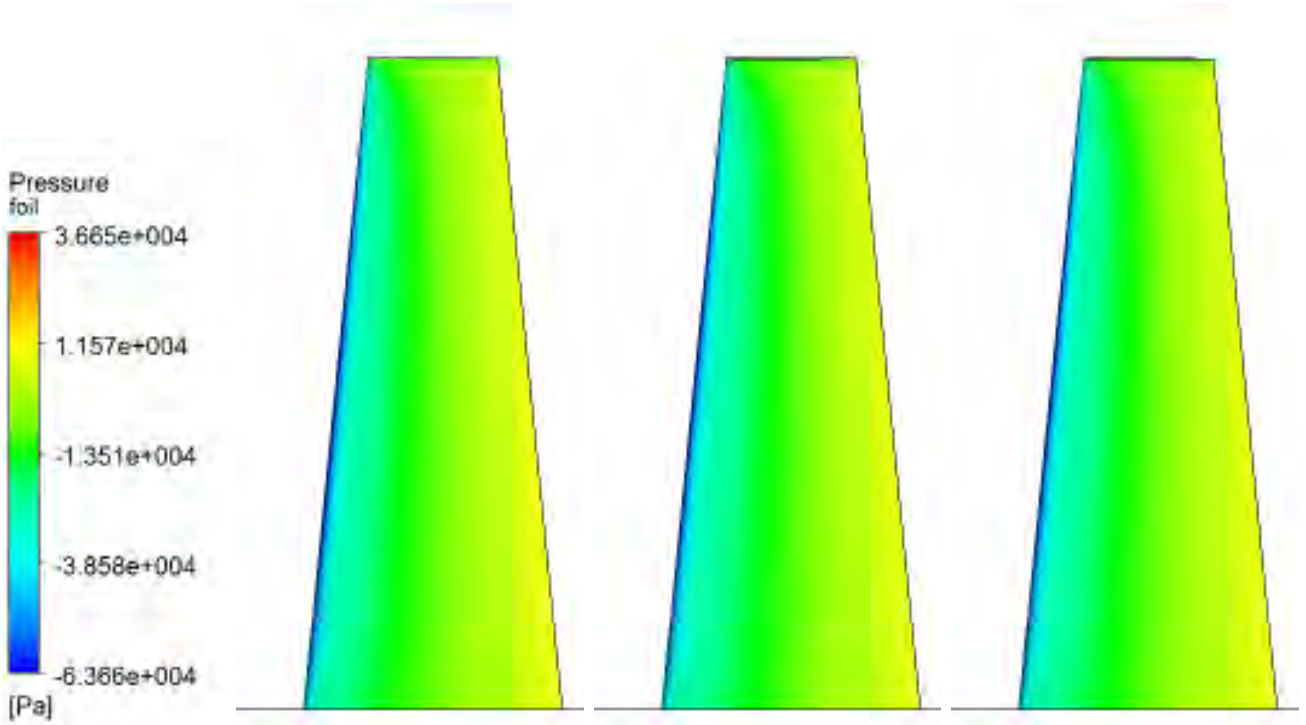

(b) Rigid (c) SS (d) Al

Figure 4.5: Comparisons of foil surface pressure distributions on the suction side for rigid, stainless steel and Aluminium foil cases for incidence angle of 5° and Reynolds number of 1.12×10^6. These results show that the differences in geometry result in essentially no differences in pressure distribution.

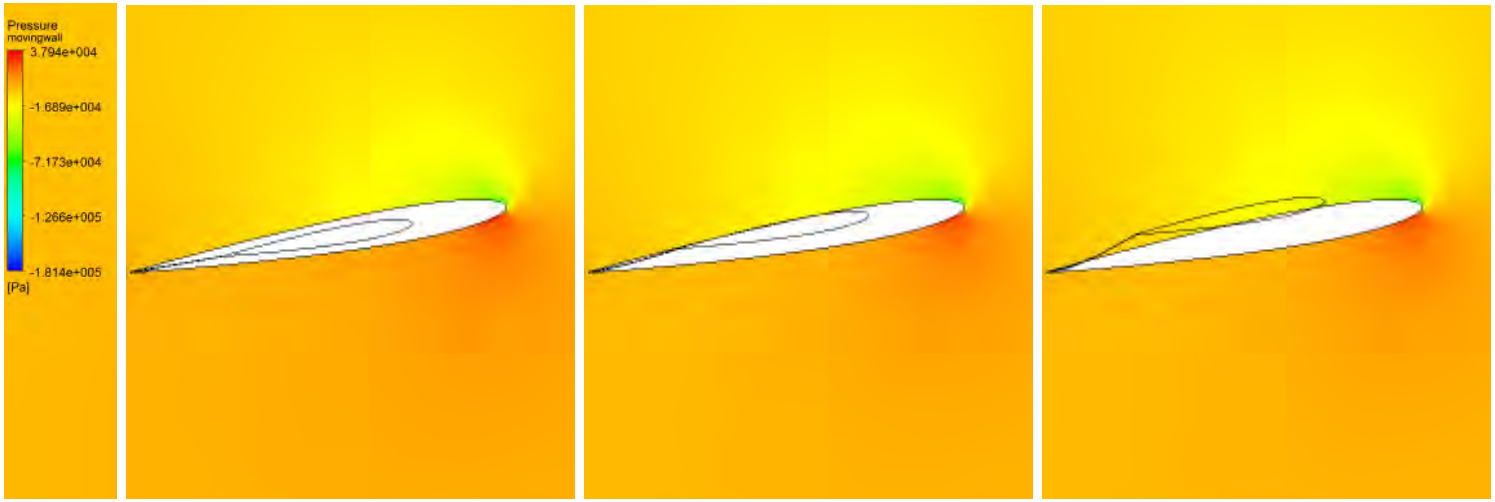

(b) Rigid (c) SS (d) Al

Figure 4.6: Comparisons of wall pressure distributions at the foil root for rigid, stainless steel and Aluminium foil cases for incidence angle of 10° and Reynolds number of 1.12×10^6. Outline of deformed foil shape shown in black. These results show that the differences in geometry result in essentially no differences in wall pressure distribution.

4.3.1 Forces and Moments

This section presents the results for a NACA 0009 3D hydrofoil at incidence angle of 1, 3, 4, 5 and 10° using a two-way coupled analysis and compares the resulting C_L, C_D and C_M to the rigid/uncoupled case. C_L, C_D and C_M respectively at incidence angle of 1, 3, 4, 5 and 10° with a Reynolds number of 3.36×10^5 and 1.12×10^6 is shown in Figures 4.7, 4.9 and 4.8. There is little variation in Reynolds number for C_L and C_M. Although, C_L and C_M are slightly higher at the higher Reynolds number. It was expected that the aluminium and stainless steel case at the lower Reynolds number would be closer to the rigid results because there will be less force acting on the surface. The results for C_L and C_M for both materials are similar to the rigid case up to incidence angle of 5° after this there is a noticeable variation. Similarly, the results for the aluminium and stainless steel foils are essentially identical at the higher Reynolds number but compare more favourably with the rigid results than those at the lower Reynolds number. The results for the pressure distribution show that deformations have little effect and the forces confirm this up to 5° incidence.

To investigate this possible artefact the percentage difference from the original rigid undeformed mesh at incidence angle of 5 and 10° for C_L and C_M is presented in Table 4.2. Three sets of runs where compared; rigid uncoupled with an undeformed mesh (rigid undeformed), coupled two-way(coupled) and a rigid uncoupled run using the resulting deformed coupled CFD mesh (deformed rigid). As there was no difference between materials in the previous results only one material needed to be compared. The rigid undeformed case is used as a benchmark for the other two cases, this case is used to calculate a percentage difference to the coupled and deformed rigid cases. It is noted that there is less of a difference in the percentage difference at the higher Reynolds number. At 5° the variation is less than 4% for all cases. Although the larger variation of C_L and C_M at 10° could be due to incipient stall characteristics, the offset of these results at each Reynolds number for the coupled cases matches the offsets for the drag. This suggests that the offsets are due to the coupling process. The C_D offset is further investigated in the next paragraph.

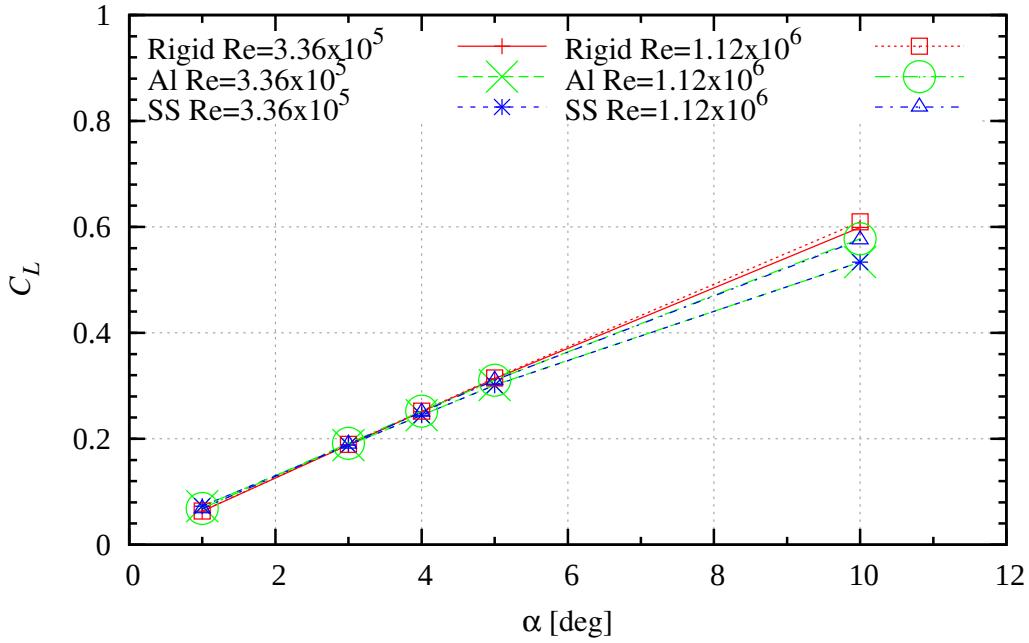

Figure 4.7: Comparison of computed C_L for aluminium, stainless steel and rigid hydrofoil at for incidence angle (α) of 1, 3, 4, 5 and 10° for Reynolds number of 3.36×10^5 and 1.12×10^6

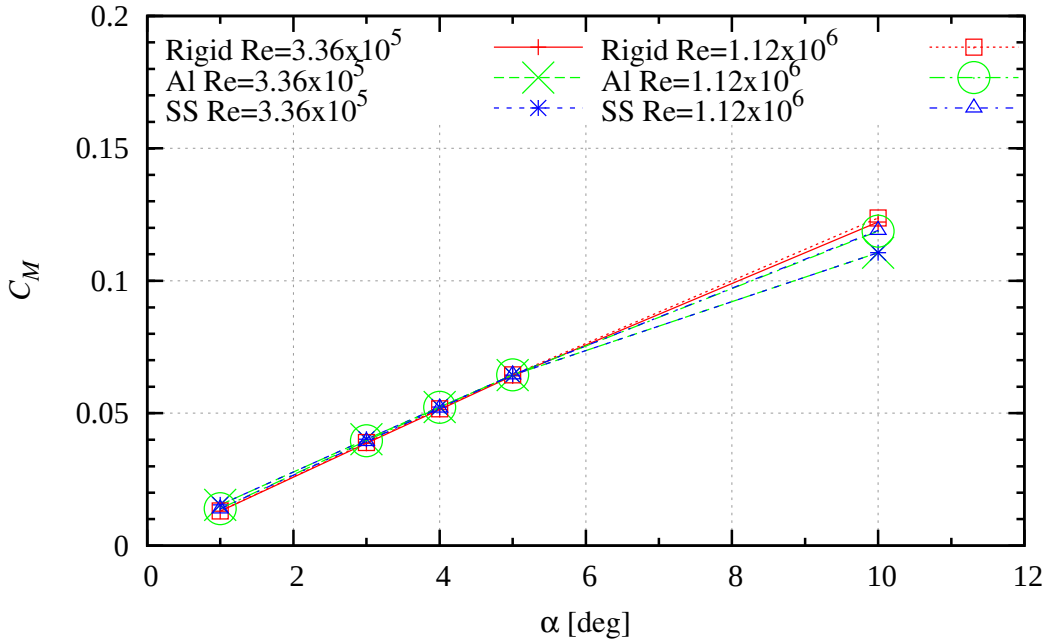

Figure 4.8: Comparison of computed C_M for aluminium, stainless steel and rigid hydrofoil at for incidence angle (α) of 1, 3, 4, 5 and 10° for Reynolds number (Re) of 3.36×10^5 and 1.12×10^6

Table 4.2: Coupled mesh comparison

Reynolds number	α [deg]	Run	C_L % diff. from rigid undeformed	C_M % diff. from rigid undeformed
3.36×10^5	5	coupled	-4	1
3.36×10^5	5	deformed rigid	0	1
1.12×10^6	5	coupled	0	1
1.12×10^6	5	deformed rigid	2	1
3.36×10^5	10	coupled	-10	-9
3.36×10^5	10	deformed rigid	-3	-2
1.12×10^6	10	coupled	-5	-1
1.12×10^6	10	deformed rigid	-1	-4

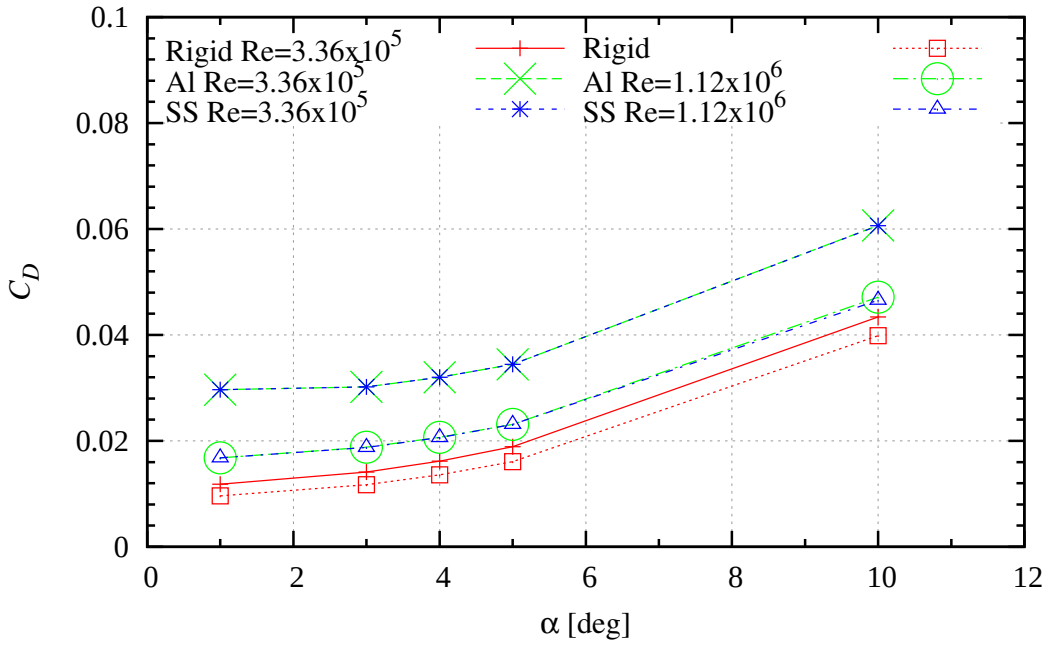

Figure 4.9: Comparison of computed C_D for aluminium, stainless steel and rigid hydrofoil at for incidence angle (α) of 1, 3, 4, 5 and 10° for Reynolds number (Re) of 3.36×10^5 and 1.12×10^6

The rigid results show that the lower Reynolds number has an increase in C_D when compared with the higher Reynolds number case (Figure 4.9). The C_D curve in the coupled case for aluminium and stainless steel has a constant offset from the rigid uncoupled analyses. This was investigated in this study by the same procedure used previously for C_L and C_M. It was found that C_D had a constant offset through all incidence angles, shown in Figure 4.9. This was approximately 0.017 and 0.007 for a freestream velocity of 2.5 and 8.3 m/s respectively. The offset in C_D was further investigated by comparing a coupled two-way(coupled) and a rigid uncoupled run using the resulting deformed coupled CFD mesh (deformed rigid), i.e. the cases used the same CFD mesh with only the method of calculation changed. Wall shear on the foil, velocity at the mid-span and velocity profile at the trailing edge are shown in Figures 4.10, 4.11 and 4.12. The wall shear in the coupled case has a wider band of wall shear at the leading edge in the spanwise direction. The wall shear is greater in the coupled case. The wall shear has minimal spanwise variation, as shown in Figure 4.10. The velocity on a plane intersecting the foil at mid-span is shown in Figure 4.11. The boundary layer at the trailing edge is clearly thicker in the coupled case. The yellow line in this figure shows the point at which the velocity was extracted to create the velocity profile in Figure 4.12. The boundary layer is thicker in the coupled case on both the suction and pressure side, with a more pronounced difference on the suction side. Therefore it was concluded that the C_D offset variation was attributed to the coupling process.

When comparing the rigid results to coupled the error is relatively small for C_L and C_M at small to moderate incidence angles. The C_D trend is later investigated in the dynamic hydroelastic analysis Chapter 5. By normalising C_D with the coupled static case, the offset error is removed and the dynamic trend can be compared to the rigid analysis. This does not affect any conclusion made in this thesis.

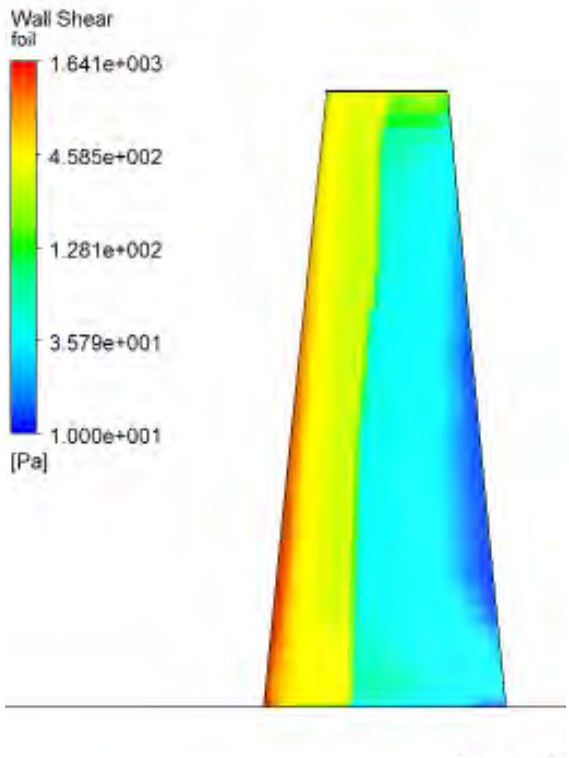

(a) Coupled

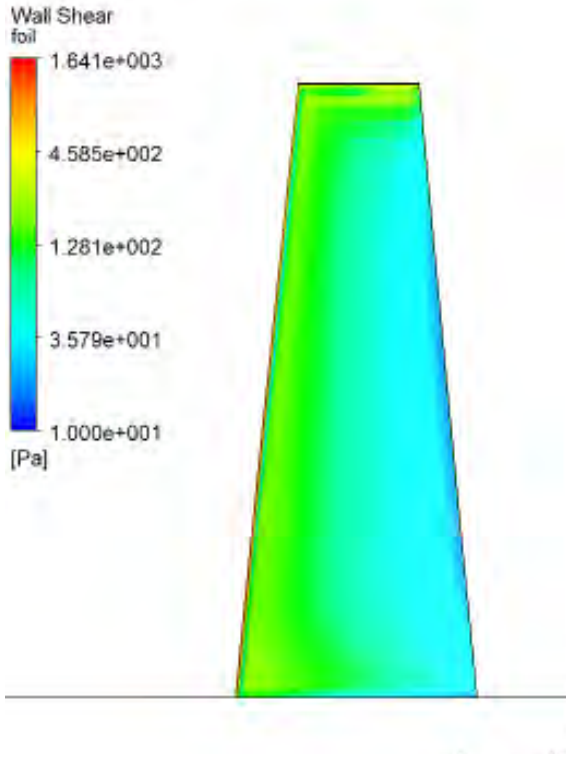

(b) Deformed Rigid

Figure 4.10: Comparisons of foil wall shear for coupled and deformed rigid cases for incidence angle of 10° and Reynolds number of 1.12×10^6.

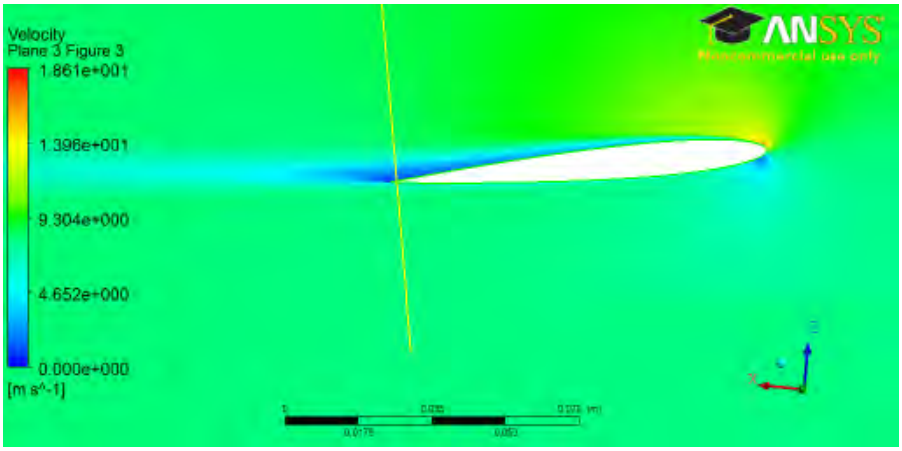

(a) Coupled

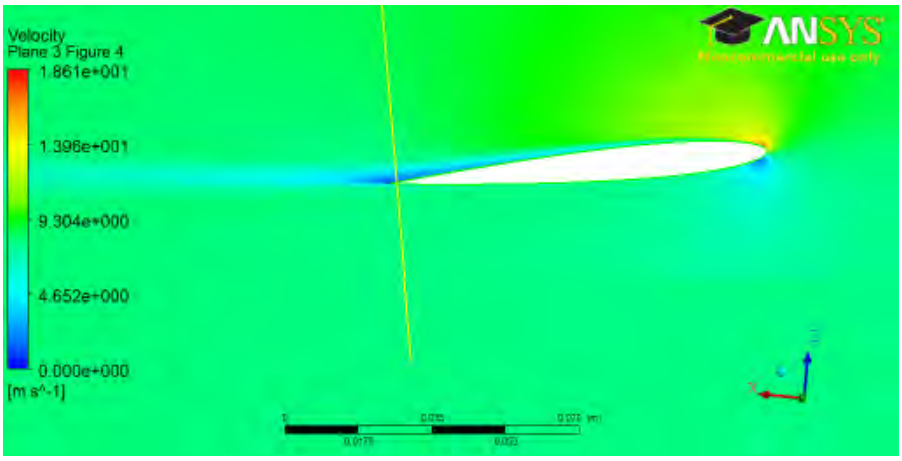

(b) Deformed Rigid

Figure 4.11: Comparisons of foil velocity for coupled and deformed rigid cases at the mid span for incidence angle of 10° and Reynolds number of 1.12×10^6. The yellow line illustrates the point at which the velocity is measured for Figure 4.12

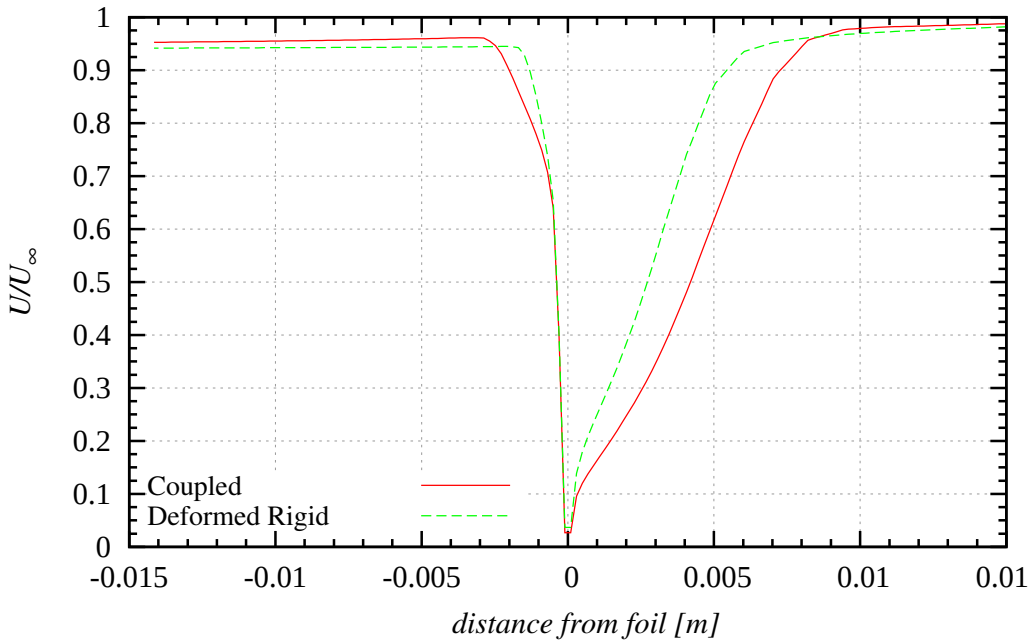

Figure 4.12: Comparison of computed foil velocity for coupled and deformed rigid cases at the mid span and trailing edge of the foil for incidence angle of 10° and Reynolds number of 1.12×10^6.

4.3.2 Deflections

The deflections for the two-way coupled foil for aluminium and stainless steel at Reynolds numbers of 3.36×10^5 and 1.12×10^6 is shown in Figure 4.13. The largest deflection is for aluminium at an incidence angle of 10° resulting a 7 mm tip deflection for a Reynolds number of 1.12×10^6 . The deflection at Reynolds number of 3.36×10^5 for aluminium is only 8.5% of the deflection at a Reynolds number of 1.12×10^6. Stainless steel has a deflection at incidence angle of 10° of 2.6 mm at a Reynolds number of 1.12×10^6 and approximatley 8% of this at Reynolds number of 3.36×10^5. Also as expected the deflection increases linearly with incidence angle. The difference in deflection between the two materials is comparable to the ratio of Young's modulus to the third significant figure.

The comparison of the one-way and two-way interaction is shown in Figure 4.14. These results shows that there are small but apparent differences between predicted bending deformations. However bending deformations have been previously shown to virtually have no effect on forces and moments at least up to moderate incidences. The twist variation with incidence angle is shown in Figure 4.15. From this plot it can be seen that the twist although small in magnitude reduces with increase in incidence angle which is the opposite to bending. The variation of the non-dimensional deflection, $C_{\delta L} = (\delta EI)/(LS^3)$ with incidence angle is shown in Figure 4.16. This figure shows at an incidence angle of 1° the lower Reynolds number has a higher non-dimensional deflection and a linear relationship from 3 to 10° with a small gradient and the larger Reynolds number marginally higher than the lower. By making the deflection non-dimensional a Reynolds number dependence is evident, this is partially attributed to the coupling procedure as described for C_L and C_M where there was a larger difference at the higher Reynolds numbers.

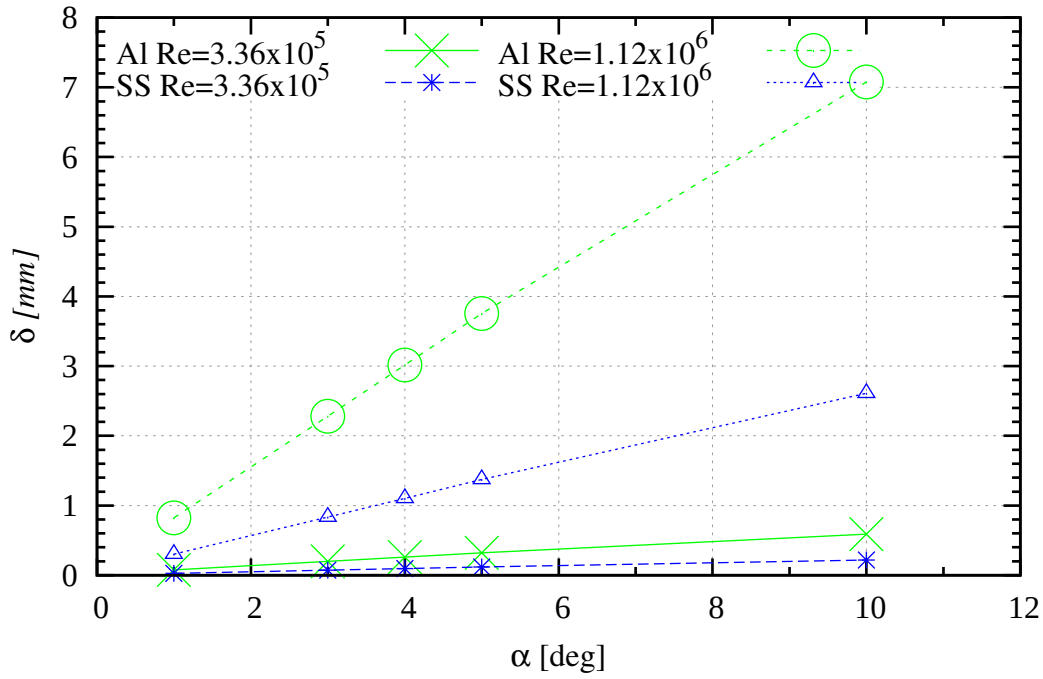

Figure 4.13: Static deflection (δ) variation with incidence angle (α).

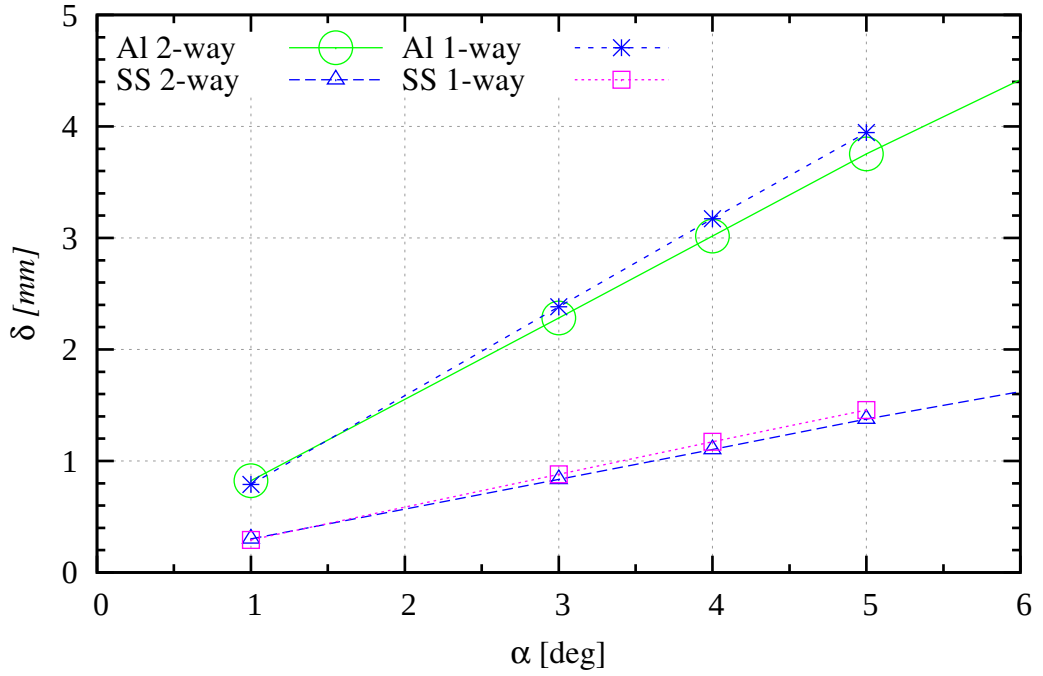

Figure 4.14: Static deflection (δ) variation with incidence angle (α) at Reynolds number of 1.12×10^6 comparing one-way to two-way coupling.

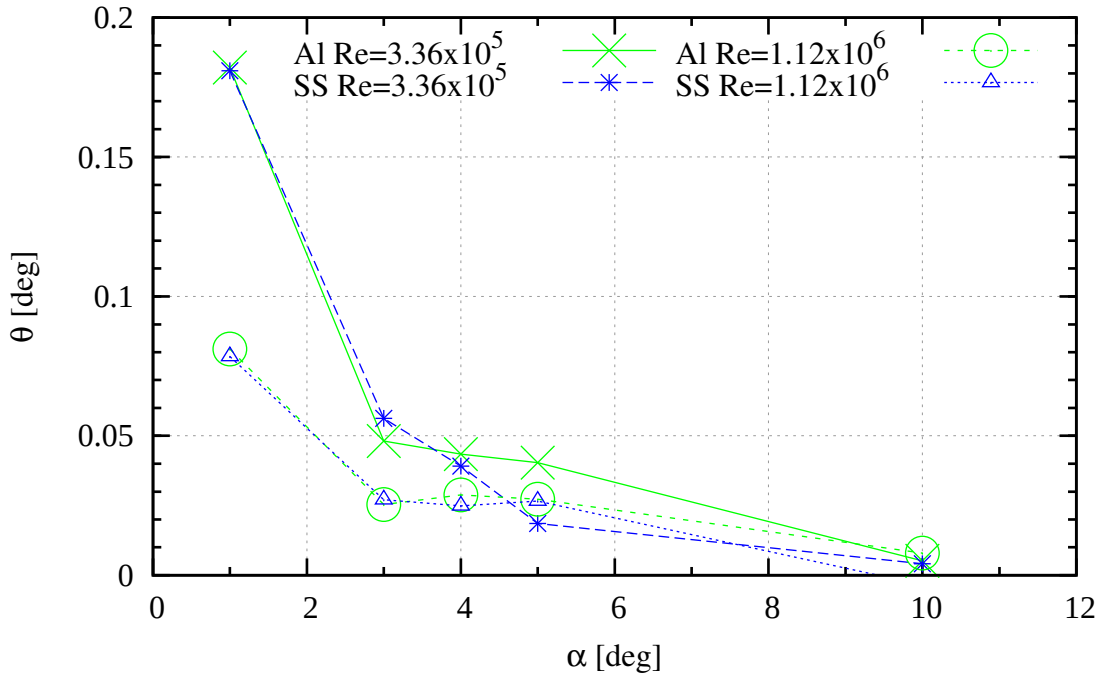

Figure 4.15: Twist (θ) variation with incidence angle (α).

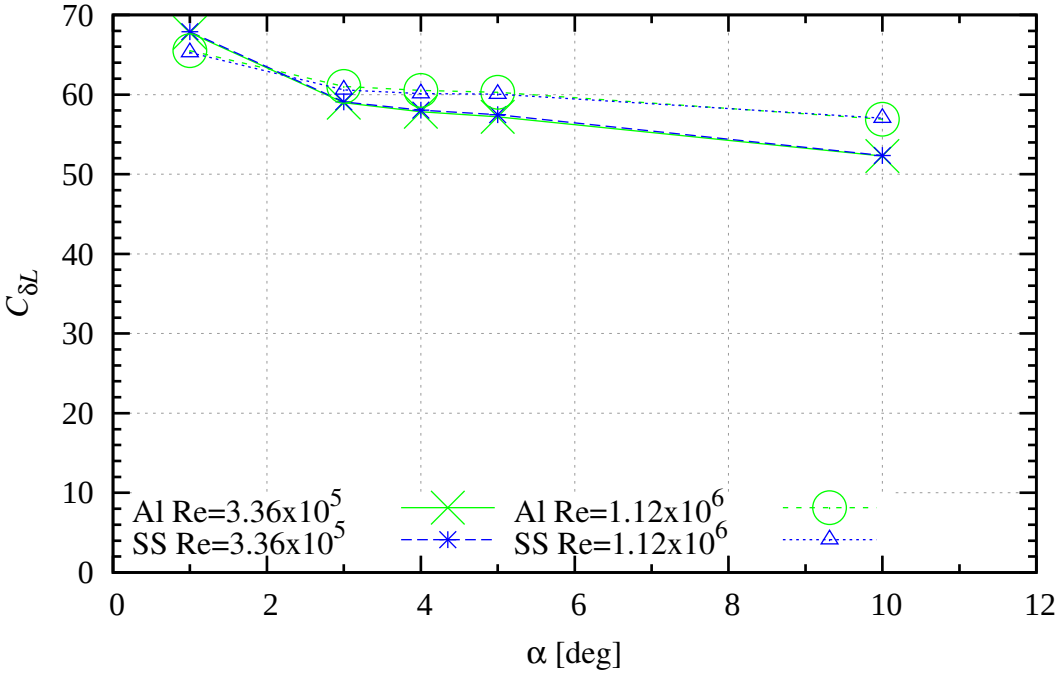

Figure 4.16: Non-dimensional static deflection ($C_{\delta L}$) variation with incidence angle (α).

4.4 Chapter Summary

The investigation of the two-way FSI of a 3D NACA 0009 hydrofoil with trapezoidal planform for steady angles of incidence is described in this chapter. There is little variation in Reynolds number for C_L and C_M. Although C_L and C_M are slightly higher at the higher Reynolds number. The results for C_L and C_M are similar to the rigid case up to an incidence angle of 5° after this there is a noticeable variation. That is, at 10° incidence the results for the aluminium and stainless steel are almost identical at the lower Reynolds number but considerably different from the rigid case for the same Reynolds number. Similarly, the results for the aluminium and stainless steel foils are essentially identical at the higher Reynolds number but compare more favourably with the rigid results for the higher Reynolds number than those for the lower Reynolds number. To investigate this possible artefact the percentage difference from the original rigid undeformed mesh at incidence angle of 5 and 10° for C_L and C_M was calculated. By comparing the three sets of runs; rigid uncoupled with an undeformed mesh (rigid undeformed), coupled (coupled) and an rigid uncoupled run but using the resulting deformed coupled CFD mesh (deformed rigid). It was found that there was a reduced difference in percentage at the higher Reynolds number. At 5° the variation is less than 4% for all cases.

The C_D curve in the coupled case for aluminium and stainless steel has a constant offset from the rigid uncoupled analyses. This is investigated in this study by this same procedure as for C_L and C_M and it was found to have a constant offset through all incidence angles. This was approximately 0.017 and 0.007 for a freestream velocity of 2.5 and 8.3 m/s respectively. Therefore it was concluded that the C_D offset and the C_L and C_M variation was attributed to the coupling process by small vibrations on the surface of the foil resulting from the moving mesh between iterations. Consequently, the boundary layer is thicker in the coupled case and has a greater viscous component. When comparing the rigid results to coupled the error is relatively small for C_L and C_M at small to moderate incidence angles. The C_D trend shows an increasing reduced frequency once normalised on the static value at maximum incidence. By normalising C_D with the coupled static case, the offset error is removed and the trend can be compared to the rigid analysis.

The effect of static incidence is investigated using a two-way coupled FSI. The static deflection increases linearly with incidence angle up to moderate angles. The difference in deflection between the two materials is comparable to the ratio of Young's modulus to the third significant figure. The foil's twist remains less than 0.2° and becomes less as the angle of incidence is increased. Comparison of static one-way and two-way coupled results shows that there are small but apparent differences between predicted bending deformations. However, bending deformations were shown to have virtually no effect on forces and moments at least up to moderate incidences.

Chapter 5

Dynamic Hydroelasticity

The investigation of the coupled (two-way FSI) 3D NACA 0009 hydrofoil with a with trapezoidal planform undergoing a sinusoidal pitch oscillation is described in this chapter. Results are presented as hysteresis plots, a summary of maximum C_L, C_D, C_M and structural deflections and twist. Comparisons are made with the 3D (uncoupled) rigid body fluid dynamic results. The previous work relating to hydroelastic foils was discussed in Chapter 4.

5.1 Methodology

This section builds upon the methodology presented in earlier chapters. From the transient CFD analyses in Chapter 2, 100 time steps per cycle was shown to achieve temporal convergence. All results that did not produce a closed hysteresis loop were excluded from the summary of maximum forces, moment and structural response. An initial estimate of time step for a coupled analysis is $\Delta t = 1/(20 \times f_{response})$ [55].

This analysis uses a coupled two-way transient structural and CFD model. This means both the structural and CFD analyses will model transient effects [37]. A dynamic structural analysis determines the dynamic response of the structure under transient loads [55]. The basic structural equation [55] solved in this analyses is:

$$(M)\ddot{u} + (c)\dot{u} + (K)u = F(t) \tag{5.1}$$

The structural constraints on the foil are shown in Figure 5.1. The base of the foil is attached to a cylinder which is surrounded by a frictionless support label 'A' in the figure and is constrained in the y direction. This arrangement enables the foil to be constrained as if mounted on a bearing allowing for rotation. The rotation is applied as a remote displacement which is shown as labelled 'B'. The fluid-solid interface is shown as labelled 'C', which is the surface of the foil.

To ensure that the fully coupled dynamic run had minimal start-up transients, the simulations were restarted from the rigid CFD results on the CFD side of the

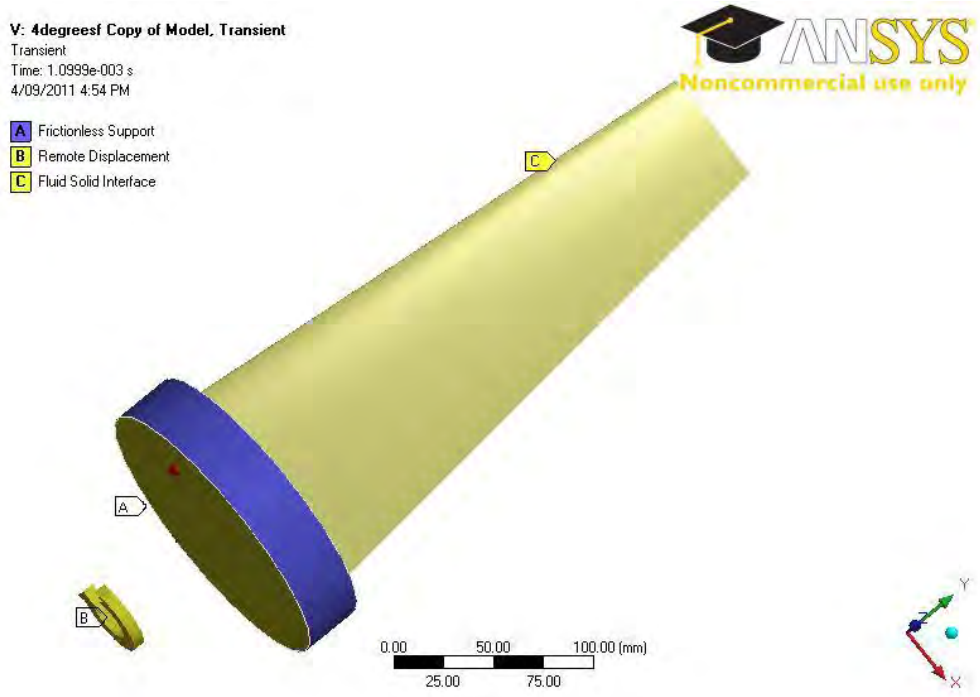

Figure 5.1: Dynamic structural numerical model

solution. This effectively prevented a sudden impulse loading from starting the foil in motion and ensuring the CFD model has already developed the induced phase angle between the forces and moments and incidence amplitude. This resulted in stable runs after half a cycle. The numerical run matrix for these analysis is shown in Table 5.1. Compared to the uncoupled simulation, this simulation models more complex physical phenomena and is more numerically intensive with the opportunity to encounter numerical and physical instability. The coupled analyses took approximately five times longer to solve than the uncoupled results.

Table 5.1: NACA 0009 1/2 c run matrix RANSE

k	$\bar{\alpha}$	$\Delta\alpha$
0.031	0,4°	3°
0.314	0,4°	3°
0.785	0,4°	3°
1.571	0,4°	3°
3.142	0,4°	3°

5.2 Results and Discussion

Initially, results from a modal analysis in air, using ANSYS, were calculated to investigate mode shapes and frequencies of interest. Using these frequencies an approximation is used to calculate the reduction in frequency due to immersion in water. Results are presented as hysteresis and summary plots of maximums. The hysteresis plots for the C_L, C_D and C_M are presented at 4° mean incidence, an incidence amplitude of 3°, a reduced frequency of 0.785 and Reynolds number 1.12×10^6. Summary plots for the maximum C_L, C_D and C_M, deflection and twist for a change in mean incidence, varying reduced frequency and incidence amplitude are detailed. Comparisons are made with the 3D (uncoupled) rigid body fluid dynamic results in both the hysteresis loops and summary plots.

5.2.1 Modal Analyses

The modal frequencies for each material is shown in Table 5.2, and the resulting mode shapes (calculated with ANSYS) are shown in Figure 5.2.

Table 5.2: Modal analyses in air [Hz]

Mode	**Stainless Steel**	**Aluminium**
1	106	108
2	446	453
3	789	796

Using an approximation from Blevins [12] the effect of added mass of the foil immersed in water will reduce the natural frequency. For the first mode this is a reduction in a natural frequency of 62% for stainless steel and 43% for aluminium which results in a natural frequency in water for stainless steel of 65 Hz and for aluminium of 46 Hz. For a velocity of 2.5 m/s ($Re = 3.36 \times 10^5$) the natural reduced frequency (equation 1.26) of stainless steel is 10 and aluminium is 7. For a velocity of 8.3 m/s ($Re = 1.12 \times 10^6$) the natural reduced frequency of stainless steel is 3 and aluminium is 2. Therefore at a velocity of 2.5 m/s ($Re = 3.36 \times 10^5$) the reduced natural frequcies are outside the run matrix. At a velocity of 8.3 m/s ($Re = 1.12 \times 10^6$) the reduced natural frequency are within the run matrix (Table 5.1). The results for the two highest reduced fequencies of 1.571 and 3.142 did not converge to a stable solution and are not included in the results.

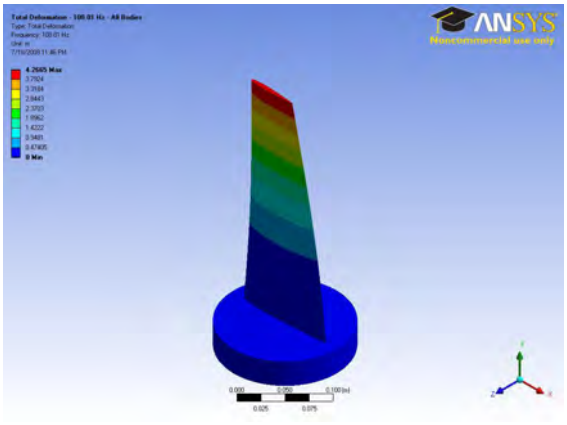

(a) Mode 1

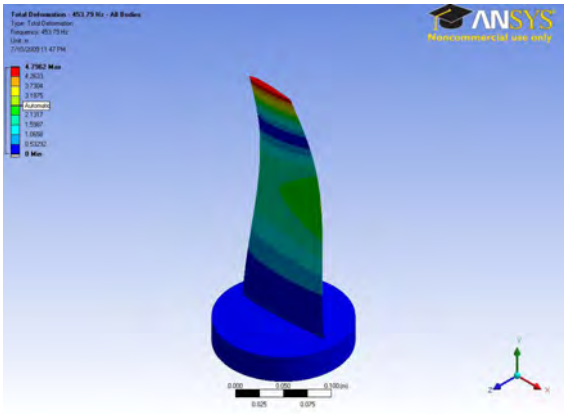

(b) Mode 2

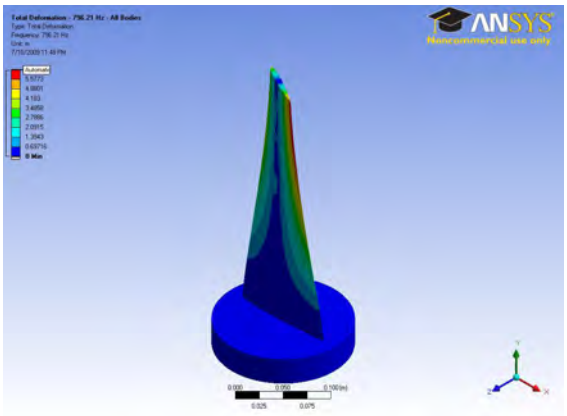

(c) Mode 3

Figure 5.2: First three mode shapes of the foil for both stainless steel and aluminium

5.2.2 Forces and Moments

The hysteresis plots of C_L, C_D and C_M for aluminium and stainless steel cases is shown in Figure 5.3. The arrows in Figure 5.3 indicate the direction of the loop on the upstroke. The first thing to note in this figure is the incidence change for the rigid case is 1 to 7°, but for the coupled case the incidence change is 1.36 to 6.64°. The coupled incidence amplitude is calculated at the root of the foil. The difference in angle is caused by the difference in the method of implementing rotation in the simulation between the rigid and coupled results. From the rigid results in Chapter 3 the effect of a 0.36° variation of incidence amplitude can be approximated. With this in mind the magnitude of the forces and moment maxima and phase is compared through normalising on the equivalent static force at maximum incidence in Figures 5.4 to 5.15. The shape of the hysteresis loops is compared to the rigid case and the coupled materials. The magnitude of the coupled materials are directly compared to each other, but compared to the rigid magnitude in the summary plots. The magnitude of variation caused by the small change in incidence angle does not affect the conclusions made.

The shape of these coupled C_L and C_M hysteresis loops are wider just prior to the maxima and minima (Figure 5.3) compared with the rigid results. The effect of this is to produce a non-linear relationship on the upstroke and downstroke, this is more pronounced in the C_M loop. The C_D is offset higher than the rigid plot with a smaller change in amplitude in comparison with the rigid case. The C_D offset was discussed in Section 4.3 where it was concluded that this was a spurious feature of the coupling process. There is a small change between aluminium and stainless steel in the coupled case at the maximum and minimum for C_L, C_D and C_M.

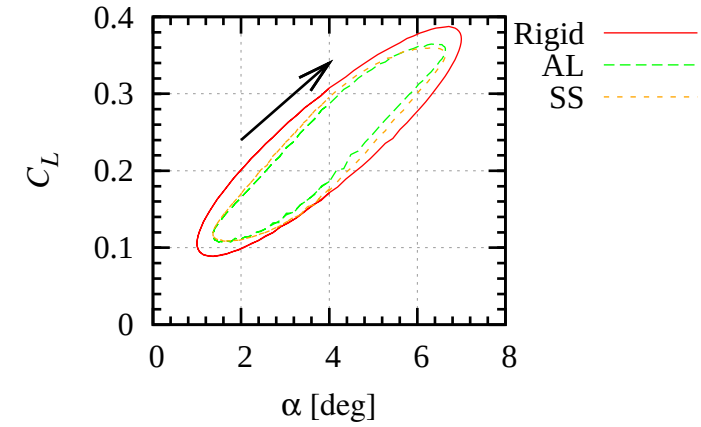

(a) C_L

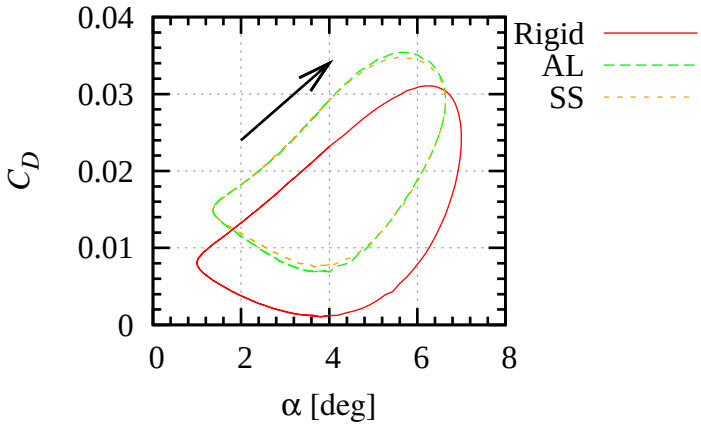

(b) C_D

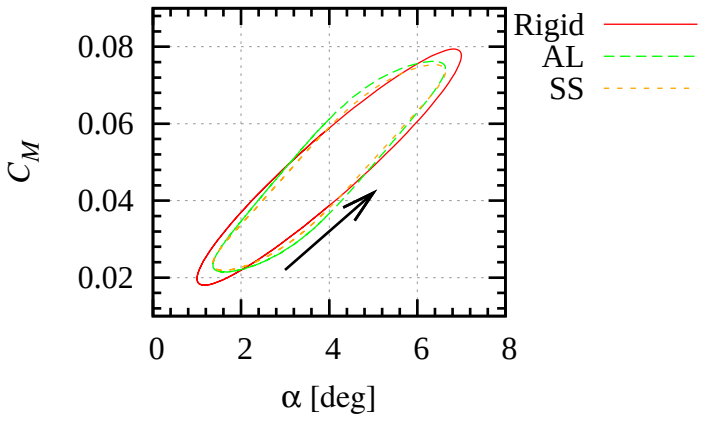

(c) C_M

Figure 5.3: Force and moment hysteresis plots comparing rigid and coupled (flexible) results for 4° mean incidence, 3° incidence amplitude, a reduced frequency of 0.785 and Reynolds number of 1.12×10^6

The normalised maximum C_L, C_D and C_M throughout one cycle and the associated phase angle is shown in Figures 5.4 to 5.15. C_L and C_M results are normalised using the rigid static value at the maximum incidence angle of the oscillation. The C_D is normalised with the coupled static force results. Each set of C_L, C_D and C_M results compares individual Reynolds numbers for rigid, aluminium and stainless steel for 0 and 4° mean incidence for varying reduced frequencies and for an incidence amplitude 3°. As previously stated any results that did not produce a closed hysteresis loop were omitted.

The normalised maximum C_L with reduced frequency for a Reynolds number of 3.36×10^5 and 1.12×10^6 is shown in Figures 5.4 and 5.5 respectively. The rigid results are shown as a solid line, and the coupled as points. At a reduced frequency of 1.571 the normalised maximum C_L result for aluminium lies above the rigid result, while at the next reduced frequency of 3.142 both aluminium and stainless steel have a higher normalised C_L. At the higher Reynolds number the 0° mean incidence results are less than the rigid results at a reduced frequency of 0.031 but match for a reduced frequency of 0.314 and 0.785.

The 4° mean incidence case has a small negative gradient and is less than the rigid case up until a reduced frequency of one. After a reduced frequency of one, the material type has an effect and the coupled case predicts a normalised C_L greater than the rigid case. The stainless steel results have the highest normalised C_L at a reduced frequency of 3.142. At the higher Reynolds number the 4° mean incidence results is under the rigid results at a reduced frequency of 0.031 but match at a reduced frequency of 0.314 and 0.785.

The lift phase angle variation with reduced frequency for a Reynolds number of 3.36×10^5 and 1.12×10^6 is shown in Figures 5.6 and 5.7 respectively. The phase angle for a Reynolds number of 3.36×10^5 varies similarly to the rigid results. The phase angle for a Reynolds number of 1.12×10^6 diverges as it approaches the point at which the simulations became unstable. Both aluminium and stainless steel diverge at approximately the same rate.

In summary, from the normalised C_L results for a Reynolds number of 3.36×10^5 and 1.12×10^6 there is minimal difference up until a reduced frequency of one. At a reduced frequency greater than one the coupled results show an increase in normalised C_L when compared to the rigid case. The lift phase angle does not vary for a Reynolds number of 3.36×10^5 but diverges at a Reynolds number of 1.12×10^6 as this is the point at which the simulations become unstable.

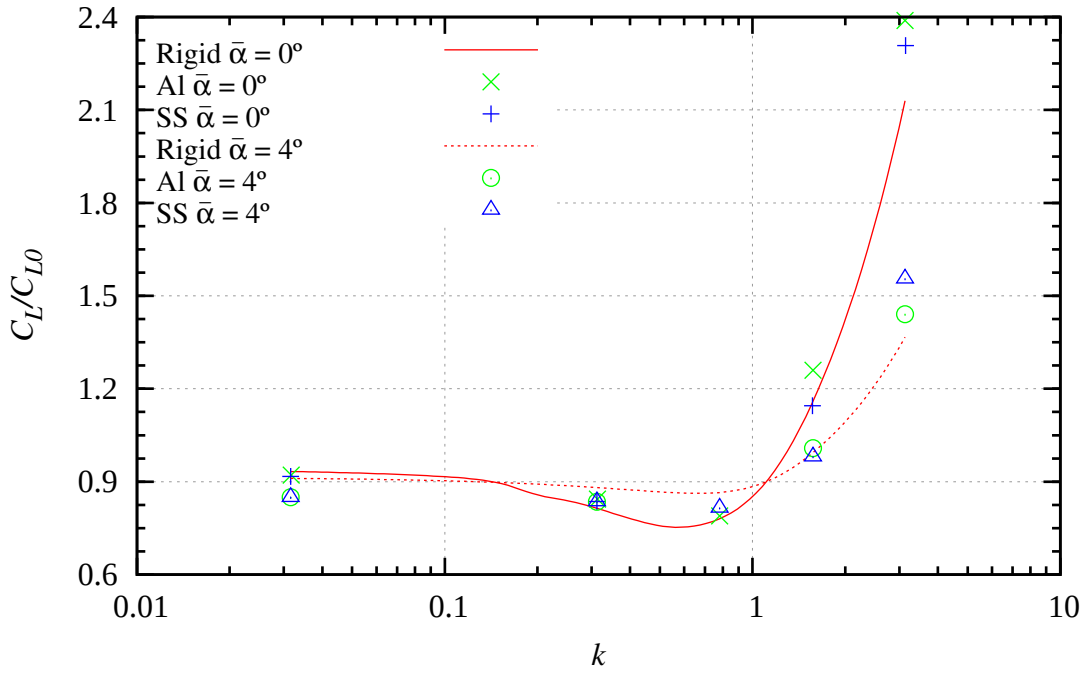

Figure 5.4: Comparison of computed maximum normalised C_L for varying reduced frequency (k) incidence amplitude ($\Delta\alpha$) of 3° and mean incidence ($\bar{\alpha}$) of 0 and 4° at a Reynolds number (Re) of 3.36×10^5

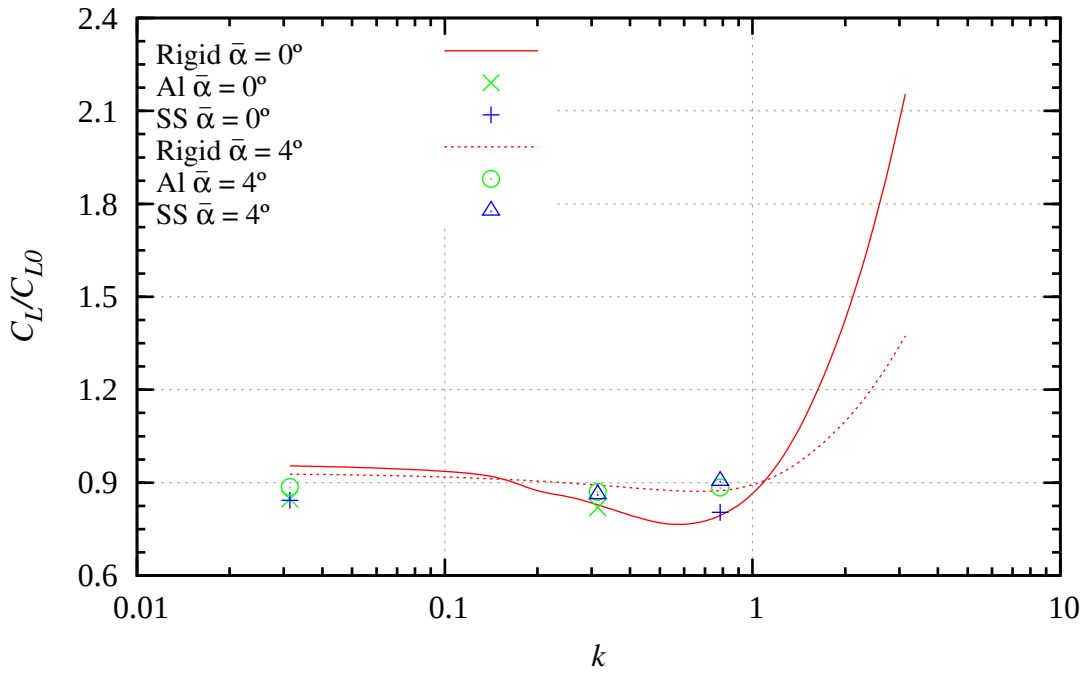

Figure 5.5: Comparison of computed maximum normalised C_L for varying reduced frequency (k) incidence amplitude ($\Delta\alpha$) of 3° and mean incidence ($\bar{\alpha}$) of 0 and 4° at a Reynolds number (Re) of 1.12×10^6

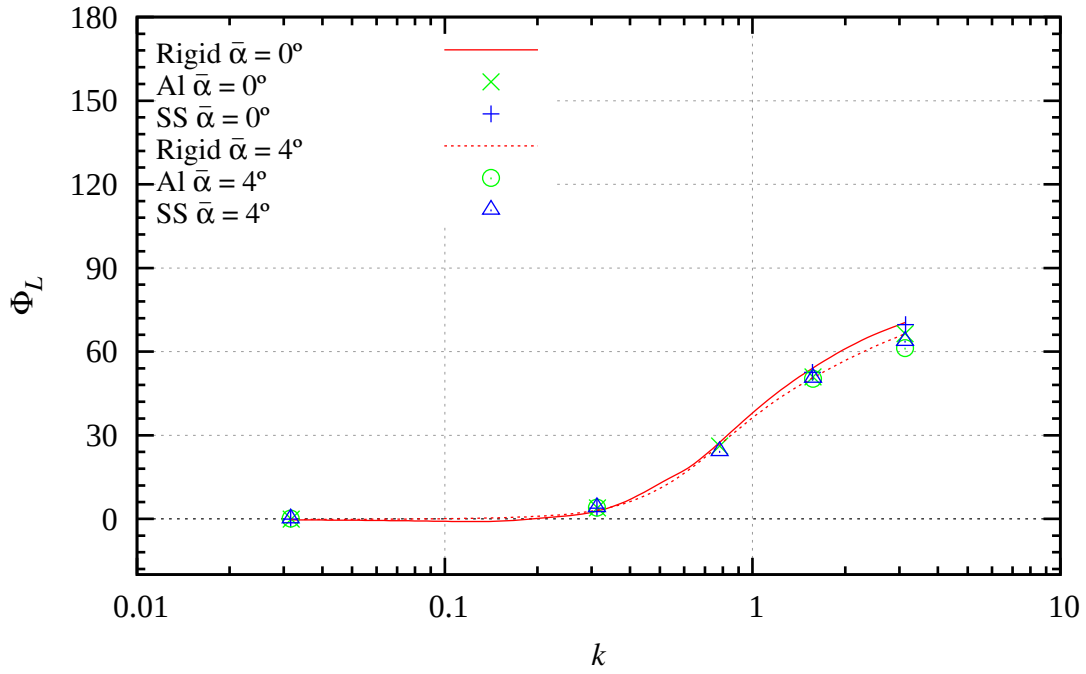

Figure 5.6: Comparison of computed lift phase angle (Φ_L) for varying reduced frequency (k) incidence amplitude ($\Delta\alpha$) of 3° and mean incidence ($\bar{\alpha}$) of 0 and 4° at a Reynolds number (Re) of 3.36×10^5

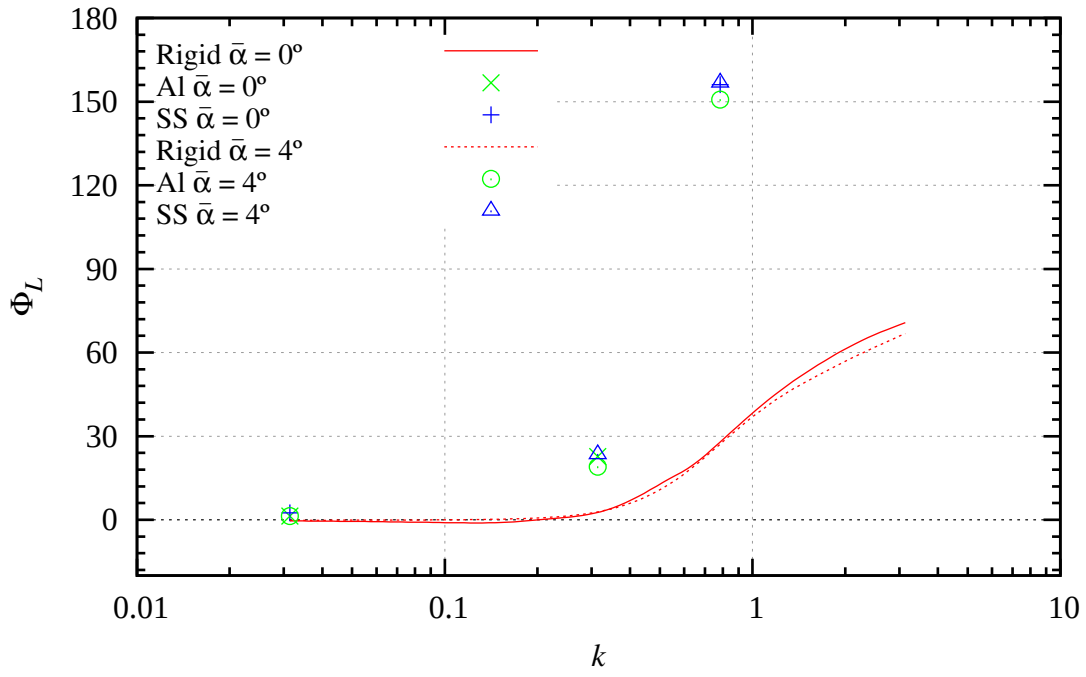

Figure 5.7: Comparison of computed lift phase angle (Φ_L) for varying reduced frequency (k), incidence amplitude ($\Delta\alpha$) of 3° and mean incidence ($\bar{\alpha}$) of 0 and 4° at a Reynolds number (Re) of1.1×10^6

The normalised maximum C_D for a Reynolds number of 3.36×10^5 and 1.12×10^6 is shown in Figures 5.8 and 5.9. The coupled results are normalised with the static coupled analyses at the point of maximum incidence. At a Reynolds number of 3.36×10^5, after normalising the coupled results, they have similar trends to the rigid results at reduced frequencies of 0.031 and 0.314. The 0° mean incidence begins to increase non-linearly after a reduced frequency of 1.571. At a reduced frequency of 3.142 the results are dependent on material, with stainless steel increasing rapidly. After a reduced frequency of 0.785 the 4° mean incidence results begins to increase non-linearly. At a Reynolds number of 1.12×10^6 all values for both 0 and 4° mean incidences are nearly constant and slightly above the rigid results.

The drag phase angle variation with reduced frequency for a Reynolds number of 3.36×10^5 and 1.12×10^6 is shown in Figures 5.10 and 5.11. At a Reynolds number of 3.36×10^5 the results are constant, and then decrease at a reduced frequency of 0.785 for a 0° mean incidence. Aluminium increases at a reduced frequency of 0.785 then reduces to a similar value as for the rigid. The phase angle for this case at 4° mean incidence behaves the same for both coupled and rigid cases. At a Reynolds number of 1.12×10^6 the drag phase angle is above the rigid and diverges similarly to the lift as it approaches the unstable solutions.

The normalised C_M for a Reynolds number of 3.36×10^5 is shown in Figures 5.12 and 5.14 respectively. The rigid results are shown as a solid line, and the coupled as points. For the 0° mean incidence, the results compare with the rigid, except at a reduced frequency of 3.142, the moment for stainless steel is reduced. At 4° mean incidence there is no material dependence with C_M remaining less than the rigid case for reduced frequencies less than one. At a reduced frequency of 1.571 the result is the same for rigid and coupled. After this, the coupled case then increases more rapidly than the rigid. The phase angle of the C_M maximum is the same for coupled and rigid results.

The moment phase angle for a Reynolds number of 3.36×10^5 and 1.12×10^6 is shown in Figures 5.14 and and 5.15 respectively. At a Reynolds number of 3.36×10^5 the phase matches for the rigid and coupled case. At a Reynolds number of 1.12×10^6 the coupled phase is less than the rigid phase until a reduced frequency of 0.785. At a reduced frequency of 0.785 the phase diverges.

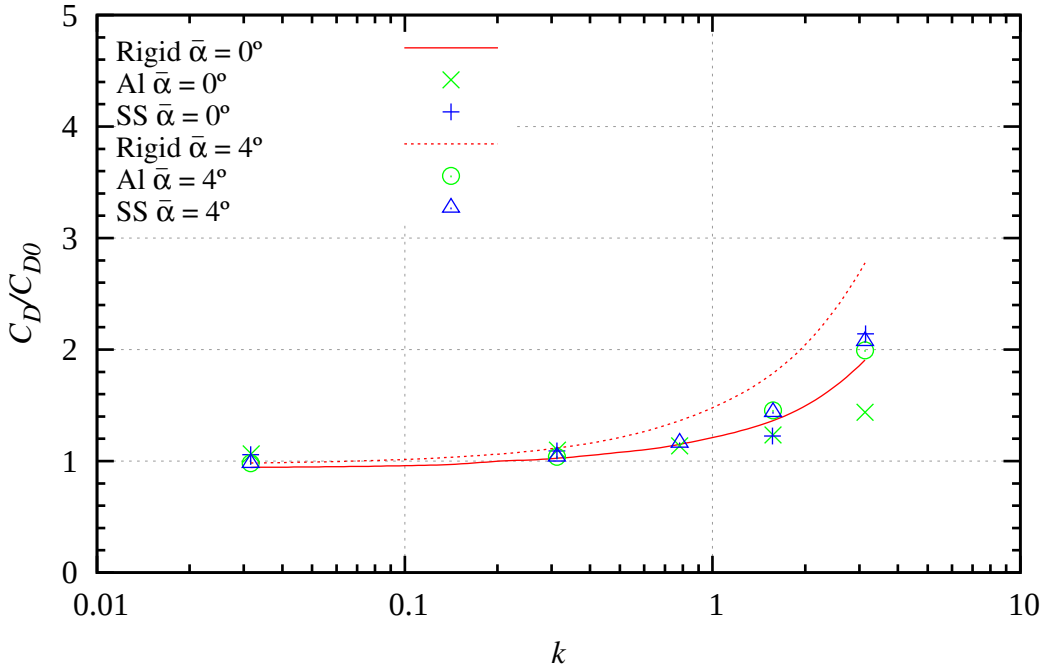

Figure 5.8: Comparison of computed maximum normalised C_D for varying reduced frequency (k), incidence amplitude ($\Delta\alpha$) of 3° and mean incidence ($\bar{\alpha}$) of 0 and 4° at a Reynolds number (Re) of 3.36×10^5

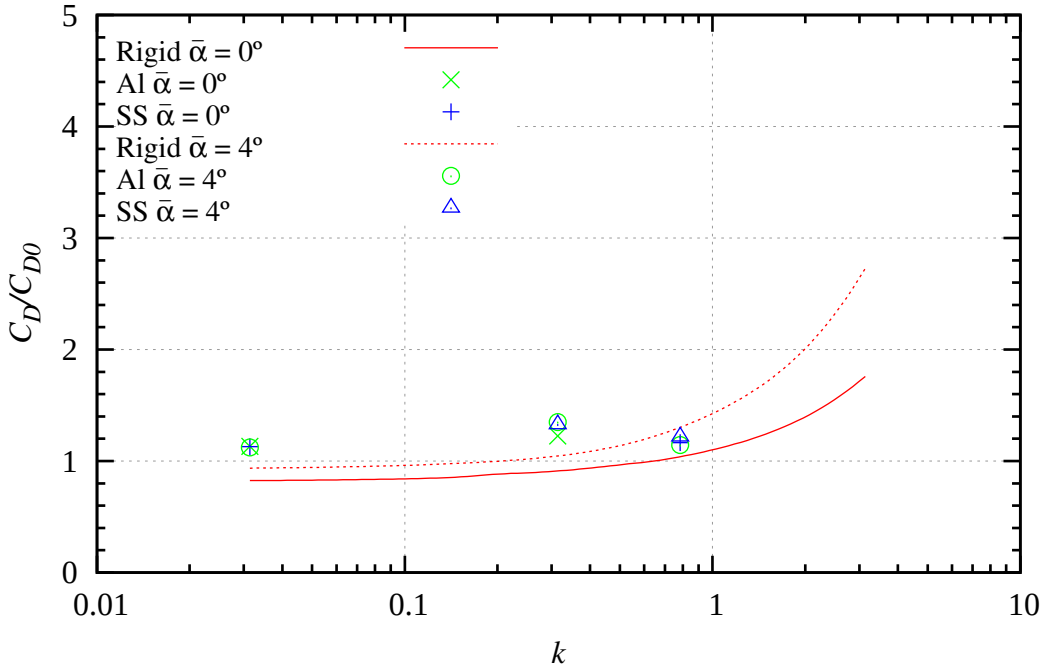

Figure 5.9: Comparison of computed maximum normalised C_D for varying reduced frequency (k), incidence amplitude ($\Delta\alpha$) of 3° and mean incidence ($\bar{\alpha}$) of 0 and 4° at a Reynolds number (Re) of 1.12×10^6

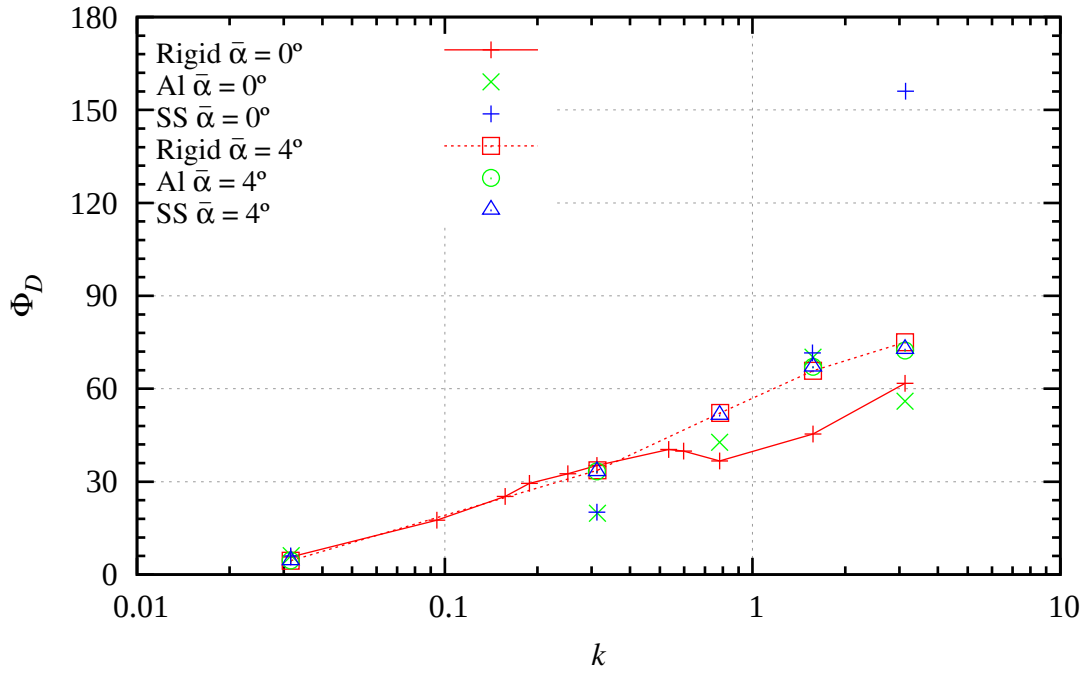

Figure 5.10: Comparison of computed drag phase angle (Φ_D) for varying reduced frequency (k), incidence amplitude ($\Delta\alpha$) of 3° and mean incidence ($\bar{\alpha}$) of 0 and 4° at a Reynolds number (Re) of 3.36×10^5

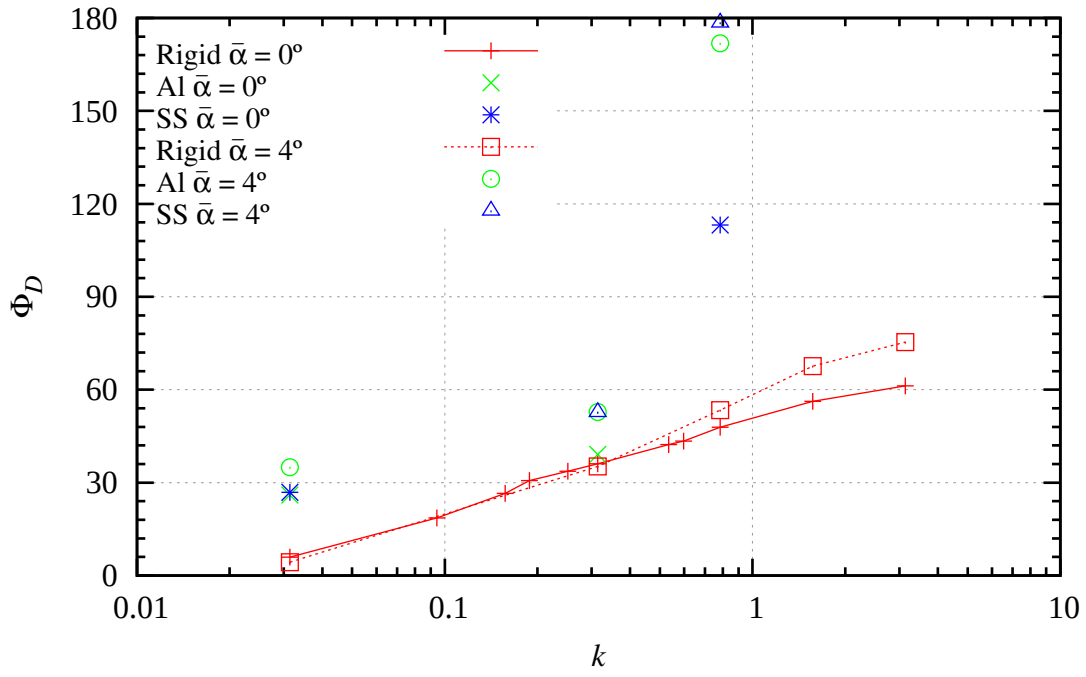

Figure 5.11: Comparison of computed drag phase angle (Φ_D) for varying reduced frequency (k), incidence amplitude ($\Delta\alpha$) of 3° and mean incidence ($\bar{\alpha}$) of 0 and 4° at a Reynolds number (Re) of 1.12×10^6

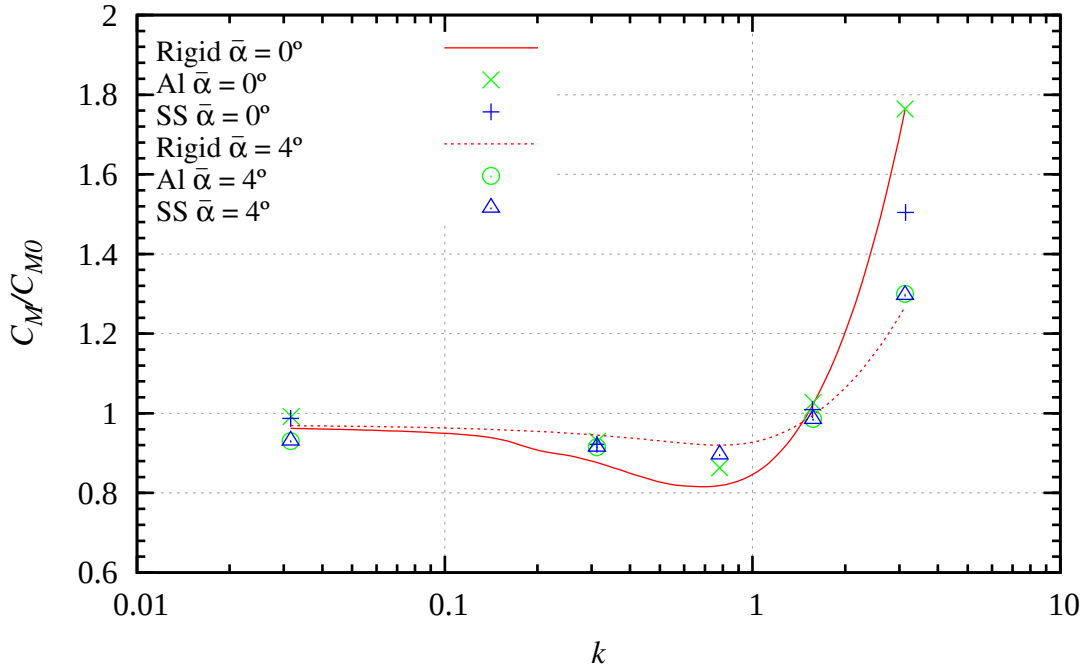

Figure 5.12: Comparison of computed maximum normalised C_M for varying reduced frequency (k), incidence amplitude ($\Delta\alpha$) of 3° and mean incidence ($\bar{\alpha}$) of 0 and 4° at a Reynolds number (Re) of 3.36×10^5

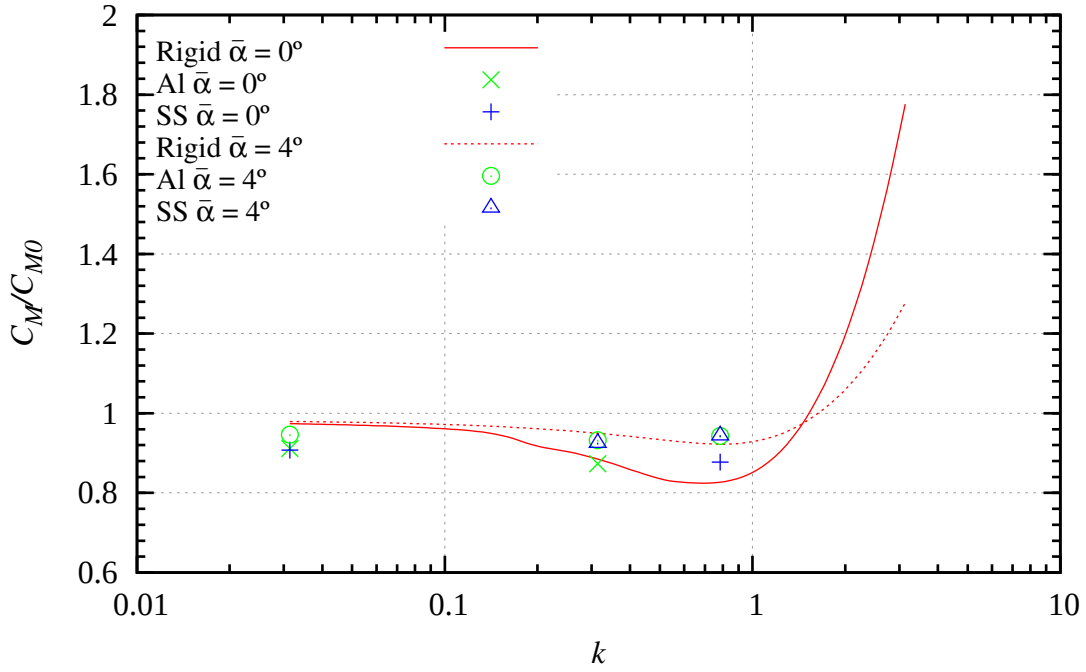

Figure 5.13: Comparison of computed maximum normalised C_M for varying reduced frequency (k) incidence amplitude ($\Delta\alpha$) of 3° and mean incidence ($\bar{\alpha}$) of 0 and 4° at a Reynolds number of 1.12×10^6

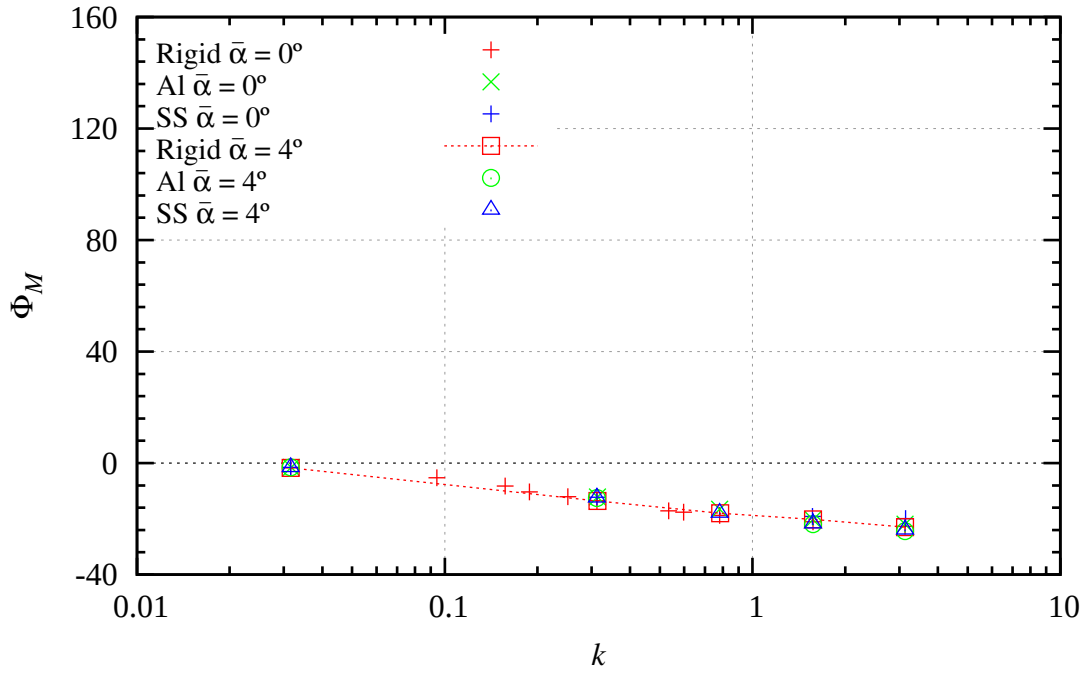

Figure 5.14: Comparison of computed moment phase angle (Φ_M) for varying reduced frequency (k) incidence amplitude ($\Delta\alpha$) of 3° and mean incidence ($\bar{\alpha}$) of 0 and 4° at a Reynolds number of 3.36×10^5

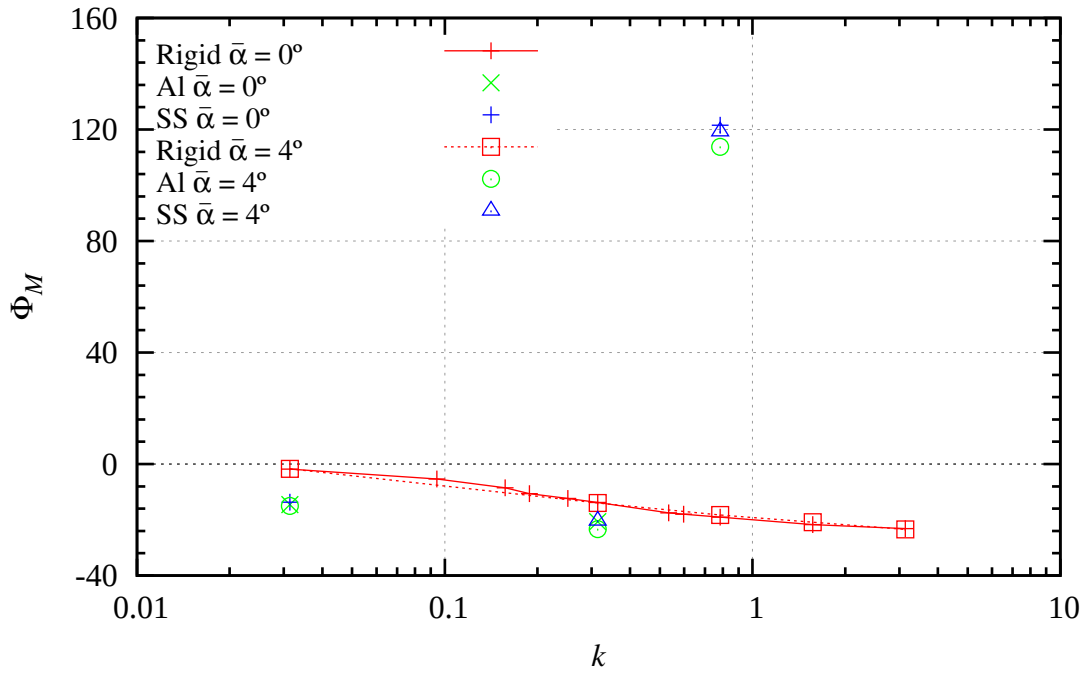

Figure 5.15: Comparison of computed moment phase angle (Φ_M) for varying reduced frequency (k) incidence amplitude ($\Delta\alpha$) of 3° and mean incidence ($\bar{\alpha}$) of 0 and 4° at a Reynolds number of 1.12×10^6

The deflection, twist and non-dimensional deflection is shown in Figures 5.16 to 5.19. The phase for all structural responses have not been presented as they were less than 3° in all cases. The last two results in the coupled case for a Reynolds number of 1.12×10^6 did not converge within the run time and became unstable. These are not presented in the summary plots.

The deflections remained small at the lower Reynolds number, less than 0.8 mm. This is greater than the static case which was approximately 0.2 mm. At the higher Reynolds number the deflection is less than the static angle equivalent at maximum incidence angle. For example, aluminium in the dynamic case at an incidence of 7° has an approximate deflection of 4 mm and 5 mm in the static case. The non-dimensional bending shows that until a reduced frequency of approximately one, the trend of non-dimensional bending in relation to reduced frequency is almost constant. Above one the deflection increases rapidly.

The twist for a Reynolds number of 3.36×10^5 and 1.12×10^6 is shown in Figures 5.20 and 5.21. The twist at a Reynolds number of 3.36×10^5 remains less than a degree for all reduced frequencies. At a reduced frequency of 3.142 there is a slight increase in twist which is greater for aluminium. The twist at a Reynolds number of 1.12×10^6 reduces approximately half a degree from a reduced frequency of 0.031 to 0.785. The twist for aluminium is larger than stainless steel at a Reynolds number of 1.12×10^6.

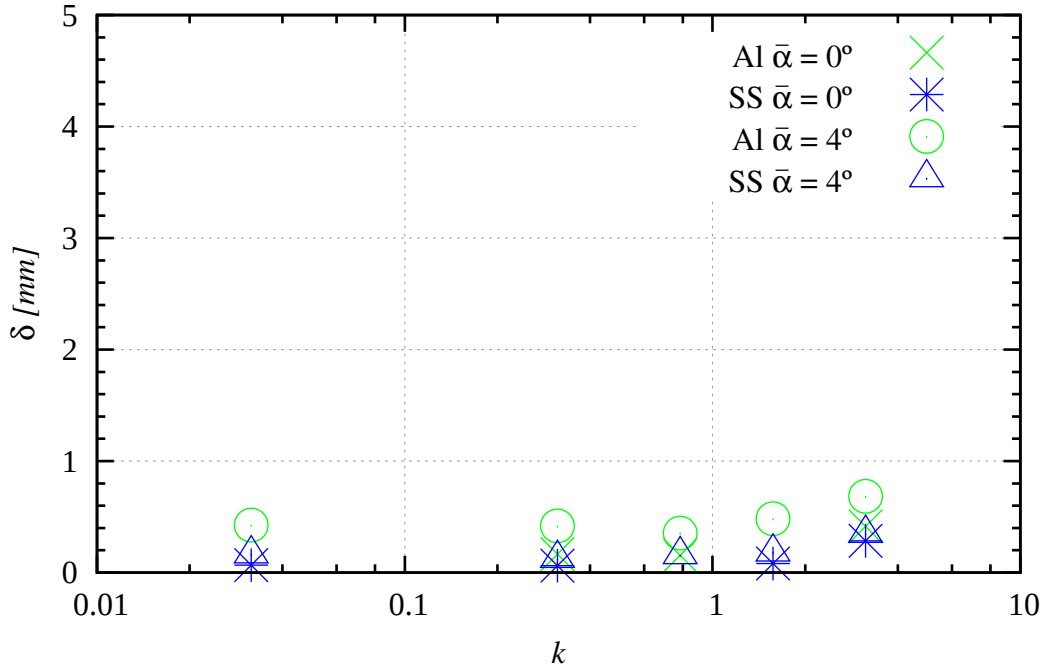

Figure 5.16: Comparison of computed maximum deflection (δ) for varying reduced frequency (k), incidence amplitude ($\Delta\alpha$) of 3° and mean incidence ($\bar{\alpha}$) of 0 and 4° at a Reynolds number of 3.36×10^5

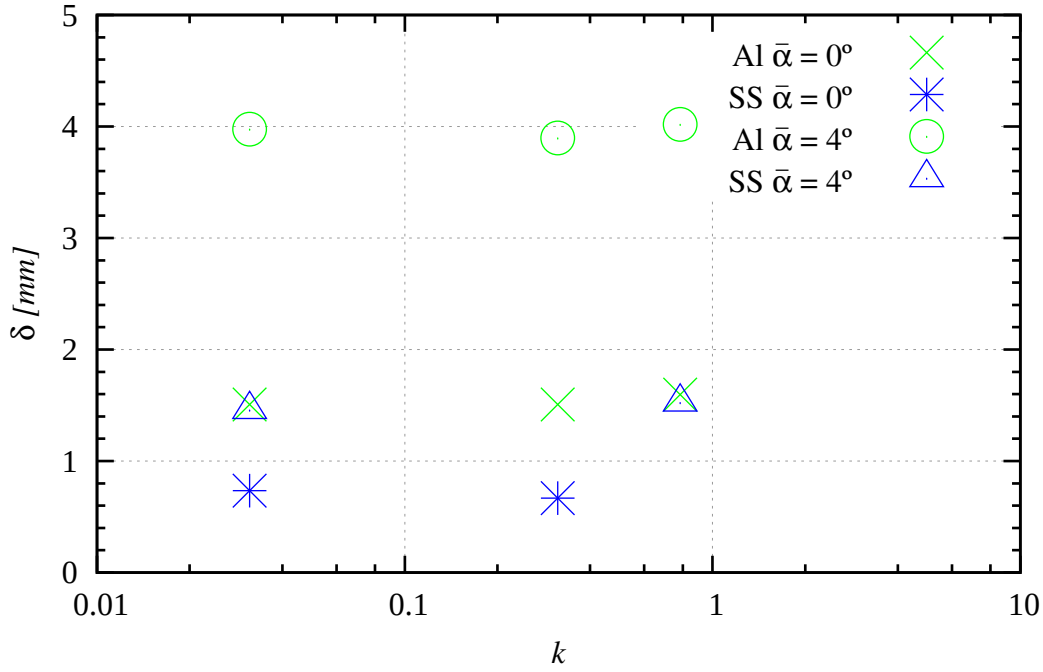

Figure 5.17: Comparison of computed maximum deflection (δ) for varying reduced frequency (k), incidence amplitude ($\Delta\alpha$) of 3° and mean incidence ($\bar{\alpha}$) of 0 and 4° at a Reynolds number of 1.12×10^6

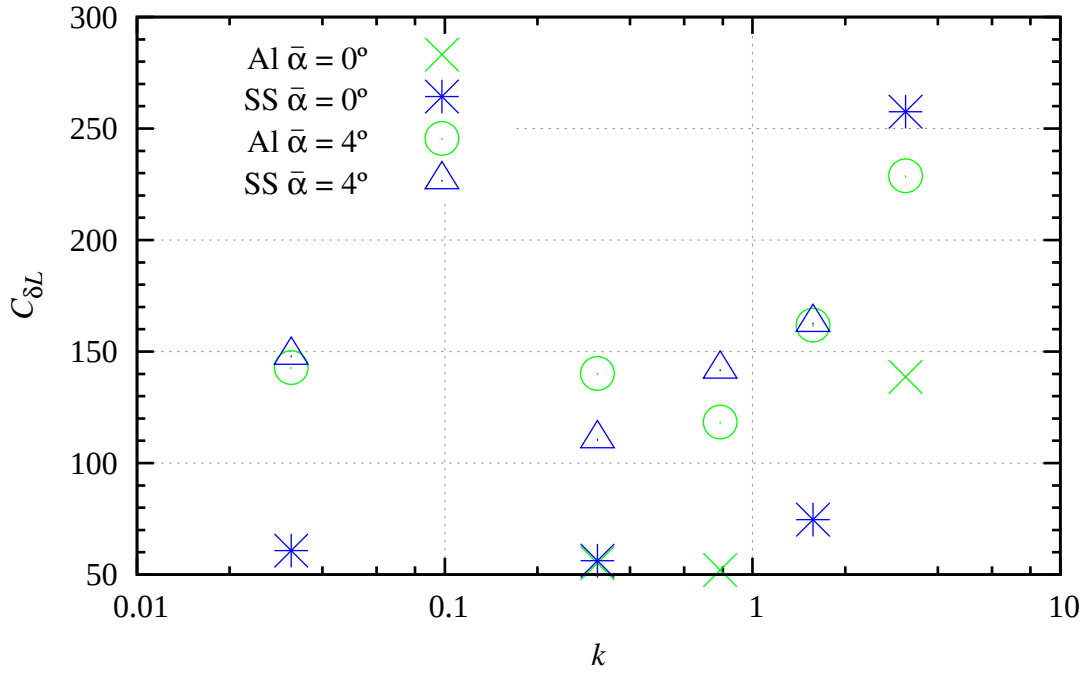

Figure 5.18: Comparison of computed maximum non-dimensional deflection ($C_{\delta L}$) for varying reduced frequency (k), incidence amplitude ($\Delta\alpha$) of 3° and mean incidence ($\bar{\alpha}$) of 0 and 4° at a Reynolds number of 3.36×10^5

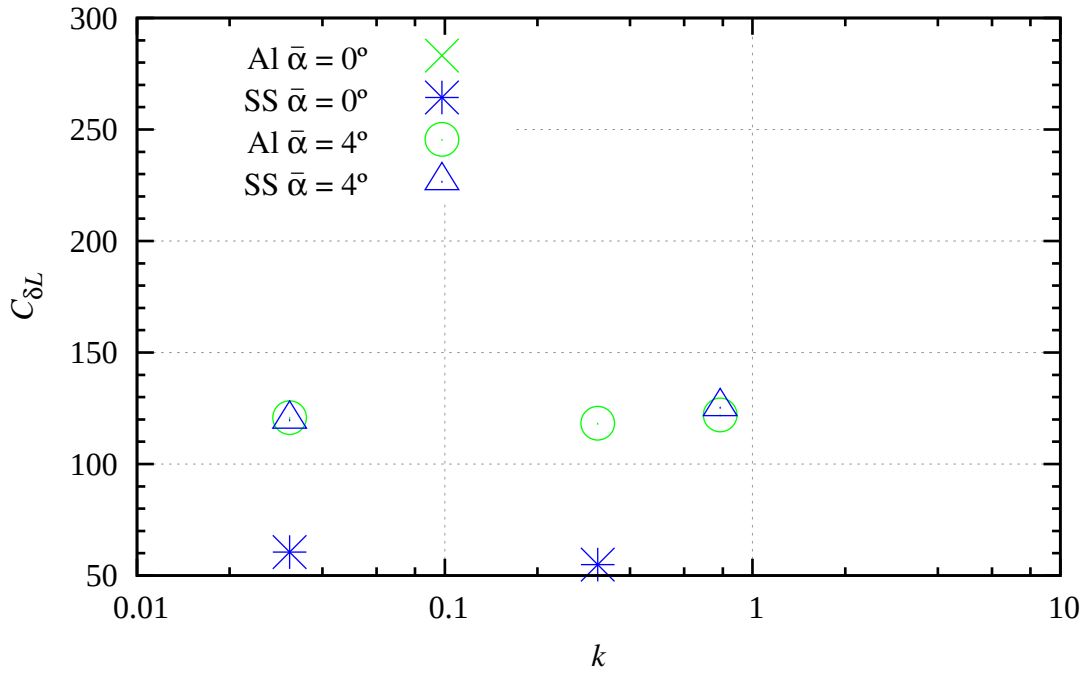

Figure 5.19: Comparison of computed maximum non-dimensional deflection ($C_{\delta L}$) for varying reduced frequency (k), incidence amplitude ($\Delta\alpha$) of 3° and mean incidence ($\bar{\alpha}$) of 0 and 4° at a Reynolds number of 1.12×10^6

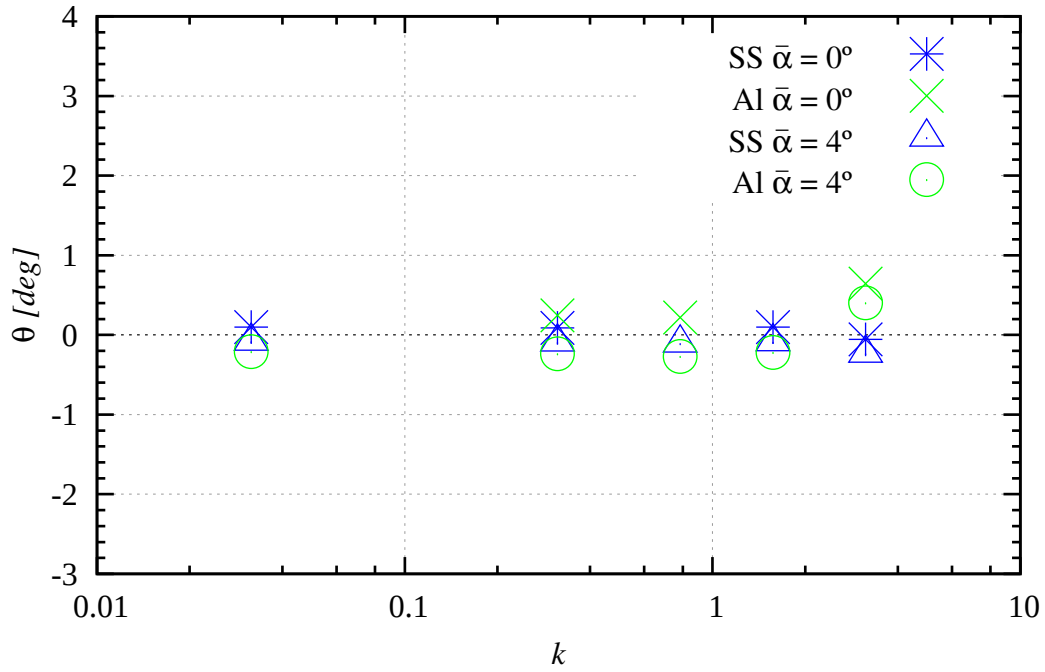

Figure 5.20: Comparison of computed maximum twist (θ) for varying reduced frequency (k), at a Reynolds number of 3.36×10^5

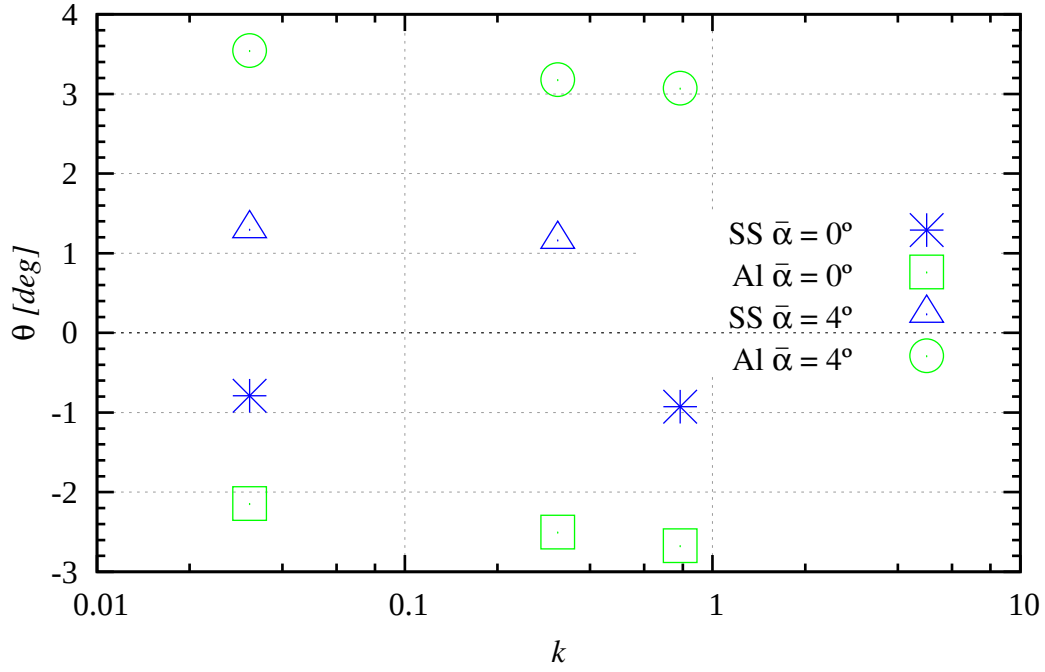

Figure 5.21: Comparison of computed maximum twist (θ) for varying reduced frequency (k), for an at a Reynolds number of 1.12×10^6

5.3 Chapter Summary

In this chapter the results of FSI simulations were presented for aluminium and stainless steel undergoing a pure pitch oscillation. Using an approximation from Blevins [12] the effect of added mass of the foil immersed in water will reduce the natural frequency. For a velocity of 2.5 m/s ($Re = 3.36 \times 10^5$) the natural reduced frequency of stainless steel is 10 and aluminium is 7. For a velocity of 8.3 m/s ($Re = 1.12 \times 10^6$) the natural reduced frequency of stainless steel is 3 and aluminium is 2. At a velocity of 8.3 m/s ($Re = 1.12 \times 10^6$) the reduced natural frequency are within the run matrix. The results for the last two reduced frequencies of 1.571 and 3.142 did not converge to a stable solution and are not included in the results.

The effect of coupling on the hysteresis to produce a non-linear relationship on the upstroke and downstroke, this is more pronounced in the C_M loop. The C_D is offset higher than the rigid plot with a smaller change in amplitude in comparison with the rigid case. The C_D offset was discussed in Section 4.3, where it was concluded that this was a spurious feature of the coupling process. There is a small change between aluminium and stainless steel in the coupled case at the maximum and minimum for C_L, C_D and C_M.

In conclusion, a reduced frequency of one is significant. At a Reynolds number of 3.36×10^5 it is the reduced frequency at which the non-dimensional deflection becomes non-linear, and C_L and C_D for both mean incidence varies with material. The C_L at a reduced frequency greater than one has a larger magnitude maxima than the rigid results, although the coupled 4° mean incidence remains less than the rigid results for a 0° mean incidence. In Chapter 3, the rigid results had an increase in incidence amplitude at 4° mean incidence increases the magnitude of normalised lift, but there was no affect at the 0° mean incidence. This implies that the bending is increasing the magnitude of lift as there is an increase in the coupled analysis for both 0° and 4° mean incidence increases and minimal change in twist.

C_M at a Reynolds number of 3.36×10^5 when coupled has little variation at reduced frequency greater than one for 4° mean incidence. At a reduced frequency greater than one for 4° mean incidence the C_M for stainless steel is less than the rigid case, with a similar C_M for aluminium. In Chapter 3, the rigid case, an increase in incidence amplitude at 4° mean incidence increases the magnitude of normalised C_M, but there was no affect at the 0° mean incidence. Therefore coupling has reversed the C_M trend between 0 and 4° mean incidence.

The twist is significant at a Reynolds number of 1.12×10^6. The twist phase angle to the incidence amplitude was small for all cases. The lift, drag and moment phase angle, as the reduced frequency approached the natural reduced frequency of stainless steel is 3 and aluminium is 2. The C_L, C_D, deflection and twist all remained constant or reduced, the C_M however marginally increased.

Reduced frequencies of 0.8, 1.6 and 2.4 were identified in Chapter 1.4 as being representative of those experienced by a propeller operating in an unsteady flow

field caused by wakes from the control surfaces and fairwater of a submarine. The approximate incidence amplitude is 2° with a 4° mean incidence. From this chapter we can conclude that coupling may affect modes that occur at reduced frequencies greater than one.

Chapter 6

Conclusions

Marine propellers operate in unsteady non-uniform wake regions generated by the hull and control surfaces subjecting the propeller to unsteady loading. Hydroelastic tailoring of propeller blades is a method to reduce unsteady loading as a propeller blade passes through a wake deficit. This project sought to gain greater insight into the effect of hydroelastic tailoring on a propeller by simplifying the problem to a single trapezoidal planform hydrofoil with a sinusoidal pitch oscillation. This simplification was achieved through comparison of the 'gust response' of a blade passing through a wake deficit to a 2D foil's unsteady sinusoidal 'gust response'. This analogy was used to determine the run matrix parameters. By considering a 3D hydrofoil of similar aspect ratio to a propeller blade and largely focusing on bending, the FSI behaviour has been investigated using the commercial ANSYS CFX for the computational fluid dynamics coupled with ANSYS mechanical structural package. To be able to accurately predict and model FSI with a stable numerical solution, a solid understanding of the rigid body dynamics was required. This was undertaken by the investigation of the rigid body dynamics both statically and dynamically.

The commercial CFD package ANSYS CFX using the RANSE Shear Stress Transport (SST) model has been shown to accurately predict the unsteady forces on an oscillating hydrofoil in pure pitch in both two and three dimensions. Validation was conducted both statically and dynamically. Static validation was undertaken with the co-efficient of pressure from experimental data at an incidence angle of 2, 5 and 10°. Results using XFOIL, $k-\epsilon$ and SST models compared well to the experimental data. However, results from the $k-\omega$ model at an incidence angle of 10° did not compare well with experimental data and indicated early stall onset and was not used in any further analyses. Dynamic validation was undertaken with experimental results for C_L, C_D and C_M. Results compared well for reduced frequency values of 0.131 and 0.188 for both $k-\epsilon$ and SST turbulence models. However, this was not the case for the lower reduced frequency values of 0.038 and 0.093, where the use of the $k-\epsilon$ turbulence models resulted in a large mean C_D offset. The SST model modifies the eddy viscosity by forcing the turbulent shear stress to be bounded by a constant time inside the boundary layer [23]. For this

reason the SST model was used for the remainder of the numerical modelling. Results from this model compared well for C_L and C_D, but under-predicted the C_M on the downstroke.

The effect of static incidence is investigated using a two-way coupled FSI. The static deflection increases linearly with incidence angle up to moderate angles. The difference in deflection between the two materials is comparable to the ratio of Young's modulus to the third significant figure. The foil's twist remains less than 0.2° and becomes less as the angle of incidence is increased. Comparison of static one-way and two-way coupled results shows that there are small but apparent differences between predicted bending deformations. However, bending deformations were shown to have virtually no effect on forces and moments at least up to moderate incidences.

At the tip of the foil there is a pronounced difference in the behaviour of the tip vortex at 0 and 4° mean incidence, although at the tip the pressures about the foil are symmetric for both 0 and 4° mean incidences. The spacing and magnitude of the vorticity travelling downstream varies between the 0 and 4° mean incidences. When the foil oscillates at 0° mean incidence the positive Q-criterion wavelength corresponds to twice the oscillation frequency. In contrast, at the tip at 4° mean incidence, the wave length between a positive region is equal to the oscillation frequency. The variation between 2D and 3D has been attributed to the spanwise circulation/lift and 3D flow has the ability to equalise over the tip. The magnitude of wake vorticity increases with increased incidence amplitude but the frequency at which the vorticity travels downstream remains equal at the mid span.

The C_L hysteresis varies about the static C_L curve with increasing hysteresis as the reduced frequency increases. The hysteresis is less in the 3D case compared to the 2D case. This was attributed to the 3D flow having the ability to equalise over the tip. The C_D has a double harmonic at a mean incidence of 0° due to the static C_D being a mirror about the incidence angle of 0°. This means C_L and C_D are odd and even functions respectively of the dynamic incidence. C_M varies in a similar shape to the C_L hysteresis loops but it does not vary around the static C_M, suggesting that C_M is dominated by the dynamics of C_L and circulation.

The effect of coupling on the C_L and C_M hysteresis loops was to produce a non-linear relationship on the upstroke and downstroke, this is more pronounced in the C_M loop. The C_D is offset higher than the rigid plot with a smaller change in amplitude in comparison with the rigid case. The C_D offset was discussed in Section 4.3 where it was concluded that this was a spurious feature of the coupling process. There is a small change between aluminium and stainless steel in the coupled case at the maximum and minimum for C_L, C_D and C_M.

Classical linearised inviscid theory for C_L and associated phase angle was used to compare to 2D RANSE results. This theory is only valid at 0° mean incidence and small incidence amplitude. The 2D magnitude and position of the minima matches the prediction using classical linearised inviscid theory. The classical theory predicted slope is approximately the same as the 2D and 3D 0° mean incidence but

the RANSE solution predicts a greater rate of change in C_L/C_{L0} at the minima. The minima for 0° mean incidence is less for the 3D case compared to the 2D case, but they occur at the same reduced frequency value. The slope of the results for the increase in C_L/C_{L0} after the minima is steeper for the 2D case than the 3D case for both 0 and 4° mean incidences. There is no variation in Reynolds number for the 3D results. A minima in C_L/C_{L0} for 0° mean incidence occurs at a reduced frequency of approximately 0.6. For 4° mean incidence there is minimal variation before a reduced frequency of 0.785 with an almost constant relationship between C_L/C_{L0} and reduced frequency. The implication of these conclusions on propeller design is that varying the mean incidence amplitude may have the largest effect on the forces and moments at a reduced frequency lower than one. In the case of a submarine as shown in Chapter 1, the first harmonic has a corresponding reduced frequency of 0.8 and an approximate mean incidence of 4°. Therefore, by reducing the mean incidence amplitude it maybe possible to reduce the maximum C_L. For other wake signatures it could be possible to adjust the response to achieve a lower maximum C_L by using equation 1.15 in combination with adjusting the mean incidence amplitude.

At a reduced frequency greater than one and 4° mean incidence, for the rigid 3D case, the results are dependent on incidence amplitude. The amplitude of maximum C_L increases with increasing incidence but is always lower than the 0° mean incidence. A reduced frequency of one is the point at which a particle in the freestream will travel a distance equal to the length of the root chord in one cycle. Therefore at frequencies higher than one, a particle does not travel a full chord length and will influence the next cycle and affect the trailing edge streamlines. Rigid 3D C_L and C_M predictions show similar behaviour to both the 2D unsteady viscous predictions and classical linearised inviscid theory for cases of 0° mean incidence. In particular, when C_L and C_M are normalised using the static incidence value at the maximum dynamic incidence, they vary linearly with incidence amplitude for all reduced frequencies for a 0° mean incidence.

When coupled at a Reynolds number of 3.36×10^5 and at a reduced frequency greater than one, the non-dimensional deflection becomes non-linear, and C_L and C_D for both mean incidences vary with material. The C_L at a reduced frequency greater than one has a larger maxima magnitude than the rigid results, although the coupled 4° mean incidence remains less than the rigid results for a 0° mean incidence. In the rigid case an increase in incidence amplitude at 4° mean incidence increases the magnitude of normalised C_L, but there was no effect at the 0° mean incidence. This indicates that the bending is increasing the magnitude of C_L as there is an increase in the coupled analysis for both 0° and 4° mean incidence.

When coupled at a Reynolds number of 3.36×10^5 there is little variation in C_M at reduced frequency greater than one for 4° mean incidence. At a reduced frequency greater than one for 4° mean incidence, stainless steel has a lower C_M than the rigid case although, aluminium is the same as the rigid. In the rigid case an increase in incidence amplitude at 4° mean incidence increases the magnitude of normalised C_M, but there was no affect at the 0° mean incidence. Therefore coupling has

reversed the C_M trend between 0 and 4° mean incidence.

The twist is significant at a Reynolds number of 1.12×10^6. The twist phase angle to the incidence amplitude was small for all cases. The C_L, C_D and C_M phase angle to the incidence amplitude increased rapidly as the reduced frequency approached the first mode of natural reduced frequency of stainless steel and aluminium is three and two respectively. The C_L, C_D, deflection and twist all remained constant or reduced. The C_M however marginally increased.

Reduced frequencies of 0.8, 1.6 and 2.4 were identified in chapter 1.4 as being representative of those experienced by a propeller operating in an unsteady flow field caused by wakes from the control surfaces and fairwater of a submarine. The approximate incidence amplitude is 2° with a 4° mean incidence. It was concluded that a 2D analysis will predict a larger change in force from the maxima to minima. A 4° mean offset may reduce the effect of unsteady loading at a reduced frequency less than one but increase it when the reduced frequency is greater than one even though the amplitudes of the forces and moments for 4° mean incidence are less than those for 0° mean incidence. At an approximate reduced frequency less than 0.1 the effect of unsteadiness on C_L and C_M magnitude may not be obvious but will affect C_D and phase angle of all responses. From the dynamic coupled results it was concluded that coupling will affect harmonics that occur at reduced frequencies greater than one.

ANSYS CFX has been demonstrated to be a suitable tool to simulate fluid structure interaction in the case of an oscillating hydrofoil in pure pitch. Solution times for uncoupled simulations are reasonable but once the simulation is coupled the results take approximately three to four times longer, therefore the jump to fully coupled analysis should only be taken when absolutely necessary for the parameters described above. A two-way fluid structure analysis is needed to assess the maximum forces and dimensionless bending for aluminium and stainless steel foils when oscillating sinusoidally in pitch at a reduced frequency greater than one.

Chapter 7

Further Work

This study has provided an insight into the effect of isotropic material with varying mass and stiffness ratios on the forces acting on a hydrofoil undergoing sinusoidally varying pitch oscillation. This study has also provided a solid foundation for the numerical investigation into the physics of fluid structure phenomena. The direct extension of this thesis would be to investigate the effect of incidence amplitude on the coupled case and analysing results closer to the reduced natural frequency. There are several variations that could be done; for instance testing of a material with a different fundamental frequency in air, or a composite material. This would enable an investigation into composite lay-up and hone in on the possibility of lowering the reduced frequency at which material property has an effect. Further investigation into the accuracy of physics of wall shear and the viscous component would enable better drag and possibly twist prediction. A sensitivity analysis of the effect of increasing or decreasing viscosity would also be interesting.

During this analysis it was noticed that the minima in the hysteresis loop produced a greater twist variation and minimal deflection. Analyses of the minima when there is minimal deflection would be interesting as this would show if bending increases the structural rigidity, thus making the force required to twist the foil greater. The amplitude of force oscillation may also be of interest in the prediction of acoustics for a potential hydroelastically tailored propeller.

An experimental data set for the hydrofoils used in this study would provide invaluable validation and complement the current analysis. As this is a foundation study there is components during the unsteady oscillation such as: the behaviour of the boundary layer; movement of stagnation point pressure; and shedding mechanisms that could be further investigated either numerically or experimentally.

References

[1] I.H. Abbott and A.E. von Doenhoff. *Theory of Wing Sections*. Dover Publications, Inc., New York, dover edition edition, 1959.

[2] P. Andersen, J. J. Kappel, and E. Spangenberg. Aspects of propeller developments for a submarine. In *International Symposium on Marine Propulsors SMP09*, volume First, Trondheim, Norway, June 2009, 2009.

[3] M. A Ashraf, J.C.S. Lai, and J. Young. Numerical analysis of flapping wing aerodynamics. In *Australasian Fluid mechanics*, 2007.

[4] P. Atkinson and E.J. Glover. Propeller hydroelastic effects. In *Propellers 1988 Symposium*, pages 21.1–21.10, Virginia Beach, Va., 1988. SNAME.

[5] J. Barlow, W. Rae, and A. Pope. *Low-speed Wind tunnel testing*. Wiley-interscience Publications, third edition, 1999.

[6] A. Belgrano and A. MacFarlan. Composite engineering of sailing yacht structures. In *Sailing Yacht Design Practice*, chapter 11. Addison Wesley Longman Limited, 1998. Ed. Claughton Wellicome and Shenoi.

[7] E. Berton, M. Nsi Mba, D. Favier, and C. Maresca. Application of laser doppler velocimetry to unsteady flow around rotating blades. In R.J. Adrian, editor, *10th International Symposium on Applications of Laser Techniques to Fluid Mechanics*, Lisboa, Portugal, 2000.

[8] E. Berton, D. Favier, M. Nsi Mba, C. Maresca, and C. Allain. Embedded LDV measurement methods applied to unsteady flow investigation. *Experiments in Fluids*, 30(1):102–110, 2001.

[9] E. Berton, D. Favier, C. Maresca, and A. Benyahia. Flow field visualizations around oscillating airfoils. In *11th International Symposium on Applications of Laser Techniques to Fluid Mechanics*, Lisbon, Portugal, 2002. printed.

[10] R. L. Bisplinghoff, A. Holt, and R. L. Halfman. *Aeroelasticity*. Addison-Wesley Publishing Company, Inc., Cambridge, Mass., 1955.

[11] R.D. Blevins. *Flow-Induced Vibration*. Krieger Publishing Company, Mamabar, Florida, second edition, 2001.

[12] Robert D. Blevins. *Structural vibrations in a fluid - Chapter 14*. Van Nostrand Reinhold Co., New York, 1979.

[13] R.J. Boswell and M.L. Miller. Unsteady propeller loading-measurement, correlation with theory, and parametric study. Technical Report Report 2625, David W Taylor Naval Ship Research and Development Center, 1968.

[14] P.A. Brandner. Blade element momentum theory for propellers, 2010. Lecture Notes.

[15] P.A. Brandner, Y. Lecoffre, and G.J. Walker. Development of an australian national facility for cavitation research. In *Sixth International Symposium on Cavitation - CAV2006*, MARIN, Wageningen, The Netherlands, 2006.

[16] P.A. Brandner, G.J. Walker, P.N. Niekamp, and B. Anderson. An experimental investigation of cloud cavitation about a sphere. *Journal of Fluid Mechanics*, 656:147–176, 2010.

[17] J. P. Breslin and P. Andersen. *Hydrodynamics of Ship Propellers*. Cambridge Ocean Technology Series 3. Cambridge University Press, Cambridge, 1994.

[18] J.P. Breslin. Review and extension of theory for near-field propeller-induced vibratory effects. In Bennett L. Silverstein, editor, *4th Symposium on Naval Hydrodynamics*, pages 603–640, Washington, D.C., U.S.A., 1962. Conference topics: Propulsion; Hydroelasiticity.

[19] J. E. Brooks. Vibrations of a marine propeller operating in a non-uniform inflow. Technical Report DTNSRDC-80/056, David W Taylor Naval Ship Research and Development Center, April 1980.

[20] J.S. Carlton. The wake field. In *Marine Propellers and Propulsion*, pages 59–81. Butterworth-Heinemann, Oxford, 1994.

[21] L. W. Carr, K. W. McAlister, and W. J. McCroskey. Analysis of the development of dynamic stall based on oscillating airfoil experiments. Technical Report A-6674; NASA-TN-D-8382, NACA, 1977.

[22] L. W. Carr, W. J. McCroskey, K. W. McAlister, S. L. Pucci, and O. Lambert. An experimental study of dynamic stall on advanced airfoil sections. volume 3: Hot-wire and hot film measurements. Technical Report TM-84245, NASA, 1982.

[23] T. Cebeci, M. Platzer, H. M. Chen, and J.P. Chang, K.C.and Shao. *Analysis of Low-Speed Unsteady Airfoil Flows*. Springer, 2005.

[24] B. Y. H. Chen, S. K. Neely, T. J. Michael, S. Gowing, R. P. Szwerc, D. Buchler, and R. Schult. Design, fabrication and testing of pitch-adapting (flexible) composite propellers. *Society of Naval Architects and Marine Engineers Propellers/Shafting 2006 Symposium*, 2006.

[25] E. Dowell, R. Clark, D. Cox, H. Curtiss, J. Edwards, K. Hall, D. Peters, R. Scanlan, E. Simiu, F. Sisto, and T. Strganax. *A Modern Course in Aeroelasticity*. Kluwer Academic Publishers, Dordrecht/Boston/London, fourth edition, 2004.

[26] M. Drela and H. Youngren. *XFOIL 6.9 User Primer*. MIT Aero and Astro and Aerocraft Inc., November 2001.

[27] A. Ducoin, F.s Deniset, T. Damay, J.-A. Astolfi, and C. Laine. Numerical investigation of deformable hydrofoils in steady flows. In *ASME Conference Proceedings*, page 8, 2006. URL `http://link.aip.org/link/abstract/ASMECP/v2006/i47551/p157/s1`.

[28] A. Ducoin, J.A. Astolfi, F. Deniset, J.F. Sigrist, and V. Soyer. An experimental and numerical investigation of flow over a hydrofoil in transient regimes based on wall-pressure analysis. In *ASME Conference Proceedings*, page 9, 2008. URL `http://link.aip.org/link/abstract/ASMECP/v2008/i48272/p239/s1`.

[29] A. Ducoin, J. A. Astolfi, F. Deniset, and J.F. Sigrist. Computational and experimental investigation of flow over a transient pitching hydrofoil. *European Journal of Mechanics - B/Fluids*, 28(6): 12, 2009. URL `http://www.sciencedirect.com/science/article/B6VKX-4WH8C52-1/2/9e854456d499bb201342826ef2f88b39`.

[30] A. Ducoin, J.A. Astolfi, F. Deniset, and J.F. Sigrist. Fluid structure interaction analysis on a transient pitching hydrofoil. In *ASME Conference Proceedings*, Prague, Czech, Republic, 2009.

[31] A. Ducoin, J.A. Astolfi, F. Deniset, and J.F Sigrist. An experimental and numerical study of the hydroelastic behaviour of an hydrofoil in transient pitching motion. In *Proceedings of SMP09, First International Symposium on Marine Propulsion*, Trondheim, Norway, 2009.

[32] A. Ducoin, F. Deniset, J.A. Astolfi, and J.F. Sigrist. Numerical and experimental investigation of hydrodynamic characteristics or deformable hydrofoils. *Journal of Ship Research*, 53(4):214–226, 2009.

[33] J. A. Ekaterinaris. Numerical investigation of dynamic stall of an oscillating wing. *AIAA Journal*, 33(10):5, 1995.

[34] J. A. Ekaterinaris and F. R. Menter. Computation of oscillating airfoil flows with one and two equation turbulence models. *AIAA Journal*, 32(12):6, 1994.

[35] L. E. Ericsson and J. P. Reding. Unsteady airfoil stall and stall flutter. Technical Report LMSC Report No. A-6j-71-1, NASA, 1971.

[36] ANSYS Europe. *ANSYS CFX release Notes V11.0*. ANSYS Europe., 2006.

[37] ANSYS Europe. *ANSYS CFX-Solver Modelling Guide*. ANSYS Europe., 2009.

[38] ANSYS Europe. *ANSYS CFX-Post User's Guide*. ANSYS Europe., 2009.

[39] H. Glauert. The force and moment on an oscillating aerofoil. Technical Report Reports and Memoranda No.1245, British A.R.C., 1929.

[40] S. Gowing, P. Coffin, and C.M. Dai. Hydrofoil cavitation improvements with elastically couples composite materials. In *Proceedings of 25th American Towing Tank Conference*, Iowa City, IA, USA, 1998.

[41] N. Gregory and C.L. O'Reilly. Low-speed aerodynamic characteristics of naca 0012 aerofoil section, including effects of upper-surface roughness simulating hoar frost. Technical Report Reports and memoranda 3726, Ministry of Defence Aeronautical Research Council, 1973.

[42] N.C. Groves, C.W. Jiang, and Y.N. Liu. Turbulence at the stern of an axisymmetric model with and without removable appendages. Technical report, David Taylor Research center, 1992.

[43] D. Hart. Boundary layer formation on an oscillating hydrofoil. In *20th Symposium on Naval Hydrodynamics*, pages 187–197, Santa Barbara, California, 1994.

[44] S. Heathcote and I. Gursul. Jet switching phenomenon for a periodically plunging airfoil. *Physics of Fluids*, 19(2):027104, 2007.

[45] S. Heathcote, D. Martin, and I. Gursul. Flexible flapping airfoil propulsion at zero freestream velocity. *AIAA Journal*, 42(11), 2004.

[46] S. Heathcote, D. Martin, and I. Gursul. Flexible flapping airfoil propulsion at zero freestream velocity. *AIAA Journal*, 42(11), 2004.

[47] S. Heathcote, Z. Wang, and I. Gursul. Effect of spanwise flexibility on flapping wing propulsion. *Journal of Fluids and Structures*, 24(2), 2008.

[48] A.O. Hiliare and F. O. Carta. Analysis of unswept and swept wing chordwise pressure data from an oscillating naca 0012 airfoil experiment. Technical Report NASA-CR-3567, NASA, 1983.

[49] D. H. Hodges and G.A. Pierce. *Introdutction to Structural Dynamics and Aeroelasticity*. Kluwer Academic Publishers, Dordrecht/Boston/London, fourth edition, 2004.

[50] S Hoerner and H. Borst. *FLUID-DYNAMIC LIFT Information on Lift and its Derivatives, in Air and Water*. Hoerner Fluid Dynamics, Vancouver, WA, second edition, 1985.

[51] F.S. Hover, . Haugsdal, and M.S. Triantafyllou. Effect of angle of attack profiles in flapping foil propulsion. *Journal of Fluids and Structures*, 19:37–47, 2004. URL `http://web.mit.edu/towtank/www/Papers/angle_attack_profiles_ffp.pdf`.

[52] T. Huang, H.L. Liu, N. Groves, T. Forlini, J. Blanton, and S. Gowing. Measurements of flows over an axisymmetric body with various appendages in wind tunnel: the darpa suboff experimental program. In *19th International Symposium on Naval Hydrodynamics*, pages 321–346, Korea, 1993. National Academy Press, Washington D.C.

[53] S.R. Hutchison, P.A. Brandner, J.R. Binns, A.D. Henderson, and G.J. Walker. Development of a cfd model for an oscillating hydrofoil. In *Australasian Fluid Mechanics Conference*, Auckland, New Zealand, 2011. Melbourne Uni. URL `http://www.mech.unimelb.edu.au/people/staffresearch/AFMS%20site/17/253_Paper.pdf`.

[54] ANSYS Inc. *ANSYS Element reference V12.0*. ANSYS Inc., 2009.

[55] ANSYS Inc. *ANSYS Structural analyses V12.0*. ANSYS Inc., 2009.

[56] ITTC. The propulsion committee, final report and recommendations to the 23rd ittc. In *23rd International Towing Tank Conference*, Venice, 2002.

[57] ITTC. The propulsion committee, final report and recommendations to the 26th ittc. In *26th International Towing Tank Conference*, Brazil, 2011.

[58] K. D. Jones and M. F. Platzer. Design and development considerations for biologically inspired flappingwing micro air vehicles. *Experiments in Fluids*, 46(5), 2009. URL `http://www.scopus.com/inward/record.url?eid=2s2.067349092102&partnerID=40`.

[59] K.D. Jones and M.F. Platzer. Numerical computation of flapping-wing propulsion and power extraction. In *35th Aerospace Sciences Meeting & Exhibit*, Reno NV, 1997.

[60] E.J. Jumper, S.J. Schreck, and R.L. Dimmick. Lift-curve characteristics for an airfoil pitching at constant rate. *Journal of Aircraft*, 24(10):680–687, 1987.

[61] J. E. Kerwin. Marine propellers. *Annual Review of Fluid Mechanics*, 18: 367–403, 1986.

[62] J. E. Kerwin and C.-S. Lee. Prediction of steady and unsteady marine propeller performance by numerical lifting-surface theory. *SNAME Transactions*, 86:218–253, 1978.

[63] S. Kinnas and N. Fine. A nonlinear boundary element method for the analysis of unsteady propeller sheet cavitation. In *19th International Symposium on Naval Hydrodynamics*, pages 717–737, Korea, 1993. National Academy Press, Washington D.C.

[64] S.A. Kinnas and N.E. Fine. Theoretical prediction of midchord and face unsteady propeller sheet cavitation. In *5th International Conference on Numerical Ship Hydrodynamics*, pages 685–700, Hiroshima, Japan, 1989.

[65] M. M. Koochesfahani. Vortical patterns in the wake of an oscillating airfoil. *AIAA Journal*, 27(9):1200–1205, 1989.

[66] leap Australia. *Introduction to Fluid-structure Interaction.* ANSYS inc., 2007.

[67] T. Lee and P. Gerontakos. Investigation of flow over an oscillating airfoil. *Journal of Fluid Mechanics*, 512, 2004. URL `http://proquest.umi.com/pqdweb?did=1399109001&Fmt=7&clientId=20931&RQT=309&VName=PQD`.

[68] J.G. Leishman. *Principals of Helicopter Aerodynamics.* Cambride university Press, first paperback edition, 2002.

[69] H.-J. Lin and J.-J. Lin. Nonlinear hydroelastic behavior of propellers using a finite-element method and lifting surface theory. *Journal of Marine Science and Technology*, 1:114–124, 1996.

[70] Z. Liu and Yin L. Young. Utiliztation of deformation coupling in self-twisting composite propellers. In *Internation Conference on Composite Materials*, number 16th in -MMMM, page 7, 2007.

[71] K. W. McAlister, L. W. Carr, and J. W. McCroskey. Dynamic stall experiments on the naca 0012 airfoil. Technical Report NACA TP-1100, NACA, 1978.

[72] K. W. McAlister, S. L. Pucci, W. J. McCroskey, and L. W. Carr. An experimental study of dynamic stall on advanced airfoil section. volume 2: Pressure and force data. Technical Report A-8925; NAS 1.15:84245-VOL-2; NASA-TM-84245-VOL-2; USAAVRADCOM-TR-82-A-8-VOL-2, NACA, 1982.

[73] W. J. McCroskey, K. W. McAlister, L. W. Carr, and S. L. Pucci. An experimental study of dynamic stall on advanced airfoil sections. volume 1: Summary of the experiment. Technical Memorandum 84245, NASA, 1982.

[74] W.J. McCroskey. Inviscid flowfield of an unsteady airfoil. *AIAA Journal*, 11 (8):1130–1137, 1973.

[75] W.J. McCroskey. Unsteady aarfoils. *Annual Review of Fluid Mechanics*, 14: 285–311, 1982.

[76] W.J. McCroskey and S.L. Pucci. Viscous-inviscid interaction on oscillating airfoils in subsonic flow. *AIAA Journal*, 20(2):167–174, 1982. AIAA 81-0051R.

[77] C. Münch, Philippe Ausoni, M. Farhat, and F. Avellan. 2d oscillating hydrofoil. In *IAHR International Meeting of the Workgroup on Cavitation and Dynamic Problems in Hydraulic Machinery and Systems*, 2007.

[78] N.L. Milcachy, B.G. Prusty, and C.P. Gardiner. Flexible composite hydrofoils and propeller blades. *Pacific*, 2010.

[79] J.H. Milgram. Effects of mast on aerodynamics of sail sections. *Marine Technology*, pages 35–42, January 1978.

[80] A.P. Mouritz, E. Gellert, P. Burchill, and K. Challis. Review of advanced composite structures for naval ships and submarines. *Composite Structures*, 53:21–41, 2001.

[81] C. Münch, O. Braun, J.L. Kueny, and F. Avellan. Numerical investigations of fluid structure coupling: Oscillating hydrofoil. In *International Symposium on Transport Phenomena and Dynamics of Rotating Machinery*, number ISROMAC12-2008-20xxx* in 12th, 2008. URL `http://infoscience.epfl.ch/record/115104/files/ISROMAC_2008.pdf`.

[82] C. Münch, P. Ausoni, O. Braun, M. Farhat, and F. Avellan. Fluid structure coupling for an oscillating hydrofoil. *Journal of Fluids and Structures*, In Press, Corrected Proof(-), 2010. URL `http://www.sciencedirect.com/science/article/B6WJG-50TYH0B-1/2/c98df5e8bae30b57b5a4890ca57695f5`.

[83] R. A. Piziali. An experimental investigation of 2d and 3d oscillating wing aerodynamics for a range of angle of attack including stall. *NASA Technical Memorandum 4623*, 1993. URL `http://ntrs.nasa.gov/archive/nasa/casi.ntrs.nasa.gov/19950012704_1995112704.pdf`.

[84] K.E. Schoenherr. Propulsion - session 2. In Bennett L. Silverstein, editor, *4th Symposium on Naval Hydrodynamics*, pages 125–236, Washington, D.C., U.S.A., 1962.

[85] T. Searle, J. Chudley, D. Short, and C. Hodge. The composite advantage. In *Propellers/Shafting '94 Symposium*, pages 22.1–22.8, Virginia Beach, Vaginia, 1994. SNAME.

[86] W.R. Sears. Some aspects of non-stationary airfoil theory and its practicle application. *AIAA Journal Special Supplement: Centennial of Powered Flight*, 8(3):104–108, 1941. URL `http://pdf.aiaa.org/downloads/TOCPDFs/03_17-21.pdf`.

[87] M. Shearer. *Simulation and evaluation of marine propeller crashback through computational fluid dynamics*. U.S. Naval Academy, United states of America, 2007.

[88] A. Spentzos, G. Barakos, K. Badcock, B. Richards, P. Wernert, S. Schreck, and M. Raffel. CFD investigation of 2d and 3d dynamic stall. In *AHS International 4th Decennial Specialists' Conference on Aeromechanics*, 2004.

[89] A. Spentzos, G. Barakos, K. Badcock, B. Richards, P. Wernert, S. Schreck, and M. Raffel. Investigation of three dimensional dynamic stall using computational fluid dynamics. *AIAA Journal*, 43(5):11, 2005.

[90] A. Spentzos, G. N. Barakos, K. J. Badcock, B. E. Richards, F. N. Coton, R. A. M. Galbraith, E. Berton, and D. Favier. Computational fluid dynamics study of three dimensional dynamic stall of various planform shapes. *Journal of Aircraft*, 44(4):10, 2007.

[91] J.A. Szantyr. A new method for the analysis of propeller cavitation and hull surface pressure. In *Trans RINA 127:153-167.*, 1984.

[92] D. W. Taylor. *The Speed and Power of Ships: a manual of marine propulsion.* United States Government printing Office: Washington, US Washington, second edition, 1943.

[93] T. Theodorsen. On the theory of wing sections with particular reference to the lift distribution. Report 383, NACA, 1930.

[94] T. Theodorsen. General theory of aerodynamic instability and the mechanism of flutter. Report 496, NACA, 1935.

[95] W.T. Thomas. *Theory of vibration with applications*, volume 3. Allen & Unwin, Great britain, 1988.

[96] M. S. Triantafyllou, A. H. Techet, and F. S. Hover. Review of experimental work in biomimetic foils. *IEEE Journal of Oceanic Engineering*, 29(3):585–594, 2004.

[97] Cameron Tropea, Alexander L. Yarin, and John F. Foss, editors. *Springer Handbook of Experimental Fluid Mechanics*. Springer Verlag, 2007.

[98] K. K. Y. Tsang, R. M. C. So, R. C. K. Leung, and X. Q. Wang. Dynamic stall behavior from unsteady force measurements. *Journal of Fluids and Structures*, 24(1), 2008.

[99] W.J. Usab, J. Hardin, and A.J. Bilanin. Bioinspired delayed stall propulsor. *IEEE Journal of Oceanic Engineering*, 29(3):10, 2004.

[100] Th. Von Karman and W.R. Sears. Airfoil theory for non-uniform motion. *Journal of the Aeronautical Sciences*, 5(10):379–390, 1938.

[101] H. Wagner. Über die Entstehung des dynamischen Auftriebes von Tragflügeln. english [On the origin of the dynamics over wings.]. *Z. f. angew. Math.*, 5:17–35, 1925.

[102] J. Wellicome. Aerodynamics of sails. In *Sailing Yacht Design Theory*, chapter 4. Addison Wesley Longman Limited, 1998. Ed. Claughton Wellicome and Shenoi.

[103] F.M. White. *Fluid Mechanics*. McGraw - Hill Book, UK, fourth edition, 1999.

[104] Y. L. Young. A simple hydroelastic model for surface-piercing propellers. In *25th Symposium on Naval Hydrodynamics*, volume 4, pages 130–146, St. John's, NL, Canada, 2004. National Academy Press, Washington D.C.

[105] Y. L. Young. Hydroelastic response of composite marine propellers. *The Society of Naval Architects and marine engineers Propellers/Shafting 2006 Symposium*, 2006.

[106] Y. L. Young. Hydroelastic behaviour of flexable composite propellers in wake inflow. In *International confernce on composite materials*, 2007.

[107] Y. L. Young and S. A. Kinnas. Prediction of unsteady performance of surface-piercing propellers. *Propellers/Shafting 2000 Symposium*, pages 7.1–7.9, 2000.

[108] Y. L. Young and S. A. Kinnas. Numerical modeling of supercavitating and surface-piercing propeller flows. In Christopher E. Brennen, R.E.A. Arndt, and S.L. Ceccio, editors, *Fourth International Symposium on Cavitation*, California Institute of Technology, 2001.

[109] Y. L. Young and S. A. Kinnas. Fluid and structural modeling of cavitating propeller flows. In *Fifth International Symposium on Cavitation - Cav2003*, pages OS–7–012, Osaka, Japan, 2003.

[110] Y. L. Young and S. A. Kinnas. Numerical analysis of surface-piercing propellers. In *Propellers/Shafting 2003*, Virgina Beach, VA, 2003.

[111] Y. L. Young and S. A. Kinnas. Numerical modeling of supercavitating propeller flows. *Journal of Ship Research*, 47(1), 2003.

[112] Y. L. Young and S.A. Kinnas. Analysis of supercavitating and surface-piercing propeller flows via BEM. *Computational Mechanics*, 32(4-6):269–280, 2003.

[113] Yin L. Young and S. A. Kinnas. Performance prediction of surface-piercing propellers. *Journal of Ship Research*, 48(4):288–304, 2004.

[114] Y.L. Young. Hydroelastic behaviour of flexible composite propellers in wake inflow. In *International conference on composite materials*, number 16th, 2007.

[115] Y.L. Young. Time-dependent hydroelastic analysis of cavitating propulsors. *Journal of Fluids and Structures*, 23:269–295, 2007.

[116] Y.L. Young. Fluid-structure interaction analysis of flexable composite marine propellers. *Journal of Fluids and Structures*, 24:799–818, 2008.

[117] Y.L. Young, T.J. Micheal, M. Seaver, and S.T. Trickey. Numerical and experimental investigations of composite marine propellers. *Symposium on Naval Hydrodynamics*, 26, 2006.

[118] Y.L. Young, Z. Liu, and M. R. Motley. Influence of material anisotropy on the hydroelastic behaviors of composite marine propellers. In *Synmposium on Naval Hydrodynamics*, 27, Korea, 2008.

[119] Q. Zhu and Z. Peng. Mode coupling and flow energy harvesting by a flapping foil. *Physics of Fluids*, 21(033601), 2009.

Appendix A

Two Dimensional Dynamic Validation

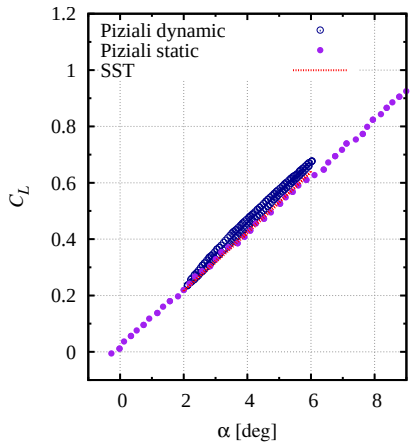

(a) $k = 0.038$ $\Delta\alpha$=2°

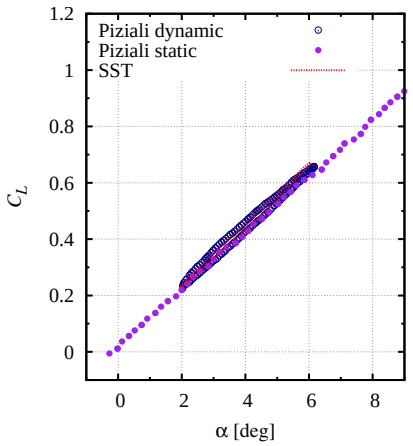

(b) $k = 0.093$ $\Delta\alpha$=2°

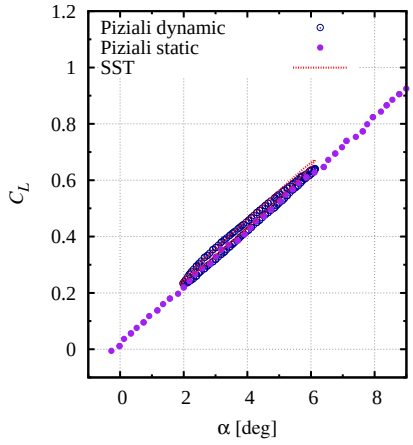

(c) $k = 0.131$ $\Delta\alpha$=2°

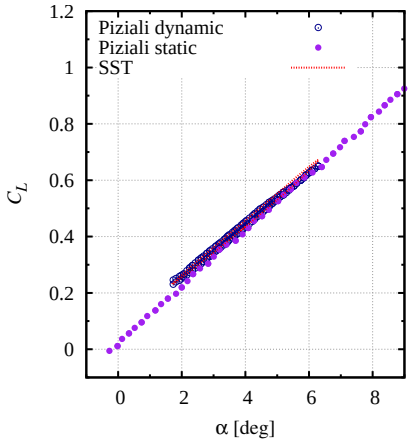

(d) $k = 0.188$ $\Delta\alpha$=2°

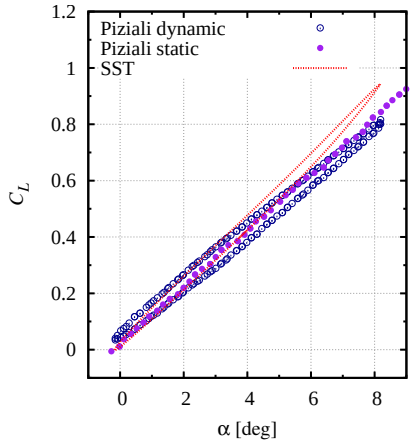

(e) $k = 0.093$ $\Delta\alpha$=4°

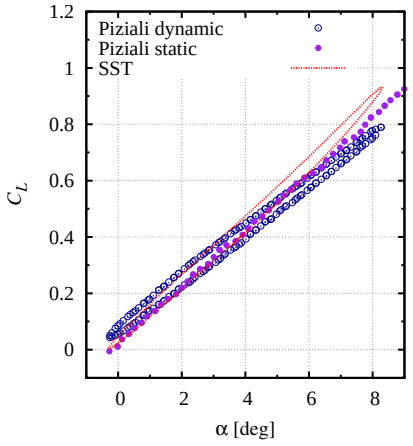

(f) $k = 0.131$ $\Delta\alpha$=4°

Figure A.1: Comparison of computed and experimental C_L for 4° mean incidence for a NACA 0015

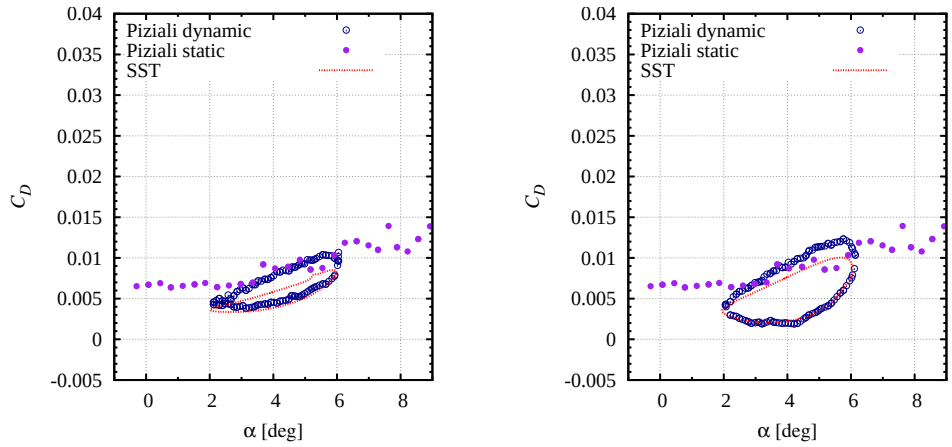

(a) $k = 0.038$ $\Delta\alpha$=2°

(b) $k = 0.093$ $\Delta\alpha$=2°

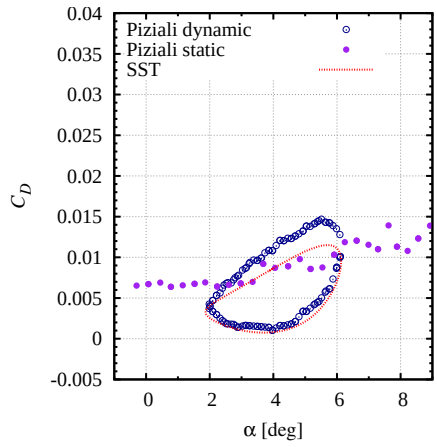

(c) $k = 0.131$ $\Delta\alpha$=2°

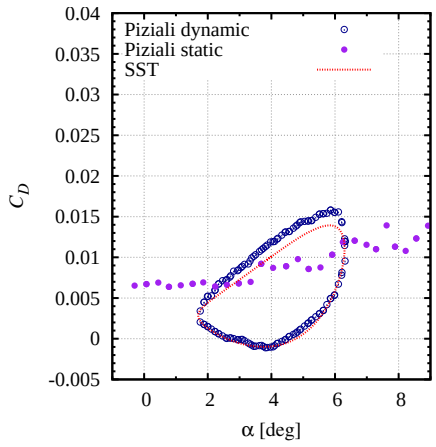

(d) $k = 0.188$ $\Delta\alpha$=2°

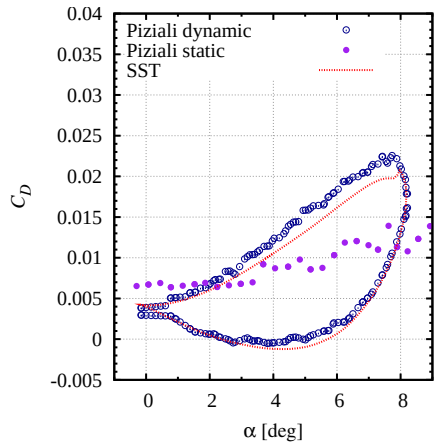

(e) $k = 0.093$ $\Delta\alpha$=4°

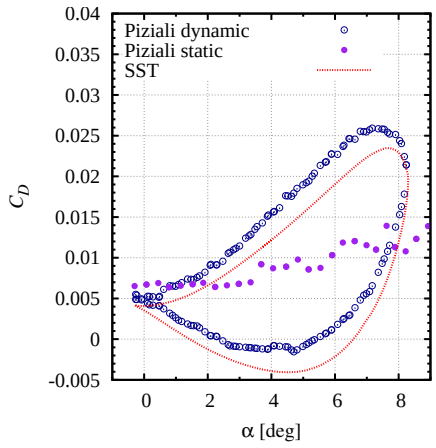

(f) $k = 0.131$ $\Delta\alpha$=4°

Figure A.2: Comparison of computed and experimental C_D for 4° mean incidence for a NACA 0015

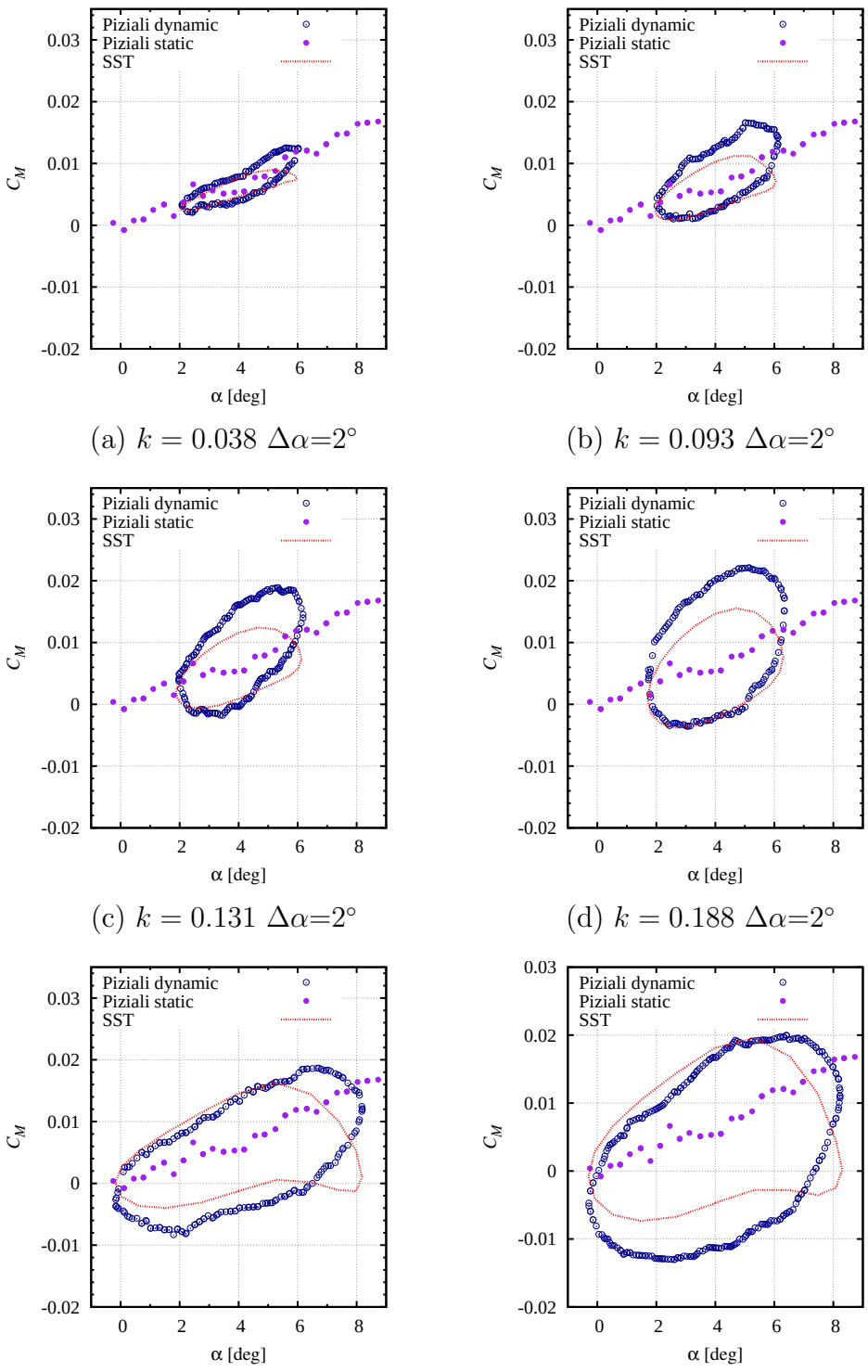

(a) $k = 0.038$ $\Delta\alpha$=2° (b) $k = 0.093$ $\Delta\alpha$=2°

(c) $k = 0.131$ $\Delta\alpha$=2° (d) $k = 0.188$ $\Delta\alpha$=2°

(e) $k = 0.093$ $\Delta\alpha$=4° (f) $k = 0.131$ $\Delta\alpha$=4°

Figure A.3: Comparison of computed and experimental C_M for 4° mean incidence for a NACA 0015

Appendix B

Three Dimensional Summary with points

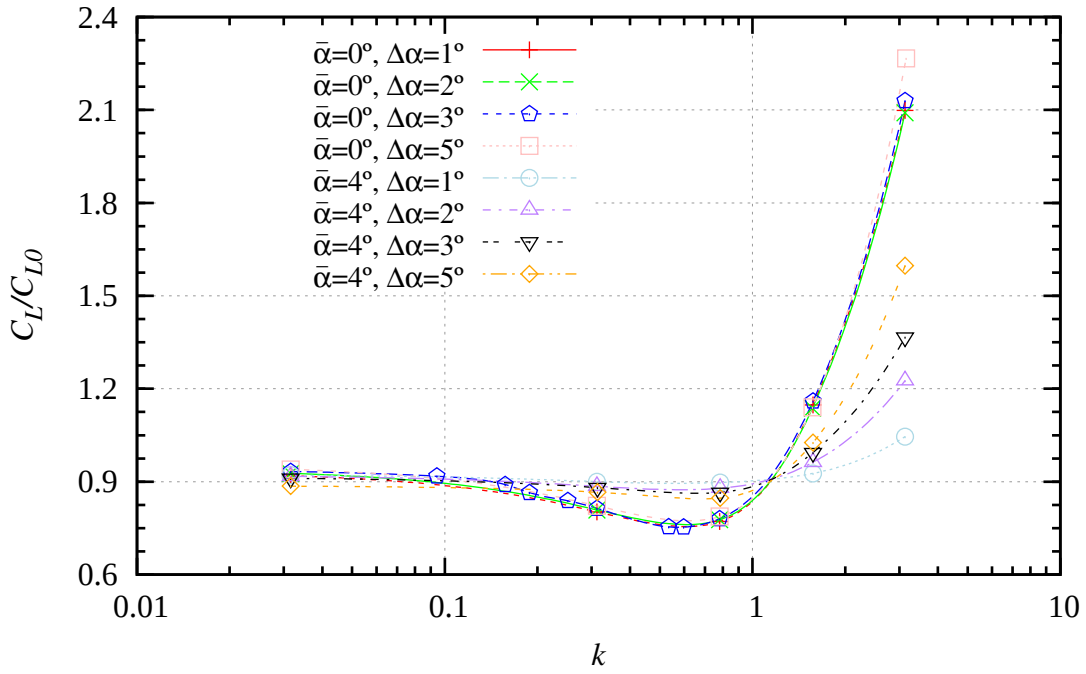

Figure B.1: 3D comparison of computed normalised maximum C_L for varying reduced frequency (k) at a Reynolds number of 3.36×10^5 for a mean incidence ($\bar{\alpha}$) of 0 and 4° at incidence amplitudes ($\Delta\alpha$) of 1, 2, 3, and 5°.

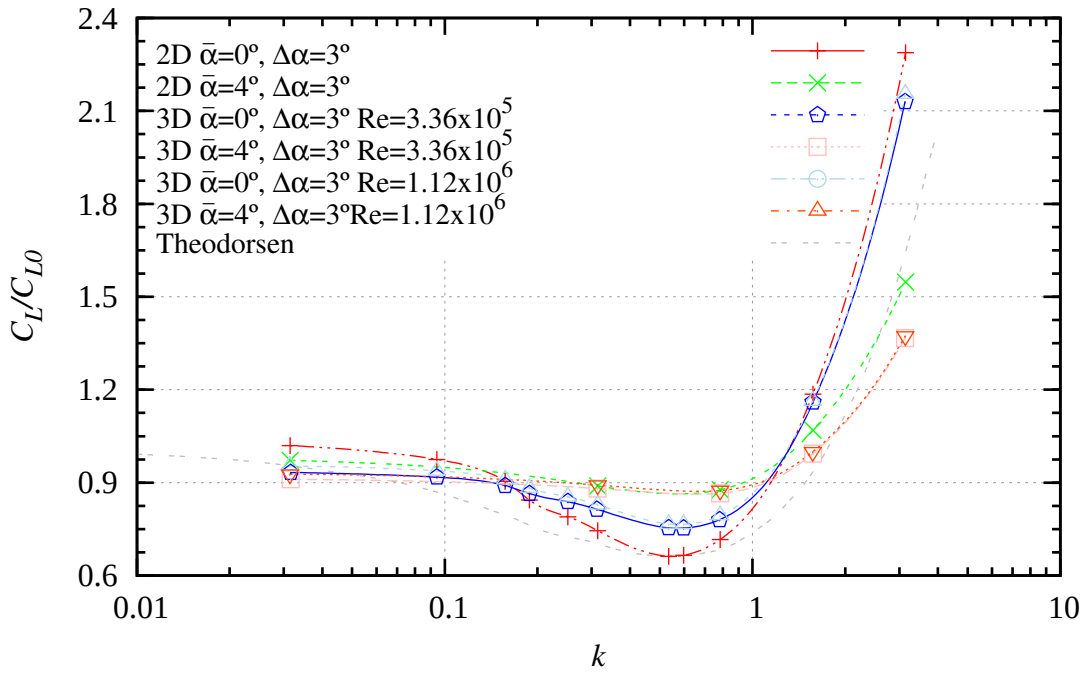

Figure B.2: 2D and 3D comparison of computed normalised maximum C_L at varying reduced frequency (k) at a incidence amplitude ($\Delta\alpha$) of 3° for a mean incidence ($\bar{\alpha}$) of 0 and 4° and Reynolds number (Re) of 3.36×10^5 and 1.12×10^6.

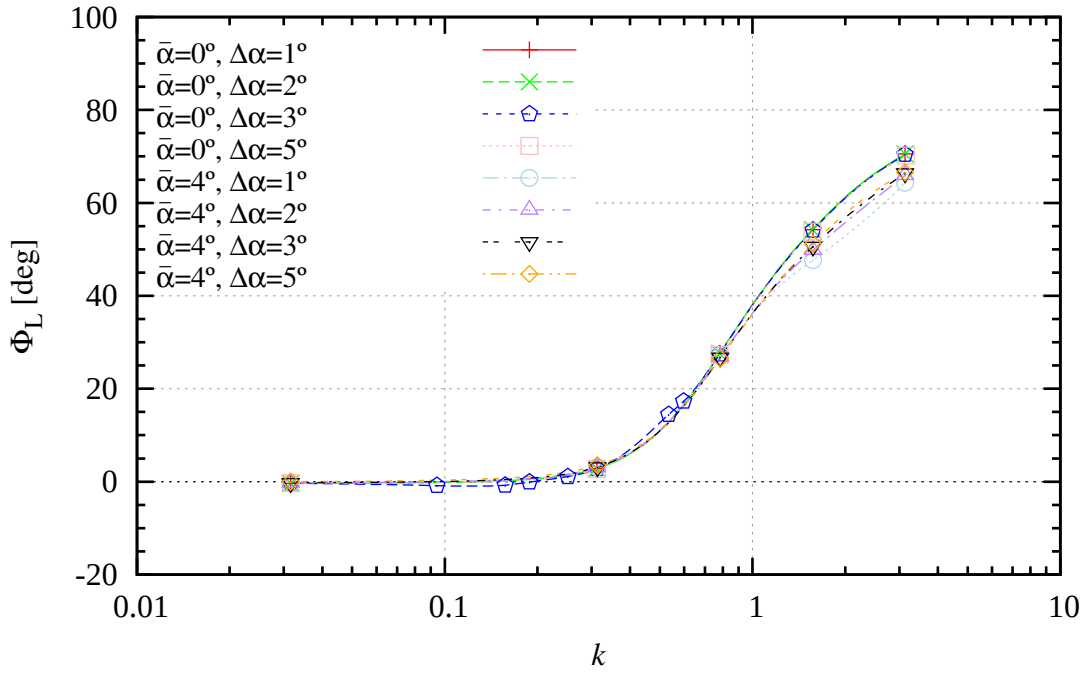

Figure B.3: 3D comparison of computed lift phase angle (Φ_L) for varying reduced frequency (k) at a Reynolds number of 3.36×10^5 for a mean incidence ($\bar{\alpha}$) of 0 and 4° at incidence amplitudes ($\Delta\alpha$) of 1, 2, 3, and 5°.

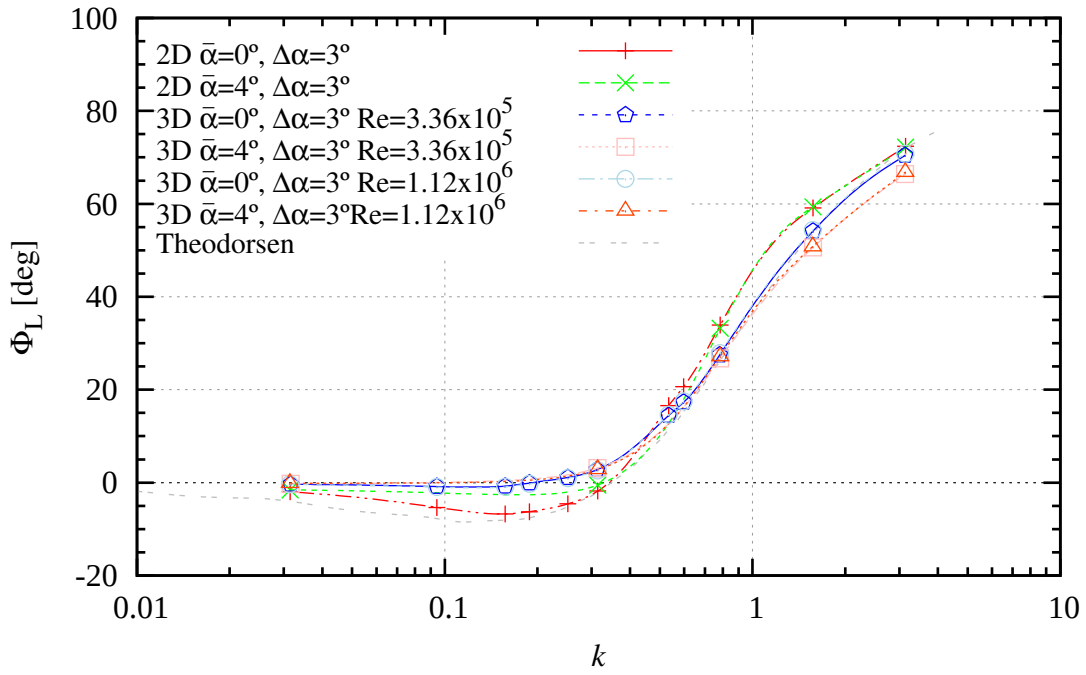

Figure B.4: 2D and 3D comparison of computed maximum lift phase angle (Φ_L) at varying reduced frequency (k) at a incidence amplitude ($\Delta\alpha$) of 3° for a mean incidence ($\bar{\alpha}$) of 0 and 4° and Reynolds number (Re) of 3.36×10^5 and 1.12×10^6.

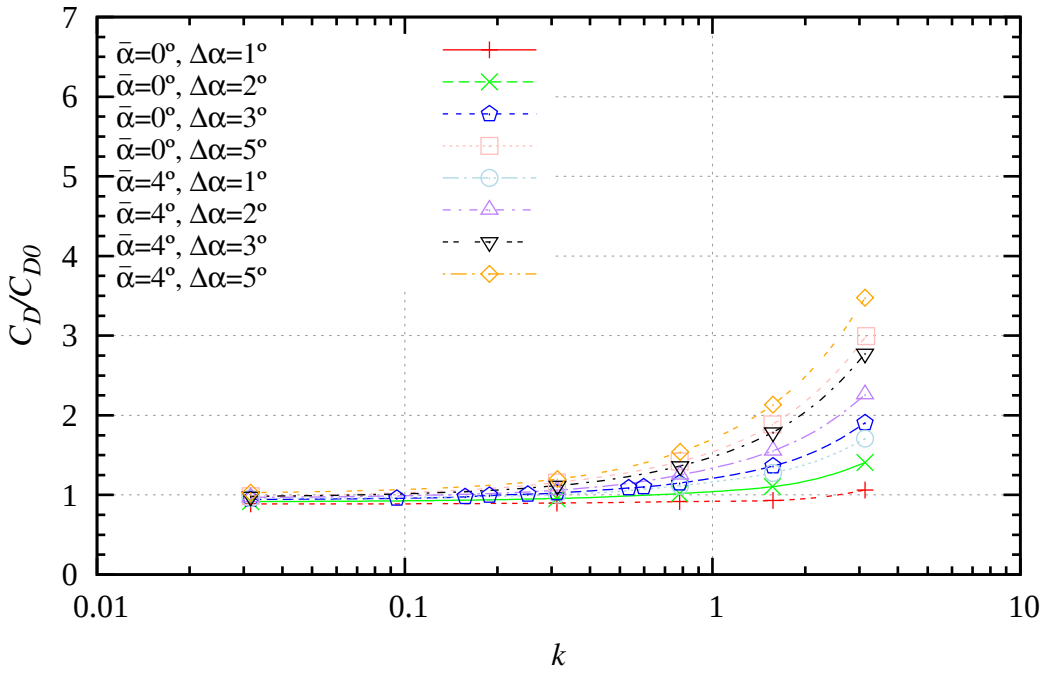

Figure B.5: 3D comparison of computed normalised maximum C_D for varying reduced frequency (k) at a Reynolds number of 3.36×10^5 for a mean incidence ($\bar{\alpha}$) of 0 and 4° at incidence amplitudes ($\Delta\alpha$) of 1, 2, 3, and 5°.

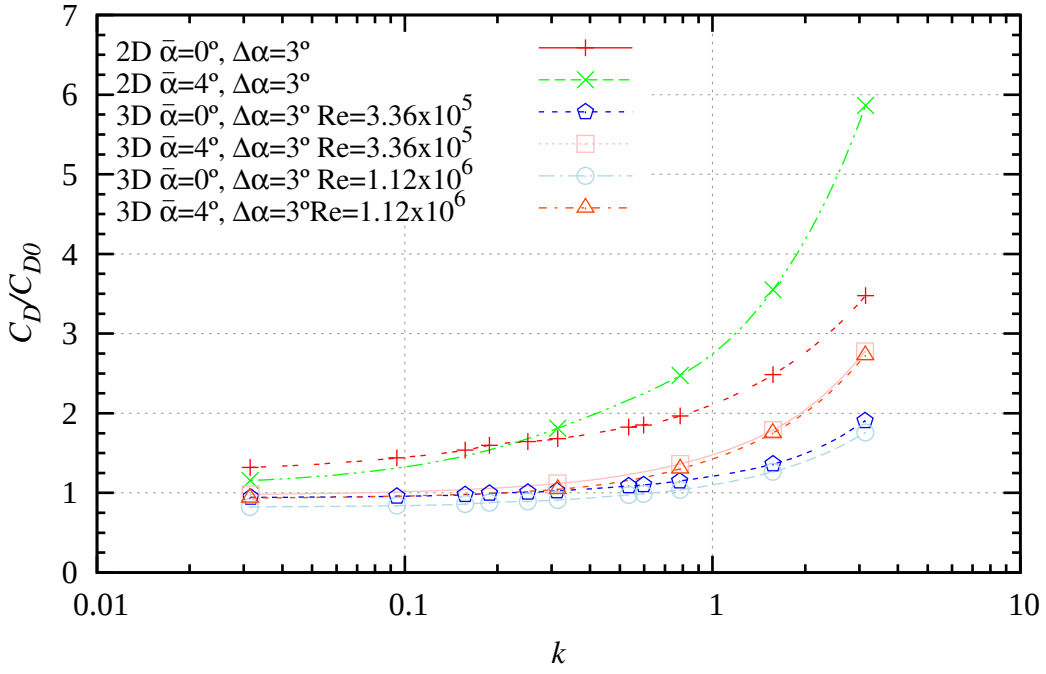

Figure B.6: 2D and 3D comparison of computed normalised maximum C_D at varying reduced frequency (k) at a incidence amplitude ($\Delta\alpha$) of 3° for a mean incidence ($\bar{\alpha}$) of 0 and 4° and Reynolds number (Re) of 3.36×10^5 and 1.12×10^6

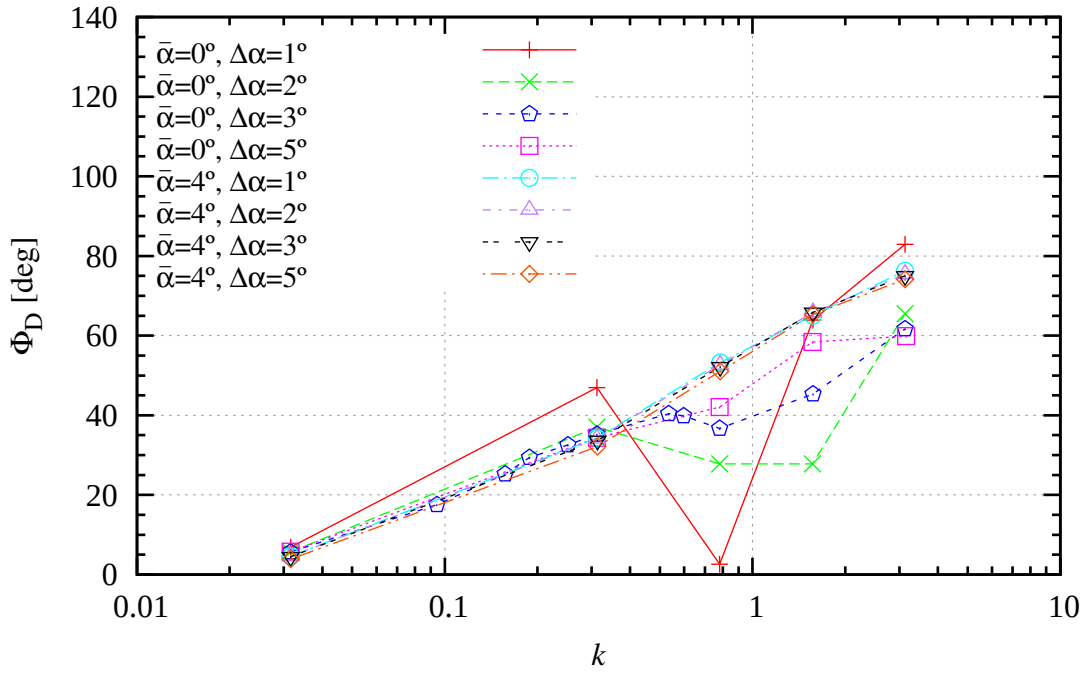

Figure B.7: 3D comparison of computed drag phase angle (Φ_D)for varying reduced frequency (k) at a Reynolds number of 3.36×10^5 for a mean incidence ($\bar{\alpha}$) of 0 and 4° at incidence amplitudes ($\Delta\alpha$) of 1, 2, 3, and 5°.

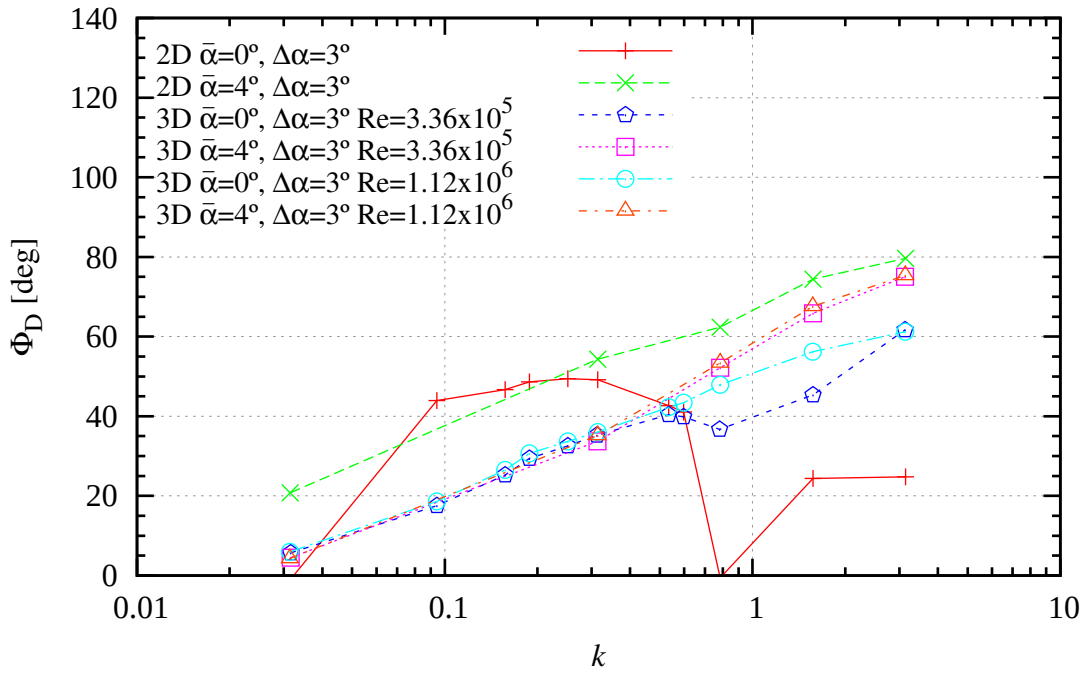

Figure B.8: 2D and 3D comparison of computed maximum drag phase angle (Φ_D) at varying reduced frequency (k) at a incidence amplitude ($\Delta\alpha$) of 3° for a mean incidence ($\bar{\alpha}$) of 0 and 4° and Reynolds number (Re) of 3.36×10^5 and 1.12×10^6.

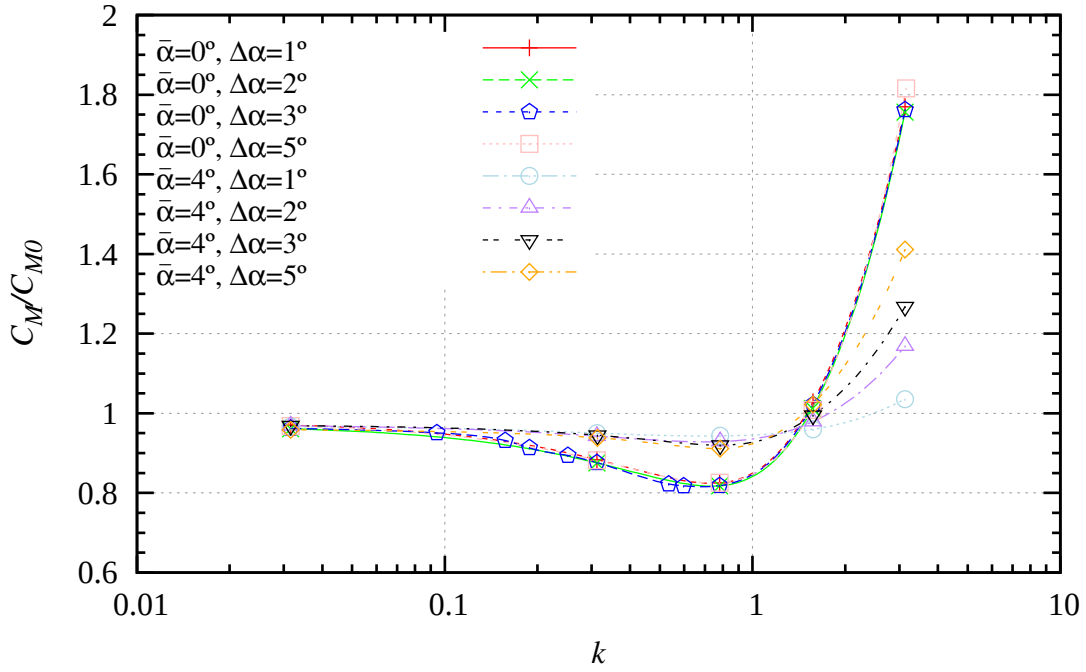

Figure B.9: 3D comparison of computed normalised maximum C_M for varying reduced frequency (k) at a Reynolds number of 3.36×10^5 for a mean incidence ($\bar{\alpha}$) of 0 and 4° at incidence amplitudes ($\Delta\alpha$) of 1, 2, 3, and 5°.

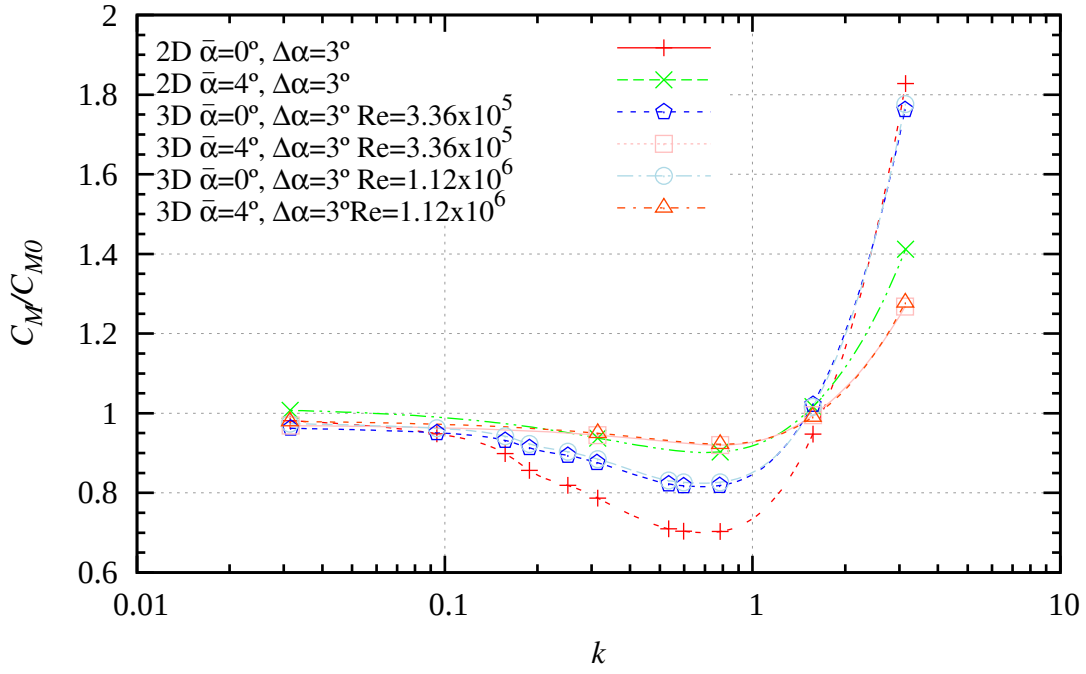

Figure B.10: 2D and 3D comparison of computed normalised maximum C_M at varying reduced frequency (k) at a incidence amplitude ($\Delta\alpha$) of 3° for a mean incidence ($\bar{\alpha}$) of 0 and 4° and Reynolds number (Re of 3.36×10^5 and 1.12×10^6

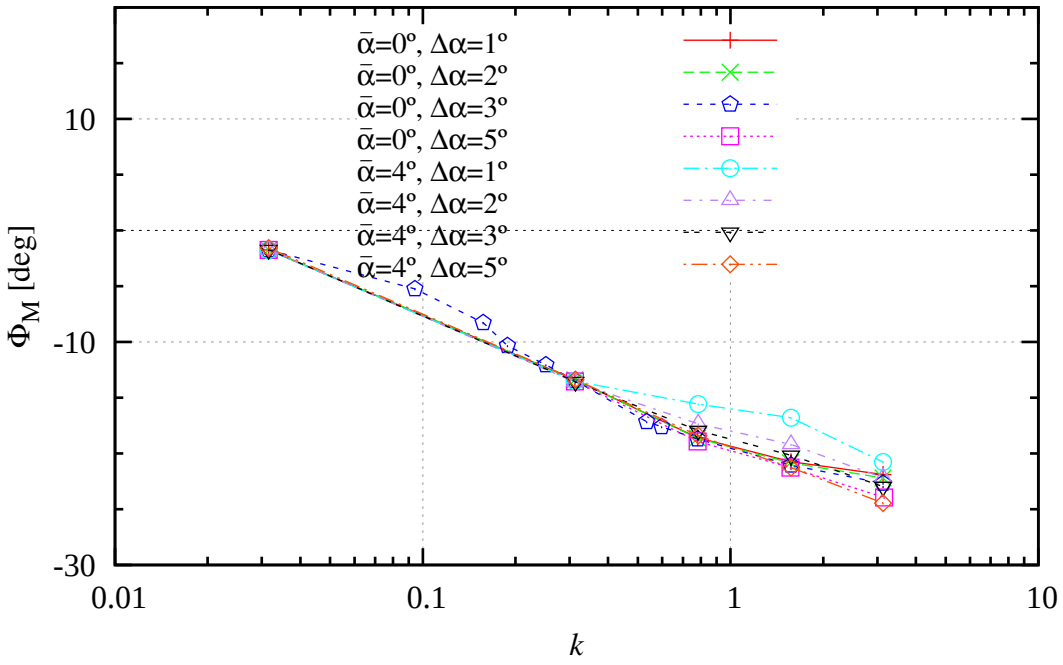

Figure B.11: 3D comparison of computed moment phase angle (Φ_M) for varying reduced frequency (k) at a Reynolds number of 3.36×10^5 for a mean incidence ($\bar{\alpha}$) of 0 and 4° at incidence amplitudes ($\Delta\alpha$) of 1, 2, 3, and 5°.

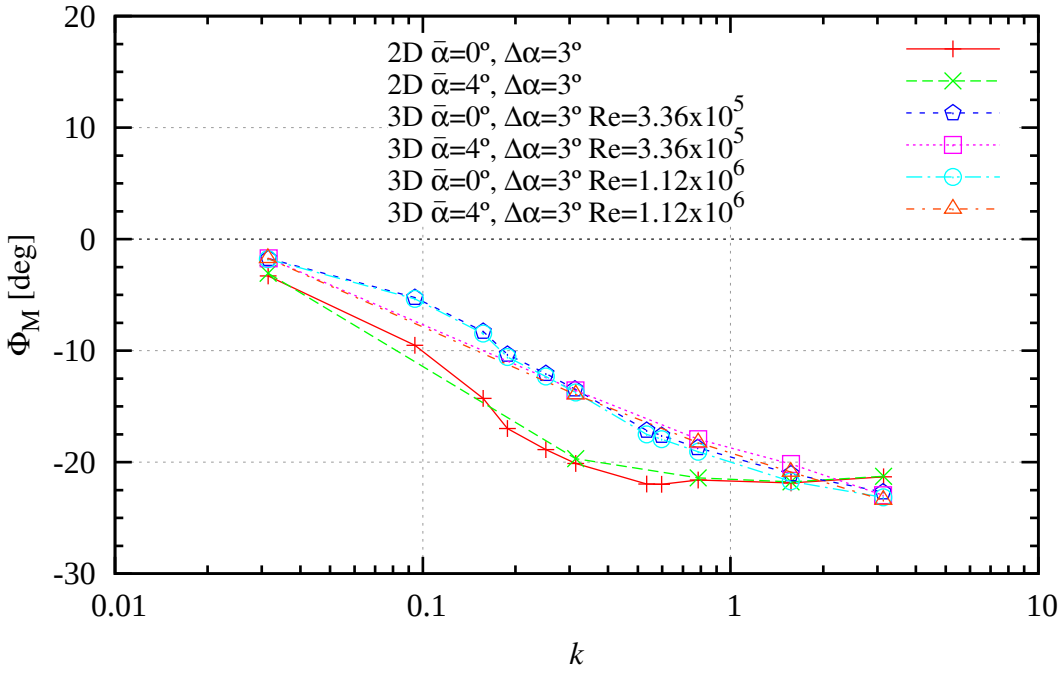

Figure B.12: 2D and 3D comparison of computed maximum moment phase angle (Φ_M) at varying reduced frequency (k) at a incidence amplitude ($\Delta\alpha$) of 3° for a mean incidence ($\bar{\alpha}$) of 0 and 4° and Reynolds number (Re) of 3.36×10^5 and 1.12×10^6.